UNIVERSITY OF STRASBOURG,

DOCTORAL SCHOOL OF CHEMISTRY SCIENCES

EDSC
École Doctorale des
Sciences Chimiques

UNIVERSITY OF BELGRADE,

DEPARTMENT OF CHEMISTRY

THESIS

presented by: **Predrag PETROVIĆ**

defended on : **10 September 2014**

Experimental and Theoretical Investigations of Intermetallic Interactions in Transition Metal Coordination and Organometallic Complexes

THESIS co-supervised by:
  Dr. Snežana ZARIĆ   Professor, Faculty of Chemistry, University of Belgrade
  Dr. Jean-Pierre DJUKIC   Directeur de Recherches au CNRS, University of Strasbourg

REVIEWERS:
  Dr. János ÁNGYÁN   Directeur de Recherches au CNRS, University of Lorraine
  Dr. Živadin BUGARČIĆ   Professor, Faculty of Sciences, University of Kragujevac

OTHER MEMBERS OF THE JURY:
  Dr. Vincent ROBERT   Professor, University of Strasbourg
  Dr. Miloš MILČIĆ   Professor, Faculty of Chemistry, University of Belgrade

UNIVERSITÉ DE STRASBOURG,

ECOLE DOCTORALE DES SCIENCES CHIMIQUES

UNIVERSITÉ DE BELGRADE,

FACULTE DE CHIMIE

THÈSE

présentée par: **Predrag PETROVIĆ**

soutenue le : **10 Septembre 2014**

Etudes expérimentales et théoriques des interactions intermétalliques en transition métal coordination et complexes organométalliques

THÈSE co-dirigée par :
  Dr. Snežana ZARIĆ   Professeur, Faculté de chimie, Université de Belgrade
  Dr. Jean-Pierre DJUKIC   Directeur de Recherches au CNRS, Université de Strasbourg

RAPPORTEURS :
  Dr. János ÁNGYÁN   Directeur de Recherches au CNRS, Université de Lorraine
  Dr. Živadin BUGARČIĆ   Professeur, Faculté de sciences, Université de Kragujevac

AUTRES MEMBRES DU JURY :
  Dr. Vincent ROBERT   Professeur, Université de Strasbourg
  Dr. Miloš MILČIĆ   Professeur, Faculté de chimie, Université de Belgrade

UNIVERZITET U STRAZBURU,

DOKTORSKA ŠKOLA HEMIJSKIH NAUKA

EDSC
École Doctorale des
Sciences Chimiques

UNIVERZITET U BEOGRADU,

HEMIJSKI FAKULTET

DOKTORSKA TEZA

prezentuje: **Predrag PETROVIĆ**

datum odbrane : **10 Septembar 2014**

Eksperimentalno i teorijsko ispitivanje intermetalnih interakcija u koordinaciji prelaznih metala i organometalnim kompleksima

Ko-mentori:
  Dr. Snežana ZARIĆ   Redovni profesor, Hemijski fakultet, Univerzitet u Beogradu
  Dr. Jean-Pierre DJUKIC   Directeur de Recherches au CNRS, Univerzitet u Strazburu

Izvestioci:
  Dr. János ÁNGYÁN   Directeur de Recherches au CNRS, Univerzitet Loren
  Dr. Živadin BUGARČIĆ   Redovni profesor, Prirodno-matematički fakultet, Univerzitet u Kragujevcu

Ostali članovi komisije:
  Dr. Vincent ROBERT   Profesor, Univerzitet u Strazburu
  Dr. Miloš MILČIĆ   Vandredni profesor, Hemijski fakultet, Univerzitet u Beogradu

The work on this thesis was performed at the Department of Chemistry, University of Belgrade, Serbia and Laboratoire de Syntèses Métallo-Induites – LSMI (UMR7177), Institute de Chimie, University of Strasbourg, France since 2010.
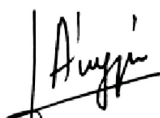
The defense took place on 10th of September, 2014 at Institute de Chimie, Strasbourg, France, in front of the PhD committee:

Prof Dr Snežana Zarić,
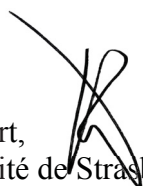Full professor, Department of Chemistry, University of Belgrade, supervisor

Dr Jean-Pierre Djukic,
Directeur de Recherches au CNRS, Laboratoire de Chimie et Systémique OrganoMétalliques (LCSOM), Institut de Chimie, Université de Strasbourg, France, supervisor

Dr Janos Angyan,
Directeur de Recherches au CNRS, Faculté des Sciences, Université de Lorraine, France

Prof Dr Živadin Bugarčić,
Full professor, Faculty of Science, University of Kragujevac

Prof Dr Vincent Robert,
Professeur à l'Université de Strasbourg, France

Dr Miloš Milčić,
Assistant professor, Department of Chemistry, University of Belgrade

Djedu Nikoli

(1932-2014)

Acknowledgements

have showed me a lot of how to work as an experimentalist. Also, I would like to thank Nicolas Renard and Genevieve Stoll who have made my life in France much easier by helping me deal with the administration issues and the rest of the people who had been part of the lab during my stay in Strasbourg: Dr. Bastien Boff, Dr. Jean-Thomas Issenuth, Dr. Noel Angel Espinosa, Mustapha Hamdaoui and Frederic LaPaglia.

Next, I would like to thank all the people working in the technical services of the University of Strasbourg: Bruno Vincent, Lionel Allouche, Jean-Daniel Sauer, Maurice Cope, Helene Nierengarten, Melanie Lebreton, Martine Heinrich, Corinne Bailly and Lydia Brelot for all the help and expertise they provided.

Also, I would like to thank Dr. Horst Borrmann from Max Planck Institute for Chemical Physics of Solids, Dresden, Germany for providing the access to CSD database and very nice discussions and Dr. Stefan Grimme from Mulliken Center for Theoretical Chemistry at University of Bonn, Germany for fruitful collaboration and huge help provided on working on number of issues addressed in this thesis.

Želeo bih da se zahvalim i svim prijateljima koji su me podržavali, verovali u mene i imali razumevanja sve ovo vreme.

Na kraju bih želeo da se zahvalim svojoj porodici, čija su me bezrezervna podrška i ljubav uvek gurali napred i pomogli da postanem osoba na koju mogu biti ponosni.

Predrag

Abstrakt

Uvod

Nekovalentne interakcije se nalaze svuda u prirodi. One su odgovorne za niz procesa i osobina molekula. Ipak, ove intermolekulske interakcije su po prirodi slabe. Svuda gde postoje molekuli, javljaju se i nekovalentne interakcije. Procesi samoorganizacije, na koje slabe intermolekulske sile imaju uticaj, igraju važnu ulogu u građenju jako kompleksnih molekula sa specifičnim osobinama. Reverzibilnost nekovalentnih interakcija omogućava molekulskim sistemima da se brzo prilagode promenama u okolini izazvanim promenom uslova prisutnih na Zemlji.

Ove slabe interakcije, to jest nekovalentne "vezivne" interakcije razlikuju se od klasičnih kovalentnih interakcija i njihovih varijacija u tome što preklapanje "elektronskih oblaka" interagujućih fragmenata postoji samo u maloj meri ili ne postoji uopšte. Ovakvo specifično ponašanje javlja se kod H-vezivanja, π-π, CH-π i X-H-π (vezivnih) interakcija, koje su sve u izvesnoj meri povezane sa efektivnom ulogom Londonove disperzione sile. Londonova disperziona sila je najslabija intermolekulska sila. To je privremena privlačna sila koja se javlja kao posledica trenutno indukovane polarizacije između multipola u molekulu. Jačina Londonove sile raste sa brojem elektrona usled povećanja polarizabilnosti, to jest disperzije elektronskog oblaka.

Zbog njihovog velikog značaja, veliki napor je uložen u bolje razumevanje i opisivanje ovih interakcija u oblasti hemije, koristeći i eksperimentalne i teoretske metode. Međutim, ovo je i dalje težak zadatak.

U poslednjoj deceniji došlo je do razvoja različitih metoda koje su korišćene u proučavanju nekovalentnih interakcija, a posebno steking interakcija. Najčešće su proučavane steking interakcije između aromatičnih molekula ili fragmenata, međutim, pokazano je da i drugi planarni molekuli i fragmenti takođe učestvuju u paralelnim interakcijama. Analizom podataka u Kembridžkoj strukturnoj banci podataka, identifikovano je postojanje steking interakcija između helatnih i C_6 aromatičnih prstenova u kvadratno-planarnim kompleksima prelaznih metala. Planarni helatni prstenovi sa delokalizovanim π-vezama takođe grade CH/π interakcije sa C_6 aromatičnim prstenovima. Međutim, analizom CSD-a utvrđeno je da su u ovim kompleksima steking interakcije zastupljenije od CH/π interakcija.Planarni helatni prstenovi takođe mogu da grade steking interakcije sa drugim helatnim prstenovima. U kristalnim strukturama koje se nalaze u CDS-u pronađen je veliki broj helat-helat steking interakcija. Kod ovih struktura su normalne udaljenosti slične onima koje postoje kod steking

interakcija između organiskih aromatičnih prstenova, ali gde se ofset dva interagujuća helatna prstenova može razlikovati od onog između dva organska aromatična molekula.

Proučavanje steking interakcija kod kvadratno-planarnih kompleksa prelaznih metala sa terpiridin, fenantrolin i bipiridin ligandima bi mogle pomoći u boljem razumevanju interesantnih osobina koje ovi kompleksi pokazuju, od luminiscencije do biološke aktivnosti. Ovi kompleksi su pronašli široku primenu, na primer kao fotoaktivni uređaji i antitumorni agensi. Otkriveno je i da oni interaguju sa DNK interkalirajući se između parova baza DNK.

Tokom poslednjih 40 godina, velika pažnja je posvećena izučavanju hemijskih i fizičkih osobina tetrakis(izonitril)Rh(I) kompleksa, što se može videti iz velikog broja izveštaja koji pokazuju njihove fizičke osobine, kao i njihovu neobičnu tendenciju da spontano grade adukte i oligomere kako u rastvoru tako i u čvrstom stanju.

Formiranje ovih oligomera je uvek praćeno velikim promenama u elektronskom spektru rastvora, što je okarakterisano pojavom nove trake absorpcije i rastom intenziteta na većim talasnim dužinama sa povećanjem koncentracije monomera. Ovaj tipičan spektroskopski zapis dimerne i trimerne forme prikazuje male promene u elektronskoj strukturi izazvane samo-agregacijom dva identična kvadratno-planarna d^8 fragmenta u orijentacije licem-ka-licu. Ova osobina je prvobitno nagovestila postojanje d^8-d^8 interakcije koja bi delovala kao vučna sila u procesu takozvane samo-agregacije. Novi elektronski prelazi koji potiču od metal-ligand prenosa šarže, bili su predmet više istraživanja posebno jer je utvrđeno da su odgovorni za specifične fotohemijske/fizičke i elektrohemijske osobine navedenih oligomera, koje se značajno razlikuju od odgovarajućih monomera. Tendencija oligomera da podležu reakcijama prenosa elektrona i oksidacijama u kojima dolazi do formiranja M-M veze kada su izloženi svetlosti pokazana je u brojnim slučajevima. Ova tendencija je podstakla razvoj premošćenih analoga ovih kompleksa i na primer procenu njihove primene kao katalizatora u reakcijama konverzije solarne energije. Uprkos velikim naporima koji su uloženi u ispitivanje fotofizičkih osobina ovih binuklearnih Rh(I)-Rh(I) agregata, malo informacija je sakupljeno o stvarnoj prirodi interakcija koje upravljaju procesom samoagregacije katjonskih monomera.

U skorašnjem radu dat je dokaz kojim se potvrđuje efektivnost Londonove disperzione sile da deluje ne samo između dva metala, već značajno i kroz sastavljene monomerne jedinice, i tako nadvladavajući Kulonovu odbojnu interakciju koja se javlja između dva pozitivno naelektrisana fragmenta kod ove klase kompleksa. Iako se fenomen koji je opisan u

Abstrakt

ovom radu može smatrati trivijalnim i značajnim u brojnim naelektrisanim hemijskim sistemima, on do tada nije bio detaljno analiziran i objašnjen za ovu klasu kompleksa.

Jedan od retkih „hemijskih događaja" u kojima se smatra da nekovalentne interakcije igraju značajnu ulogu je „hiralno prepoznavanje" koje se ogleda u spontanom razdvajanju enantiomera od dijastereomera u katalitičkim ciklusima kao i u stehiometrijskim reakcijama. Razumevanje uzroka evolucije sistema u jednom određenom pravcu, i pored drugih, kinetički ili termodinamički povoljnijih, i otkrivanje zašto se stereo-diskriminacija javlja u prividno jako konfiguraciono labilnim kompleksima ili sistemima molekula, je aktivna oblast istraživanja u hemiji. Štaviše, uzimajući u obzir najnovija saznanja o ulozi Londonove disperzione sile u nekovaletnim interakcijama za dizajn novih katalizatora je trenutni trend u sintetičkoj i računarskoj hemiji.

Razvoj novih lekova i razumevanje njihovih osobina i aktivnosti je direktno povezano sa razumevanjem nekovalentnih interakcija. Počev od otkrića citotoksičnosti Cisplatina sredinom 1960-ih godina otvoreno je novo poglavlje u hemiji prelaznih metala koje sadrži primenu koordinacionih kompleksa u terapeutske svrhe za tretiranje bolesti kao što je kancer. Klinička ograničenja usled toksičnosti Cisplatina podstakla su razvoj novih antikancerogenih agenasa pozajmljujući cis-bisaminoplatina(II)$^{2+}$ motiv iz Cisplatina koji se smatra esencijalnim za očuvanje citotoksičnosti jer proizilazi iz deformacije i denaturacije tumorne DNA Cisplatinom. Oksaliplatin (Eloxatin™) i Karboplatin pripadaju ovoj klasi klinički odobrenih lekova koje pokazuju spektar aktivnosti za razne grupe malignih ćelija kao i čitav novi set sporednih efekata koji zahtevaju pažljivu formulaciju. Ovi kompleksi su pokazali interesantno ponašanje, a to je dug rok trajanja u koncentrovanim rastvorima. Dabrovijak i saradnici su predložili postojanje ovih kompleksa kao dimera u relativno koncentrovanim rastvorima, što bi moglo objasniti zašto ne dolazi do njihove hidrolize do bis-akva kompleksa u koncentrovanim infuzijama, procesa koji se najverovatnije događa u razblaženim neutralnim i baznim rastvorima. Postojanje oligomera u rastvoru koje su oni pokazali ^{1}H NMR spektroskopijom je donekle upitno, ali je ESI masena spektroskopija pokazala postojanje oligomera u gasnoj fazi. Međutim, pitanje prirode sila koje utiču na formiranje oligomera ovih kompleksa u rastvoru ili gasnoj fazi i dalje postoji. Iz kristalografskih podataka je očigledno da je organizacija ovih kompleksa cis-platinskog tipa uslovljena direkcionim efektom intermolekulskog H-vezivanja, čime se favorizuju različiti modovi intermolekulskih uređenja (gomile, trake). Prosto posmatranje supramolekulskih mreža, međutim, ne može reći mnogo o verovatnom ponašanju ovih molekula u molekulskim agregatima na manjoj razmeri u gasnoj

fazi ili rastvoru, gde disperzione sile, često previđene Londonove sile, u kombinaciji sa H-vezivanjem možda igraju ključnu ulogu u osiguravanju „nekovalentne dimerne" strukture. Spontana agregacija kvadratno-planarnih d^{10} platinskih kompleksa takođe postavlja pitanje i stvarnog doprinosa korelaciono zasnovanih d^{10}-d^{10} interakcija.

Nekovalentne interakcije takođe igraju veliku ulogu u supramolekulima i supramolekuskoj hemiji. Bilo to dizajn lekova, razumevanje ćelijske strukture ili bioloških/biohemijskih procesa, ispitivanje nekovalentnih interakcija u supramolekulskoj hemiji koristeći teoretske i eksperimetalne metode pokazalo se kao esencijalno.

Ciljevi

Glavni cilj ove teze bio je da se ispita uloga koju nekovalentne interakcije, a posebno Londonova (disperziona) sila, igra u koordinacionoj hemiji prelaznih metala. Istraživanje je sprovedeno na nekoliko tema kao što su steking interakcije u bipy kompleksima, samoagregacija organometalnih kompleksa u gasnoj fazi i rastvoru i td., koristeći razne eksperimentalne i teorijske metode koje su nam bile dostupne.

Metodologija

Pretraga CSD baze (izdanje Novembar 2012, verzija 5.34) je izvršena koristeći *ConQuest1.15* program kako bi se pronašle sve strukture sa kvadratno-planarnim bipy kompleksima. Pretraga kristalnih struktura je izvedena koristeći sledeće kriterijume: a) kristalografski R faktor < 10%, b) koordinate bez grešaka po kriterijumima korišćenim u CSD-u, c) položaji H atoma su normalizovani koristeći standardne X-H dužine veza iz CSD-a (O-H = 0.983 Å; C-H = 1.083 Å i N-H = 1.009 Å), d) bez polimernih struktura, e) strukture sa disorderom su isključene, f) strukture rešene difrakcijom iz praha nisu uzete u obzir.

DFT proračuni su izvedeni koristeći disperziono-korigovane Becke-Lee-Yang-Parr (BLYP-D3, D3-BJ), Tao-Perdew-Staroverov-Scuseria (TPSS-D3) i Perdew-Burke-Ernzerhof (PBE) funkcionale implementirane u ADF$^{®}$: Amsterdam Density Functional programskom paketu (ADF2012.01) i Gaussian09 programskom paketu (verzija D.01) na model sistemima konstruisanim na osnovu kristalnih struktura nađenih u CSD-u. *Ab initio* proračuni su urađeni u Gaussian09 programu koristeći MP2 i CCSD(T) funkcionale. Skalarni relativistički efekti su tretirani ZORA pristupom dok su korišćeni bazis setovi bazirani na orbitalama Slejterovog tipa (STO): all-electron (AE) ZORA/TZP, ZORA/TZ2P i ZORA/QZ4P i na orbitalama

Gausijanskog tipa (GTO): def2-TZVP, aug-cc-pVDZ, aug-cc-pVTZ i aug-cc-pVQZ. Svi proračuni su rađeni u gasnoj fazi ili su tretirani koristeći solvatacioni model. Solvatacija vodom, DMSO-om i hlorobenzenom je simulirana COSMO solvatacionim modelom koristeći Klamtove vrednosti Van der Valsovih radijusa za atome. Kako bi se odredile Gibsove entalpije solvatacije, koje bi dale $\Delta\delta G_{solv}$ parametar potreban za procenu vrednosti Gibsove entalpije formiranja inkluzionih kompleksa u idealizovanom rastvaraču (vodi), korišćen je COSMO-RS kontinualni solvatacioni model. Termodinamički parametri su izračunati iz statističkih podataka, tj. unutrašnje energije i entropije koje su dobijene računanjem vibracionih frekvencija. Optimizacije geometrija minimizacijom energetskog gradijenta je u svim slučajevima izvedeno koristeći C_1 i C_2 tačkovne grupe simetrije. Inter-fragmentna Kon-Šam orbitalna analiza interakcija je izvedena na geometrijama optimizivanim ADF paketom. Wiberg-ovi indeksi veze za ADF-optimizovane geometrije (koristeći AE-TZP bazis set) su izračunati pomoću GENNBO 5.0 ekstenzije za ADF. BSSE je izračunata counterpoise metodom (CP). Standardna „zero-damping" formula i racionalni damping do konačnih vrednosti za male interatomske udaljenosti po formulaciji Bekea i Johnsona- (BJ-damping) je korišćena za konstrukciju kriva disperzione energije. Grimme-ova DFT-D3 šema računanja disperzionih koeficijenata je korišćena u svim proračunima. ETS-NOCV kao i ELF analize su izvedene koristeći optimizovane geometrije u paketu ADF2012. Šeme molekulskih struktura i orbitala su prikazane pomoću programa ADFview.

Sva ITC merenja su izvedena korišćenjem Waters-SAS nanoITC uređaja opremljenog sa dve „hastealloy" ćelije od nerđajućeg čelika, svaka zapremine 1 mL. Svi vodeni rastvori su pripremljeni sonikacijom suspenzija kompleksa u čistoj vodi i naknadno su temeljno degazirani pod sniženim pritiskom. Organski rastvarači su sveže destilovani i degazirani pre upotrebe.

Rezultati i diskusija

Rezultati prikupljeni tokom izrade ove teze organizovani su u nekoliko zasebnih poglavlja koja su tematski različita, ali su i dalje povezana u pokušaju da se bolje razumeju nekovalentne interakcije, a posebno uloga disperzije u interesantnim osobinama organometalnih kompleksa prelaznih metala. Odgovori na postavljena pitanja traženi su koristeći razne eksperimentalne i teorijske metode koje su nam bile dostupne.

U kvadratno-planarnim kompleksima sa bipiridinskim ligandom, u kojima je helatni prsten spojen sa dva piridinska prstena, kompleksi mogu biti strukturno organizovani tako da

Abstrakt

omogućavaju lak pristup helatima kako bi međusobno interagovali. Široka primena ovih kompleksa čini ih interesantnim za proučavanje nekovalentnih steking interakcija u čvrstom stanju. Stoga smo proučavali kvadratno-planarne komplekse sa bipiridinskim ligandima statistički analizirajući strukture dostupne u CSD-u. Steking interakcije između kvadratno-planarnih kompleksa metala koji sadrže bipiridine (bipy) kao ligande, proučavane su analiziranjem podataka iz CSD-a i DFT proračunima. Kako bismo pronašli intermolekulske steking interakcije između bipiridina, sproveli smo tri pretrage. U prvoj smo tražili sve strukture tako da rastojanje između centroida između bilo kojih piridinskih fragmenata (udaljenost d_{PP}) bude manje od 4,6 Å, u drugoj je kriterijum bio da je udaljenost između centara piridina i helatnog prstena (udaljenost d_{PC}) manja od 4,4 Å, a u trećoj je kriterijum bio da udaljenost između centroida helata (udaljenost d_{CC}) bude manja od 4,2 Å. Rezultati sve tri pretrage su spojeni i analizirani zajedno kako bi se osiguralo da sve moguće steking interakcije budu uključene. Podrazumevali smo da dva prstena grade steking interakciju kada je diedralni ugao između srednjih ravni bipiridina manji od 10°. U najvećem broju kristalnih struktura dva bipiridinska liganda orjentisani su glava-ka-repu.

Na osnovu geometrijskih parametara, torzionog ugla T_2, udaljenosti r_{MM}, i ugla φ, klasifikovali smo međusobno preklapanje bipy liganada u šest tipova (I_a, I_b, I_c, I_d, II_a, i II_b tip). Najbrojnije su strukture sa preklapanjem tipa Ib sa velikom površinom preklapanja ($r_{MM} \leq 5$ Å, $\varphi \leq 35°$): tu postoji međusobno preklapanje piridinskih fragmenata, helatnih prstenova i preklapanje piridinskog i helatnog prstena. Geometrija kod ovih interakcija je često uslovljena sa preostala dva liganda koordinovana na trećem i četvrtom koordinacionom mestu, ili često molekulima (jonima) iz okoline u kristalnoj strukturi. Steking interakcije kvadratno-planarnih kompleksa sa bipy grade stekovane lance i dimere u kristalnim strukturama, gde je steking lanac sa naizmeničnim preklapanjem preferentan tip pakovanja za ove komplekse.

Proračuni pokazuju da energija steking interakcija između dva $[Ni(bipy)(CN)_2]$ kompleksa može biti veoma jaka, najjača izračunata energija je -31.7 kcal/mol. Najslabija izračunata energija interakcije, u kojoj dolazi do preklapanja samo jednog para piridinskih prstenova, ima energiju -7.3 kcal/mol. Kao što se može i pretpostaviti, rezultati proračuna pokazuju da smanjenje površine preklapanja dovodi do slabljenja energije interakcije. Rezultati nagoveštavaju i da su helat-aril interakcije jače od aril-aril interakcija, kao i to da je interakcija između piridinovih prstenova koji su koordinovani za metal jača od nekoordinovanih piridina.

Abstrakt

Oligomerizacija kvadratno-planarnih kompleksa Rh(I) je dobro dokumentovan u literaturi. Kako bi proučavali uticaj hiralnosti na ovaj proces samo-asocijacije i potencijal za hiralnim prepoznavanjem, nekoliko novih hiralnih Rh(I) kompleksa je sintetizovano i okarakterisano. Proces oligomerizacije je praćen UV/Vis spektroskopijom i ITC eksperimentima.

Nekoliko novih hiralnih Rh(I) kompleksa je sintetisano iz enantio-obogaćenih izonitrilnih liganada i fizički je okarakterisano. Naša namera je bila da proučavamo kako njihovu samoagregaciju u čvrstom stanju i rastvoru, tako i njihovu sposobnost da stabilizuju velike reaktivne anjone. Uprkos svim naporima, različitim tehnikama i velikom broju različitih kontra anjona, kao i različitim tehnikama kristalizacije, nismo uspeli da dobijemo kristale zadovoljavajućeg kvaliteta kako bi mogli da rešimo X-ray strukture.
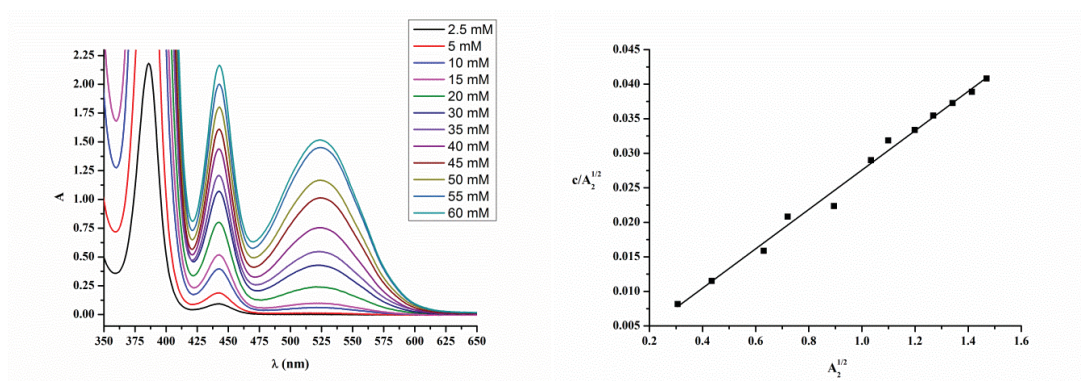
UV/Vis spektri RH1 u CH_3CN za različite koncentracije (levo). Grafik zavisnosti $[Rh]/\sqrt{A_{441nm}}$ vs. $\sqrt{A_{441nm}}$ (desno)

Oligomerizacija ovih kompleksa u rastvoru praćena je porastom nove trake absorpcije na većim talasnim dužinama sa porastom koncentracije monomera. Ova osobina nam je omogućila procenu konstante ravnoteže za formiranje dimera i trimera iz UV/Vis spektara koristeći metodu Grey-a i saradnika za raspon koncentracija.

$$\frac{[Rh]}{\sqrt{A_2}} = \frac{1}{\sqrt{\varepsilon_2 K_1}} + \frac{2\sqrt{A_2}}{\varepsilon_2} + \frac{3K_2 A_2}{\varepsilon_2\sqrt{\varepsilon_2 K_1}}$$

$$A_3 = \frac{\varepsilon_3 K_2 \sqrt{A_2^3}}{\varepsilon_2\sqrt{\varepsilon_2 K_1}}$$

Gibsova slobodne energije izračunate iz dobijenih konstanti ravnoteže su ΔG_f^{dimer} = -5.7 kcal/mol i ΔG_f^{trimer} = - 2.2 kcal/mol za Tetrakis(S-(-)-1-feniletilizocijanid)rodijum(I) hlorid (**RH1**) u acetonitrilu pri konstantnoj jonskoj sili (0.1 M (n-Bu₄N)PF₆ kao bufer). Ovi rezultati nagoveštavaju da je proces oligomerizacije u rastvoru acetonitrila povoljan. Koristeći

istu metodologiju, procenili smo ΔG_f^{dimer} za enantio-čiste tetrakis(R-(-)-1-cikloheksiletilizocijanid)rodijum(I) hlorid (**RH3**, ΔG_f^{dimer} = -5.7 kcal/mol) i tetrakis(S-(+)-1-cikloheksiletilizocijanid)rodijum(I) hlorid (**RH4**, ΔG_f^{dimer} = -9.7 kcal/mol). ΔG_f^{dimer} za mešavinu ovih enantiomera (50%(R)-50%(S), 60%(R)-40%(S), 70%(R)-30%(S), 80%(R)-20%(S) i 90%(R)-10%(S)) procenjena je u rasponu od -6 do -10 kcal/mol, ali jasna korelacija između vrednosti ΔG_f^{dimer} i odnosa enantiomera nije mogla da se uspostavi. ΔG_f^{dimer} je takođe procenjen iz absorpcionog spektra u rastvoru hlorobenzena (-3,89 kcal/mol) i upoređen je sa rezultatom dobijenim ITC titracijom 20,4 mM rastvora RH3 u čist hlorbenzen (-2,7 kcal/mol). Ovi rezultati pokazuju prilično dobro slaganje i ukazuju na slabiju tendenciju kompleksa da formira dimere u hlorobenzenu.

Dabroviak i saradnici su proučavali neobičnu stabilnost i neaktivnost Oksaliplatina i Karboplatina u koncentrovanim rastvorima. Oni su kao objašnjenje predložili oligomerizaciju ovih platinskih kompleksa u rastvoru. Analiza neobične stabilnosti leka Oksaliplatina u koncentrovanom rastvoru je detaljno sprovedena. U skladu sa prethodno objavljenim rezultatima koje su prikazali Dabowiak i saradnici, potvrdili smo težnju Oksaliplatina (**1**), Oksalipaladijuma (**2**) i Karboplatina (**3**) da grade dimere, kao i više oligomere u gasnoj fazi pod blagim uslovima elektrosprej jonizacije u prisustvu tragova mravlje kiseline i natrijumovih soli.

M= Pt, **1** (Oxaliplatin)
M= Pd, **2**   **3** (Carboplatin)
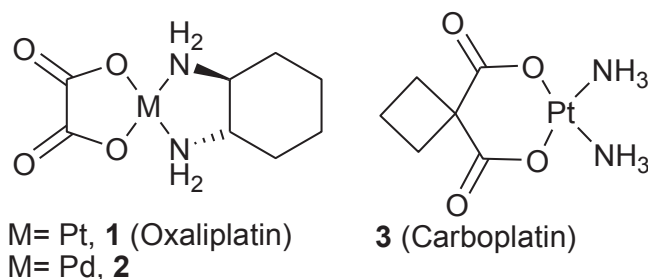
Cis-platinski kompleksi

Sva tri jedinjenja daju kompleksan signal u pozitivnom jonskom modu masenog spektra. Razlike u ESI+ masenim spektrima nisu primećene bilo da je rastvarač bila boda ili DMSO. ^{1}H DOSY NMR je tehnika koja se koristi kod stukturne analize makromolekulskih sistema i koja u nekim slučajevima može dati važne strukturne informacije za male molekulske sisteme. U slučaju rastvora **1**, **2** i **3**, građenje oligomera nije detektovano. Velike varijacije u koncentracijama pri graničnim vrednostima njihove rastvorljivosti nisu pokazale značajne promene u izmerenim hidrodinamičkim difuzionim koeficijentima, što je ukazalo na neefikasnost DOSY-ja delimično zbog nepreciznosti koja se nalazi u samoj definiciji

hidrodinamičke zapremine u Stoke-Einstein-ovoj jednačini; ova zapremina nije direktno povezana sa zapreminom analita koja može da se aproksimira, na primer sa van der Valsovom zapreminom isključenog rastvarača molekula.

Dalje ispitivanje samo-agregacije je bilo ograničeno na skoro planarne komplekse **1** i **2** koristeći ITC, koji omogućava precizno određivanje termodinamičkih parametara kao što je entalpija formiranja/disocijacije oligomera.

$$2\ \mathbf{2} \rightleftharpoons [\mathbf{2}]_2 \qquad K_2 = \frac{c_{[2]_2}}{c_1^2}$$

$$\mathbf{1} + \mathbf{2} \rightleftharpoons [\mathbf{1,2}] \qquad K_{1,2} = \frac{c_{[1,2]}}{c_1 \cdot c_2}$$

$$c_1^0 = c_1^* + c_{[1,2]} \quad c_2^0 = c_2^* + c_{[1,2]} \qquad K_{1,2}^* = \frac{c_{[1,2]}}{c_1^* \cdot c_2^*}$$

$$c_1^* = c_1 + c_{[1]_2} \quad c_2^* = c_2 + c_{[2]_2}$$

Formulacija konstanti asocijacije po Jangu i saradnicima

Disocijacija hipotetičkih dimera $[\mathbf{1}]_2$ i $[\mathbf{2}]_2$ (slika 9) je ispitivana titracijom 20 (**2**) i 10 mM (**1**) vodenim rastvorima analita u relativno veliku zapreminu čiste vode. Za jedinjenje **1**, ITC eksperimenti nisu dali značajan endotermni zapis preko pozadinskog signala koji potiče od razblaženja, što bi moglo da znači da su, ili proporcija oligomera u rastvoru ili entalpija disocijacije suviše slabi da bi dali značajan toplotni zapis. Za jedinjenje **2**, tipičan endotermni zapis je zabeležen, i on odgovara +0,5 ± 0,1 kcal/mol vrednosti entalpije za disocijaciju i konstanti asocijacije monomer-dimer od oko 3×10^{-4}. Ova vrednost konstante odgovara približnoj vrednosti Gibsove entalpije ΔG_{f2} od oko +4,6 kcal/mol i promeni entropije ΔS_{f2} od oko -17 cal/(K·mol). Jedinjenja **1** i **2** koja se razlikuju samo po prirodi metala i manjim strukturnim razlikama su testirana i na moguću međusobnu interakciju. Titracijom je, u seriji mikroinjekcija, pomešana ekvimolarna količina rastvora (10 mM) jedinjenja **1** i **2**. Rezultujući termogram je pokazao jasan egzotermni zapis dajući entalpiju asocijacije od -0,6 kcal/mol i prividnu konstantu asocijacije K_{12}^* od 5.1×10^{-4}, sa odgovarajućom Gibsovom entalpijom ΔG_{f12} od +4,5 kcal/mol i promenom entropije od -17 cal/(K·mol).
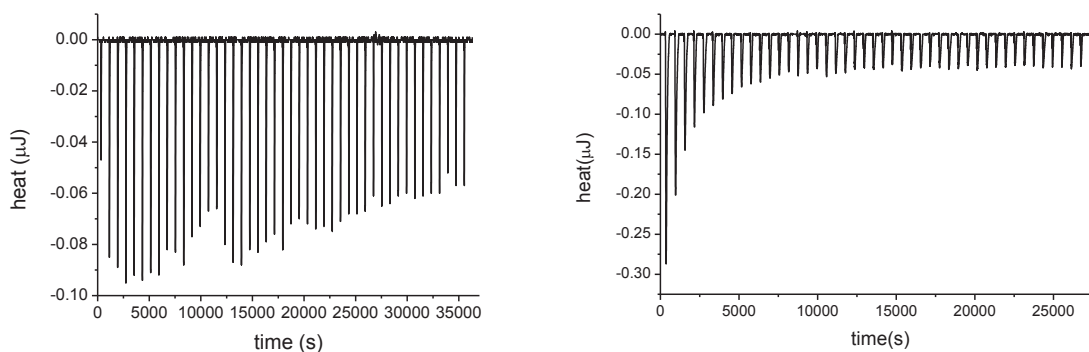
Termogrami razblaživanja koncentrovanih vodenih rastvora **1** (c = 20mM) u čistu vodu na 25 (levo) i **2** (c = 20 mM) u čistu vodu na 25 °C (desno)

Agregacija kompleksa **1-3** bilo u gasnoj fazi ili rastvoru je modelovana delimično na osnovu struktura pronađenih u CSD, i ispitivana koristeći DFT-D3 metode dizajnirane tako da na fizički pravilan način tretiraju privlačni doprinos Londonove sile uz ostale inter i intramolekulske interakcije koje su već pravilno tretirane konvencionalnim DFT metodama. Model sistemi korišćeni u istraživanju su glava-ka-repu sendvič α, glava-ka-repu smaknuta β i strana-ka-strani γ orijentacija.
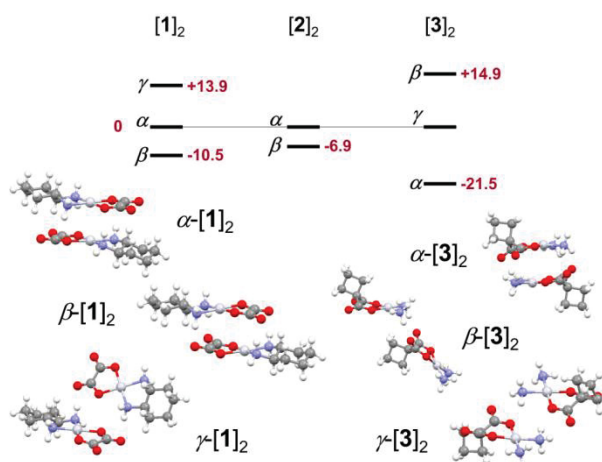
Relativne energije interakcije α, β i γ geometrija u gasnoj fazi za dimere **1-3** (u kcal/mol)

Energije interakcije za ova tri tipa orijentacija u gasnoj fazi pokazuju da je najpovoljnija β za [**1**]$_2$ i [**2**]$_2$ za otprilike 10, tj. 7 kcal/mol. Razdvajanje ΔE_{int} na doprinos Paulijevog odbijanja, orbitalnu, elektrostatičku i disperzionu komponentu daje informaciju o značaju poslednjeg terma, koja iznosi 27 %, 39 % i 49 % od ukupne energije interakcije za γ-[**1**]$_2$ (ΔE_{int} = -44,0 kcal/mol), β-[**1**]$_2$ (ΔE_{int} = -73,4 kcal/mol) i α-[**1**]$_2$ (ΔE_{int} = -60,1 kcal/mol). Orbitalni term je razdvojen u slučaju β−[**1**]$_2$ i β−[**2**]$_2$ koristeći ETS-NOCV metodu koju su razvili Mitoraj, Mihalak i Cigler i koja daje jasniju sliku o doprinosu H-vezivanja u

formiranju dimera u gasnoj fazi i koja je pokazala da ne postoji značajna metal-metal orbitalna interakcija.

Modelovanje efekata polarizacije na okolni rastvarač je izvedeno koristeći COSMO solvatacioni model u prvom slučaju. Krive potencijalne energije za α i β orijentacije su poređene u kontinuumu rastvarača DMSO (COSMO) kao način da se odbace orijentacije koje imaju pogrešno asimptotsko ponašanje. Ovo istraživanje izvedeno na orijentacijama α- i β-[**1**]$_2$ pokazalo je da prva orijentacija dovodi do nastajanja dimera koji nisu mogući u DMSO, dok druga orijentacija daje bolje asimptotsko ponašanje pretpostavljajući postojanje ovog dimera u rastvoru.

Solvatacija dovodi do apsolutnog smanjenja Gibsove entalpije formiranja za oko 30 kcal/mol. U svim slučajevima α orijentacija daje pozitivne vrednosti ΔG_f^{298} dok β orijentacija generalno daje negativne vrednosti. Ne uzimanje u obzir specifične interakcije molekula vode sa rastvaračem u solvatacionom modelu koji je ovde korišćen (COSMO) takođe može da bude odgovorno za primećeno odstupanje između teorijskih rezultata i eksperimenata, naime, teorija precenjuje sposobnost sistema da se samo-agreguje.

Jedan od načina da se proveri tačnost teorijskih modela je da se porede izračunati termodinamički parametri sa onima koji su dobijeni iz merenja standardnih nekovalentnih procesa asocijacije ITC tehnikom u rastvoru. Ovaj pristup je međutim ograničen tretiranjem solvatacije konvencionalnim DFT metodama. Tretiranjem podataka dobijenim ITC eksperimentom inkluzije kompleksa **1** (20 mM) u CB[7] (0,7 mM) u čistoj vodi koristeći model višestrukih vezivnih mesta (MSCBS) dobijena je entalpija inkluzije ΔH_{mod} od -8.7 kcal/mol i konstanta asocijacije K_1 od 2,4·10^5. Slično tretiranje podataka za inkluziju kompleksa **2** (17 mM) u CB[7] (1 mM) u čistoj vodi dalo je entalpiju inkluzije ΔH_{mod} od -6,6 kcal/mol i konstantu asocijacije K_1 od 7·10^4. S obzirom na visoke vrednosti konstante asocijacije, samosaglasnost termohemijskog modela je proverena računanjem entalpije asocijacije ΔH_{raw} integraljenjem ukupne molarne toplote oslobođene u procesu sa ITC termografa dajući vrednosti od -7,8 i -6,2 kcal/mol za formiranje inkluzionih kompleksa **1**@CB[7] i **2**@CB[7] potvrđujući tako izabrani termohemijski model.

Proračuni termodinamičkih parametara inkluzionih kompleksa su izvedeni na geometrijama optimizovanim krošćenjem COSMO pristupa solvataciji iz kartezijanskih koordinata koje je Kim objavio za **1**@CB[7] a koji su korišćenji i za modelovanje **2**@CB[7]. Ove geometrije su naknadno tretirane COSMO-RS pristupom kako bi se odredila Gibsova slobodna entalpija solvatacije i dobio $\Delta_\delta G_{solv}$ parametar, korišćen za procenu Gibsove

slobodne entalpije formiranja inkluzionog kompleksa u idealizovanoj vodi iz monomera **1-2** i CB[7]. Izračunata ΔG_f^{298} iznosi -12,3 kcal/mol za formiranje **1**@CB[7] i -13,6 kcal/mol za formiranje **2**@CB[7]. U slučaju kompleksa **1** i **2**, koji su oba blago lipofilna i sposobna da grade specifične reakcije sa molekulima vode, vrednosti afiniteta ka CB[7] dobijeni kombinacijom DFT-D i COSMO-RS metoda ostaju u okviru vrednosti dobijenih eksperimetalnim putem, posebno ako se uzme u obzir da je zanemarljiv energetski penal potrebno platiti za disocijaciju dimera $[\mathbf{1}]_2$ i $[\mathbf{2}]_2$.

$$\Delta G_f(water) = \Delta E_g + \Delta G_{RRHO} + \Delta G_{solv} + \Delta E_{disp}^{(3)} + \Delta E_{BBSE}$$

Uzimajući u obzir da je vrednost teorijske ΔG suma pojedinačnih velikih termova suprotnog znaka (jednačina), koji su izračunati bez specifičnog empirizma, tačan znak i red veličine izračunate vrednosti ΔG se čini kao dobar rezultat. Zato što je vrednost ΔH_{solv} indirektna veličina za koju COSMO-RS model nije razvijen, entalpija solvatacije nije tražena.

Još jedna reakcija koju smo razmatrali za procenu DFT-D metoda sa COSMO-RS modelom solvatacije je inkluziona reakcija $[Cp^*Ir^{III}(H_2O)_3](PF_6)_2$ (**4**) u CB[7]. ITC titracija 2 mM rastvora u čistoj vodi sa 10 mM rastvorom **4** dala je značajan egzotermalni zapis, za koji je utvrđeno da zavisi dosta od koncentracije CB[7]. Termograf sadrži dva važna dela: prvi je egzotermski doprinos koji potiče od interakcije domaćin-gost, i drugi endotermski koji potiče od razblaživanja rastvora **4** u rastvor CB[7]. Ukupna entalpija formiranja inkluzionog kompleksa je procenjena oduzimanjem termografskog zapisa razblaženja istog rastvora 4 u čistoj vodi. Ovo je dalo približnu vrednost entalpije formiranja kompleksa domaćin-gost između CB[7] i **4** od -3,7 kcal/mol u vodi, što je u granicama tipičnih vrednosti za nekovalentnu inkluziju koordinacionih kompleksa u ovoj klasi kavitanada.

Proračuni u gasnoj fazi osnovnog stanja relaksirane geometrije pokazuju da je formiranje kompleksa domaćin-gost podstaknuto disperzijom, koja čini 50% od ukupne energije interakcije ($\Delta E_{int} = -160,5$ kcal/mol, $\Delta E_{disp} = -86,8$ kcal/mol) za „pripremljene strukture" $[\mathbf{4}]^{2+}$ i CB[7] u inkluzionom kompleksu. Utvrđeno je da oko 79% privlačne disperzione energije potiče od CB[7] – Cp^* interakcije a da preostalih 21% potiče od CB[7]–$[Ir(H_2O)_3]$ interakcije. Vrednost energije formacije u gasnoj fazi za formiranje kompleksa domaćin-gost je $\Delta E_{fgas} = -127,5$ kcal/mol što nagoveštava da je formiranje $\{\mathbf{4}@CB[7]\}^{2+}$ u gasnoj fazi termodinamički povoljno. Kako bi se povećala tačnost pristupa solvataciji, sistem je preveden u neutralnu verziju koja je sastoji od istih struktura sa pridružena dva hlorova atoma (koji podražavaju PF_6^- anjon) koji se nalaze dalje od akva liganada i u oblasti niske gustine naelektrisanja u geometrijama lokalnog minimuma. Utvrđeno je da ΔG_f u mnogome

zavisi od relativnog položaja hloridovih anjona u odnosu na akva ligande. Iako vrednosti energije kompleksacije u gasnoj fazi za sva tri sistema idu od -69 do -137 kcal/mol, odgovarajuća Gibsova slobodna entalpija kompleksacije u vodi ΔG_f^{water} pokazuje samo male varijacije u vrednosti (4-10 kcal/mol). Ovo demonstrira precizost COSMO-RS modela koji kompenzuje nepovoljne katjon-hlorid interakcije bolje odgovarajući Gibsovoj entalpiji solvatacije i tako daje realistične vrednosti za ΔG_f^{water}.

Reakcije raskidanja halidnih mostova pokazale su se kao hemijski čiste i odgovarajuće za ITC eksperimente dajući jasan termohemijski signal. Ove reakcje su ispunile uslov koji je kao glavni cilj imao pronaći odgovarajuće procese za koje bi se mogli prikupiti precizni termohemijski podaci. Ti podaci bi kasnije mogli biti iskorišćeni za benčmarking najnovijih DFT-D metoda.

Sa ciljem dobijanja termohemijskih podataka za reakcije Pd(II) i Ru(III) dimera, koji poseduju halidne mostove, sa nukleofilima, sintetisali smo i fizički okarakterisali nekoliko novih kompleksa i izveli ITC titracione eksperimente. Korišćeni su sledeći kompleksi: [Pd(tBupTP)Cl]₂, [Pd(dmba)Cl]₂ i [Ru(p-cym)Cl₂]₂ (tBupTP − 4-(t-butil)-2-(p-tolil)piridin; dmba - N, N-dimetilbenzilamin; p-cym - η^6-p-cimen). Reakcije su odabrane tako da daju jedan stabilan proizvod jednostavnim mehanizmom raskidanja halidnog mosta nukleofilnom adicijom liganda, i njegovom koordinacijom za metal.

Četiri liganda su korišćena u titracionim reakcijama: trifenilfosfin (PPh₃), tricikloheksilfosfin (PCy₃), piridin (Pyr) i 4-terc-butilpiridin (tBuPyr). Koncentrovani rastvori liganada su korišćeni za titrovanje 1 mM rastvora dimera, dajući jak termografski zapis.

Entalpije reakcija dobijene titracijom:

1) Pyr (39,5 mM) u [Pd(tBupTP)Cl]₂ (1 mM), ΔH = -12,1 kcal/mol; tBuPyr (30,5 mM) u [Pd(tBupTP)Cl]₂ (1 mM), ΔH = -15,4 kcal/mol; PPh₃ (26,3 mM) u [Pd(tBupTP)Cl]₂ (1 mM), ΔH = -23,6 kcal/mol; PCy₃ (23,3 mM) u [Pd(tBupTP)Cl]₂ (1 mM), ΔH = -25,3 kcal/mol;

2) Pyr (37,9 mM) u[Pd(dmba)Cl]₂ (1 mM), ΔH = -15,1 kcal/mol; tBuPyr (24,9 mM) u [Pd(dmba)Cl]₂ (1 mM), ΔH = -16,4 kcal/mol; PPh₃ (23,8 mM) u [Pd(dmba)Cl]₂ (1 mM), ΔH = -26,5 kcal/mol; PCy₃ (24,5 mM) u [Pd(dmba)Cl]₂ (1 mM), ΔH = -32,8 kcal/mol;

3) Pyr (39,5 mM) u [Ru(p-cym)Cl₂]₂ (1 mM), ΔH = -16,2 kcal/mol; tBuPyr (27,5 mM) u [Ru(p-cym)Cl₂]₂ (1 mM), ΔH = -19 kcal/mol; PPh₃ (23,3 mM) u [Ru(p-cym)Cl₂]₂ (1 mM), ΔH = -28,4 kcal/mol; PCy₃ (23,3 mM) u [Ru(p-cym)Cl₂]₂ (1 mM), ΔH = -23,3 kcal/mol

Abstrakt

Termohemijski podaci dobijeni izvođenjem ITC eksperimenata sakupljeni su sa ciljem da se dobiju precizne eksperimentalne vrednosti za reakcije u rastvoru koje uključuju velike paladijumove i rutenijumove komplekse gde intramolekulske Londonove disperzione sile dugog dometa navodno igraju značajnu ulogu u stabilizaciji kompleksa. Ovi podaci su korišćeni za benčmark najnovijih DFT metoda sa korekcijom za disperziju kao i novih WFT metoda koje su razvili Grime i saradnici.

Resumé

Introduction

Les interactions non-covalentes sont omniprésentes dans la nature. Elles interviennent dans une large gamme de processus, au niveau des propriétés des molécules et des substances de la matière. Partout oû se trouvent des molecules, se trouvent egalement les interactions non-covalentes. Les forces intermoléculaires, faibles et réversibles, jouent un rôle dominant dans la construction de structures très complexes aux propriétés bien spécifiques, (ex. les processus d'auto-assemblage). C'est par cette réversibilité rapide rendu possible par les interactions non-covalentes que le système à la capacité de s'adapter, de manière dynamique, aux changements imposés par les conditions régnant sur Terre.

Ces faibles interactions, plus communément appelées, les interactions de "liaison" non-covalentes, se différencient des interactions covalentes, dans la mesure qu'il n'y a peu ou pas de recouvrement entre les "nuages d'électrons". Cette particularité se rencontre essentiellement dans la formation de liaisons hydrogènes, au niveau des interactions (liaisons) π-π, CH-π et XH-π qui sont liés, à des degrés divers, à la force de dispersion de London. La force de dispersion de London est la force intermoléculaire la plus faible. Il s'agit d'une force d'attraction temporaire qui résulte de la polarisation induite instantanément entre multipoles dans la molécule. La puissance des forces de London augmente avec l'accroissement du nombre d'électrons en raison de l'augmentation de la polarisabilité, c'est à dire la dispersion de nuage d'électrons.

Compte tenu de leur importance, un grand effort a été mis en oeuvre afin de pouvoir mieux comprendre et de décrire ces interactions dans le domaine de la chimie, à la fois expérimentalement que théoriquement. Pourtant, cela reste une tâche difficile.

Cette dernière décennie a montré le développement de différentes méthodes qui ont été utilisées pour étudier les interactions non-covalentes et en particulier les interactions de type "stacking". En général, ce sont les interactions d'empilement entre les molécules ou fragments aromatiques de molécules organiques qui sont étudiées, mais il a été démontré que d'autres molécules et fragments planes peuvent également faire des interactions parallèles. En analysant les données de la Cambridge Structural Database (CSD), les interactions d'empilement entre le chélate et les anneaux aromatiques C_6 ont été identifiées dans les structures cristallines de complexes de métaux de transition plan-carrés. Les anneaux de chélation plans avec des liaisons π délocalisées peuvent également former les interactions CH/π avec des anneaux aromatiques C_6. Cependant, l'analyse de la CSD a démontré que les interactions d'empilement sont préférables à des interactions π/CH dans ces complexes. Les

anneaux de chélation plans peuvent également former des interactions d'empilement avec des autres anneaux de chélation. Un grand nombre d'interactions d'empilement chélate-chélate ont été trouvé dans les structures cristallines de la CSD. Là, les distances normales sont similaires à celles trouvées dans les interactions d'empilement entre les anneaux organiques aromatiques. Où le décalage des deux anneaux de chélation en interaction pourrait être différent de celui entre les anneaux aromatiques organiques.

Les études des interactions d'empilement des complexes de métaux de transition plan-carrés avec des ligands terpyridyle (*terpy*), phénantroline (*phen*) ou bipyridine (*bipy*), pourraient contribuer à une meilleure compréhension des propriétés très intéressantes, allant de la luminescence à l'activité biologique de ces complexes. Ces derniers ont trouvé de nombreuses applications, par exemple dans des dispositifs photo-actifs et des agents anti-tumoraux. Il a également été constaté qu'ils interagissent avec l'ADN en s'intercalant entre les paires de bases.

Une grande attention a été portée au cours des 40 dernières années sur les propriétés chimiques et physiques des complexes tétrakis (isonitrile) Rh (I). Il a été mis en évidence et cela par un grand nombre de rapports, les propriétés physiques qui leur sont associées ainsi que leur prédisposition inhabituelle à former spontanément des adduits et oligomères en solution ainsi que dans l'état solide.

La formation de ces oligomères est toujours accompagnée de changements importants dans le spectre électronique (Uv-vis) de la solution. Ce dernier est caractérisé par la croissance d'une nouvelle bande d'absorption à des longueurs d'onde plus longues, lorsque la concentration en monomères augmente. Cette signature classique pour des formes dimères et trimères exprime les perturbations sensibles causées à la structure électronique du système par l'auto-association de deux fragments d^8 plan- carrés identiques disposés face à face. Cette propriété a initialement suscité des hypothèses sur une interaction spécifique d^8-d^8 qui agirait un peu comme une force motrice dans le processus nommé "l'auto-assemblage". Les nouvelles transitions électroniques provenant de transfert de charge métal-ligand, a fait l'objet d'une grande attention car il a été soupçonné responsable pour les propriétés spécifiques photochimiques/physiques et électrochimiques de ces oligomères, qui diffèrent clairement du comportement des monomères correspondants. La capacité des oligomères à facilement subit des réactions de transfert d'électrons et des oxydations mène à des complexes de liaisons M-M lors de l'exposition à la lumière a été démontrée dans de nombreux cas. Cette propriété a incité le développement d'analogues pontés et leur évaluation en tant que catalyseurs pour la conversion de l'énergie solaire par exemple. Malgré les efforts qui ont été investis dans la

recherche des propriétés photo-physiques de ces assemblées Rh(I)-Rh(I) binucléaires, que peu de résultats concernant l'origine réelle des interactions qui régissent le processus d'auto-agrégation des monomères cationiques on été obtenues.

Dans un récent rapport, il a été démontré que la force de dispersion de London ne s'applique pas exclusivement entre les deux centres métalliques mais significativement dans toutes les unités monomères assemblées, en contrecarrant l'interaction de Coulomb répulsive entre les fragments chargés positivement. Bien que le phénomène qui a été décrit puisse en fin de compte sembler banal il est cependant pertinent pour de nombreux systèmes chimiques chargés, il n'a pas été clairement démontré et analysé jusqu'à présent pour cette classe particulière de complexes de coordination.

L'un des rares "événements chimiques" dans lequel les interactions non-covalentes sont généralement considérées comme jouant un rôle central est "la reconnaissance chirale" qui fonctionne dans la résolution spontanée des énantiomères et diastéréoisomères, dans les cycles catalytiques et également dans les réactions stœchiométriques. Comprendre ce qui conduit un système à évoluer dans une direction privilégiée alors que de nombreux autres chemins sont cinétiquement ou thermodynamiquement plus favorable, et de découvrir pourquoi une stéréo-discrimination se produit entre les molécules – entre systèmes de molécules – qui sont apparemment de configuration très labiles, est un domaine de recherche très actif dans la chimie.

De plus, force de dispersion de London intervient dans la conception rationnelle de nouveaux catalyseurs se trouve être une tendance croissante parmi les chimistes de synthèse et de calcul.

Le développement de nouveaux médicaments, la compréhension de leurs propriétés ainsi que leur activité est directement liée à une meilleure compréhension des interactions non-covalentes. Depuis la découverte de la cytotoxicité du cisplatine au milieu des années 1960's, un nouveau paradigme pour la chimie de métal de transition a été ouvert, étant l'utilisation de complexes de coordination pour le traitement thérapeutique des maladies telles que les cancers. Les limites cliniques liées à la toxicité du cisplatine ont motivé le développement de nouveaux agents anti-cancéreux en considérant le cis-bisamminoplatinum(II)$^{2+}$ motif, comme bon substitut préservant les propriétés cytotoxiques. Découlant de la déformation et la dénaturation d'ADN tumoral induite par le cisplatine. L'oxaliplatine (Eloxatine™) et carboplatine appartiennent à une classe de médicaments cliniquement approuvés qui affichent un autre spectre d'activité sur différentes lignées de cellules malignes et montrent également toute une gamme de nouveaux effets secondaires nécessitant une utilisation prudente. Ces complexes peuvent être conservé sur une longue

durée dans des solutions concentrées. Dabrowiak et al. ont montré que ces complexes existent sous forme de dimères en solution relativement concentrée. Ce qui expliquerait pourquoi leur hydrolyse en complexes bis-aquo, un processus probable qui a lieu dans les préparations aqueuses diluées de manière neutres et basiques, est apparemment exclue dans les infusions concentrées. Les résultats obtenus dans la perspective de démonter l'existence en solution d'oligomères par spectroscopie RMN ^{1}H sont peu concluants, en revanche il a été possible de les identifier en phase gazeuse par spectroscopie de masse ESI. La question visant à déterminer la nature des forces motrices qui interviennent dans la formation de ces oligomères en solution ou en phase gazeuse est restée ouverte. Il est évident que d'après les informations structurales disponibles par le biais notamment de la cristallographie, qu'à l'état solide les complexes de type cisplatine est régie par l'effet directeur des liaisons H intermoléculaires, favorisant les différents modes d'arrangements intermoléculaires. Une simple observation des réseaux supramoléculaires n'en dit pas beaucoup sur le comportement probable de ces molécules lors d'assemblages moléculaires de petite échelle en phase gazeuse ou en solution dans lequel les forces de dispersion, souvent négligés par les forces de London, combinées avec des liaisons hydrogène peuvent jouer un rôle clé en assurant la cohésion d'un "dimère non-covalent". Le problème de l'agrégation spontanée des complexes de platine d^{10} plan-carrés soulève également la question du poids réel des interactions d-d intermétalliques à base de corrélation électronique.

Les interactions non-covalentes jouent également un rôle important dans les supermolécules et la chimie supramoléculaire. Que ce soit la conception de médicaments, la compréhension de la structure cellulaire ou des processus biologiques / biochimiques, l'étude sur les interactions non-covalentes dans la chimie supramoléculaire utilise des méthodes théoriques et expérimentales qui se sont avérées essentielle.

Objectifs

L'objectif principal de la thèse était d'étudier le rôle que les interactions non-covalentes, et en particulier les forces (de dispersion) de London, jouent dans la chimie de coordination des métaux de transition. L'étude a été menée en abordant plusieurs questions telles que les interactions d'empilement en complexes bipy, l'auto-agrégation des complexes organométalliques en phase gazeuse etc, ceci en utilisant diverses méthodes expérimentales et théoriques dont nous disposions.

Méthodes

Une recherche CSD (publié en Novembre 2012, version 5.34) a été effectuée en utilisant le programme ConQuest1.15 pour extraire toutes les structures contenant des complexes bipy plan-carrés. La recherche de structures cristallines a été faite selon les critères suivants: a) le facteur R cristallographique <10%, b) les coordonnées sans erreur selon les critères utilisés dans la CSD, c) les positions d'atome H ont été normalisées en utilisant les longueurs des liaisons X-H par défaut CSD (O-H = 0.983 Å; C-H = 1.083 Å et N-H = 1.009 Å), d) aucune structure de polymère, e) les structures en désordre n'ont pas été incluses, f) les structures résolues de poudre n'ont pas été prises en compte non plus.

Les Calculs DFT ont été effectués en utilisant des fonctionnelles de dispersion corrigée Becke-Lee-Yang-Parr (BLYP-D3, D3-BJ), Tao-Perdew-Staroverov-Scuseria (TPSS-D3) et Perdew-Burke-Ernzerhof mises en œuvre dans l'ADF®: Amsterdam Density Functional paquet (ADF2012.01) et le paquet Gaussian09 (version D.01) sur des systèmes modèles fabriqués à partir de structures cristallines de la CSD. Les calculs ab initio ont été effectués avec le programme Gaussian09 en utilisant la théorie des perturbations de second ordre Møller–Plesset (MP2) et cluster couplé avec excitations fonctionnelles (CCDS (T)) simples, doubles et triples. Effets relativistes scalaires ont été traités dans l'Approximation régulière d'ordre zéro (Zeroth Order Regular Approximation, ZORA), avec l'ensemble des bases ZORA / TZP, ZORA/TZ2P et ZORA/QZ4P des orbitales de type Slater (Slater-type orbitals, STO) tous les électrons inclus (AE) et de l'orbital de type gaussien (GTO) def2-TZVP, aug-cc-pVDZ, aug-cc-pVTZ et aug-cc-pVQZ ont été utilisés. Tous les calculs ont été effectués en phase gazeuse ou traités avec le modèle de solvatation. Solvatation par l'eau, le DMSO et le chlorobenzène a été comptabilisée selon la procédure de COSMO avec les valeurs de Klamt des rayons de van der Waals pour les atomes. Pour déterminer les enthalpies de Gibbs de solvatation qui produirait le paramètre $\Delta\delta G_{solv}$ utilisé pour approcher les valeurs de l'enthalpie de formation de Gibbs du complexe d'inclusion dans l'eau idéalisée de monomères, le modèle de solvatation du continuum COSMO-RS a été utilisé. Les paramètres thermodynamiques ont été calculés à partir des données statistiques, à savoir que l'énergie et l'entropie interne, générés par des calculs de fréquences vibratoires. Les optimisations de géométrie par la minimisation du gradient d'énergie ont été effectuées dans tous les cas avec les symétries de groupes de points C_1 et C_2. Les analyses de l'interaction orbitale inter fragmentaire Kohn-Sham ont été réalisées avec des géométries optimisées dans le paquet ADF. Les indices de liaison de Wiberg pour des géométries optimisées ADF (en utilisant l'ensemble des bases

TZP tous les électrons inclus) ont été calculées avec le GENNBO 5.0 l'extension d'ADF. L'erreur de superposition de base (basis set superposition error, BSSE) a été calculée par la méthode de contre-poids (CP), en effectuant à nouveau tous les calculs à l'aide d'un mélange d'ensemble des bases, et l'erreur est ensuite soustraite a posteriori à partir de l'énergie non corrigé. Une formule standard "zéro amortissement" et l'amortissement rationnel pour des valeurs finies pour les petites distances interatomiques selon Becke et Johnson (BJ-amortissement) ont été utilisés pour la construction des courbes d'énergie de dispersion. Le schéma DFT-D3 de Grimme pour le calcul des coefficients de dispersion a été utilisée. ETS-NOCV ainsi que des analyses ELF ont été réalisées avec les géométries optimisées utilisant les sous-programmes ADF2012. Les représentations des structures moléculaires et orbitales ont été dessinées à l'aide d'ADFview.

Toutes les mesures ITC ont été effectués avec un appareil Waters-SAS nanoITC équipé de deux cellules hastealloy en acier inoxydable de volume de 1mL chacune. Toutes les solutions aqueuses ont été préparées par la sonication des suspensions des complexes dans l'eau pure et par la suite elles ont été complètement dégazées sous pression réduite. Les solvants organiques ont été fraîchement distillés et dégazés avant utilisation.

Résultats et discussion

Les résultats recueillis au cours des travaux de cette thèse sont organisées en plusieurs chapitres séparés qui sont thématiquement différents, mais ayant toujours pour but de mieux comprendre les interactions non-covalentes. En particulier le rôle de la dispersion dans le comportement intéressante et les propriétés des complexes organométalliques des métaux de transition. Ces problèmes ont été abordés en utilisant diverses méthodes expérimentales et théoriques dont nous disposons.

Les complexes plans carrés avec ligand bipirydine, où le chélate est fusionné à deux cycles pyridines, peuvent être structurellement organisés de telle manière à permettre un accès facile pour des interactions mutuelles entre chelates. Les possibles applications de ces complexes en font des cibles intéressantes pour l'étude de l'empilement des interaction non-covalentes à l'état solide. Ainsi, nous avons réalisé une étude statistique des complexes métaux plans carrés avec des ligands bipyridines en analysant les structures disponibles dans la base de donnée CSD.

Les interactions d'empilement entre les complexes métalliques plan-carrés contenant des ligands bipyridine (*bipy*) ont été étudiées en analysant les données de la CSD et par des

calculs DFT. Afin de trouver des interactions d'empilement intermoléculaires entre bipyridines, nous avons effectué trois recherches. Nous avons tout d'abord recherché toutes les structures dont la distance entre les centroïdes des quelconques fragments de la pyridine (distance d_{PP}) était inférieur à 4,6 Å, nous avons ensuite imposé une distance entre les centres de pyridine et les anneaux de chélation (distance d_{PC}) inférieur à 4,4 Å, et finalement une distance entre les centroïdes des chélates (distance d_{CC}) qui soit inférieure à 4,2 Å. Les résultats de toutes les trois recherches ont été combinés et analysés de manière simultané afin de garantir que toutes les interactions d'empilement possibles soient incluses. Nous avons considéré que deux anneaux forment une interaction d'empilement lorsque l'angle dièdre entre les plans moyens des bipyridines est trouvé inférieur à 10°. Dans la plupart des structures cristallines deux ligands *bipy* sont orientées tête-bêche.

Basé sur les paramètres géométriques: l'angle de torsion T_2, distance r_{MM} et l'angle φ, nous avons classé les recouvrements mutuels des ligands bipy en six catégories (type I_a, I_b, I_c, I_d, II_a et II_b). Les plus nombreux étaient les structures avec des types de recouvrement I_b, avec une très grande zone de recouvrement ($r_{MM} \leq 5$ Å, $\varphi \leq 35$ °): il existe un recouvrement mutuel: de fragments de la pyridine, des anneaux de chélation ou un recouvrement de la pyridine et des anneaux de chélation. La géométrie de l'interaction est très souvent influencée par les deux ligands coordonnés en troisième et en quatrième position, ou par des molécules (ions) dans l'environnement de la structure cristalline. Les interactions d'empilement de complexes bipy plan-carrés peuvent entraîner la formation de l'empilement des chaînes et des dimères dans les structures cristallines, l'empilement des chaînes avec des recouvrements alternés est le type préféré de l'empaquetage de ces complexes.

Les résultats des calculs montrent que les énergies d'interactions d'empilement entre les deux complexes [Ni(bipy)(CN)$_2$] peuvent être très fortes; la plus forte interaction calculée a une énergie de -31,66 kcal/mol. La plus faible interaction calculée, dans laquelle une seule paire des anneaux pyridyle se recouvrent, a une énergie de -7,26 kcal/mol. Comme on peut s'y attendre, les résultats des calculs montrent que la réduction de la zone de recouvrement entraîne une diminution de l'énergie d'interaction. Les résultats indiquent également que des interactions chélate-aryle sont plus fortes que les interactions aryle-aryle et que l'interaction des anneaux pyridine coordonnés au métal est plus forte que l'interaction des pyridines non-coordonnés.

L'oligomérisation des complexes plans carrés de Rh(I) est très bien décrite dans la littérature (cf. Chapitre 1). Dans le but d'étudier l'influence de la chiralité sur cette auto-agrégation et le potentiel de reconnaissance chirale, de nouveaux complexes chiraux de Rh(I)

ont été synthétisés et caractérisés. Le processus d'oligomerisation a été suivi par spectroscopie UV/Vis et par titration calorimétrique isotherme (Isothermal titration calorimetry, ITC).

Plusieurs nouveaux complexes chiraux Rh(I) ont été synthétisés et totalement caractérisés à partir des ligands isonitrile énantio-enrichis. Notre intention était d'étudier leurs deux modes d'auto-agrégation à l'état solide et en solution, mais aussi leur capacité à stabiliser de gros anions réactifs. Malgré tous nos efforts mise en oeuvres, les différentes techniques de cristallisation utilisées, une grande variété de contre-anions utilisés, nous n'avons pas été en mesure d'obtenir des cristaux de qualité satisfaisante pour un analyse par diffraction de rayons X.
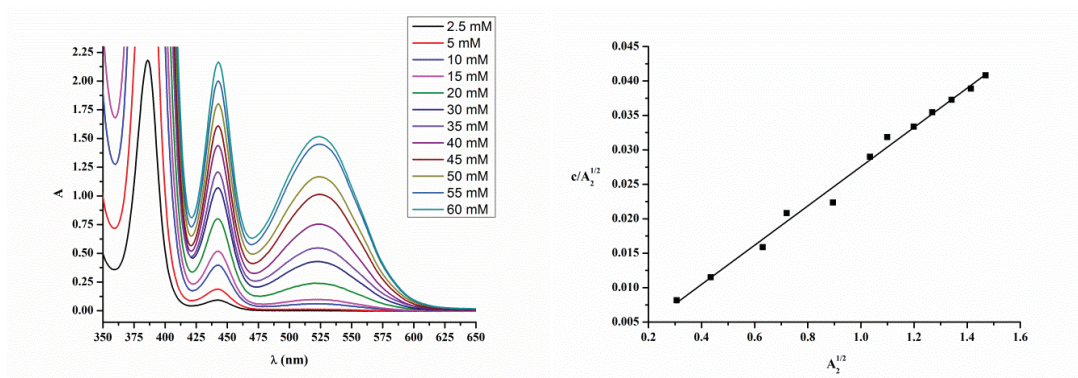
Les spectres UV/Vis de PP004 dans CH_3CN pour la gamme des concentrations (à gauche). La représentation graphique de $[Rh]/\sqrt{A_{441nm}}$ vs. $\sqrt{A_{441nm}}$ (à droite)

L'oligomérisation de ces complexes en solution a été caractérisée par UV-visible. On observe, la croissance d'une nouvelle bande d'absorption aux longueurs d'onde plus grandes lorsque la concentration en monomère augmente. Cette caractéristique nous a permis d'évaluer les constantes d'équilibre de la formation de dimère et de trimère en utilisant la méthode de Grey et al. sur une gamme de concentrations.

$$\frac{[Rh]}{\sqrt{A_2}} = \frac{1}{\sqrt{\varepsilon_2 K_1}} + \frac{2\sqrt{A_2}}{\varepsilon_2} + \frac{3K_2 A_2}{\varepsilon_2 \sqrt{\varepsilon_2 K_1}}$$

$$A_3 = \frac{\varepsilon_3 K_2 \sqrt{A_2^3}}{\varepsilon_2 \sqrt{\varepsilon_2 K_1}}$$

Les valeurs des énergies libres de Gibbs obtenues à partir de ces constantes sont $\Delta G_f^{\text{dimère}}$ = - 5,75 kcal/mol et $\Delta G_f^{\text{trimère}}$ = - 2,22 kcal/mol pour le chlorure de tétrakis(S-(-)-1-phenylethylisocyanide)rhodium(I) (PP004) dans l'acétonitrile à force ionique constante (0,1 M (n-Bu₄N) PF₆ comme tampon). Ces résultats suggèrent que le processus d'oligomérisation dans une solution d'acétonitrile est clairement favorable. En utilisant la même méthode, nous avons également procédé à une évaluation de la $\Delta G_f^{\text{dimère}}$ du chlorure de tétrakis(R-(-)-1-

cyclohexylethylisocyanide)rhodium(I) énantiopur (PP023, $\Delta G_f^{dimère}$ = -5,7 kcal / mol) et du chlorure de tétrakis(*S*-(+)-1cyclohexylethylisocyanide)rhodium(I) (PP044, $\Delta G_f^{dimère}$ = -9,7 kcal/mol). La valeur du $\Delta G_f^{dimère}$ pour les mélanges de ces énantiomères (50%(*R*)-50%(S), 60%(*R*)-40%(*S*), 70%(*R*)-30%(*S*), 80%(*R*)-20%(*S*) et 90%(*R*)-10%(*S*)) variait de -6 à -10 kcal/mol, mais aucune relation claire entre la $\Delta G_f^{dimère}$ et le rapport des énantiomères n'a pu être établie. La valeur du $\Delta G_f^{dimère}$ a également été obtenue à partir des spectres d'absorption dans du chlorobenzène (-3,89 kcal/mol), et comparée aux résultats du titrage ITC d'une solution 20,4 mM de PP023 au chlorobenzène pur (-2.67 kcal/mol). Ces résultats montrent que les complexes ont une tendance légèrement plus faible à former des dimères dans le chlorobenzène.

M= Pt, **1** (Oxaliplatin)
M= Pd, **2**
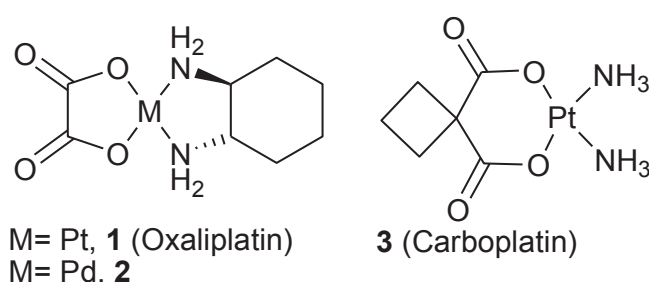
3 (Carboplatin)

Des complexes de type cisplatine

Dabrowiak et collaborateurs ont étudié la stabilité et inactivité inhabituelles de l'oxaliplatine et du carboplatine dans une solution concentrée, les menant à proposer une oligomérisation en solution de ces complexes de platine. Une étude complète sur la question de la stabilité particulière du médicament Oxaliplatin dans les solutions concentrées a été menée. Conformément aux résultats rapportés précédemment par Dabrowiak et al., nous avons confirmé la prédisposition de l'Oxaliplatine (1), de l'Oxalipalladium (2) et du Carboplatine (3), à former les dimères, ainsi que les oligomères supérieurs en phase gazeuse dans des conditions douces d'ionisation par électronébulisation en présence de traces d'acide formique et de sels de sodium.

Les trois composés ont produit des caractéristiques complexes dans le mode ions positifs (Not clear). Aucune différence dans le spectre de masse (ESI+) n'a été remarquée, en utilisant de l'eau ou le DMSO. La spectroscopie RMN ^{1}H de diffusion ordonnée (^{1}H DOSY RMN) est un outil de choix pour l'analyse structurelle des systèmes macromoléculaires qui permet, dans certains cas, l'obtention d'informations structurelles importantes sur les petits systèmes moléculaires. Dans le cas des solutions de 1, 2 et 3 la formation d'oligomères n'a pas pu être établie. De grandes variations de la concentration de l'analyte dans les limites de leur solubilité, n'a pas induit de modifications majeures du coefficient de diffusion

hydrodynamique mesuré, ce qui indique que la DOSY était partiellement inefficace en raison de l'imprécision que réside dans la définition même du volume hydrodynamique inclus dans l'équation de Stoke-Einstein; ce volume n'est pas directement lié au volume de l'analyte qu'on peut approximer, par exemple, par le volume de van der Waals à l'exclusion de solvant d'une molécule.

D'autres études concernant l'auto-association ont été limitées aux complexes presque plans 1 et 2, dans l'eau à l'aide d'ITC, permettant la détermination précise de paramètres thermodynamiques telles que l'enthalpie de formation / dissociation des oligomères.

$$2\ \mathbf{2} \rightleftharpoons [\mathbf{2}]_2 \qquad K_2 = \frac{c_{[2]_2}}{c_1^2}$$

$$\mathbf{1} + \mathbf{2} \rightleftharpoons [\mathbf{1,2}] \qquad K_{1,2} = \frac{c_{[1,2]}}{c_1 \cdot c_2}$$

$$c_1^0 = c_1^* + c_{[1,2]} \quad c_2^0 = c_2^* + c_{[1,2]} \qquad K_{1,2}^* = \frac{c_{[1,2]}}{c_1^* \cdot c_2^*}$$

$$c_1^* = c_1 + c_{[1]_2} \quad c_2^* = c_2 + c_{[2]_2}$$

Expression des constantes d'association selon Young et al.

La dissociation des dimères hypothétiques $[1]_2$ et $[2]_2$ (figure) a été étudiée par la dilution de 20 (2) à 10 mM (1) de solutions d'analyte aqueuses dans un volume relativement important d'eau pure. Pour le composé 1, les expériences de l'ITC n'ont donné aucun flux de chaleur endothermique notifiable au-dessus du bruit de fond, en d'autres termes, suggère que soit la proportion d'oligomère(s) en solution ou l'enthalpie de dissociation était trop faible pour produire des flux de chaleur mesurables. Pour le composé 2, une trace endothermique typique a été rapportée qui correspondait à une valeur de 0,46 ± 0,08 kcal/mol pour l'enthalpie de dissociation et à une constante d'association monomère-dimère K_2 de ca. 3×10^{-4}. Cette dernière valeur correspond à une enthalpie de Gibbs ΔG_{f2} approximative de ca. 4,6 kcal/mol et à une valeur de la variation d'entropie ΔS_{f2} de ca. -17 cal/K.mol. Les composés 1 et 2, qui ne diffèrent que par la nature du métal et par quelques caractéristiques structurelles, ont été étudié pour leur possible interaction mutuelle. Le titrage a été réalisé en mélangeant par le biais de micro-injections, des solutions équimolaires (10 mM) de 1 et 2. La trace thermographique obtenue a fourni un comportement exothermique clair en résultant dans une enthalpie d'association de -0,56 kcal/mol et une valeur de $5,1 \times 10^{-4}$ pour la constante d'association apparente K_{12}^* associée à une valeur d'enthalpie de Gibbs ΔG_{f12} de 4,5 kcal/mol et d'un changement d'entropie de -17 cal/K.mol.

Resumé
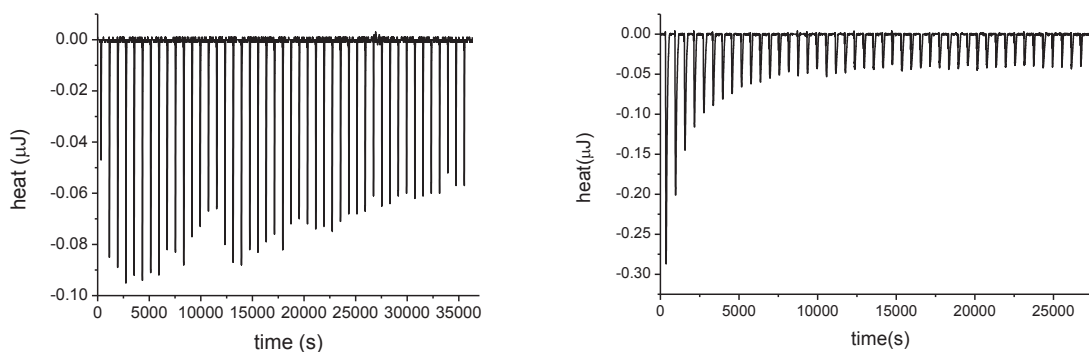
Les traces thermographiques de la dilution d'une solution aqueuse concentrée de **1** (c = 20 mM, v = 2,06 uL) dans de l'eau pure à 25 ° C (à gauche); et **2** (c = 20 mM, v = 2,06 uL) dans de l'eau pure à 25 ° C (à droite)

L'agrégation de **1-3** soit en phase gazeuse ou en solution a été modélisée en se basant sur les structures cristallines trouvés dans la CSD, par des méthodes DFT-D3 destinés à traiter, d'une manière physiquement correcte, la contribution attractive de la force de London, en plus de toutes les autres interactions inter et intramoléculaires adéquatement traités par le DF conventionnel. Les systèmes modèles utilisés dans l'étude étaient la pile tête-bêche α, la pile décalé tête-bêche β et l'arrangement côté à côté γ (figure).
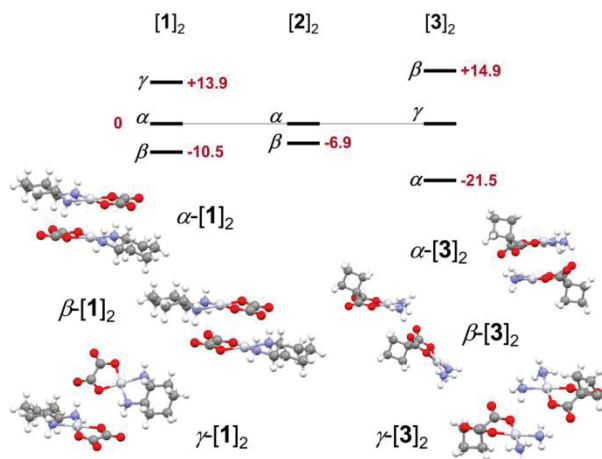
Les représentations symboliques des dispositions des agrégats dans les minima locaux d'énergie pour les dimères tête-bêche de 1-3 (à gauche); Énergies relatives des arrangements des dimères α, β et γ en phase gazeuse de 1-3 (en kcal/mol) (à droite)

L'inspection des énergies de ces trois types d'arrangements en phase gazeuse indiquent que le plus favorisé est le β pour [1]$_2$ et [2]$_2$ de ca. 10 et 7 kcal/mol respectivement. Décomposer ΔE_{int} dans ses principeles composantes : Pauli, orbitales, électrostatiques et de dispersion, informent de l'importance particulière de ce dernier terme, qui s'élève à 27%, 39% et 49% de l'énergie totale d'interaction en γ-[1]$_2$ (ΔE_{int} = -44,0 kcal/mol), β-[1]$_2$ (ΔE_{int} = -73,4

kcal/mol) et α-[1]$_2$ (ΔE$_{int}$ = -60,1 kcal/mol) respectivement. Le terme d'énergie d'interaction orbitalaire a été décomposé dans les cas de β-[1]$_2$ et β [2]$_2$, en utilisant la méthode NOCV-ETS développé par Mitoraj, Michalak et Ziegler. Elle a fournie une image claire de la contribution des liaisons hydrogène dans la cohésion du dimère en phase gazeuse et a confirmé l'absence d'interactions métal-métal orbitales significatives.

Dans un premier temps, la modélisation de l'effet de la polarité du solvant environnant a été effectuée en utilisant le modèle de solvatation COSMO. Les PEC des arrangements α et β ont été comparés dans le continuum de solvant DMSO (COSMO) comme un moyen d'exclure les modalités associées à un comportement asymptotique incorrect. Cette étude, réalisée avec des α-et β-[1]$_2$, a révélé que l'arrangement antérieur mène à des dimères non viables dans le DMSO, tandis que ce dernier produit un meilleur comportement asymptotique, ce qui indique la persistance du dimère en solution.

La solvatation conduit à une baisse de la valeur absolue d'enthalpie de la formation de Gibbs d'environ 30 kcal/mol. Dans tous les cas l'arrangement α conduit à des valeurs positives de ΔG$_f^{298}$ alors que la disposition β est généralement associée à des valeurs négatives. Le manque de considération pour les interactions spécifiques de l'eau avec du soluté par le modèle de solvatation utilisé ici (COSMO) peut également être tenu pour responsable des décalages observés entre la théorie et l'expérience; la théorie surestime la prédisposition du système à s'auto-assembler.

Une des manières d'évaluer la pertinence des modèles théoriques est de comparer les paramètres thermodynamiques calculées avec celles obtenues pour un processus d'association standard non-covalent obtenue par l'ITC en solution. Cette approche est cependant limitée par le traitement de la solvatation dans les méthodes DFT conventionnelles. Le traitement des données ITC pour l'inclusion de 1 (20 mM) en CB[7] (0,74 mM) dans de l'eau pure en utilisant le modèle de plusieurs ensembles de sites de liaison indépendants (MSCBS) a fourni une enthalpie d'inclusion ΔH$_{mod}$ de -8,7 (1) kcal/mol et une constante d'association K$_1$ de 2,4·10^5. Un traitement similaire des données relatives à l'inclusion de 2 (17 mM) en CB[7] (1 mM) dans de l'eau pure a donné une enthalpie d'inclusion ΔH$_{mod}$ de -6,6 (5) kcal/mol et une constante d'association K$_1$ 7·10^4. Étant donné les valeurs élevées des constantes l'association calculées K$_1$, l'auto-cohérence du modèle thermochimique a été vérifiée par le calcul de l'enthalpie d'association brute ΔH$_{raw}$ en intégrant le dégagement de chaleur molaire totale du thermographe ITC: les valeurs résultantes de -7,8 et -6,2(3) kcal/mol pour la formation de 1@CB[7] et 2@CB[7] respectivement ont validé le modèle thermochimique choisi.

Resumé

Notre calcul des paramètres thermodynamique des complexes d'inclusion a été réalisée avec des géométries optimisées avec un traitement de solvatation COSMO des coordonnées cartésiennes de la première structure de Kim de 1@CB [7], elle a également été utilisée pour développer le modèle de 2@CB[7]. Ces géométries ont ultérieurement été appliquées un traitement COSMO-RS pour déterminer les enthalpies libres de Gibbs de solvatation conduisant au paramètre $\Delta_\delta G_{solv}$ utilisé pour estimer les valeurs de l'enthalpie libre de Gibbs de formation du complexe d'inclusion dans l'eau idéalisée de monomères 1-2 et CB[7]. ΔG_f^{298} qui a été calculée, s'élève à -12,3 kcal/mol pour la formation de 1@CB[7] et -13,6 kcal/mol pour la formation de 2@CB[7]. Dans le cas de 1 et 2, qui sont les deux modérément lipophiles et plutôt désireux d'établir des interactions spécifiques avec l'eau désordonnée. Les valeurs des affinités pour CB[7] calculé en combinant DFT-D et le modèle de solvatation COSMO-RS restent en accord raisonnable avec les données expérimentales, particulièrement si on considère que le coût énergétique devant être payés est négligeable pour la dissociation des parties de dimères [1]$_2$ et [2]$_2$.

$$\Delta G_f \text{ (water)} = \Delta E_g + \Delta G_{RRHO} + \Delta\delta G_{solv} + \Delta E_{disp}^{(3)} + \Delta E_{BBSE} (1)$$

Considérant que la valeur théorique ΔG est une somme de termes individuellement larges de signe opposé (équation 1), ont été calculés sans l'empirisme spécifique, le signe correctement calculé et le bon ordre de grandeur pour ΔG semblent d'être un résultat satisfaisant. Parce que les valeurs $\Delta_\delta H_{solv}$ sont des quantités indirectes pour lesquelles le modèle COSMO-RS n'a pas été développé, l'enthalpie de solvatation n'a pas été déterminée.

Une autre réaction que nous avons considéré pour l'évaluation de la DFT-D avec le modèle de la solvatation COSMO-RS était l'inclusion de la $[Cp^*Ir^{III}(H_2O)_3]$ $(PF_6)_2$ (4) au CB[7]. Le titrage ITC d'une solution 2 mM de CB [7] dans de l'eau pure par une solution 10 mM de 4, a produit une réponse exothermique significative qui a été trouvé être largement dépendante de la concentration de CB [7]. Le thermographe contenait deux contributions importantes qui doivent être pris en considération ici: la première est l'élément exothermique correspondant à l'interaction hôte-invité, la deuxième est l'élément endothermique produit par la dilution de la solution du composé 4 dans la solution de CB[7]. La valeur de l'enthalpie de formation du complexe d'inclusion a été obtenue par la soustraction de la trace thermographique de la dilution de la même solution de 4 dans l'eau pure. Cela a fourni une valeur approximative de l'enthalpie de la formation du complexe hôte-invité entre CB [7] et 4 de -3,70 (7) kcal/mol dans l'eau, qui reste dans les valeurs typiques pour l'inclusion non-covalente e complexes de coordination dans une telle classe de cavitands.

Resumé

Les calculs en phase gazeuse sur la géométrie relaxée de l'état fondamental indiquent que la formation du complexe hôte-invité est favorisée par la dispersion et represente environ 50% de l'énergie d'interaction (ΔE_{int} = -160,5 kcal/mol, ΔE_{disp} = -86,8 kcal/mol) entre les "structures préparées" de $[4]^{2+}$ et CB [7] dans le complexe d'inclusion. Il a été constaté qu'environ 79% du terme de l'énergie de dispersion attractif résultent de l'interaction CB[7]-Cp* et que les 21% restants ont été fournis par l'interaction CB[7]-$[Ir(H_2O)_3]$. La valeur de l'énergie de formation ΔE_{fgas} = -127,5 kcal/mol en phase gazeuse pour la formation du complexe hôte-invité indique une formation thermodynamiquement favorisée du complexe d'inclusion $\{4@CB[7]\}^{2+}$ en phase gazeuse. Pour améliorer la précision du traitement de la salvatation, le système a été converti en une version neutre composé des mêmes structures associées à deux atomes de chlore analogues l'anion PF_6^- qui étaient situés à l'écart des ligands aquo et dans des zones à faible densité de charge des géométries de minima d'énergie locales. ΔG_f ont été trouvées à être fortement dépendant de la position relative de l'anion chlorure par rapport aux ligands aquo. Bien que les énergies de complexation en phase gazeuse pour les trois systèmes avec des positions différentes des contre-ions varient considérablement entre -69 et -137 kcal/mol, les enthalpies de complexation ΔG_f^{water} libres associées mais cette fois-ci dans l'eau montrent uniquement de faibles variations (4-10 kcal/mol). Cela démontre la précision du modèle COSMOS-RS qui compense une interaction cation-chlorure défavorable par une meilleure l'enthalpie de Gibbs de solvatation correspondant et fournit ainsi des valeurs réalistes pour ΔG_f^{water}.

Le clivage de ponts halogènés est une réaction chimiquement pure, appropriée à l'utilisation d'ITC et qui donne une signature thermochimique claire. Ces réactions répondent à l'objectif principal étant de trouver la méthode appropriée pour obtenir des résultats thermochimiques cohérents. Ces résultats peuvent être par la suite utilisés pour référencer les méthodes DFT-D. Avec un objectif principal étant d'obtenir des données thermochimiques pour la réactivité de dimères de Pd (II) et Ru (III) (qui possèdent un ligand pontant de type halogénure) vis à vis de nucléophiles, nous avons synthétisé et physiquement caractérisé plusieurs nouveaux complexes ainsi qu'effectué des réactions de titrage ITC. Les complexes suivants ont été utilisés: $[Pd(tBupTP)Cl]_2$, $[Pd(dmba)Cl]_2$ et $[Ru(p-cym)Cl_2]_2$ (tBupTP – 4-(t-butyl)-2-(p-tolyl)pyridine; dmba - N, N-diméthylbenzylamine; p-cym - η^6-p-cymène). Les réactions ont été conçues de manière à obtenir un produit unique et stable par simple mécanisme de clivage du pont par l'addition nucléophile du ligand, et la coordination ultérieure avec un centre métallique.

Resumé

Quatre ligands ont été utilisés pour les réactions de titrage: triphenilphosphine (PPh_3), tricyclohexylphosphine (PCy_3), pyridine (Pyr) et 4-tert-Butylpyridine (tBuPyr). Les solutions concentrées de ligands ont été titrés aux solutions 1 mM de dimères, donnant de fortes signatures thermiques.

Les enthalpies de la réaction ont été obtenues pour un titrage de:

1) Pyr (39.5 mM) à $[Pd(tBupTP)Cl]_2$ (1 mM), ΔH = -12.1 kcal/mol; tBuPyr (30.5 mM) à $[Pd(tBupTP)Cl]_2$ (1 mM), ΔH = -15.4 kcal/mol; PPh_3 (26.3 mM) à $[Pd(tBupTP)Cl]_2$ (1 mM), ΔH = -23.6 kcal/mol; PCy_3 (23.3 mM) à $[Pd(tBupTP)Cl]_2$ (1 mM), ΔH = -25.3 kcal/mol;

2) Pyr (37.9 mM) à $[Pd(dmba)Cl]_2$ (1 mM), ΔH = -15.1 kcal/mol; tBuPyr (24.9 mM) à $[Pd(dmba)Cl]_2$ (1 mM), ΔH = -16.4 kcal/mol; PPh_3 (23.8 mM) à $[Pd(dmba)Cl]_2$ (1 mM), ΔH = -26.5 kcal/mol; PCy_3 (24.5 mM) à $[Pd(dmba)Cl]_2$ (1 mM), ΔH = -32.8 kcal/mol;

3) Pyr (39.5 mM) à $[Ru(p\text{-}cym)Cl_2]_2$ (1 mM), ΔH = -16.2 kcal/mol; tBuPyr (27.5 mM) à $[Ru(p\text{-}cym)Cl_2]_2$ (1 mM), ΔH = -19 kcal/mol; PPh_3 (23.3 mM) à $[Ru(p\text{-}cym)Cl_2]_2$ (1 mM), ΔH = -28.4 kcal/mol; PCy_3 (23.3 mM) à $[Ru(p\text{-}cym)Cl_2]_2$ (1 mM), ΔH = -23.3 kcal/mol;

Les résultats thermochimiques des réactions obtenus par ITC ont pour but de dresser un bilan expérimental précis des réactions en solution impliquant de complexes palladium et ruthénium où les forces de dispersion de London seraient essentielles pour la stabilisation. Ce résultat a été utilisé pour le « benchmarking » des méthodes théoriques DFT corrigée par la dispersion, et méthodes WFT développés par Grimme et collaborateurs.

Summary

Table of Contents

List of abbreviations

ADF – Amsterdam density functional
AE – all-electron
Bipy – 2,2' bipyridine
BJ – Becke-Johnson
BLYP – Becke-Lee-Yang-Parr
BSSE – basis set superposition error
CB[n] – cucurbit[n]uril
CBS – complete basis set
CCSD(T) – coupled-cluster, single, double (triple)
CD – cyclodextranes
CDs – circular dichroism
CIF – crystallographic information file
COD – 1,5-cyclooctadiene
COSMO – conductor like screening model
COSMO-RS – COSMO for realistic solvents
CP – counterpoise
CPCM – conductor-like PCM
CR – competitive replacement
CSD – Cambridge structural database
DFT – density functional theory
Dmba – N,N-dimethylbenzylamine
DMSO – dimethyl sulfoxide
DOSY – diffusion-ordered spectroscopy
DPCM – dielectric PCM
DSC – dye-sensitized solar cells
EDA – energy decomposition analyses
ELF – electron localisation function
ESI – electron-spray ionization
ETS-NOCV – extended transition state – natural orbitals for chemical valence
GB – generalized Born
GGA – generalized-gradient approximation
H-bonds – hydrogen bonds
HEPES – 4-(2-hydroxyethyl)-1- piperazineethanesulfonic acid
HF – Hartree-Fock
IEF – integral equation formalism
IEFPCM – integral equation formalism PCM
ITC – isothermal titration calorimetry
KS – Kohn-Sham
LC – long-range corrected
LDA – local density approximation
MC – Monte Carlo
MD – molecular dynamic
MM – molecular mechanic
MO – molecular orbital
MP2 – second order Møller–Plesset
MPE – multipole expansion
MSCBS – multiple set of independent binding sites
NCI – non-covalent interaction

NEI – *S*-(-)-1-(1-Naphthyl)ethylisocyanide
PBE – Perdew-Burke-Erzenhof
PCM – polarizable continuum model
PCy$_3$ – tricyclohexylphosphine
p-cym – η^6-1-isopropyl-4-methylbenzene
PDB – protein data bank
PEC – potential energy curve
PEI – *S*-(-)-1-phenylethylisocyanide
Phen – phenantroline
PID – proportional/integral/derivative
PPh$_3$ – triphenylphosphine
Pyr – pyridine
R-CEI – *R*-(-)-1-cyclohexylethylisocyanide
SA – solvent accessible
S-CEI – *S*-(+)-1-cyclohexylethylisocyanide
SCF – self-consistent field
SCRF – self-consistent reaction field
SE – solvent exclusion
Sqp – square-planar
tBpTP – 4-(t-Butyl)-2-(p-tolyl)pyridine
tBPyr – 4-(t-Butyl)-pyridine
TED – thermoelectric devices
Terpy – terpyridine
THF – tetrahydrofuran
TPSS – Tao-Perdew-Staroverov-Scuseria
TRIS – tris(hydroxymethyl)aminomethane
UFF – universal force field
vdW – van der Waals
XDM – exchange-hole dipole moment
ZORA – zeroth order regular approximation

Chapter 1

1. General Introduction

1.1. Non-covalent interactions

Non-covalent interactions (NCI)[1, 2] can be found everywhere in the nature. They are responsible for wide range of processes and properties of the molecules and substances. Existence of the condensed phase and solvation phenomena can be attributed to the NCI. Existence of the liquid water at broad range of temperatures is probably most important example of the NCI, without this, life as we know would not exist on Earth.

NCI are also responsible for the structure and activity of the biomacromolecules such as proteins, RNA, and DNA. The double-helix structure of the DNA, discovered and described by Watson and Crick[3] is mainly the consequence of the NCI, where the interactions between nucleic bases play lead role. These bases are polar, aromatic heterocycles that interact by hydrogen bonding and stacking interactions giving the secondary and tertiary structure of the DNA.

These non-covalent intermolecular interactions are weak compared to the covalent interactions. Still, NCI are wide spread. Everywhere where there are molecules, NCI can be found. Systems in which the NCI occur are highly dynamic. In building complex structures with specific properties, self-assembly processes, governed by reversible weak intermolecular forces, play dominant role. This quick reversibility of the NCI allows the considered systems to dynamically adapt to almost any changes imposed by the conditions found on planet earth, usually on a very short time-scale, thus making them omnipresent.

Historically speaking, van der Waals[4] was the first one to realize that the inconsistencies in the behaviour of real gasses compared to the ideal gas law could be contributed to the attractive forces between the molecules of the gas. Van der Waals formulated an equation of state that modified the ideal gas law by taking into account the nonzero size of the molecules, and attractive interaction between them. Even though this formulation of the real gas is not exactly correct, it made a great impact by introducing a concept of the new type of bond. Several decades later, London[5] and Hellmann[6] have made important step in describing and understanding these bonds. London rationalized the origin of attraction between apolar molecules whereas Debye[7] and Keesom provided some rational

based on the electrostatics and classical physics. There were numerous other authors during the last century who contributed as well.[8-12]

There are many different ways NCI could be classified. Here, description of the NCI is separated in two categories. The first group of NCI are result of the fundamental forces that are recognised in the physics as basic NCI (e.g. ion-dipole, dispersion interactions). Second group of interactions represent are systemic NCI, appearing in systems of molecules as a result of the simultaneous effects of the different interactions from the first group.

1.2. Non-covalent interactions: basic interactions

Schematic representation for basic NCI with the example for each type is presented in Figure 1.1.
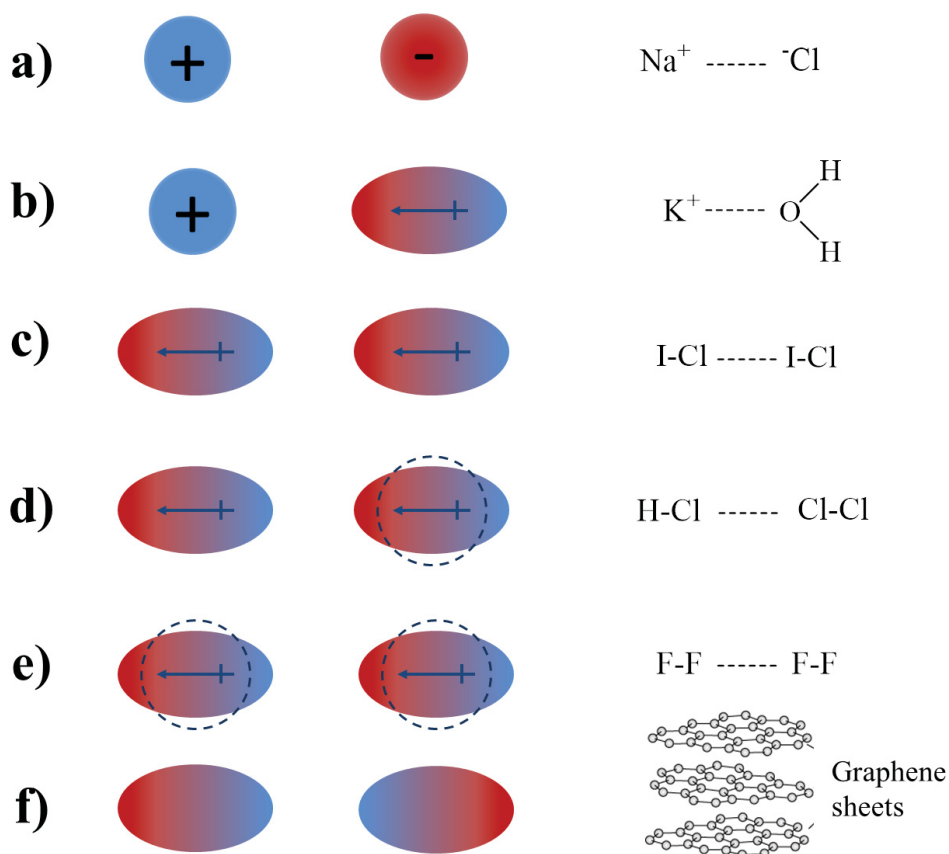

Figure 1.1. Schematic representation of the basic NCI with examples: a) ion-ion; b) ion-dipole; c) dipole-dipole; d) dipole-induced dipole; e) induced dipole-induced dipole (dispersion); f) short-range repulsion

1.2.1.   Ion-ion interactions

Ion pair is formed when the two ions of the opposite, full permanent charge are interacting. Ionic compounds have atoms bound by stronger electrostatic force than in case of covalent compounds. Typical example for these bonds is in the table salt NaCl or in interaction of the Mg^{2+} ion with the negatively charged nucleic bases of RNA. They can be very strong (energy is in range of ca. 100-1000 kcal/mol) in the absence of solvent, but highly polar solvents can break them relatively easy by forming ion-dipole interactions with ions. This process is favoured by increase in the entropy of the system. Strength of ion-ion interactions falls off slowly with distance, i.e. energy of interaction is proportional to 1/r.

1.2.2.   Ion-dipole interaction

Ion-dipole interactions involve an interaction between ion and a polar molecule, i.e. a molecule with a dipole. The negative end of the dipole is attracted by anions, while the partially positive end is attracted by cations. The relative strength of these interactions depends on the charge of the ion Q, the dipole moment of the molecule μ and the distance r from the centre of the ion to the midpoint of the dipole, i.e. energy can be quantitatively expressed with $E \sim \frac{Q\mu}{r^2}$. The example is the interactions of the simple ions (Na^+, K^+, Mg^{2+}) with water in aqueous solutions. The energies of these interactions are in the range of ca.10-250 kcal/mol.

1.2.3.   Dipole-dipole interactions

Dipole-dipole interactions are electrostatic interactions between permanent dipoles in molecules. These interactions tend to align the molecules to increase attraction reducing potential energy of the system. Normally, dipoles are caused by the difference in the electronegativity of the atoms in molecule. One atom attracts the electrons, becoming more negative, while the other becomes more positive. Dipole-dipole interactions are very short ranged; strength falls off with distance, i.e. energy of interaction is proportional to $1/r^3$. Substances with large dipole moments have high boiling points compared to the molecules of the same molecular mass, because of the stronger intermolecular interactions holding the molecules in the liquid state. The energies are usually in the range of ca. 1-5 kcal/mol.

1.2.4. Dipole-induced dipole

A molecule with a permanent dipole can induce a dipole in other molecule that is located nearby in space. The strength of the interaction depends on the dipole moment of the first molecule and the polarizability of the second. Dipole-induced dipole interactions are always attractive and can contribute as much as 0.5 kcal/mole to the stabilization of the system. Strength falls off with distance, i.e. energy of interaction is proportional to $1/r^4$.

1.2.5. Dispersion interactions

Dispersion interactions are consequence of the London (dispersion) forces, named so after Fritz London, who suggested that the motion of electrons within an atom or non-polar molecule can result in a transient dipole moment.[5, 11, 13] Due to electron repulsion, a temporary dipole on one atom can induce a similar dipole on a neighbouring atom. The ease with which an external electric field can induce a dipole (alter the electron distribution) with a molecule is referred to as the "polarizability" of that molecule. Greater polarizability of a molecule will result in easier induction of a momentary dipole and by that the dispersion forces will be stronger. Dispersive interactions are always attractive and occur between any pair of molecules, even non-polar molecules. Energetic contribution of the dispersion interactions for atom-atom contact is usually pretty small, but the net effect due to the large number of these interactions, can be very significant (e.g. proteins). The energies are usually in the range of ca. 0.1 - 1 kcal/mol. Fluctuating dipole interactions fall off with distance, i.e. energy of interaction is proportional to $1/r^6$.

1.2.6. Short-range repulsive interactions

Overlap of orbitals of two non-bonded atoms that are very close together in space results in electrostatic repulsion between occupied orbitals. This repulsive energy is very short range in nature, i.e. energy of interaction approximately proportional to $1/r^{12}$. Because this repulsive term rises as sharply as distance decreases it is reasonable to think of atoms as hard spheres defined by van der Waals radii. The same principle applies to molecules although the shapes are more complex. The smallest distance between two non-bonded atoms is the sum of the van der Waals radii of the two atoms.

1.3. Non-covalent interactions: systemic interactions

Systemic interactions are usually result of several influences and simultaneous effects of different basic NCI taking place in simple, and more complex molecular systems. There are different NCI that could be considered as systemic. Some of these interactions that were addressed in the studies covered in this thesis are presented briefly in following sections.

1.3.1. Hydrogen bonds

Hydrogen bonds (H-bonds) are special case of dipole-dipole interactions. H-bonds are formed by electrostatic interactions involving a hydrogen atom bound to an electronegative atom such as N, O or F. Water molecules provide a classic example of hydrogen bonding (Figure 1.2). The hydrogen atom in one water molecule is attracted to a partially negative charge of the oxygen atom in an adjacent molecule. Not only do water molecules hydrogen-bond with one another, they also form hydrogen bonds with other kind of molecules. These bonds are highly directional, as the strength depends on the proper alignment of the atoms. Hydrogen bonds can vary in strength from very weak (0.25–0.5 kcal/mol in the proteins) to extremely strong (ca. 40 kcal/mol in the ion HF_2^-).
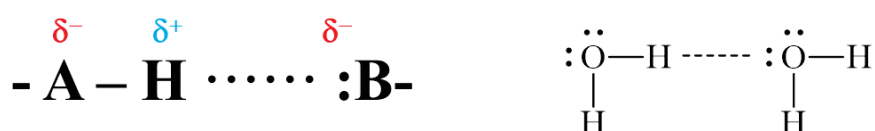
$$- A - H \cdots\cdots :B-$$

Figure 1.2. Schematic representation of the H-bond. A, B = N, O, F atoms

1.3.2. Hydrophobic interactions

The hydrophobic effect is the desire for non-polar molecules to aggregate in aqueous solutions in order to separate from water.[14] This phenomenon leads to minimum exposed surface area of non-polar molecules to the polar water molecules (typically spherical droplets).[14] When a hydrophobic substance dissolves in water, a region of relatively low entropy (high order) water forms at the interface between the solvent and the solute. The decrease in entropy at the interface arises from the strong intermolecular forces between water molecules. In bulk water, these forces are isotropic, i.e. extending in all directions. At the interface, these forces are anisotropic because the solvated molecule does not form hydrogen

bonds. Thus water at the interface is rotationally and translationally constrained. When isolated nonpolar molecules aggregate in aqueous solution, the total volume of interfacial water decreases (Figure 1.3).
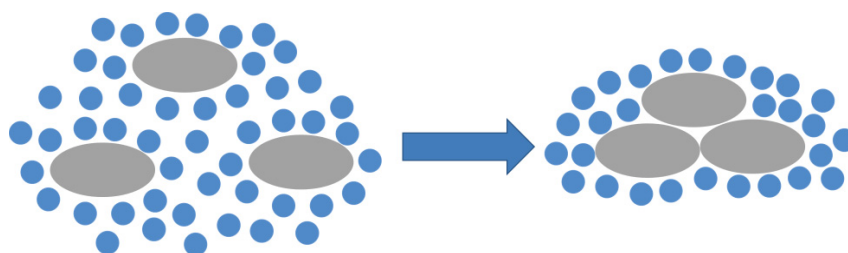

Figure 1.3. Hydrophobic effect. Blue circles – water molecules, grey ellipsoids – non-polar molecules

Thus, the driving force for aggregation of hydrophobic substances arises from an increase in entropy of the aqueous phase, and not from intrinsic attraction between hydrophobic solute molecules. This effect is very important in a lot of processes and especially in protein folding.

1.3.3. Aromatic interactions

Aromatic interactions are non-covalent attractive force between aromatic rings in chemical and biological systems, which play a crucial role in many processes, e.g. molecular recognition, catalysis, and molecular transport.[15-19] Aromatic interactions not only determine structures of the systems but also modulate their physical and chemical properties. It is interesting to notice that the majority of drug molecules contain aromatic rings and their interactions are important for activity.[15]

The benzene dimer is the prototypical system for the aromatic interactions (Figure 1.4). Experimentally, it is bound by 2-3 kcal/mol in the gas phase, with an estimated 4.96 Å separation between the centres of mass.[19] Note that unlike many hydrogen bonds, these are weak interactions which are outside the sum of the relevant van der Waals radii. First attempts in interpretation of the nature of π-π stacking interactions assumed that electrostatic forces were responsible.[20, 21] However, later studies on parallel stacking interactions showed important role of London dispersion forces.[22] London forces are considered to involve instantaneously correlated multipole-induced multipole charge fluctuations. Grimme suggested that π-π stacking between unsaturated molecules may involve particularly favourable dispersion interactions between π- systems, and suggests that generalized stabilizing interactions should exist even between saturated residues.[23] Additionally, it was

noticed that adding substituents to the benzene rings also changes the relative energies of the various configurations of substituted benzene dimers.[24, 25]
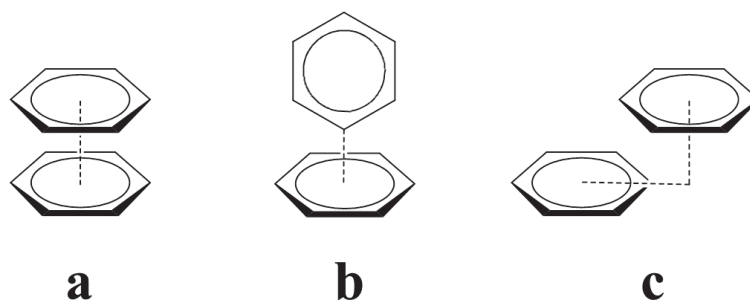

Figure 1.4. Aromatic interactions in benzene dimer: a) sandwich; b) T-shaped; c) displaced. H atoms are omitted for clarity.

Geometries and the effect of the substituents can be explained in part using electrostatic Hunter-Sanders model,[21] and in part "direct interaction" model proposed by Wheeler and Houk. [24-26]

Experimental evidence of the π-π stacking of aromatic fragments in solution was obtained from NMR spectroscopy.[20, 27] Another experimental evidence was provided by the Double Mutant experiments.[28]

Another type of aromatic interactions that involve the interaction between ion and aromatic ring are so called "cation-π" interactions.[29] The association of metal cations with aromatic systems is very well documented in the literature.[30-35] In the gas phase the interaction between cations and benzene is very strong. In water, there is a substantial desolvation effect: the benefit of the cation-π interaction is offset by the penalty of losing the solvation of the ion by water. Interestingly, the cation-π interaction is strong enough that it can even outcompete the strength of salt bridges, which are in fact formed by hydrogen bonds.[36] The binding most probably comes in part from dispersion, but also from the induced electrostatic interactions,[37] and it is influenced by geometry, i.e. the mutual orientation, of the interacting units.[38] Substituent effects were found influential as well.[39-41]

Studies on the aromatic interactions involved benzene or other aromatic molecules mostly organized in sandwich, T-shaped or displaced arrangements. However, recent studies showed that stacking interaction energies between aromatic molecules at large horizontal displacements are significant as well.[42, 43] Large number of interactions at large horizontal displacements that have been found in the crystal structures deposited in the Cambridge structural database (CSD) and Protein data bank (PDB) indicate the significance of these interactions.

Although the benzene dimer has been extensively studied, both experimentally and theoretically, this model system is not relevant in understanding of general properties of aromatic residues in proteins and nucleic acids, because the interactions of heteroaromatic groups (stacking interactions) have the a major role in protein structure, protein–ligand recognition[44, 45, 46] and DNA structure.[21, 46, 47] This is the reason why the recent theoretical studies increasingly examine the effects such as the substituent effects,[24, 26, 41, 48, 49] effects of heteroatoms introduced in aromatic ring, cooperative effects with other intermolecular interactions,[50] and the effects of transition-metal coordination.[51]

1.3.3.1   Aromatic interactions with chelate rings

In chelate rings a metal atom is a member of the ring. Some of the chelate rings can be planar and can have delocalized π-bonds, and, it is believed, some of these rings can be aromatic.[52, 53] In last decade, the different types of interactions with chelate rings, in terms of their abundance, energetics, and geometric preferences were analysed. It was found that the chelate rings can form XH/π[54-59] and stacking interactions. If we take into account that the chelate ring, besides metals, may include heteroatoms and the substituents, it is clear that the study of stacking interactions involving these rings, is much more demanding than study on stacking interactions of simple organic molecules.

Several studies on stacking interactions of chelate rings are based on the analysis of the crystal structures of metal complexes from the CSD, and the density functional theory (DFT) and *ab initio* calculations.[60-65]

1.4.   Significance of non-covalent interactions

NCI play a crucial role in biological systems, and it has been shown that they contribute greatly to the stereo-specificity of chemical processes in natural systems.[66-68] They have been considered in the design of supramolecular assemblies[69-72] and coordination polymers.[73-76] These interactions also heavily influence drug design,[77-79] crystallinity and materials design,[80, 81] and, in general, the synthesis of many organic molecules.[28, 82, 83]

One illustrious example of the amazing application of the NCI, i.e. London (dispersion) forces in nature is the gecko. This animal is notorious for its climbing prowess, regardless of the surface. Be it the sheer cliff, brick or concrete wall, some metal construction or even glass panels, gecko will be found seemingly defying gravity. This remarkable feature

is possible due to the existence of the several thousand microscopic keratinous setae on its feet.[84, 85] These setae have been shown to form NCI with the surface causing the strong adhesive force. The explanation for these phenomena, and its practical application was searched by various authors.[86-88]

In the last decade the list of publications that indicates the importance of stacking interactions, including chelate rings, intensively increased. It was shown that properties of an extensive series of pyridine- and pyrazine- derivate complexes (geometries, supramolecular structure, nuclearities, and reactivity) can be controlled by the change in the coordination mode of chelating ligands in the coordination sphere of metal ions.[89] It is known that the electron density of nitrogen heterocycles, such as pyridine, bipyridine, phenantroline, therpyridine, further decreases by coordination to metal ions.[90] For these reasons, the stacking interactions of chelate rings, fused with nitrogen heteroaromatics, are often found in crystal structures of these metal complexes.

Systematic studies on the NCI of the chelate rings in the last couple of years by Zarić et al.,[62, 63, 91-95] have provided the most significant information on the chelates and the nature of these interactions.

Given the importance and the omnipresence of the NCI, great effort has been given to better understand and describe these them in the field of chemistry, both experimentally and theoretically. Still, this remains a difficult task.

1.5. Calorimetry

Most chemical processes are followed by release (exothermic processes) or absorption (endothermic processes) of the heat. In order to measure this change, calorimetry techniques have been developed. Calorimeters are ideal instruments to measure the rate at which the heat is exchanged with the surroundings during the chemical reaction.

Historically speaking, first mentioning of heat some body possesses date from ancient times. Ancient Greek philosophers Aristotle, Plato and Hippocrates have been mentioning the "innate heat" that was in the hearth and somehow connected with food. Scientifically, this was partially explained only much later, in the second half of the 18th century by Lavoisier.[96, 97] Based on Black's discovery of the latent heat, Lavoisier and Laplace have constructed the first calorimeter to determine the heat evolved in various chemical changes in the late 1780's. They have constructed the ice calorimeter and measured the metabolic heat released by guinea pig placed in the measuring chamber.

Depending on the type and conditions of the reactions, or different information that needs to be obtained, there are various types of calorimeters, e.g. adiabatic, bomb, constant-pressure, differential scanning, isothermal titration calorimeters, etc. It is important to understand basic design of the calorimeter in order to effectively plan the experiment and analyse the data. This knowledge is also important to understand what exactly the acquired raw signal represents.

In principle, there are three ways in which the heat released in the reaction could be measured. Calorimetric instruments based on all three techniques are commercially available:

1) **Temperature change instrument** – the heat produced or consumed by the reaction taking place in the calorimeter results in change in temperature in the measuring cell. The raw signal represents the temperature of the calorimeter cell as a function of time. Appropriate calibration (chemical or electrical) can enable determination of the energy equivalent of the adiabatic calorimeter cell. Measured temperature change can be converted to heat change by multiplying the energy equivalent of the calorimeter (ε_c) with the measured temperature change (ΔT).

2) **Heat conduction calorimeter** – the measurement cell is passively maintained at constant temperature by being coupled with heat flow sensors to a heat sink that is actively controlled at constant temperature. The raw signal represent small voltage proportional to the very small ΔT temporarily developed across the heat flow sensors due to the heat produced by the chemical reaction. Calorimeter made by Lavoisier is an example of heat conduction calorimeters.

3) **Power compensation instrument** – the calorimeter measurement cell is kept on constant temperature by applying constant cooling to the cell, and using heater and temperature controller. As the chemical reaction takes place, any change in heat is detected, and the power applied to the control heater is changed so that the temperature stays constant. The heating power from controlled and reaction heater are kept at constant level so that the input heat from the reaction can be compensated by the heat input from controlled heater. The raw signal is the power applied to the control heater that is required to keep the calorimeter cell from changing the temperature as function of time, expressed in µJ/sec (µcal/sec). The heat change is then calculated by integrating the area under the signal, i.e. the time required for the control heater power to return to the baseline value. The principle of work and

preparation of the experiment for this type of calorimeter instrument will be presented in more detail in Chapter 2.

1.5.1.   Applications

Calorimetry has found application in various fields like biology, biochemistry, and supramolecular chemistry. Titration calorimetry was first described as a method for the simultaneous determination of K_{eq} and ΔH by Christensen and Izatt.[98, 99] The method was originally applied to a variety of weak acid–base equilibria and to metal ion complexation reactions.[100, 101] Due to the very crude design comparing to the modern standard, study on these systems was limited to the determination of equilibrium constant K_{eq}, with values less than ca. $10^4 - 10^5$. The determination of larger association constants requires more dilute solutions and the calorimeters of that day were simply not sensitive enough.

One of the first calorimetric binding studies of biological systems using a small volume adiabatic titration calorimeter was published by Beaudette and Langerman.[102] Soon after, Langerman and Biltonen published a description of microcalorimeters application in biochemistry. Their reports included a discussion of available instrumentation, applications, experimental design, and analysis and interpretation of the data.[103, 104] This marked the beginning of the use of titration calorimetry in studying biological equilibria.

The first commercially available titration calorimeter specifically designed for the study of biological systems became available from MicroCal.[105] This first commercial isothermal titration calorimeter – ITC, was marketed as a device for ''Determining K in Minutes''.[105]

The measurement of heat occupies a well-established place in the investigation of molecular association processes in solution. Understandably, biological studies claim the largest share and a number of excellent review articles have been published dealing with the subtleties, benefits and failings of the method in these fields.[106-112]

ITC is now routinely used in direct characterization of the thermodynamics of biopolymer binding interactions.[113, 114] Modern ITC instruments make it possible to measure heat effects in these systems as small as 0.1 µcal (0.4 µJ), which allows the determination of binding constants as large as 10^{12}.

One of the first calorimetric studies of enzyme activity was published by Spink and Wadso.[115] Improvements in modern microcalorimeters include higher sensitivity, faster response, and the ability to make multiple additions of substrate (or inhibitors). Due to these

improvements, ITC is now routinely used to directly characterize the kinetic parameters (K_M and k_{cat}) in enzyme studies.[116-118] Kinetic studies take advantage of the fact that the calorimetric signal (heat rate) is a direct measure of the reaction rate and the ΔH for the reaction.

Another area where the ITC was found to be very useful is the study on the interaction between DNA and cationic ligands.[119-125]

In order to take full advantage of the powerful ITC technique, the user must be able to design the optimal experiment, understand the data analysis process, and appreciate the uncertainties in the fitting parameters. ITC experiment design and data analysis have been the subject of numerous papers.[110, 126-129]

A number of experts also evaluate the progress in applications in mostly annual reviews of the literature on ITC applications.[130-132]

1.5.2.   Isothermal Titration Calorimetry

Isothermal Titration Calorimetry provides a direct measurement of the heat of the process that take place in sample cell during titration experiment. The direct measurement of this heat (or change in enthalpy, ΔH_{obs}) is unique to calorimetric methods. Other methods require indirect calculation of enthalpy term via the van 't Hoff relationship. There are some other advantages compared to the other analytical methods. For example, in contrast to optical methods, calorimetric measurements can be done over a range of biologically relevant conditions (temperature, salt pH, etc.), with reactants that are spectroscopically inactive (a chromophore or fluorophore tag is not necessary) or on opaque or heterogeneous solutions (e.g., cell suspensions).

In simple binding process, obtained ΔH_{obs} is proportional to the number of molecules going from the free to the bound state. This term can also provide an information of the extent of interaction as solution of one component is added to the solution of another during the titration. From this, the equilibrium binding constant, K_B (it is equal to $1/K_d$, where K_d is the dissociation constant) can be determined. The advantage of the ITC experiment is that it is possible, in a single experiment, to obtain accurate values for K_B (or ΔG), ΔH, $-T\Delta S$, and n, where n is the stoichiometry of the interaction, i.e. mol of ligand per mol of complex.

Having the H_{obs} and the K_B determined, a complete thermodynamic characterization of the interaction can be obtained. The G_{obs} and S_{obs} can be calculated from the following relationships:

$$\Delta G_{obs} = -RTlnK_B$$

$$\Delta S_{obs} = \frac{(\Delta H_{obs} - \Delta G_{obs})}{T}$$

It should be mentioned that the calorimetric experiment does not just include measurement of the heat associated with the formation of a complex, but also the heat that is associated with other potential events such as conformational changes in the interacting molecules, solvent rearrangement, and protonation/deprotonation. To emphasize this fact, 'obs' subscript is usually used.[132]

What information on interaction we can obtain from determining the thermodynamic parameters?

- The G_{obs} reports on the affinity, as it is derived from the equilibrium binding constant.

- The H_{obs} is the heat associated with the making and breaking of non-covalent bonds going from the free to the bound state. For example, an interaction in which a net increase in the number of hydrogen bonds of the system occurs would be accompanied by a favourable, i.e. negative, H_{obs}. However, it shouldn't be forgotten that often, when a hydrogen bond is made in chemical system, it is replacing bonds that solvent water made previously and hence the net enthalpic effect of the bond on complex formation is reduced due to desolvation.

- The S_{obs} show overall change in the degrees of freedom of a system. Most of the time, this can be largely associated with the effect of liberating solvent molecules from the surfaces of the binding molecules as they form new complex. Degrees of freedom of the system increase as these solvent molecules are released from the surface into bulk solvent.

1.6. Density Functional Theory (DFT)

Density Functional Theory was introduced in two publications[133, 134] in middle of 60's by Hohenberg, Kohn and Sham. Nowadays, DFT is established as most successful approach for computing the electronic structure of matter. It has found the application in studying atoms, molecules, solids, fluids, bulk and complex materials, and so on.

In original formulation DFT provides the ground state of a system, where electron density plays a key role. DFT predicts, with great accuracy, various molecular properties,

such as molecular structure, electric and magnetic properties, reaction paths, ionization energies, vibrational frequencies, etc.

The goal of most approaches in quantum chemistry is to solve non-relativistic, time independent Schrödinger equation:

$$\hat{H}\Psi(r_1, \dots, r_N) = E\Psi(r_1, \dots, r_N)$$

where many electron wave function $\Psi(r_1,\dots,r_N)$ is function of 3N variables (N – number of electrons). If we could solve Schrödinger equation, we could predict behaviour of any electronic system. However, this is impossible due to existence of too many degrees of freedom. DFT tries to describe an interacting system of electrons via its density and not via its many-body wave function. For N electrons in a solid, which obey Pauli principle and repulse each other via the Coulomb potential, this means that the basic variable of the system depends only on three - the spatial coordinates x, y, and z - rather than 3N degrees of freedom.

DFT is based on two theorems proved by Hohenberg and Kohn, and set of equations derived from these theorems by Kohn and Sham. The first theorem states that the electronic density of the system (in a form of a functional) determines all ground-state properties of the system. This theorem does not explain the nature of the functional, so the second theorem introduces variational principle for minimizing the energy of the functional in order to obtain relevant electron density. However, this principle is limited to the ground-state, and cannot be easily applied in excited states.

These two theorems are the basis of the DFT, but they don't offer practical way for the calculations. Kohn and Sham showed that the problem of finding the right electron density can be solved by using the set of equations where only one electron is involved. The density has the same expression as if it was derived from a Slater determinant.

$$\rho(\boldsymbol{r}) = \sum_i |\Psi_i(r)|^2$$

In this expression, Ψ_i represent occupied orbitals (Kohn-Sham – KS orbitals). Kohn and Sham suggested calculating exact kinetic energy of the non-interacting system with the same density as the real, interacting one, where the non-interacting electrons are moving in effective potential. The energy is separated in "known" –that can be explicitly calculated and "unknown" – that cannot be explicitly calculated, terms:

$$E[\rho] = T[\rho] + E_{ext}[\rho] + E_{Coul}[\rho] + E_{ion} + E_{xc}[\rho]$$

i.e. "known": kinetic energy T, electron-nuclei attraction E_{ext}, Coulomb repulsion E_{Coul}, interaction between nuclei E_{ion} and "unknown": exchange-correlation term E_{xc}. Minimizing the energy functional leads to the Kohn-Sham (KS) equations.

$$\left[-\frac{\hbar^2}{2m}\nabla^2 + V_{eff}(\boldsymbol{r}) \right] \Psi_i(\boldsymbol{r}) = \varepsilon_i \Psi_i(\boldsymbol{r})$$

$$V_{eff}(\rho, \boldsymbol{r}) = V_{ext}(\rho, \boldsymbol{r}) + V_H(\rho, \boldsymbol{r}) + V_{XC}(\rho, \boldsymbol{r})$$

$$\rho(\boldsymbol{r}) = \sum_i |\Psi_i(\boldsymbol{r})|^2$$

$$V_{xc} = \frac{\delta E_{xc}}{\delta \rho(\boldsymbol{r})}$$

Solving of the KS equations must be done using iterative technique by self-consistent field method because effective potential V_{eff} depends on $\rho(\mathbf{r})$, and hence on $\Psi(\mathbf{r})$, which is the solution of the equation. From the eigen-energies and eigen-functions obtained it is possible to get ground state total energy, charge density, vibrational properties, etc.

The exchange-correlation potential term is defined as the functional derivative of E_{xc} with respect to the electron density. Finding this functional is very challenging task, so there have been developed approximate functionals such as Local Density Approximation (LDA), Generalized-Gradient Approximation (GGA) or Hybrid Functional.

1.6.1.   Approximation functionals

The first attempt to approximate the exchange-correlation functional was made by using the LDA method.[133, 134] In LDA, the E_{xc} is calculated by assuming the system behaves locally as a uniform electron gas, i.e.

$$E_{xc} = \int \rho(\boldsymbol{r}) \varepsilon_{xc}^{LDA}(\rho(\boldsymbol{r}))$$

$\varepsilon_{xc}^{LDA}(\rho)$ is the exchange-correlation energy density per electron of a uniform gas with density ρ. The performance of the LDA in calculations is surprisingly good for such a method, but the gross overestimation of the bond energies, and the poor thermochemistry, had diminished its usefulness in dealing with most of the questions of interest in chemistry.

The most basic class of functionals that improve upon LDA are based on the generalized gradient approximation (GGA). In this approach the exchange-correlation functional depends on both the value and the gradient of the electron density:

$$E_{xc} = \int \rho(\boldsymbol{r}) \varepsilon_{xc}^{GGA}(\rho(r), \nabla\rho(r)) dr$$

Local inhomogeneity in the electron density can be accounted for by making the energy density depend on the density gradient. Now, unlike LDA, the expression ε_{xc}^{GGA} is not unique, thus, there are numerous GGA functionals being used. These functionals vary in the exact constraints that they fulfil, in the number of adjustable parameters they contain as well as in the amount of empiricism in their construction. In general, GGA functionals provide much better results for the calculation of most properties; however, they are not sufficient enough to be useful in the calculation of chemical reaction energies. GGA functionals are also very popular in the solid-state field because they give accurate geometries, elastic properties of periodic solids and qualitatively correct electronic band structures. However, they severely underestimate the electronic band gaps.

Meta-GGA functionals increase the flexibility in the functional definition by using, the Kohn-Sham kinetic energy density (τ_{KS}) in addition to the density and its derivatives.

$$E_{xc} = \int \rho(\boldsymbol{r}) \varepsilon_{xc}^{GGA}(\rho(r), \nabla\rho(r), \nabla^2\rho(r), \tau_{KS}(r)) dr$$

$$\tau_{KS}(\boldsymbol{r}) = -\frac{1}{2}\sum_i |\nabla\psi_i(r)|^2$$

Having an increased degree of freedom, meta-GGA functionals usually improve accuracy in calculating the properties compared to GGA.

The above mentioned LDA, GGA and meta-GGA are semilocal functionals. This means that exchange-correlation energy density on a point, depends only on the properties of that point. Becke showed[135] that it is possible to greatly improve calculations of molecular thermochemistry by using a mixture of GGA and fraction of exact exchange, which is calculated as exchange Hartree-Fock energy, but obtained from KS orbitals.

The use of exact exchange in a functional is justified by invoking the adiabatic connection formula,[136, 137] a rigorous formula for the calculation of the exact exchange correlation functional.

$$E_{xc}[\rho] = \int_0^1 \left(\langle \sum_{i>j} r_{ij}^{-1} \rangle_\lambda - J[\rho^\lambda] \right) d\lambda = \int_0^1 U_{xc}^\lambda d\lambda$$

$\lambda = 0$ for non-interacting Kohn-Sham system, and $\lambda = 1$ for fully-interacting real system, i.e. parameter λ turns on electron correlation. Potential exchange correlation energy (U_{xc}) at the $\lambda = 0$ is exact exchange energy calculated using KS orbitals.

$$U_{xc}^0 = -\frac{1}{2} \sum_{ij}^{occ} \int \frac{\Psi_i^*(\mathbf{r}_1)\Psi_j^*(\mathbf{r}_2)\Psi_j^*(\mathbf{r}_1)\Psi_i^*(\mathbf{r}_2)}{r_{12}} d\mathbf{r}_1 d\mathbf{r}_2$$

Exchange-correlation functional can be approximated by interpolation between the known $\lambda = 0$ limit (exact exchange) and $\lambda = 1$, represented by the semilocal functional.

$$E_{xc}[\rho] = a_x U_{xc}^0 + (1 - a_x) E_{xc}^{semilocal}[\rho]$$

These functionals that use fraction of the exact exchange are called hybrid functionals. These functionals are no longer semilocal, because exact-exchange involves double integration over real-space. This makes them significantly more demanding computationally than semilocal functionals, thus limiting their wide spread use.

Even though hybrids provide improved accuracy in many chemically-relevant properties, they still face problems. One of these is "self-interaction" error. Because the antisymmetry of the wavefunction is not imposed as in HF, overestimation (or underestimation) of electron-electron interaction can occur. This in turn results in electrons interacting with themselves. One way of dealing with this is to use long-range corrected (LC) functionals.[138, 139] LC combine exact exchange with the semilocal function similar to the hybrids, difference being the electron correlation term ($1/r_{ij}$) which is separated in the short-range ($(1 - \text{erf}(\omega r_{ij}))/r_{ij}$) and long range ($\text{erf}(\omega r_{ij})/r_{ij}$), where erf is standard error function. Aim of the LC functionals is to recover the correct long-range behaviour of the exchange-correlation potential. This does not mean that they would model dispersion, but that the improvement is made in treatment of non-dispersive intermolecular electron-electron interactions.

1.6.2. DFT and non-covalent interactions

The last couple of decades have seen extensive use of the DFT functionals. These functionals can provide information on wide range of properties, such as spectroscopic properties, prediction of the molecular structure, excitation and reaction energies, etc., at a relatively small computational cost. DFT has found wide application in chemistry and physics; however, current density-functionals possess several shortcomings, such as the failure to accurately calculate NCI.

The first reports on the application of the DFT functionals in treatment of NCI were made in the 1990s.[133, 134] These studies showed the same problems density-functionals face today.

In a recent review DiLabio et al.[140] have made an extensive comparison on the performance of different DFT functionals in standard thermochemical tests, but most importantly, in dealing with the NCI (Figure 1.5).

Figure 1.5 shows the performance of several common density-functional approximations in the calculation of three kinds of intermolecular interactions. All density-functionals failed in correct description of the dispersion binding in Ne dimer. Results go from overly attractive (LDA, PBE), to very repulsive (BLYP). Even more complex meta-GGA, hybrid and LC functionals fail to describe binding. This is not very surprising, since all these functionals haven't been designed to take into account the long-range correlation effects.

The result for the π-π interactions shows that all functionals except LDA are repulsive to the various degrees. The trend is similar to the one observed in the binding energies of Ne.

The treatment of the H-bonding in the HF shows that most functionals perform decently, even in absence of dispersion. This can be explained by mostly electrostatic and orbital character of the interactions in hydrogen bonding. However, in the more complex systems, density-functionals fail to provide accurate bonding for hydrogen-bonded molecules.
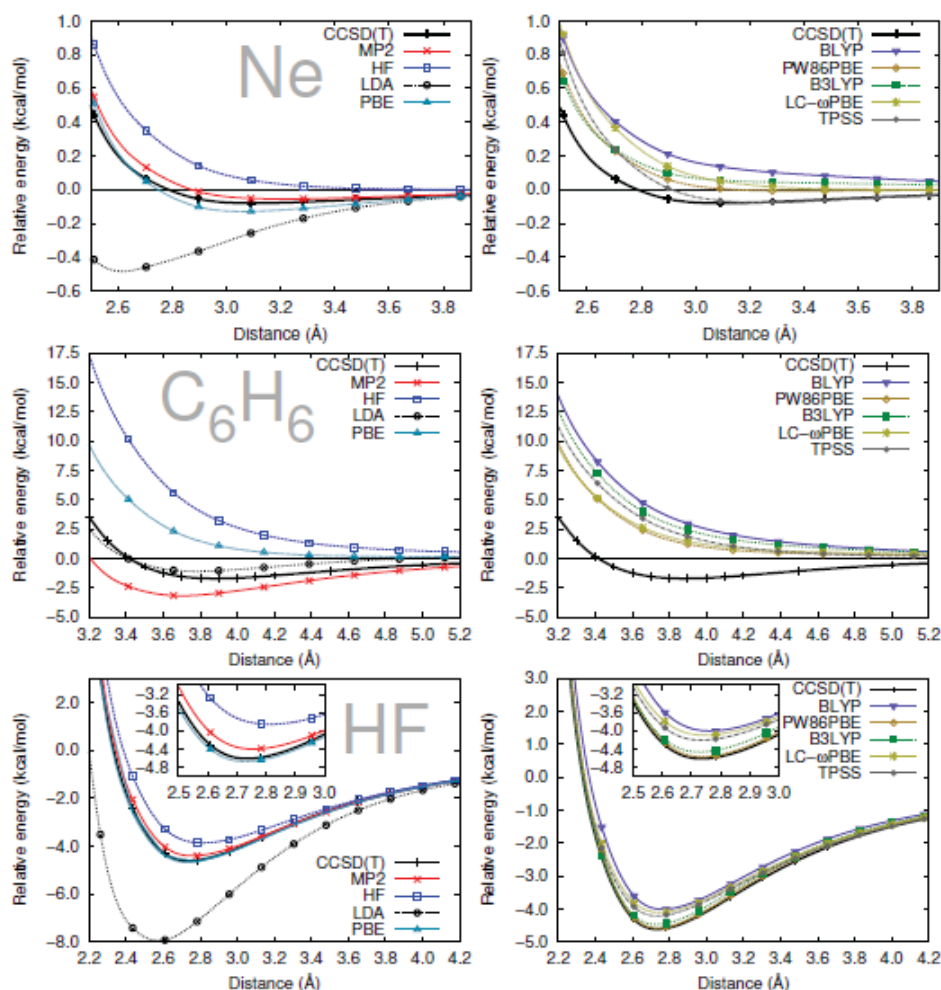
Figure 1.5. Binding energy curves of neon (top), benzene (middle), and hydrogen fluoride (bottom) dimers, calculated using wavefunction theory methods, LDA, and PBE (left), and other common density functionals (right) and compared to MP2 and CCSD(T) values.[140]

The difficulties in calculations of NCI energies are caused in part by the relative weakness of the non-covalent binding compared to the covalent. The simplest way to deal with the problem of missing dispersion is to add another energy term for dispersion, assuming that the base density functional approximately accounts for all other NCI, i.e.

$$E = E_{base} + E_{disp}$$

E_{disp} is the dispersion correction to the base functional. This term have to account for the missing dispersion energy, and also correct uncontrolled effects from the base functional on the binding energies.

1.6.3.   Dispersion treatment

For two interacting neutral atoms on sufficient distance, dispersion energy is always attractive, decaying as 6th power of the intermolecular distance.

$$E_{disp} = -\frac{C_6^{AB}}{r_{AB}^6}$$

C_6^{AB} is the dispersion coefficient. It can be estimated from the London's formula:

$$C_6^{AB} = \frac{3}{2}\left(\frac{I_A I_B}{I_A + I_B}\right)\alpha_A \alpha_B$$

I – atomic ionization potentials, α – atomic polarizabilities. The coefficient estimated using London's formula have little practical value. The interaction coefficient depends on the polarizabilities of both atoms which are proportional to the number of valence electrons and atomic size.[141] A more accurate value for the C_6^{AB} can be obtained from the second-order perturbation theory,[141] or more rigorously, using the Casimir-Polder formula.[142]

Dispersion energy term can be generalized to the interaction between molecules, or distant fragments of the same molecule, by considering that all atoms in the system interact with one another in a pairwise fashion.

$$E_{disp} = -\sum_{A>B} C_6^{AB} R_{AB}^{-6} f_6(r_{AB}) - \ldots$$

The f_6 factor is called the damping function, a one-dimensional function of the interatomic distance that goes to zero when $r_{AB}\rightarrow 0$ and to one when $r_{AB}\rightarrow\infty$. This function has two roles in dispersion-corrected DFT. One is to correct for the error introduced by the approximations. The other is to deactivate the dispersion contribution at very short range to avoid the singularity at $r_{AB} = 0$. The damping function also performs the role of fixing the problems the base functional has in reproducing other terms in the intermolecular interaction energy (e.g. electrostatics) through its adjustable parameters.

The basis of all pairwise dispersion corrections is the calculation of the C_6^{AB}. The interaction coefficients traditionally used in classical force fields are not adequate, because they are treated as fitted parameters rather than physical quantities, so they account for other effects in addition to dispersion[143] and therefore are widely variable across different classical force fields.[144]

In the last ten years, a number of approximations have been proposed for the C_6^{AB} and higher-order coefficients with varying degrees of accuracy and empiricism. Some of the most popular are: DFT-D[145-147] family of dispersion corrections developed by Grimme, the Tkatchenko-Scheffer method,[148] exchange-hole dipole moment (XDM) model of dispersion,[149] the method by Tao, Perdew and Ruzsinszky.[150]

The latest method developed by Grimme (DFT-D3)[147] will be briefly presented in the Chapter 2 of this thesis.

1.6.4.   Solvation treatment

The development of the computational methods during the last decades has made possible fairly accurate description, and prediction of wide range of molecular properties in vacuum and gas phase. However, nearly all processes in chemistry and biochemistry take place in condensed phase, mostly in fluid. Thus, there is a need for proper theoretical and computational approach in the treatment of the molecules in solution. This important issue of predicting the behaviour and thermodynamic properties of solute-solvent systems is one of the actual challenges for computational chemistry.[151]

The proper description of a solute molecule in a solvent on a molecular scale is a very hard task, because the solute is interacting with several surrounding solvent molecules, and these again interact with others and so on.[152] This makes consideration of a large group of molecules, typically at least several hundreds of molecules, i.e. several thousands of atoms, for accurate description of the system.

There are several limiting factors in the computational treatment of these ensembles. Because of the huge influence of the surface effects even in the case of small number of molecules, it is necessary to introduce some periodic boundary conditions. Also, calculating ground state of such systems by energy minimization is futile, since the behaviour of said systems is determined by the thermodynamic average of conformationally excited states.[152] One more limiting factor is the computational cost such calculations would demand given that

the molecular orbital calculations scale with the third power of the number of atoms in the system.

1.6.5.   Explicit and implicit approaches

There are two main approaches in dealing with the solvation issue. The first one is based on the use of the explicit molecules of solvent, used by molecular mechanic (MM) and molecular dynamic (MD) calculations. The most widely used approximation is the use of force fields for the description of intra- and intermolecular interactions and to do the thermodynamic averaging by a dynamical (MD) or random (Monte Carlo, MC) sampling of the relevant states.

Total potential energy of the system is the sum of the bonding and non-bonding interactions contributions. In this approach, new type of functions is not introduced in the force field, but the solvation effects are defined by parameterization. The calculation of the potential energy includes the sum of atoms of the solute and all the molecules of solvent in the simulation box. The results of such calculations are restricted by the fundamental approximation, i.e. the description of the interactions by classical force fields. While intramolecular forces and also dispersive interactions between molecules appear to be quite well parameterized in many force fields, the proper treatment of electrostatic interactions is more of a problem. These interactions are usually calculated using dielectric constant of vacuum, which usually differ considerably from the dielectric constant of surrounding solvent. Since for most polar or polarizable molecules the majority of the solvation effects arise from electrostatic screening of the molecular polarities, this is a crucial limitation for the application of MD or MC methods for the description of solvation phenomena.

The explicit approach to solvation generally gives more accurate information on the molecular structures and realistic physical information, but often solute and solvent are not polarizable and the computational cost in quite demanding. They generally require orders of magnitude more computational time than corresponding gas phase calculations on the same molecule.

The implicit (continuum) solvation approach is mostly used to estimate free energy of solute-solvent interactions in structural and chemical processes, such as association of biological macromolecules with ligands, transport of drugs across biological membranes, and folding or conformational transitions of proteins, DNA, polysaccharides.

1.6.5.1 Implicit (continuum) model

Based on the early work of Born,[153] Kirkwood,[154] and Onsager[155] continuum solvation models have been proposed. These primarily focus on the solute molecule or a small cluster of the solute with a few solvent molecules and try to represent the influence of the rest of the solvent by an effective continuum surrounding them.

A continuum model in computational molecular sciences can be defined as: *"a model in which a number of the degrees of freedom of the constituent particles are described in a continuous way, usually by means of a distribution function".*[151]

Dispersive interaction energies can be quite accurately expressed by a term proportional to the exposed surface area, and because electrostatic interactions in solvation are extremely important, the main task of these models is to give a proper description of the electrostatic screening within this continuum approximation. The use of the dielectric theory for macroscopic systems is widely accepted in this approach.

There have been developed different classes of these dielectric continuum solvation models, which are often called self-consistent reaction field (SCRF) models. In all of these models a surface is constructed around the solute. This defines the boundary to the dielectric continuum. For a given electrostatic field of the solute derived from a single molecule MO calculation, the dielectric medium screens this field by a polarization of the medium. This medium may be represented by well-defined surface charges on the boundary surface. Once these are calculated, the MO calculation can be repeated self-consistently, taking into account the field of these screening charges.

In summary, for the continuum models, solvent is defined as a uniform polarizable medium of fixed dielectric constant ε having a solute molecule M placed in a suitably shaped cavity.

1.6.6. Free energy of solvation

Potential energy of the system in this approach is calculated as a sum of the contributions of bonding interactions, non-bonding interactions and contribution of solvation. The last term can be expressed as a free energy of solvation ΔG_{solv}. In SCRF models free solvation energy is calculated as:

$$\Delta G_{solv} = \Delta G_{elec} + \Delta G_{disp} + \Delta G_{cav}$$

The terms ΔG_{elec} – due to polarization between solute and solvent which induces charge redistribution until self-consistency, and ΔG_{disp} – form dispersion interactions between solute and solvent, lower the total free energy. The last term destabilizes the system, representing the creation of the cavity in the medium. This destabilization comes from the entropic penalty due to the reorganization of the solvent molecules around the solute and the work done in creating the cavity. For proper description of the solvation it is necessary to define cavity, a basic concept in all continuum models.[151]

1.6.7.   Cavity

The model for cavity is composed of the solute, a molecule (or a few molecules) which is placed into an empty cavity within a continuous dielectric medium mimicking the solvent. The shape and size of the cavity differ in definition depending on the continuum model, but there is one main requirement in the definition of cavity for each model. Cavity should have a physical meaning, and not only be a mathematical creation, as often happens in other descriptions of solvent effects.[151] This means that the cavity should contain within its boundaries the largest possible part of the solute charge distribution and exclude the solvent completely.

Computational costs are very much dependent on the modelling of the cavity. They are far simpler and faster when simple shapes are used, such as spheres or ellipsoids, but molecules often have an irregular shape. There are several models for defining the cavity shape.

The simplest models consider the cavity to be simple sphere or ellipsoid encompassing the molecule. This model starts from the idea proposed by Kirkwood[154] and Onsager[155] to describe the interaction between a set of classical point charges that are placed in a spherical cavity embedded in a structureless polarizable dielectric medium (with dielectric constant ε).

Another approach uses van der Waals radii (vdW) of individual atoms to define the surface of the cavity. The cavity is constructed from interlocking spheres near the vdW value of radii for each atom.[151] The values for radii are taken from the sets defined by Bondi,[156] Pauling[157] of from the universal force field (UFF).[158]

Due to the irregular shape of the molecules, solvent often cannot penetrate to the small portions of space. To deal with this problem, approximations have been made. Here, definition of the surface given by Tomasi et al.[151] will be presented.

The solvent molecule is reduced to a sphere, with a volume equal to the vdW volume. The positions assumed by the centre of a solvent sphere rolling on the vdW surface of the solute define the solvent accessible (SA) surface, that is, the surface enclosing the volume in which the solvent centre cannot enter. The same sphere used as a contact probe on the solute surface defines the solvent exclusion (SE) surface, that is, the surface enclosing the volume in which the whole solvent molecule cannot penetrate (Figure 1.6). In the literature, the SE surface is also called "Connolly surface", due to Connolly's fundamental work in this field.[159, 160]
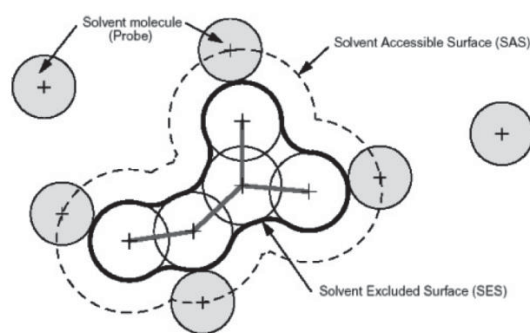
Figure 1.6. Solvent accessible surface (SAS) traced out by the centre of the probe representing a solvent molecule. The solvent excluded surface (SES) is the topological boundary of the union of all possible probes that do not overlap with the molecule.[151]

1.6.8. Solving the electrostatic problem

The physics of the electrostatic solute-solvent interaction is simple. The charge distribution of the solute, inside the cavity, polarizes the dielectric continuum, which in turn polarizes the solute charge distribution. This definition of the interaction corresponds to a self-consistent process, which is numerically solved following an iterative procedure.

To describe the electrostatic component of solvation energy ΔG_{elec} in molecules, the Poisson equation can be used. The Poisson equation relates the variation of the potential φ within a medium of uniform dielectric constant ε to the charge density ρ.

$$\nabla^2 \varphi(\vec{r}) = -\frac{4\pi\rho(\vec{r})}{\varepsilon}$$

If the dielectric ε is not constant, but changes with position $\vec{r}$ and there are mobile ions in the medium, linear Poisson-Boltzmann equation has to be solved:

$$\nabla \cdot \varepsilon(\vec{r})\nabla\varphi(\vec{r}) - \kappa'\varphi(\vec{r}) = -4\pi\rho(\vec{r})$$

Where κ' is connected to the Debye-Hückel inverse length κ.

The equation cannot be solved analytically for complex geometries, so it is solved numerically by Finite Difference method, in which the solute is placed in a cubic grid along with the solvent. Values of the electrostatic potential, charge density, dielectric constant and ionic strength are assigned to each grid point. The derivatives in the Poisson-Boltzmann equation are then determined by the finite difference formula.

Numerical calculations of the Poisson equation is complicated, so different approximations have been developed in order to simplify the calculations. In one of the models called Generalized Born (GB) model, approximation to the linearized Poisson-Boltzmann equation is used. It GB model solute is considered as a set of spheres with internal dielectric constant that differs from the external solvent. The form of GB equation for the system of N atoms is:

$$\Delta G_{elec} = -\frac{1}{2}\left(\frac{1}{\varepsilon_0} - \frac{1}{\varepsilon}\right)\sum_{i,j}^{N}\frac{q_i q_j}{f_{GB}}$$

$$f_{GB} = \sqrt{r_{ij}^2 + a_{ij}^2 e^{-D}}$$

$$D = \left(\frac{r_{ij}}{2a_{ij}}\right)^2 ; \; a_{ij} = \sqrt{a_i a_j}$$

where ε_0 is the permittivity of free space, ε is the dielectric constant of the solvent being modelled, $q_{i(j)}$ is the electrostatic charge on particle i(j), r_{ij} is the distance between particles i and j, and a_i is the effective Born radius.

Extension to this approach is GB model augmented with the hydrophobic solvent accessible surface area (SA) term. Here, terms for the solvent-solute interactions and creation of the cavity are expressed as:

$$\Delta G_{disp} + \Delta G_{cav} = \gamma A + b$$

where A is the solvent accessible (SA) area, and b and γ are parameters obtained from experiments.

1.6.9.   Some continuum models

Generally, all continuum SCRF models differ in several aspects: the size and shape of the cavity they adopt; the method of calculating the cavity creation and the dispersion contributions; how the charge distribution of the solute is represented; the description of the solute and dielectric medium. Here, some of these models will be presented briefly.

Polarizable Continuum Model – PCM is a set of codes, all based on the same philosophy and sharing many features, some specialized for some specific purposes and others for general use. These are dielectric PCM (DPCM), conductor-like PCM (CPCM), integral equation formalism PCM (IEFPCM).

Tomasi[151] says that DPCM is able to describe an unlimited number of solutes, each equipped with its own cavity, interacting among them through the dielectric. In this way, DPCM permits an extension of the basic model to association-dissociation phenomena, molecular clustering, etc. It also can account for a continuous shift from a single cavity to two cavities during dissociation and the merging of two or more cavities during association. In parallel, it permits an extension to models in which the medium is composed by a set of nonoverlapping dielectric regions at different permittivity, constant within each region.

DPCM uses the van der Waals radii of the atoms to determine the cavity surface. The surface is in turn divided into a number of small surface elements with area ΔS. If $\vec{E}_i$ is the electric field gradient at point i due to the solute then an initial charge, q_i is then assigned to each element via:

$$q_i = -\left(\frac{\varepsilon - 1}{4\pi\varepsilon}\right)\vec{E}_i\Delta S$$

The potential due to the point charges $\varphi_\sigma(r)$ is then found, giving a new electric field gradient. The charges are modified until they converge. The solute Hamiltonian is modified as:

$$H = H_0 + \varphi_\sigma(r)$$

After each SCF new values of q_i and $\varphi_\sigma(r)$ are computed until self-consistency is achieved.

Conductor like screening model – COSMO, is the variant of the continuum solvation models, which uses a scaled conductor boundary condition instead of much more complicated dielectric boundary condition for the calculation of the polarization charges of a molecule in a continuum.[161] If the solvent would be an ideal conductor, the electric potential on the cavity surface should disappear. Modelling of the cavity and the type of radii used in this model differ between various implementations of the method.

It is possible to calculate the charge q^* on the surface segments if the distribution of the electric charge in the molecule is known. For solvents with finite dielectric constant this charge q is lower by approximately a factor $f(\varepsilon)$:

$$q = f(\varepsilon)q^*$$

$$f(\varepsilon) = \frac{\varepsilon - 1}{\varepsilon + x}$$

where x vary depending on the shape of the cavity and distribution of the charges, and the value is set on 0.5 based on theoretical arguments.

The energy of the interaction between the solvent and the solute molecule can now be calculated from the solvent charges q and the known charge distribution of the molecule. Having done this step, corresponding fully self-consistent total energy of the system in the presence of the dielectric environment can be calculated in a standard SCF-cycle with the modified Hamiltonian.

COSMO-RS (conductor-like screening model for real solvents), an extension of the COSMO model, has been proposed by Klamt,[152] starting from the analysis that solvents do not behave linearly when we consider strong electric fields on the molecular surfaces of fairly polar solutes. COSMO-RS is a theory that describes the interactions in a fluid as local contact interactions of molecular surfaces. The interaction energies are quantified by the values of the two screening charge densities that form a molecular contact.

COSMO-RS has become a predictive method for the thermodynamic properties of pure and mixed fluids. In contrast to group contribution methods, which depend on an extremely large number of experimental data, COSMO-RS calculates the thermochemical

data from molecular surface polarity distributions, which result from quantum chemical calculations of the individual compounds in the mixture. The different interactions of molecules in a liquid, i.e. electrostatic interactions, hydrogen bonding, and dispersion, are represented as functions of surface polarities of the partners. Using an efficient thermodynamic solution for such pairwise surface interactions, COSMO-RS finally converts the molecular polarity information into standard thermodynamic data of fluids, that is, vapour pressures, activity coefficients, excess properties, etc.;[162, 163] the corresponding computational code is called COSMOtherm.[164]

Besides COSMO and PCM family of models, there exist others, based on different approaches. Some of these are Integral Equation Formalism (IEF),[165, 166] Surface and Volume Polarization for Electrostatic (SVPE and SS(V)PE),[167-170] MultiPole Expansion (MPE),[155, 171-175] Generalized Born (GB).[176-179]

1.7.   Focus of the research

Main goal of the this thesis was to study non-covalent interactions using different experimental and theoretical techniques on subjects that have been based on misconception, or not addressed before, perhaps due to the lack of the adequate methodology, or underdevelopment of the existing methods. In following sections some of these subjects will be briefly presented

1.7.1.   Stacking interactions studies

Stacking interactions, where aromatic molecules are parallel, have been extensively studied for several decades. Last couple of years have seen development of the new methods used in the studies of stacking interactions.[23, 147, 180-190] Generally, stacking between aromatic organic molecules or fragments was considered.[15-18, 26, 43, 50, 191-207] However, number of studies showed that various non-aromatic molecules can also form stacking interactions with aromatic molecules.[92, 94, 95, 208-211] Among these molecules is water molecule, where whole water molecule or one of OH bonds can lay parallel to the aromatic ring.[210, 211] Namely, the analysis of crystal structures from the CSD that involve close contact between water and aryl rings revealed the existence of structures where the whole water molecule or one of its O–H bonds is parallel to the aromatic ring plane at distances typical for stacking interactions

(Figure 1.7).[211] The crystallographic evidence from the CSD search that most water molecules are found at the large horizontal displacements, out of the aromatic ring and out of the C-H bond region, with one water O–H bond parallel to the aromatic ring plane.[210]
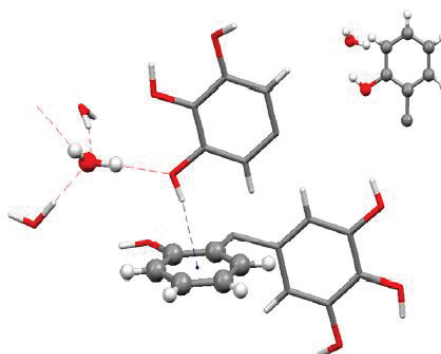
Figure 1.7. The fragment of crystal structure EBAQII selected as an example of the structure with the parallel interaction between the water and the aryl ring at the large displacement (r_O= 3.56 Å). Parallel water O-H group also builds two additional classical hydrogen bonds with groups from environment. [211]

The observed parallel interactions at the large displacement are a consequence of attractive interactions between water and the aryl ring (Figure 1.8). The energies of the most stable parallel interactions are significant ($\Delta E_{CCSD(T)(limit)}$= -2.45 kcal/mol, at horizontal displacement of 2.6 Å)[210] and comparable with the energy of slipped-parallel benzene/benzene dimer ($\Delta E_{CCSD(T)(limit)}$= -2. 73 kcal/mol).[183]
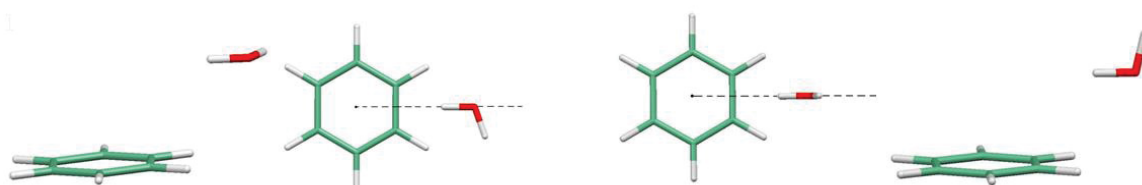
Figure 1.8. The most stable parallel interactions of the water–benzene dimers with the whole water molecule (ΔE= -1.60 kcal/mol) or one of its O–H bonds (ΔE= -2.45 kcal/mol) is parallel to the aromatic ring plane.[210]

1.7.2.   Parallel interactions at large displacements

Recent studies on the stacking interactions between parallel aromatic rings, i.e. benzene and pyridine dimers have shown some interesting results.[42, 43] Crystallographic analysis of the structures in the CSD has shown that numerous contacts between the aromatic molecules exist at large horizontal displacements - offsets (at distances greater than 4.0 Å).

Both benzene-benzene and pyridine-pyridine have shown clear preference for large displacements Figure 1.9.
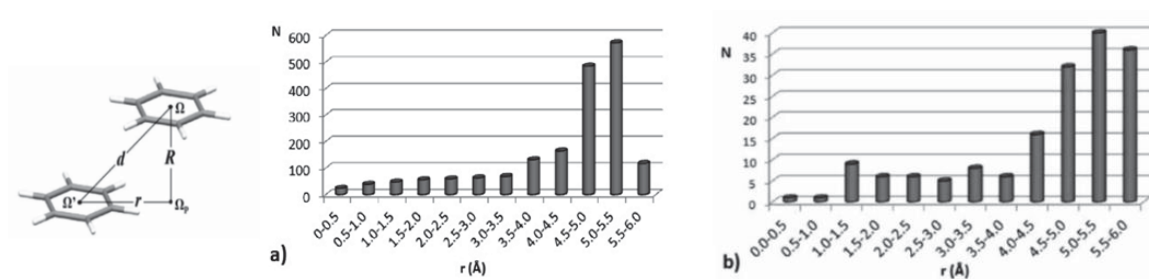
Figure 1.9. Geometrical parameters used for the description of parallel interactions between two aromatic molecules and the distributions of offsets for mutually parallel benzene (a) and pyridine (b) molecules. N – number of structures, r – parallel displacements[42, 43]

Explanation for this trend was sought by performing DFT calculations on the dimers of benzene, pyridine and their combination by varying the distance between molecules. Calculations have shown that significant interaction exists at the large horizontal displacements. Interaction energies that were calculated for all three cases at large displacements show values of ca. -2 kcal/mol. Examples for benzene-benzene interaction at the large displacement are shown in Figure 1.10.

$\Delta E = -1.74$ kcal/mol $\Delta E = -1.92$ kcal/mol $\Delta E = -1.93$ kcal/mol
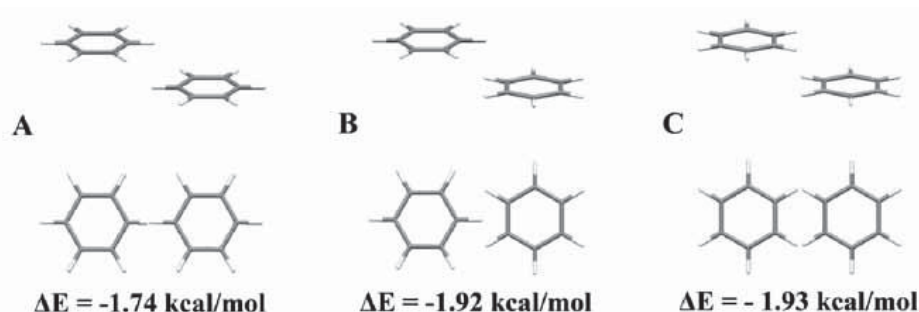
Figure 1.10. Two views of three parallel benzene-benzene orientations (A, B and C) calculations with interaction energies; geometries shown are at offset values of 5.0 Å.[42, 43]

Trends in the interaction energies for benzene-benzene at different displacements are shown in Figure 1.11. Global energy minimum (ca. -2.8 kcal/mol) corresponds to the displaced benzene dimer at offset of 1.8 Å. Another minimum (ca. -2 kcal/mol) can be observed at large offsets (4.5 Å).
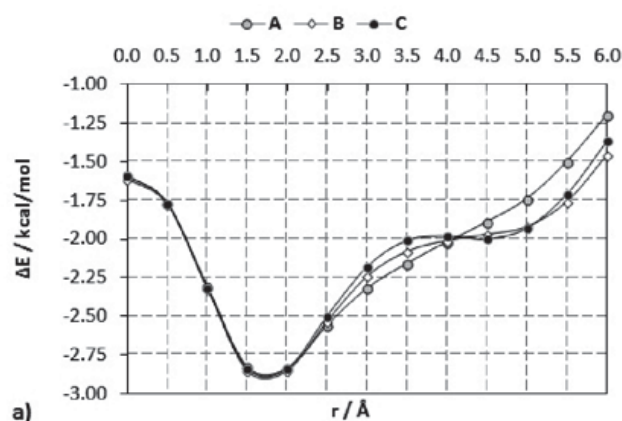
Figure 1.11. Calculated interaction energies (ΔE) for three different orientations of benzene molecules plotted as a function of the r value. The A, B, and C orientations are presented in Figure 1.10.[42, 43]

Interestingly, crystallographic analysis of the stacking interactions of parallel aromatic molecules showed that the most numerous structures in the CSD appear at the large horizontal displacements (above 4.0 Å), while the calculations showed that the most stable geometries have offsets of around 1.5 - 2 Å. This discrepancy is the consequence of the packing and the surrounding in the supramolecular structures. Aromatic molecules can form additional interactions with the environment in the structures with the large displacements (Figure 1.12).
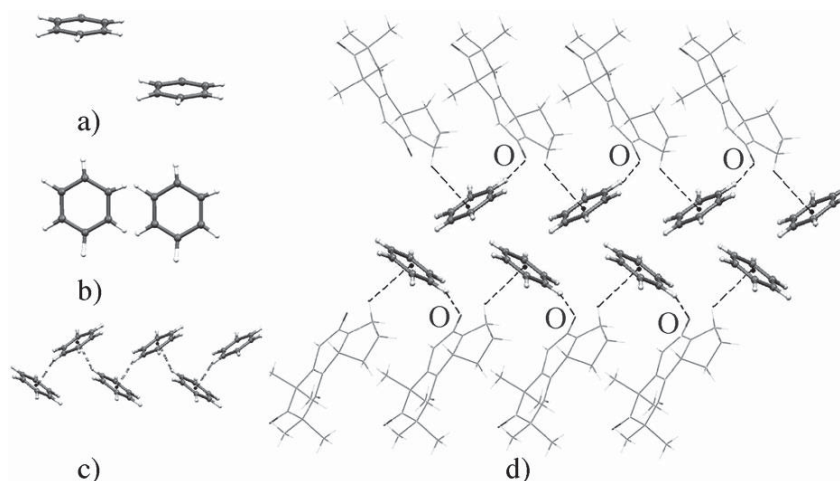
Figure 1.12. Several points of view on the parallel benzene–benzene interactions with a large offset in the crystal structure.[42, 43]

Similar observations have been made in the study of the stacking interactions of pyridine-pyridine molecules at large displacements.[42]

1.7.3. Stacking interactions of chelate rings

First investigations of chelate-aryl interactions have showed that the presence of chelate ring influence the short metal-aryl contact, suggesting the existence of interactions between the chelate ring and aryl ring (Figure 1.13).[94, 212]
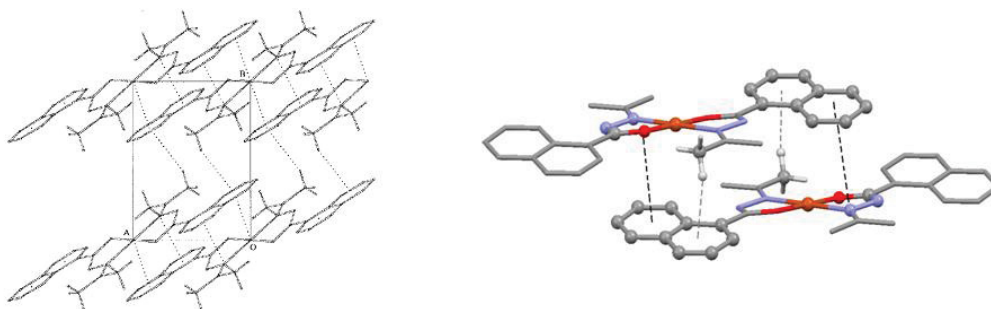
Figure 1.13. The fragment of crystal structures, in with "chelate-aryl" π–π stacking interactions were first recognized and characterized. [94, 212]

By analysing the data in the CSD, stacking interactions between chelate and C_6-aromatic rings were identified in the crystal structures of square-planar transition metal complexes.[94, 95, 213]

The crystallographic analysis of metal complexes with and without chelate rings, has shown that the presence of a chelate ring with delocalized π-bonds has an influence on the close contact between the metal atom and the carbon atom of the aryl ring.[95]

The tendency of a chelate ring to make the stacking interaction with the C_6-aryl ring, is independent of the metal type in a chelate ring; although, there are small differences in trends among metals.[213] In the structures of metal complexes with CN ligands, it was found that the cyano ligands have a tendency to make parallel interactions with the aryl ring (Figure 1.14), which is independent of the metal in the complex. The interactions of the aryl ring and the CN-complex are probably influenced by presence of π- bonds in CN ligand. Calculations have shown that the nature of metal ions strongly influences on the strength of these interactions.[91, 92]

The energies of stacking interactions of benzene with chelate ring were calculated[91] and results show that chelate-benzene stacking interactions are remarkably stronger than benzene-benzene interactions. Calculations have shown that the nature of metal ions strongly influences on the strength of these interactions (

Figure **1.15**). The calculated stacking energies of copper and nickel chelates with benzene are -6.39 kcal/mol and -4.77 kcal/mol respectively,[91] while calculated energy of benzene-benzene interaction is -2.73 kcal/mol.[183]
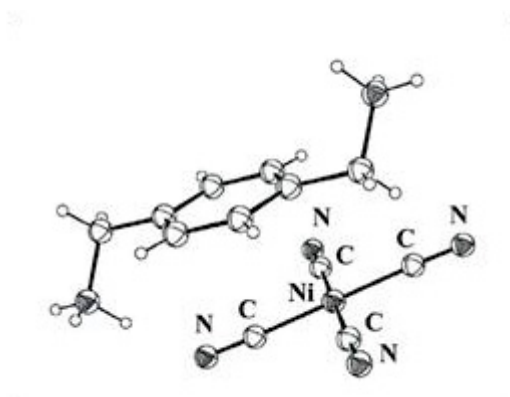
Figure 1.14. The example of crystal structures (recode ZURRUZ), where C_6-group of the p-xylene di-ammonium cation is oriented parallel to the mean plane of $[Ni(CN)_4]^{2-}$ complex. The distance between Ni and center of phenyl ring is 3.55 Å.[214]

Planar chelate rings with delocalized π-bonds can also form CH/π interactions with C_6-aromatic rings.[54, 56, 215-221] However, analysis of the CSD has shown that stacking interactions are preferred to CH/π interactions in these complexes.[222]
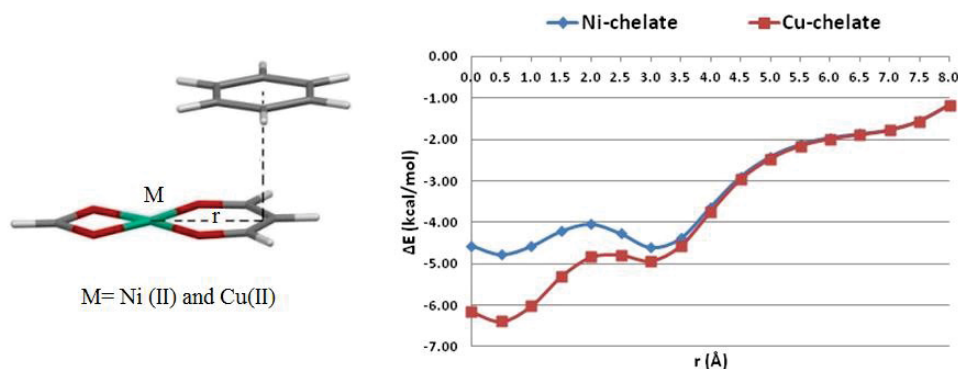
Figure 1.15. The model system and energy curves for stacking interaction between metal-chelates and benzene; r is the horizontal displacement.[91]

Planar chelate rings can also form stacking interactions with other chelate rings. The first detailed study describing the chelate-chelate stacking interactions was based on crystal structures of square-planar complexes from the CSD.[93] Large number of chelate-chelate stacking interactions have been found, while certain geometrical regularities in the packing have been observed. The normal distances in chelate-chelate stacking interactions are similar to those found in stacking interactions between organic aromatic rings, while the displacement of two interacting chelate rings can be different[93] than between organic aromatic rings.

The distribution of the torsion angles τ (M-Ω-Ω'-M'), which describes the mutual orientation of two chelate rings, show that the most of the interactions have the values of the angle τ less than 10° or near 180°, it means that the parallel (or *head-to-head*) and antiparallel (or *head-to-tail*) orientations are the most common (Figure 1.16).
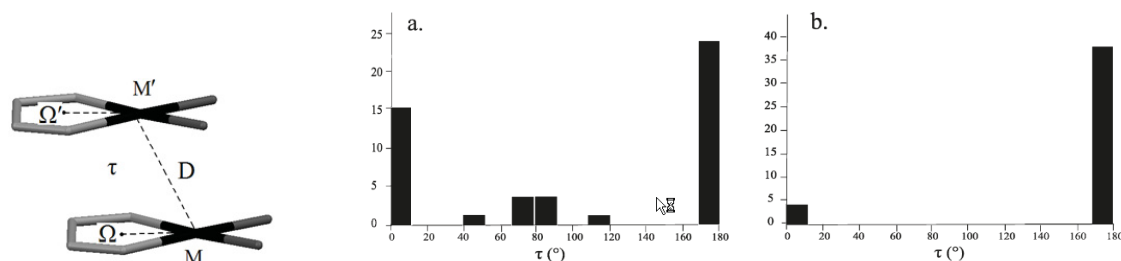
Figure 1.16. The definition of τ parameter (left); The distribution of τ parameter for chelate-chelate interactions in crystal structures with isolated (a) five-membered and (b) six-membered chelate rings.[93]

The five-membered chelates have a tendency for slipped parallel orientations, which is in accordance with the most stable conformation of two benzene rings,[183] while the six-membered rings have a tendency for *face-to-face* orientation with a very small displacement. Most of these complexes have two six-membered chelate rings in mutual *trans* positions with substituents on the rings. In order to avoid clashing of substituents, the stacked chelate rings have an antiparallel orientation and small displacement (Figure 1.17).
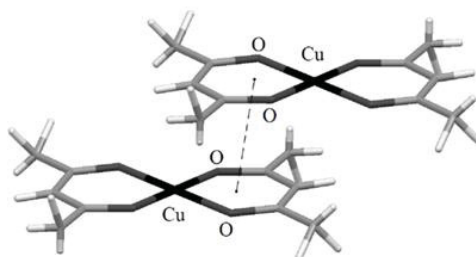
Figure 1.17. The view on chelate-chelate stacking interaction with antiparallel orientation (τ ~180°) in the structure of isolated six-membered rings.[93]

A terpyridine (*terpy*) molecule coordinating to a metal ion forms a large planar system of five fused rings: three pyridine and two chelate rings (Figure 1.18). This planar system has tendency to form stacking interactions which were studied by analysing the crystal structures from the CSD.[62] The most numerous are structures found have *head-to-tail* orientation of the two *terpy* ligands and quite large area of overlap. The terminal pyridine and both chelate rings completely overlap, while the central pyridine rings are partially included in the overlap (Figure 1.18).
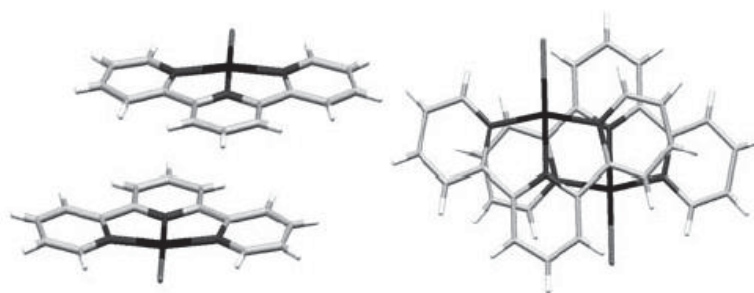
Figure 1.18. The stacking interaction in structure selected as an example of structure with most numerous overlap type of terpy ligands.[62]

Similar to the *terpy* ligand, the phenanthroline (*phen*) molecule coordinating to a metal ion forms a planar system with four fused rings: two pyridines, one C_6-aryl and one chelate ring (Figure 1.19). Study on the systems with *phen* ligand was based on the analysis of the crystal structures from the CSD in a similar way as for *terpy* analogue.[63] In most of the crystal structures, two stacked *phen* ligands have *head-to-tail* orientation of the ligands and quite large area of overlap (Figure 1.19).
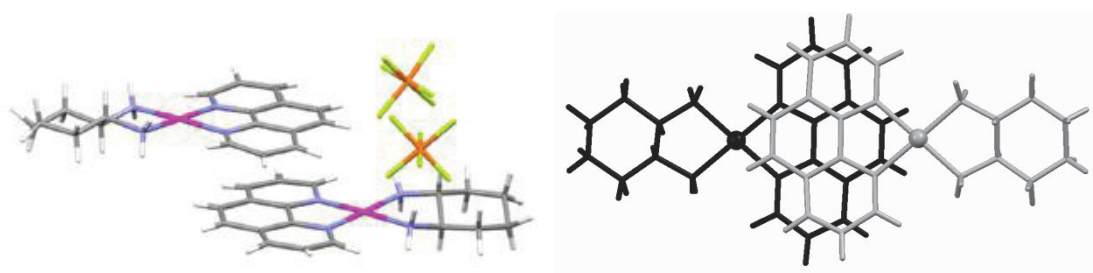
Figure 1.19. The most frequent type of ligand overlap in crystal structures of square-planar *phen* complexes.[63]

The results of the both studies showed that the stacking interactions between the complexes occur by overlapping of the large surface of the ligands, while influenced by the nature of the ligands coordinated to the remaining coordination sites. One important difference was that while *terpy* ligand has two fused chelate rings involved in mutual interactions, *phen* ligand has only one chelate. The existence of additional fused aryl ring in the structure of the *phen* ligand, results in the overlapping of the complexes where the interaction between the chelate rings is far less present compared to the *terpy* complexes.

Bipyridine (*bipy*) complexes are structurally similar to *terpy* and *phen* complexes. They have two pyridine rings fused with the chelate, thus making the approach of the chelates easier for the mutual interaction. This in turn makes them a good candidate for study of the chelate-chelate stacking interactions.

These complexes can be used for various applications. They can be used in photo-induced[223-228] and electron-transfer[224, 227, 229] processes, or in supramolecular architectures and materials science.[227, 230, 231] Unfunctionalized, many mono-functionalized,[224, 230] symmetrical and unsymmetrical multifunctionalized bipyridines[232] have been synthesized and used for dye-sensitized solar cells (DSC),[223, 226, 228] functional polymers, new catalytic species, molecular recognition systems, etc.[227, 230] For example, $[Ru(bipy)_3]^{2+}$ have been used in various cases: from unique photoprobe of host-guest interfaces with enhanced potential for photonic and sensor applications with intense luminescence,[225] to usage in combined tiny films of modified electrodes which exhibit improved electron transfer, electrocatalytic and fluorescence activity.[226, 233, 234] It was found that some *bipy* complexes can bind to DNA with high binding constants. It was also shown that the complexes can bind to DNA by intercalation that is proven by hypochromism and bathochromism of electronic absorption spectra, or interact with DNA surface by π-π stacking interactions.[235-237]

1.7.4. Oligomerization of Rh(I) *sqp* complexes

Great attention was focused during the last 40 years on the chemical and physical properties of tetrakis(isonitrile)Rh(I) complexes,[238-240] which have been highlighted by a large number of reports that illustrated their physical properties as well as their unusual propensity to spontaneously form adducts and oligomers in solution as well as in the solid state (Figure 1.20).[241-244]

L = R-NC
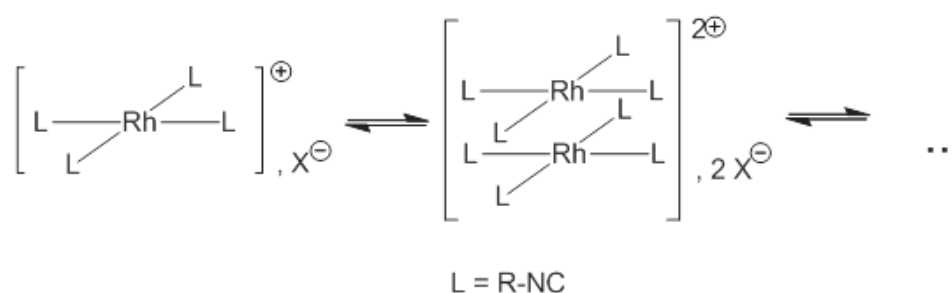
Figure 1.20. Formation of the oligomers in the Rh(I) square-planar complexes

The formation of these oligomers is always accompanied with major changes in the electronic spectrum of the solution, which is characterized by the growth of a new absorption band at longer wavelengths as the concentration in monomer increases.[245, 246] This typical spectroscopic signature[247] of the dimeric and trimeric forms expresses the sensible perturbations caused to the electronic structure of the system by the self-association of two

identical square planar d^8 fragments in a face-to-face arrangement.[248] This property[249, 250] has originally sparked conjectures on a specific "d^8-d^8" interaction that would act somewhat as a driving force in the process of so-called self-assembly.[251-255] The new electronic transitions, which originates from metal-to-ligand charge transfer,[252, 256] has been the subject of great attention[257] especially because they were also found responsible for the peculiar photo-chemical/physical[258-262] and electrochemical properties of those oligomers, which clearly differ from the behaviour of the corresponding monomers.[263-265] The oligomers' propensity to readily undergo electron transfer reactions[263, 266, 267] and oxidations[263, 268] leading to M-M bound complexes[269] upon exposure to light was demonstrated in many instances. This property has prompted the development of bridged analogues and their evaluation as catalysts for solar energy conversion, for instance.[270-273]

Oligomeric forms were characterized in the crystal by structural X-ray diffraction analysis.[252, 274, 275] Numerous examples of dimers[276, 277] and trimers[278, 279] can be found in structural databases, which clearly demonstrate the reality of the propensity of cationic Rh(I) tetrakis(isonitrile) complexes to self-aggregate in the solid state. Self-aggregation with metal-metal contacts is precluded by steric effects created by bulky isonitrile ligands.[280, 281] In the most common cases, Rh(I)-Rh(I) dimers display an average metal-metal distance of ca. 3.1 A.[282, 283] The metal-metal interaction was studied in so-called bridged systems whereby the two metal fragments are somewhat forced to remain in close vicinity.[274, 284, 285] It was demonstrated that the Rh-Rh distance would be significantly shorten by ca. 0.85 Å in a bridged complex brought to its triplet exited state upon exposure to the radiation of a pulsed laser beam,[282] thus confirming earlier results inferred from the spectroscopic study of these bridged species.[286-288] If great efforts have been invested in investigating the photo-physical properties of these binuclear Rh(I)-Rh(I) assemblies,[282, 289, 290] not much knowledge about the real origin of the interactions that govern the process of self-aggregation of the cationic monomers was sought.[291]

In a recent report,[292] addressing the issue of oligomerization of Rh(I) complexes, Grimme and Djukic provided evidence to the driving capability of London dispersion force that operates not exclusively between the two metal centres but significantly throughout the assembled monomer units, hence counteracting the repulsive Coulomb interaction between the positively charged fragments (Figure 1.21), that was favoured only by proper application of the solvation treatment.
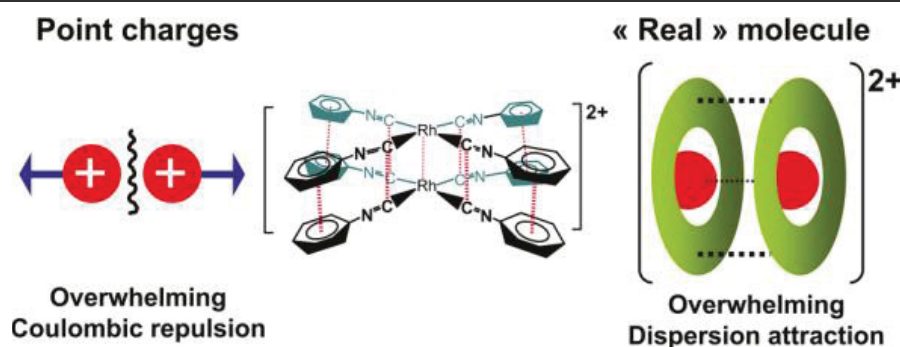
Figure 1.21. Stabilization of the Rh(I) dimer due to London dispersion force.[292]

Although the phenomenon that they described may in the end seem to be trivial and perhaps irrelevant to many charged chemical systems, it had not been demonstrated and analysed clearly until this report for this peculiar class of coordination complexes.

1.7.5. Oligomerization of Cisplatin type complexes

The discovery of the cytotoxicity of Cisplatin[293] in the mid 1960's has opened a new paradigm for transition metal chemistry, which is the use of coordination complexes for the therapeutic treatment of diseases such as cancers. Clinical limitations imparted to the toxicity of Cisplatin motivated the development of new anticancer agents by borrowing to Cisplatin the cisbisamminoplatinum(II)$^{2+}$ motive which is considered essential in preserving cytotoxic properties, originating from the Cisplatin-induced deformation and denaturation of tumor DNA.[294, 295] Oxaliplatin (Eloxatin™) and Carboplatin belong (Figure 1.22) to this class of clinically approved drugs that display a different spectrum of activity on various lineages of malign cells[295, 296] and also show a whole range of new side effects[297] that dictate cautious formulations.[298]

In a recent report, Dabrowiak et al.[299] raised the issue of the unusual shelf stability of concentrated infusions of Carboplatin and Oxaliplatin and proposed, basing their conclusions on NMR spectroscopic analyses, that these complexes exist as dimers in relatively concentrated solution, which would explain why their hydrolysis to bis aquo complexes,[300-302] a likely process in dilute neutral and basic aqueous preparations,[303] is apparently precluded in concentrated infusions. This proposal was supported by striking spectroscopic evidence of oligomer formation in the gas phase thanks to ESI mass spectroscopy.[299] Such behaviour in solution and in the gas phase was already known[304] for other Cisplatin-type structures but never investigated before Dabrowiak's paper.
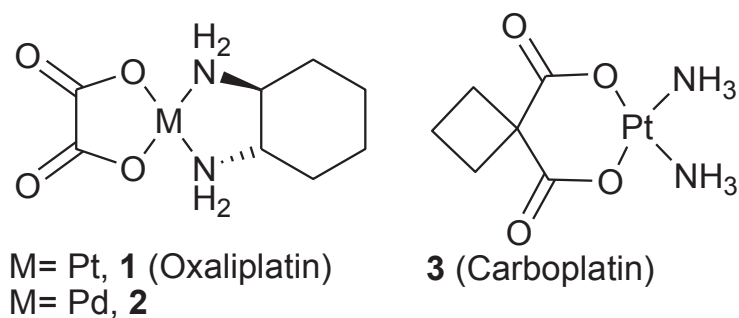
Figure 1.22. Cisplatin type complexes considered in Chapter 5.

Nonetheless, the question of the nature of the forces driving these complexes to form oligomers of sufficient persistence in solution or in the gas phase remained open. It is evident from a scrutiny of available crystallographic information that the solid state structuration of these Cisplatin type complexes is governed by the directing effect of intermolecular H-bonding, favouring various modes of intermolecular arrangements (stacks, strands).[305, 306] However, a simple observation of supramolecular networks does not tell much about the likely behaviour of these molecules in molecular assemblies of smaller scale in gas phase or solution wherein dispersion forces, i.e. the often overlooked London forces, combined to H-bonding may play a key role in ensuring the cohesion of a putative "non-covalent dimer" of different structure. This issue of the spontaneous aggregation of square planar d^{10} platinum complexes raises also the question of the real weight of correlation-based intermetallic d-d interactions[147, 307, 308] in the overall cohesion of the aggregates that was addressed recently.[292]

1.7.6. Inclusion of metal complexes to CB[n] hosts

As the research to find new and efficient anti-cancer drugs progress, so is the research on development and refinement of the methods to deliver these drugs to the target cells or tissue where they can exhibit their function. One of the methods used to achieve this goal is to utilize big supramolecular systems, in which the drug will be encapsulated inside the carrier molecule. These molecules help in controlled release of the drug, decrease the metabolism of the drug and control drug toxicity. Several classes of molecules have been considered as drug carrier candidates, e.g. cyclodextranes (**CD**), crown ethers, cucurbit[n]urils (**CB[n]**), with the goal of improving the bioavailability, solubility and stability of the drug molecules.[309-311]

These molecules will form inclusion complex with the drug. In the IUPAC Gold Book[312] the definition for the inclusion complex is:

"Inclusion compound (complex). A complex in which one component (the host) forms cavity or, in the case of a crystal, a crystal lattice containing spaces in the shape of long tunnels or channels in which molecular entities of a second chemical species (the guest) are located. There is no covalent bonding between guest and host, the attraction being generally due to van der Waals forces. If the spaces in the host lattice are enclosed on all sides so that the guest species is "trapped" as in a cage, such compounds are known as "clathrates" or "cage" compounds."

Cucurbit[6]uril (**CB**[6]) is a macrocyclic cavitand consisting of six glycoluril units which has a hydrophobic cavity that can be accessed by two identical openings. It has been widely used as a synthetic receptor[313-317] and as a building block for supramolecular assemblies. Syntheses[318, 319] of cucurbituril homologues, cucurbit[n]uril (**CB**[n], n = 5, 7, and 8) containing five, seven and eight glycoluril units, respectively, have sparked new research and widened the scope of cucurbituril chemistry.[320-322] Among them, **CB**[7] has a cavity large enough to form stable 1 : 1 inclusion complexes with for example ferrocene,[323] or carborane.[324] Unlike **CB**[6] or **CB**[8] which are sparingly soluble in water, **CB**[7] has a moderate solubility in water ($2-3 \cdot 10^{-2}$ M), which is comparable to that of β-**CD** ($1.6 \cdot 10^{-2}$ M).[322] The moderate solubility in water as well as cavity size of **CB**[7] prompted Kim et al.[325] to study its inclusion of drugs and explore its potential as a drug carrier. Inclusion of coordination complexes into the lipophilic cavity of cucurbit[*n*]urils (Figure 1.23) was already well documented by them and it was show that the thermochemistry of such non-covalent association process particularly suits the sensitivity of ITC.
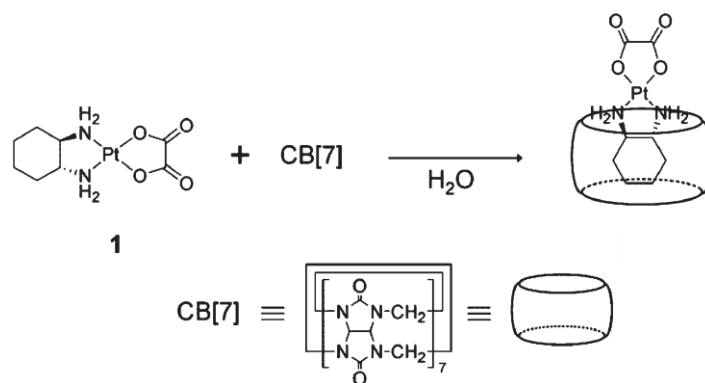
Figure 1.23. Formation of inclusion complex by mixing an equimolar amount of oxaliplatin **1** and **CB**[7] in water.[318]

A way to probe the pertinence of the theoretical models is to compare the computed thermochemical parameters with those obtained for a standard non-covalent association process obtained by ITC in solution. This approach is however limited by the treatment of solvation in conventional DFT methods.

1.7.7.   Cleavage of halogen bridges in cyclometallated complexes

For a long time it was considered that NCI between closed-shell metals in organometallic complexes play significant role only for heavy elements, mainly late transition metals.[326-330] These so-called metallophilic interactions result from a combination of short-range electron correlation, medium-range dispersion interaction, and relativistic effects of the metal centre.[331-335] However, this metal centred view is incomplete, particularly for bimetallic complexes of 3d and 4d transition metals where attractive dispersion interactions with surrounding ligands become more significant and often support deficient donor-acceptor bonding between the two metals.[336-338] It has been shown that larger organic ligands contribute to the ligand-metal association energy by means of a significant dispersion contribution in reactions involving ligand-metal bond formation (e.g. those encountered in catalytic processes).[307, 308, 339-343]

Cleavage of halogen bridges (X) in cyclometallated palladium(II) complexes by various donor ligands (L) is a classical reaction that has been widely used, e.g. in the synthesis of monomeric metallacycles from the corresponding dimers, for the structural characterization of cyclometallated species, and for the separation of enantiomers.[344-348] In addition, reactions of the type shown on Figure 1.24 are suggested as key pre-equilibria in synthetically important insertion reactions of alkenes,[349] alkynes[350] and other unsaturated molecules[351] into the Pd-C bonds of dimeric palladacycles.
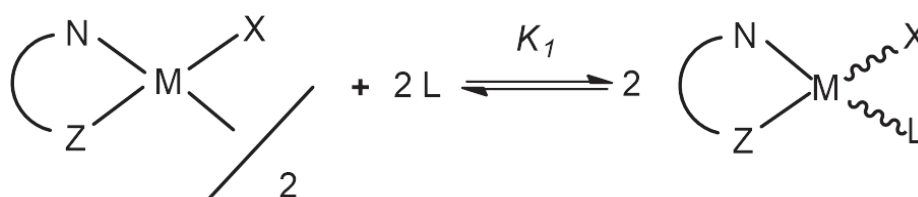
Figure 1.24. Cleavage of halogen bridges in cyclometallated Pd(II) complexes

The kinetic and mechanism of these reactions were studied by several groups.[352-355] It was shown that the bridge cleavage by nucleophilic ligands is a rather fast, bimolecular, associatively driven reaction in which bond making plays the dominant role. Resulting monomeric product usually have ligand molecule in the *trans-* position in respect to the nitrogen on pyridine, but that does not always have to be true.[356, 357]

1.8. **Introduction to the Chapters of the thesis**

Chapter 2 contains methodology used in the work on this thesis. Brief theoretical introduction, accompanied with the explanations for the procedures will be presented.

Chapter 3 covers the results of the theoretical study and analysis of the stacking interactions in the *sqp* metal complexes with 2,2'-bipyridine (*bipy*) ligands. In order to better understand stacking interactions of *bipy* complexes, we have analysed the geometries of stacking interactions and observed certain overlapping patterns between *bipy* square-planar metal complexes in crystal structures from the CSD. We have tried to explain these observations by performing DFT-D calculations on the model systems, constructed in such a way as to best represent the results obtained from CSD analysis. All results presented in this chapter were published recently. [A1]

In Chapter 4, results of the study on the role of the dispersion interaction in the *sqp* rhodium complexes with isonitrile ligands are presented. Several new chiral tetrakis(isonitrile)Rh(I) complexes have been synthesized and characterized. Oligomerization of these complexes in acetonitrile and chlorobenzene solutions was followed by the UV-Vis spectroscopy and ITC.

Chapter 5 contains results of the study on the subject of the unusual stability and long shelf life of the Oxaliplatin anti-cancer drug. We have relied heavily on the ITC technique in analysis of the behaviour of the Oxaliplatin, Carboplatin, and Oxalipalladium in solution, because other experimental techniques like ^{1}H NMR or DOSY failed to give conclusive evidence on the self-aggregation. We have then compared our experimental thermodynamic data with the results from theoretical calculations. All results presented in this chapter were published recently. [A2]

In Chapter 6 we have, using again ITC and theoretical methods, analysed host-guest chemistry and the role of non-covalent interaction of inclusion complexes with cucurbit[n]urils – **CB[n]**. All results presented in this chapter were published recently. [A2, A3]

In the Chapter 7 of this thesis, synthesis and characterization of several new complexes of palladium(II) and rhodium(II) is presented. We have used the ITC as a tool to acquire accurate experimental information on the thermochemistry of the cleavage of the halogen bridges in cyclometallated complexes by several ligands. Some of the results presented in this chapter were published recently. [A4]

Chapter 8 contains experimental details for the synthesis and characterization of the prepared complexes.

Chapter 2

2. Methodology

New knowledge in coordination chemistry and organometallic systems can only be acquired by using theoretical chemistry as a complement to experiment. This is possible only with the creation of a new "type of experimental chemists" who are both able to build their own objects and to study their intimate electronic structures and properties with modern theoretical methods.

This chapter will cover various theoretical and experimental methods that were used during the work on this thesis for gathering and analysis of the data with the goal of better understanding of the NCI in transition metal chemistry.

2.1. CSD search

The Cambridge Structural Database has been established in 1965, and represent world's repository for small-molecule organic and organometallic crystal structures. This database contains the results of over 600,000 neutron diffraction and X-ray analyses, with accurate 3D structures saved in Crystallographic Information File - CIF format.[358, 359] Entries in the database contain additional bibliographic, chemical and physical property information, enabling the interpretation of structures in chemically meaningful way. New entries and improvements to the existing ones are uploaded constantly, and checked meticulously by the expert chemists and crystallographers.

Information contained in the CSD is essential to structural chemistry research, both in its broadest sense, and specifically to the fields such as: materials design, drug discovery and drug development. More than 2,000 papers and reviews[360-362] have been published worldwide that describe research applications using the data accumulated in the CSD.

CSD analyses are also indispensable in our understanding and control of intermolecular interactions of all types, particularly weaker interactions such as C-H⋯X,[363] X-H⋯π[56, 220, 364] and dipole-dipole interactions.

CSD search (November 2012 release, version 5.34)[360] was performed using the *ConQuest1.15* program[365] to extract all structures containing square-planar *bipy* complexes. The queries for the crystal structures search were made according to the following criteria: a) the crystallographic R factor < 10%, b) the error-free coordinates according to the criteria used in the CSD, c) the H-atom positions were normalized using the CSD default X-H bond

lengths (O-H = 0.983 Å; C-H = 1.083 Å and N-H = 1.009 Å)[10], d) no polymer structures, e) structures with disorder were not included, f) structures solved from powder were not taken into account either.

This method was used to analyse the interactions between the square-planar complexes of transition metals that contain *bipy* ligands. Further details and results of the investigations are covered in Chapter 3.

2.2.   Theoretical calculations

2.2.1.   DFT calculations

In the Chapter 1, it was mentioned that there are several methods being developed today which are used to treat the dispersion correction term. Here, the approach of Grimme et al. will be explained briefly.

DFT-D family of functionals, designed by Grimme et al., are the most widely-used dispersion corrections today due to their relative simplicity, accuracy, and its widespread implementation in popular software packages. The DFT-D family consists of three generations: first generation DFT-D[145] (proposed in 2004), second generation DFT-D2[146] (2006), and the last development, DFT-D3[147] (2010), which is nowadays replacing DFT-D2 as the method of choice in most calculations.

The -DX functionals are all based on the pairwise dispersion energy correction with increased complexity and improved accuracy in later versions of the code. The most recent development in the DFT-D family is DFT-D3, which is based on pre-computed quantities using TDDFT.

The total DFT-D3 energy is given by:

$$\Delta E_{DFT-D3} = \Delta E_{KS-DFT} - \Delta E_{disp}$$

$$E_{disp} = E^{(2)} + E^{(3)}$$

$E^{(2)}$ stands for the two-body and $E^{(3)}$ three body term. The most important $E^{(2)}$ term is given by the following equation:

$$E^{(2)} = \sum_{AB} \sum_{n=6,8,10\ldots} s_n \frac{C_n^{AB}}{r_{AB}^n} f_{d,n}(r_{AB})$$

Here, the first sum is over all atom pairs in the system, C_n^{AB} denotes the averaged isotropic nth-order dispersion coefficient (orders n=6,8,10,...) for atom pair AB, and r_{AB} is their internuclear distance. Scaling factors s_n are adjusted only for n>6 to ensure asymptotic exactness which is fulfilled when the C_6^{AB} are exact. In this case, in difference to DFT-D2, there is no s_6 scaling parameter, and s_8 is an adjustable parameter. The C_{10} and other higher-order contributions are not used because the correction becomes unstable.

In order to avoid near singularities for small r_{AB} and mid-range double-counting effects of correlation at intermediate distances, damping functions $f_{d,n}$ are used which determine the range of the dispersion correction. The damping functions are the same as the Chai and Head-Gordon[366] have proposed:

$$f_n(r_{AB}) = \frac{1}{1 + 6\left(r_{AB}/\left(s_{r,n}R_0^{AB}\right)\right)^{-\alpha_n}}$$

In this equation for $n = 6$ and 8, the $s_{r,8}$ is set to 1 and the $s_{r,6}$ is treated as an adjustable parameter. The other parameters are set to $\alpha_6 = 14$, $\alpha_8 = 16$, choice made so that the dispersion energy contribution is less than 1% of the maximum total dispersion energy for interatomic interactions at covalent distances.

The dispersion coefficients are obtained by considering the hydrides of all the elements in the periodic table, and by calculating their frequency-dependent polarizabilities using TDDFT with PBE functional. The calculated frequency-dependent polarizabilities enter a Casimir-Polder-like equation[142] in the calculation of the atomic interaction coefficients:

$$C_6^{AB} = \frac{3}{\pi}\int_0^\infty \frac{1}{m}\left[\alpha^{A_m H_n}(i\omega) - \frac{n}{2}\alpha^{H_2}(i\omega)\right] \times \left[\alpha^{B_k H_l}(i\omega) - \frac{l}{2}\alpha^{H_2}(i\omega)\right]d\omega$$

where m, n, k, and l are the stoichiometric numbers of the corresponding hydrides. The formula involves the frequency-dependent polarizability of the hydrogen molecule.

Calculation of the higher-order coefficients makes use of recurrence formulas. In particular,

$$C_8^{AB} = 3C_6^{AB}\sqrt{Q^A Q^B}$$

$$Q^A = s_{42}\sqrt{Z^A}\frac{\langle r^4\rangle^A}{\langle r^2\rangle^A}$$

where $<r^2>$ *and* $<r^4>$ are moments of the electron density, s_{42} is chosen so that the C_8^{AA} for He, Ne, and Ar are reproduced and the $\sqrt{Z^A}$ is an term introduced to get consistent interaction energies for heavier elements.

Coefficients of order higher than C_8 can be calculated as well, using other recurrence relations but they are not used in the energy expression. The three-body interaction coefficient C_9, that enters the Axilrod-Teller-Muto term as derived from the third-order perturbation theory for three atoms ABC[367, 368] is calculated in DFT-D3 using another approximate formula:

$$C_9^{ABC} = -\sqrt{C_6^{AB}C_6^{AC}C_6^{BC}}$$

Finally used formula for the nonadditive energy contribution in three-body dispersion is:

$$E^{(3)} = \sum_{ABC} f_{d,(3)}(\bar{r}_{ABC})E^{ABC}$$

Even though not recommended in the first instance when the original paper was published,[147] it was later shown that the three-body dispersion contribution becomes very important. In his recent work[369] Grimme shows that three-body dispersion effects, which were unimportant in small benchmark systems, must be considered for accurate results in predicting supramolecular binding thermodynamics. Accounting for this contribution of the three-body dispersion term $\Delta E^{(3)}_{disp}$ improves computed supramolecular interaction energies considerably. The three-body dispersion term is always repulsive and roughly an order of magnitude smaller than the binding energies. However, the contributions in the considered supramolecular systems were mostly 1–3 kcal/mol, which is very significant in relation to the magnitude of the ΔG_a for which the target quantity is typically in the range − 8 to 0 kcal/mol. Neglecting those contributions would then lead to overbinding for the majority of the complexes they have considered by typically 1–3 kcal/mol (with a maximum value of 4.6 kcal/mol).[369] The cutoff radii R_0^{AB} used in the damping function are derived from the

distance for which the first-order E_1 DFT interaction energy between the atoms A and B equals a cutoff energy. The value of this cutoff energy is chosen so that the R_0 of the carbon-carbon interaction is the same as in DFT-D2.

2.2.1.1 Methods used in analysis of *bipy* complexes

In order to evaluate the energy of stacking interaction between two square-planar *bipy* complexes, the single-point calculations were done in Gaussian09 (version D.01)[370] program, using the Tao-Perdew-Staroverov-Scuseria (TPSS-D3)[147, 371] method and the def2-TZVP[372] basis set. The calculations were performed on model systems of (2,2'-bipyridyl)dicyanonickel(II) complexes, made from crystal structures. Since the molecules in which these interactions occur are rather large, and there are at the same time other intermolecular interactions, the calculations were performed on smaller model systems. These model systems were built from the crystal structures by substituting all metal ions by Ni(II) ion and by substituting all other ligands with CN ligands. The geometries of the stacked bipy ligands were kept the same as they were in the crystal structures. The geometry of the two remaining ligands (CN ligands) were taken from the optimized structure of (2,2'-bipyridyl)dicyanonickel(II) complex, obtained by using TPSS-D3/SDD[373]/def2-TZVP level of theory. The interaction energies between two bipy nickel(II) complexes were calculated at TPSS-D3/def2-TZVP level and the basis set superposition error (BSSE) was removed by counterpoise (CP) correction.[374] Dispersion corrected TPSS functional was chosen because it is one of the well-established method for transition metal chemistry, [92, 375, 376] it was shown that TPSS-D3/def2-TZVP level is in excellent agreement with CCSD(T)/CBS values.[91] Calculations at TPSS-D3/def2-TZVP level do not consume very long time which is appropriate for a large systems calculated in this work.

Further details and results of the investigations are covered in Chapter 3.

2.2.1.2 Methods used in analysis of Pt,Pd and Ru complexes

Calculations were performed by DFT methods using the "zero damped" dispersion-corrected Becke[377]-Lee-Yang-Parr[378] (BLYP- D3, D3-BJ[379, 380]), Perdew-Burke-Erzenhof[381, 382] (PBE-D3(BJ)) and TPSS-D3(BJ) functionals implemented in the ADF®: Amsterdam Density Functional package (ADF2012.01).[383, 384] Scalar relativistic effects were treated within the Zeroth Order Regular Approximation (ZORA),[385] with all-electron (AE)[386]

ZORA/TZP, ZORA/TZ2P and ZORA/QZ4P basis sets were used. Larger basis sets (TZ2P, QZ4P) were used for checking the final geometries against the optimal TZP basis set. Because the changes in the final geometries were minimal, larger basis sets were not used further. All calculations were done in gas phase, or treated with solvation model. Solvation by water, DMSO and chlorobenzene was accounted for using the COSMO procedure with Klamt's values of van der Waals radii for atoms.[152, 161, 387] To determine the Gibbs enthalpies of solvation that would yield the $\Delta\delta G_{solv}$ parameter used to approximate the values of the Gibbs enthalpy of formation of the inclusion complex in idealized water from monomers, COSMO-RS[388] continuum solvation model was used. Thermochemical parameters were computed from the statistical data, namely internal energy and entropy, generated by vibrational frequency calculations. The latter were computed analytically and by two point numerical differentiation for geometries optimized respectively in the gas phase and in modelled water, DMSO and chlorobenzene (COSMO). Geometry optimizations by energy gradient minimization were carried out in all cases with the C_1 and C_2 point group symmetries, where the differences in the energies obtained for the same system were negligible. Integration grid accuracy spanned 4.5-6, the energy gradient convergence criterion was set to 10^{-3} au, and tight SCF convergence criteria (10^{-7} au) were used. Inter-fragment Kohn-Sham orbital interaction analyses were performed with optimized geometries within the ADF package. Wiberg bond indices for ADF-optimized geometries (using all-electron TZP basis sets) were computed with the GENNBO 5.0[389] extension of ADF. The BSSE was calculated by the counterpoise method, by reperforming all the calculations using a mixed basis sets, and the error is then subtracted a posteriori from the uncorrected energy. The mixed basis sets are realized by introducing "ghost orbitals", basis set functions which have no electrons or protons. A standard "zero-damping" formula and rational damping to finite values for small interatomic distances according to Becke and Johnson (BJ-damping) have been used for construction of dispersion energy curves. Grimme's DFT-D3 scheme for the computation of the dispersion coefficients was used. ETS-NOCV[390], NCI[391, 392] as well as ELF analyses[393] were performed with optimized geometries using ADF2012 and ADF2013 subroutines. Representations of molecular structures and orbitals were drawn using ADFview.

Further details and results of the investigations are covered in Chapters 5, 6 and 7 of this thesis.

2.2.2. *Ab initio* calculations

The GAUSSIAN 09, revision B.01[370] program was used for calculations of interaction energies at the second order Møller–Plesset (MP2)[394] and coupled-cluster single double[395-398](triple)[399] (CCSD(T)) basis set limit level (CCSD(T)/CBS) with frozen core orbitals on metals.

The CCSD(T) at basis set limit (CCSD(T)/CBS) energies were estimated by applying the extrapolation scheme proposed by Mackie and DiLabio.[400] This scheme uses interaction energies obtained by both accounting and not accounting the BSSE, and calculates average values. The average values obtained by using MP2 method with aug-cc-pVTZ and aug-cc-pVQZ (with pseudopotential for metal atoms)[401, 402] basis sets are used to estimate of MP2/CBS energies.

CCSD(T)/CBS values for the model system shown on Figure 5.13 were evaluated by assuming that the difference in energies between MP2/CBS and MP2/aug-cc-pVDZ is similar to the difference in CCSD(T)/CBS and CCSD(T)/aug-cc-pVDZ:[403]

$$\Delta E_{(CCSD(T)/CBS)} = \Delta E_{(CCSD(T)aug\text{-}cc\text{-}pVDZ)} + \Delta E_{(MP2/CBS)} - \Delta E_{(MP2aug\text{-}cc\text{-}pVDZ)}$$

2.3. Isothermal Titration Calorimetry

As already shown in Chapter 1, ITC is a unique method that provides direct heat, or change in enthalpy of the reaction taking place in the calorimeter. In this section instrumentation, principle of ITC measurements, and treatment of the data will be explained.

2.3.1. Instrumentation

All measures were carried out with a TA Instruments Nano Isothermal Titration Calorimeter device (nanoITC) equipped with two stainless steel Hastelloy® alloy cells of 1 mL volume each. This calorimeter is designed to use a differential power compensation for maximum sensitivity and responsiveness. Semiconducting thermoelectric devices (TED) are used for temperature control and to detect temperature differences between the sample and reference cells. A proportional/integral/derivative (PID) control loop uses a control heater on the sample cell to maintain a zero temperature difference between the sample and reference cells. The power required to maintain this zero difference is used as the calorimeter signal and

is monitored as a function of time. If a reaction that produces heat occurs in the sample cell, the heat required to maintain the zero difference decreases by the amount of heat supplied by the reaction, resulting in a peak in the thermogram.

A calibration heater located on the outside of the sample cell is used to provide precisely controlled heat pulses for electrical calibrations, and to verify instrument performance.

The entire measuring unit is encased within an insulated air-tight canister which has been purged on a vacuum pump and filled with dry nitrogen at the factory. This prevents possible condensation and evaporation of moisture around the unit which would create excessive baseline noise.

The Nano ITC (Figure 2.1) consists of the measuring unit (calorimeter block and two nonremovable reaction vessels), the buret assembly, which includes the stirring system, and a cleaning accessory. With the exception of the power on/off switch located on the back of the calorimeter unit, all functions of the Nano ITC are controlled remotely by the computer through the USB connection.

Figure 2.1. TA instruments Isothermal Titration Calorimeter

All aqueous solutions were prepared by sonication of suspensions of the complexes in pure water and were subsequently thoroughly degassed under reduced pressure. All organic solvents were freshly distilled and degassed. Solutions of air sensitive substances were prepared directly in the glove box, under inert atmosphere.

2.3.2. Measuring Unit

The measuring unit (Figure 2.2) consists of the calorimeter block and two non-removable reaction vessels - sample and reference cells. Access tubes extend downward from inside the buret mounting cavity on the top of the calorimeter. The access tubes serve as conduits for the filling syringe, titrant delivery, and reference needle. They also provide for titrant equilibration and as a thermal barrier to the environment outside the calorimeter.
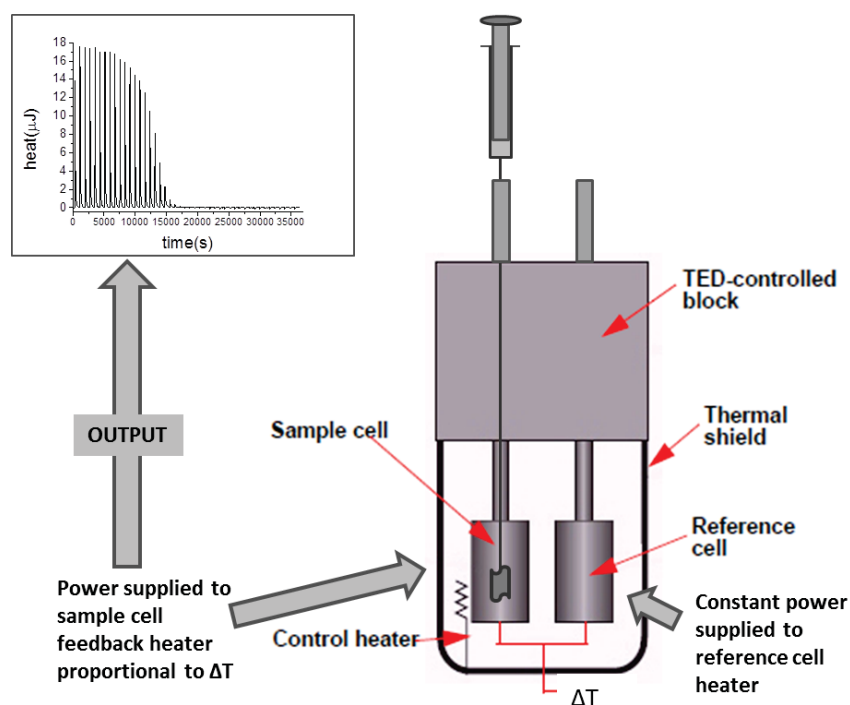
Figure 2.2. NANO ITC measuring unit

The calorimeter uses two matched reaction vessels of 1-mL Hastelloy®. The vessels are accessed through platinum tubes. The reference cell is constructed to match as closely as possible the thermal properties of the sample cell. Accordingly, a reference needle is placed inside the reference cell during operation to correspond to the titrant needle in the sample cell.

The titrant syringe needle also functions as the stirrer and extends down into the reaction vessel from the top when the buret is mounted. The needle is balanced for optimum stirring efficiency. It has two Teflon bushings to help dampen stirring noise and ensure that the needle spins true within the cell access tube.

The buret accurately delivers the titrant to the reaction vessel at specified volumes and intervals. The assembly also functions as the stirring mechanism for the reactants in the cell when the titrant syringe is installed.

2.3.3. Measurements and treatment of data

In incremental or continuous titration, one of the reactants is placed in a syringe or buret external to the reaction vessel.

The first step in running the ITC experiment is to determine the concentrations for the macromolecule and ligand solutions. The concentration of the titrant has to be sufficiently larger than that of the titrand in order to observe accurately measurable heat effect, and that is sufficiently larger than heat of dilution of solvent (usually ≥ 10 µJ).

The baseline data, i.e. heat flow in the regions before and after each titrant pulse, shows the power required to maintain a zero temperature difference between the sample and reference cells. The baseline in this region is a function of heating by stirring. The baseline is used to calculate the area or the heat from each pulse in the reaction vessel during the titration or batch reaction. The thermogram constructed from the integrated peak areas is then used for data analysis.

A single titration calorimetric experiment yields heat data as a function of the ratio of the concentrations of the reactants. Titration data, in the form of heat change versus volume of titrant added, can be examined for both analytical (thermometric titrimetry) and thermodynamic (titration calorimetry) information.

Other corrections must be made to the heat data to account for heat effects associated with titrant dilution and any temperature difference between titrant and titrate solutions. These corrections are most easily accomplished by performing a blank titration experiment and subtracting the blank heat data from the experimental thermogram.

A typical Nano ITC experiment involves the following:

- Preparing and degassing the solutions
- Preparing the sample and reference cells
- Mounting the buret
- Running the baseline
- Performing an analysis
- Cleaning the calorimeter

2.3.4. Analysis of thermodynamic data

In order to analyse the data obtained in ITC experiment, it is first necessary to know what kind of process is taking place in the reaction (dimer dissociation, one or multiple site binding, etc.). Proper understanding of the chemical process will result in relevant thermochemical parameters.

Thermogram that is recorded in the experiment gives raw heat that is collected during titration. Area below the peaks is than integrated and then the nonlinear regression procedure is used to fit the data to the appropriate model. The model is a mathematical representation of a chemical, physical or biological process that is taking place in the calorimeter and in which the dependent variable (e.g. heat or heat rate) is defined as a function of the independent variable (e.g. moles of titrant added) and one or more model parameters. Nonlinear regression is used along with the model equations to determine the best values of the fitting parameters (e.g. ΔH, K, and n).

The nonlinear regression analysis of ITC data is iterative process. The first step is to make an initial guess for each of the parameters in the model equation. Using these values, a fit or theoretical curve is generated and then compared to the actual data curve. An error function is calculated as the sum of the squared deviations between the model curve and the data. An accepted algorithm is then used to adjust the fit parameters to move the calculated curve closer to the data points. Process is then repeated until the error function insignificantly changes with subsequent iterations. If the fitting is not possible, another model has to be applied. Final, "best fit" parameters will depend in large measure of the starting assumptions, so it is important to have precise concentrations of used solutions.

Chapter 3

3. Stacking interactions between 2,2' - bipyridine ligands in square-planar metal complexes

In square-planar complexes with bipyridine ligand, where the chelate ring is fused with two pyridine rings, the complexes can be structurally organized in such a way as to allow easy approach of the chelates for mutual interactions. Wide application of these complexes as mentioned in Chapter 1 makes them interesting target for the study of the stacking NCI in solid state. To this extent, we have performed statistical study on square-planar metal complexes with bipyridines ligands by analysing the structures available in CSD.

3.1. CSD search

In order to find intermolecular stacking interactions between bipyridines, we conducted three searches. In the first search, we looked for the structures with the distance between centroids of any pyridine fragment (d_{PP} distance, Figure 3.1) below 4.6 Å,[90] in the second the criterion was that the distance between centres of pyridine and chelate rings (d_{PC} distance, Figure 3.1) is shorter than 4.4 Å, and in the third the criterion was that distance between centres of the chelates (d_{CC} distance, Figure 3.1) is below 4.2 Å. Results from all three searches were combined and analysed together in order to insure that all possible stacking interactions are included. We considered that two rings form stacking interaction when the dihedral angle between the mean planes of bipyridines is less than 10°.

The data related to the intermolecular stacking interaction were analysed by the use of the structural parameters presented in Figure 3.1. Coordinated *bipy* ligand has three fused rings: two pyridine fragments and one chelate ring. Distances d_{PP} and d_{CC} are the shortest intermolecular distances between centroids of two pyridine fragments (Ω_{P1} and Ω_{P2}) and two chelate rings (Ω_{C1} and Ω_{C2}), respectively. The shortest distance from the pyridine ring centre (Ω_{P1}) of the first *bipy* ligand to the centre of chelate ring of the second one (Ω_{C2}) is referred to as d_{PC}. The distance between the metal ion of the first complex (M_1) and the projection of the metal ion of the second complex (M'_2) onto the average plane of the first one represents the horizontal r_{MM} displacement. The normal distance between the planes of the interacting rings is R. The angle between the M_1-M'_2 and M_1-Ω_{C1} directions in the plane of the first complex is denoted φ, where the centre of chelate ring is shown as Ω_{C1}. Torsion angle T_1 is the Ω_{C1}-M_1-

M_2-Ω_{C2} angle, while T_2 is Ωp_1-$\Omega' p_1$-$\Omega' p_2$-Ωp_2 angle. Ωp_1 and Ωp_2 are the centres of pyridine rings in two complexes with shortest d_{PP} distance.
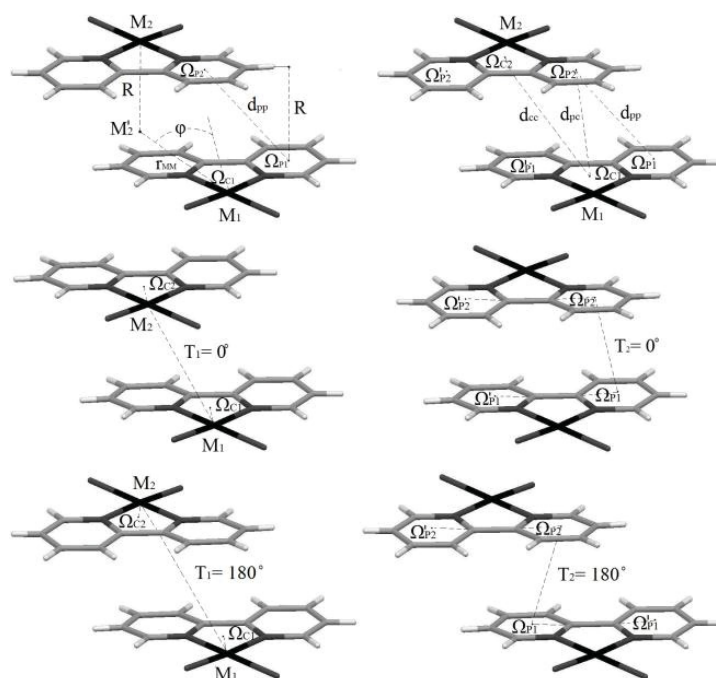
Figure 3.1. Geometrical parameters used for describing the stacking interactions between *bipy* ligands. Figure shows orientations with $T_1 = 0.0°$ and $180°$ and $T_2 = 0.0°$ and $180°$.

To illustrate the geometry of stacking interactions and the effect of the supramolecular structure on stacking interactions of two *bipy* ligands, a few examples of crystal structures were given in the following paragraphs. For this purpose, the structures with typical geometric parameters for a certain type of overlap (parameters r_{MM} and φ) and structures with simple metal complexes were selected.

By searching the crystal structures of square-planar *bipy* metal complexes in the CSD, 325 interactions were found in which two complexes with mutual parallel orientation are in close contact, with the distance between the centres of the two pyridine rings shorter than 4.6 Å, or the distance between centres of pyridine and chelate rings shorter than 4.4 Å, or distance between centres of two chelate rings shorter than 4.2 Å. Mutual orientations of interacting complexes are described by geometrical parameters shown in Figure 3.1.

In most of the structures the normal distances between the planes of interacting square-planar *bipy* complexes are in the range from 3.2 to 3.7 Å. The maximum of the distribution is at 3.3-3.5 Å (Figure 3.2). Similar normal distances were found for *terpy* and *phen* complexes.[62, 63]
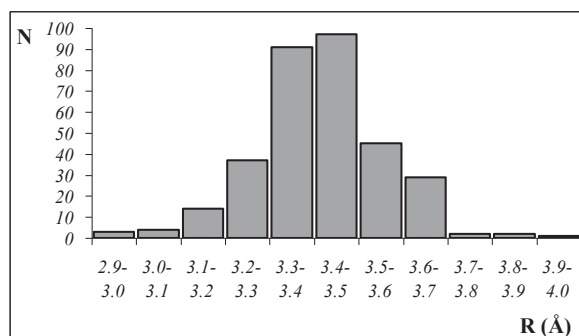
Figure 3.2. The histogram shows the distributions of the normal distances (R) for stacking interactions of square-planar *bipy* complexes.

To define the orientation of metal complexes two torsion angles (T_1 and T_2) have been analysed. Geometries with T_1 angle value from 0° to 10° correspond to head-to-head orientation, while geometries with T_1 angle value from 170° to 180° correspond to head-to-tail orientation. In geometries with T_2 angle from 0° to 10°, both pyridine rings of *bipy* ligand participate in the stacking interaction, while in geometries with T_2 angle from 170° to 180°only one pyridine ring participates in the interaction (Figure 3.1).

The distribution of T_1 torsion angle values shows preferred orientation with the angle from 170° to 180° (*head-to-tail* orientation) (Figure 3.3). Only 18 interactions have *head-to-head* orientation (T_1values of 0° to 10°). The number of interactions with T_1 between 10° and 170° is quite small. In studies on stacking interactions of square-planar *terpy* and *phen* complexes[62, 63] preference for *head-to-tail* orientations was also found.

The distribution of T_2 torsion angle also shows two preferred orientations; the first orientation with T_2 values of 0° to 10° and the second one with 170° to 180° (Figure 3.3). Small number of the interactions has T_2 value between 10° and 170°. The values of T_2 torsion angle of 0° to 10° correspond to the interactions with overlap of large part of *bipy* ligands, while the values of 170° to 180° correspond to only partial overlap of *bipy* ligands (Figure 3.1). The interactions with the values of T_2 in the range from 0° to 10° occur more frequently. We obtained similar results for *terpy* complexes,[62] while for *phen* complexes[63] there is less pronounced tendency for orientation with T_2 values of 170° to 180°. The reason for such behaviour of *phen* complexes might be the existence of additional aromatic ring in *phen* ligand.
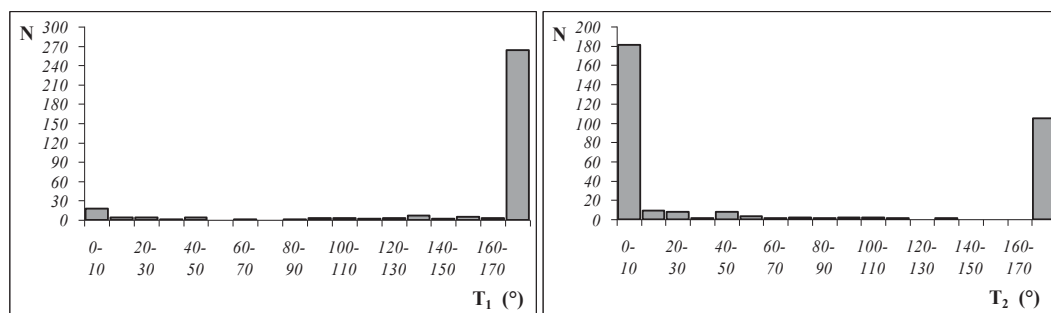
Figure 3.3. Histograms showing the distributions of torsion angles T_1 and T_2, for interactions of square-planar *bipy* complexes.

Because of the small number of structures with *head-to-head* orientation (T_1 values of 0° to 10°) (Figure 3.3), we analysed only the structures with *head-to-tail* orientation (T_1 values of 170° to 180°). Structures with *head-to-tail* orientation form two groups of contacts; in the first group of contacts (I) T_2 torsion angle is close to 0°, while in the second group (II) torsion angle T_2 is close to 180°.

The first group of structures (I) includes 170 interactions. Histograms presenting the distribution of horizontal displacements r_{MM} and normal distances R are shown in Figure 3.4. The histogram shows that most of the displacements r_{MM} are distributed in the range of 3.0 to 7.0 Å, with the maximum between 4.0 and 6.0 Å. In most of these structures, the normal distances R between the planes of interacting *bipy* ligands are in the range of 3.3 to 3.7 Å, with maximum at 3.3-3.5 Å (Figure 3.4).

In this first group of structures (I), with T_2 torsion angle close to 0°, large area of the *bipy* ligand can be involved in overlap (Figure 3.1). For the description of these interactions two geometrical parameters were used: horizontal displacement r_{MM} and angle φ (Figure 3.1). In recent studies it was shown that using these two parameters enables the description of stacking interactions of *terpy* and *phen* complexes.[62, 63] The plot of angle φ versus the *offset* r_{MM} for group I of *bipy* complexes is shown in Figure 3.5. In group I values of angle φ are less that 40°.
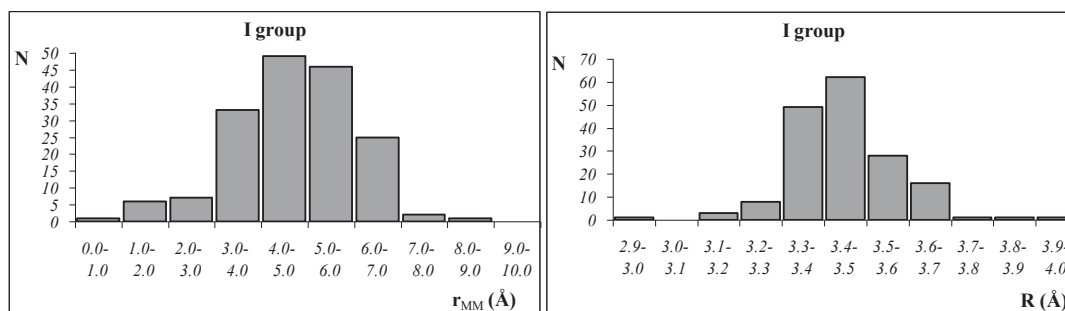
Figure 3.4. The distributions of r_{MM} parameter and normal distance R (Å) for the interactions in group I.

The scattergram in Figure 3.5 for group I does not show clustering. However, the interactions in this group can be quite versatile, as indicated by the wide range of observed r_{MM} values. Different types of overlap in group I are defined based on rings (chelate and pyridine) of *bipy* ligand involved in overlap. At different values of r_{MM} different rings overlap. In geometries with r_{MM} values lower than 3.0 Å (overlap type I_a), only chelate rings of *bipy* ligands overlap (Figure 3.6). At larger r_{MM} values, between 3.0 and 5.0 Å, chelate-chelate, chelate-pyridine and pyridine-pyridine overlaps occur (overlap type I_b, Figure 3.7). At r_{MM} values between 5.0 and 6.0 Å, pyridine-chelate and pyridine-pyridine overlaps occur (overlap type I_c, Figure 3.8), while in geometries with r_{MM} values larger than 6.0 Å (overlap type I_d), only pyridine-pyridine overlap occurs (Figure 3.9). Data in Table 3.1 show geometrical parameters for all overlap types.

The data in Figure 3.5 seems to be scattered along a trendline with negative slope. Such trend is the consequence of the geometric constrains for group I. Namely, all interactions in group I have T_2 torsion angle close to 0°, and it causes that with increasing r_{MM}, angle φ decreases. The structures with large r_{MM} and large angle φ, belong to group II, since they have T_2 torsion angle close to 180° (Table 3.1).
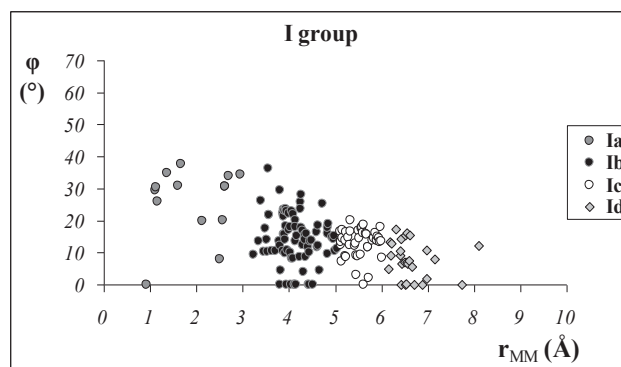
Figure 3.5. The plot of angle φ versus *offset* r_{MM}, for the interactions in group I.

The structures with overlap type I_a include 14 interactions (Table 3.1). *Bipy* ligands are oriented in such way that overlap occurs only between chelate rings. In most of the structures other ligands coordinated to a metal are planar. In these structures pyridine rings of *bipy* overlap with other ligands from the other interacting complex. Structure AREHOU[404] (Figure 3.6), which represents thiocyanato-(isothiocyanato)-(2,2'-bipyridine)-platinum(II), is an illustration of this overlap. For this overlap geometry we calculated interaction energy for model system with two (2,2'-bipyridyl)dicyanonickel(II) complexes (Figure 3.6) based on this structure, AREHOU, by substituting thiocyanato and isothiocyanato ligands with cyano

ligands, and by substituting metal ion with nikel(II). The calculated energy of stacking interaction in this model system is -31.7 kcal/mol (Table 3.1).
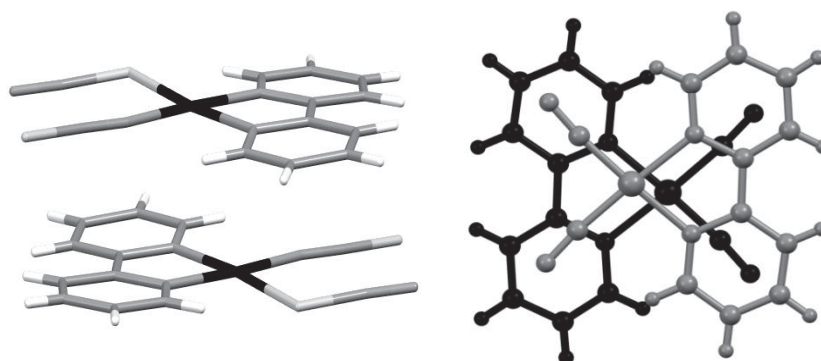
Figure 3.6. The perspective view of crystal fragment of AREHOU[404] (thiocyanato-(isothiocyanato)-(2,2'-bipyridine)-platinum(II)), as a selected example for structures of type I_a and view on model system of (2,2'-bipyridyl)dicyanonickel(II) complexes, based on this crystal structure.

The group of structures with overlap type I_b, with r_{MM} *offset* values between 3.0 and 5.0 Å and the value of angle φ lower than 40°, is the most numerous and includes 82 interactions (Table 3.1). *Bipy* ligands overlap in such way that there are chelate-chelate, pyridine-chelate and pyridine-pyridine overlaps (Figure 3.7). The metal ions do not overlap with *bipy* ligand from the other complex. Visual inspection of the structures shows that in most of them ligands at third and fourth coordination position are planar or not voluminous, and *bipy* ligands interact with ion (or molecule) from external coordination sphere of the complex, which is located above other ligands, in the vicinity of the metal ion. Structure GETMIC[405] (Figure 3.7), which represents bis(acetamidato-N)-(2,2'-bipyridyl-N,N')-platinum(II) hydrate, is an illustration of this overlap. In this structure, *bipy* ligands, besides the stacking, form simultaneous C-H/O intermolecular interactions with surrounding water molecules ($H_1 \cdots O_X = 2.95$ Å, $H_2 \cdots O_Y = 3.10$ Å and $H_3 \cdots O_Y = 2.52$ Å). The water molecules are located above other ligands and form additional hydrogen bonds as H acceptors ($H_4 \cdots O_X = 2.46$ Å and $H_5 \cdots O_Y = 2.44$ Å).

For this overlap geometry we also calculated energy of the interaction for model system (2,2'-bipyridyl)dicyanonickel(II) complexes (Figure 3.7). Calculated energy of stacking interaction between two (2,2'-bipyridyl)dicyanonickel(II) complexes is -26.11 kcal/mol (Table 3.1). The calculated energy shows that interaction with this overlap (Figure 3.7) is weaker than with overlap presented in Figure 3.6. This can be anticipated based on the overlap area; overlap area in I_a (Figure 3.6) is larger than in I_b (Figure 3.7).
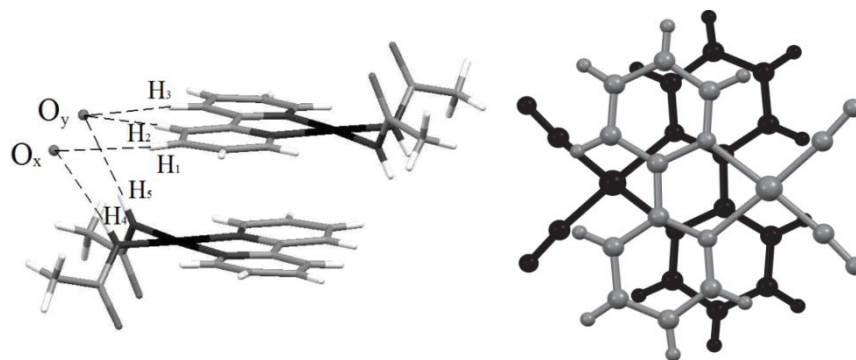
Figure 3.7. The perspective view of crystal fragment of GETMIC[405] (bis(acetamidato-N)-(2,2'-bipyridyl-N,N')-platinum(II) hydrate), as a selected example for structures of type I_b, and view on model system of (2,2'-bipyridyl)dicyanonickel(II) complexes, based on this crystal structure.

In type I_c, r_{MM} *offset* values are larger than in type I_b (above 5.0 Å and below 6.0 Å), and values of angle φ are below 20° (Figure 3.5). The group I_c is smaller group than I_b; it includes 46 interactions (Table 3.1). In these structures pyridine-pyridine and chelate-pyridine overlaps can occur, while chelate-chelate overlap does not occur (Figure 3.8). The other two ligands are not planar and stacking interaction is very often additionally stabilized by the interaction of C-H group of *bipy* ligand in the first complex with other ligand of the second complex. In crystal structure GETMIC, stacking interactions form chains, where I_b and I_c types of overlap alternately appear in the chains. I_c type of overlap (Figure 3.8) coexists with interaction of *bipy* ligand with the other ligands ($H_1 \cdots O_X$=2.81 Å, $H_2 \cdots O_Y$=3.20 Å and $H_3 \cdots O_Y$=2.60 Å). The calculated energy of stacking interaction between two model systems of bipy complexes (Figure 3.8) is -16.5 kcal/mol (Table 3.1).
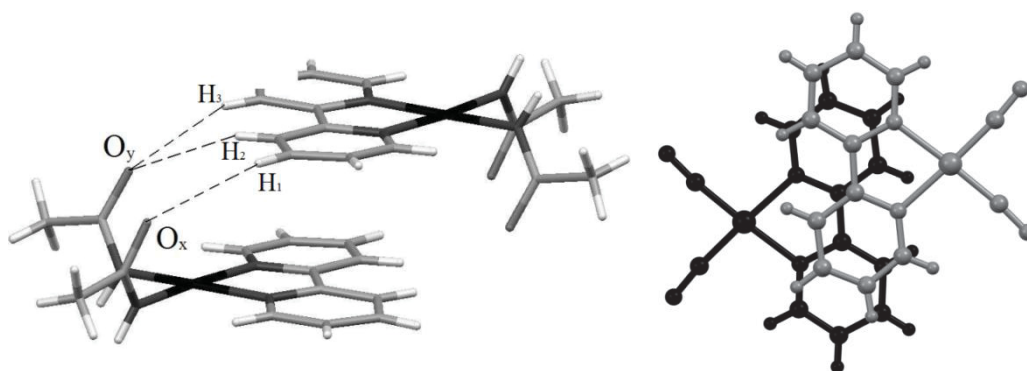
Figure 3.8. The perspective view of crystal fragment of GETMIC (bis(acetamidato-N)-(2,2'-bipyridyl-N,N')-platinum(II) hydrate) as a selected example for the structures of type I_c and view on model system of (2,2'-bipyridyl)dicyanonickel(II) complexes, based on this crystal structure.

The group of structures with overlap type I_d includes 28 interactions. In this group of structures, with r_{MM} *offset* values larger than 6.0 Å, the value of angle φ is less than 20° (Table

3.1) and only pyridine rings are involved in overlap (Figure 3.9). In this overlap type *bipy* ligand interacts with the ion or molecule which is located above metal ion. An example of this overlap is structure of (2,2'-bipyridyl)-bis(2-hydroxy-3-(3-methyl-2-butenyl)-1,4-naphthoquinone)-copper(II)(structure NEZPIR[406]), shown in Figure 3.9. In this structure *bipy* ligand interacts with oxygen atom of 2-hydroxy-3-(3-methyl-2-butenyl)-1,4-naphthoquinone ligand ($H_1\cdots O=2.48$ Å and $H_2\cdots O=2.61$ Å), pseudo-coordinated to Cu^{2+} ion ($Cu^{2+}\cdots O=2.40$ Å). The calculated energy of stacking interaction for model system (Figure 3.9) is -12.6 kcal/mol (Table 3.1).
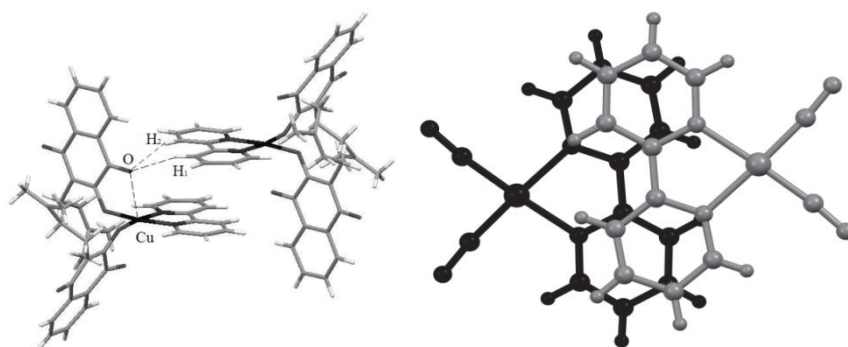
Figure 3.9. The perspective view of crystal fragment of NEZPIR[406] ((2,2'-bipyridyl)-bis(2-hydroxy-3-(3-methyl-2-butenyl)-1,4-naphthoquinone)-copper(II)), as a selected example for the structures of type I_d, and view on model system of (2,2'-bipyridyl)dicyanonickel(II) complexes, based on this crystal structure.

The second group of structures (II) with torsion angle T_1 close to 0°, and T_2 close to 180° is smaller than group I, and it includes 94 interactions (Table 3.1). In group II, *bipy* ligands only partially overlap and this partial overlapping always includes at least one pyridine-pyridine overlap. The histograms showing the distribution of the r_{MM} and R values for structures in group II are presented in Figure 3.10.
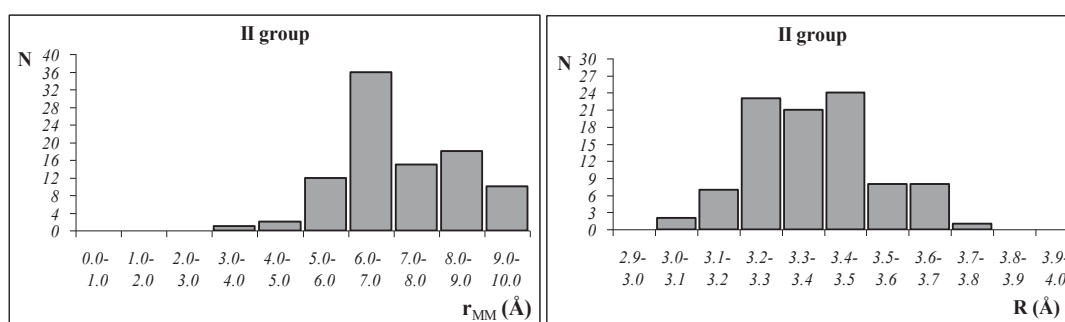
Figure 3.10. The distributions of r_{MM} parameter and normal distance R (Å) for the interactions in group II.

For the substantial number of interactions the r_{MM} is in the range of 5.0 to 10.0 Å and the distribution of the *offset* values shows maximum between 6.0 and 7.0 Å (Figure 3.10). The

r_{MM} values are higher than in group I (Figure 3.5) as a consequence of smaller overlap area. The normal distances (R) in group II have lower values (Figure 3.10) than in group I (Figure 3.4). This could be the result of higher repulsion between *bipy* ligands, caused by larger overlapping surface in the interactions of the group I. The plot of angle φ versus the *offset* r_{MM} for group II is shown in Figure 3.11. The overlap manner in this group is not a unique one, as indicated by the wide range of r_{MM} and φ values. In some structures, chelates-pyridines overlaps also exist, however, in group II there are no chelate-chelate overlaps. The pyridine-chelate overlaps occur in contacts with r_{MM} values lower than 7.0 Å and the values of angle φ lower than 20° (II_a) (Table 3.1), while in the other contacts of group II (II_b) there are only pyridine-pyridine overlaps.
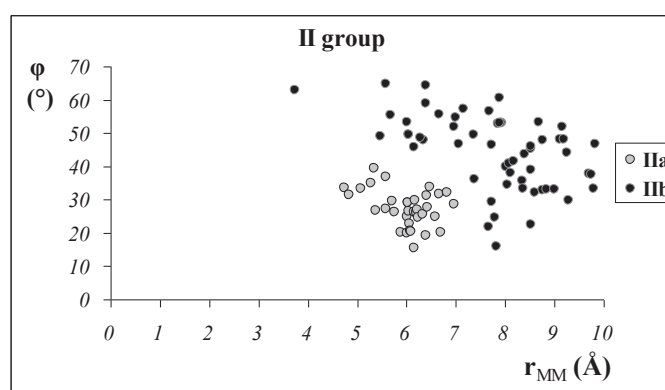
Figure 3.11. The plot of angle φ versus *offset* r_{MM}, for interactions in group II.

In the structures of group II at least one of the other ligands besides *bipy* is usually voluminous and stacking interaction between two complexes can be additionally favoured by the interaction of *bipy* ligand of one complex with the other ligand in second complex. This manner of overlap is very often a consequence of steric overlaid by other species, which interacts with π- system of *bipy* ligand.

The type II_a overlap was found in 36 interactions. These are interactions where one of pyridine rings of the first ligand overlaps with pyridine and chelate ring of the second complex, simultaneously. Chelate-chelate overlap does not occur and metal ion is not involved in overlap with *bipy* ligand. An example of such overlap is the crystal structure LASXUY,[407] representing (2,2'-bipyridyl)-(1,1,1,3,3,3-hexafluoro-2-propanolato)-phenolato-palladium(II) phenol solvate (Figure 3.12).
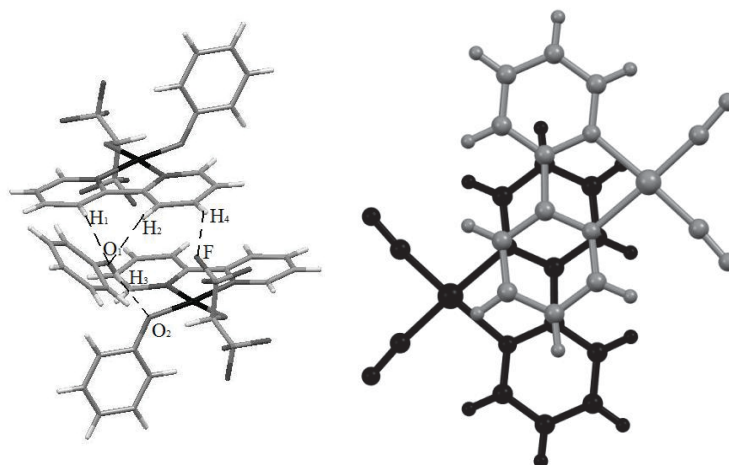
Figure 3.12. The perspective view of crystal fragment of LASXUY[407] ((2,2'-bipyridyl)-(1,1,1,3,3,3-hexafluoro-2-propanolato)-phenolato-palladium(II) phenol solvate), as a selected example for the structures of type II_a, and view on model system of (2,2'-bipyridyl)dicyanonickel(II) complexes, based on this crystal structure.

In this structure *bipy* ligand interacts with oxygen atom of phenol molecule ($H_1\cdots O_1 = 2.45$ Å and $H_2\cdots O_1 = 2.55$ Å), which is located above one of the other ligand ($H_3\cdots O_2 = 1.74$ Å) and with flouro atom ($H_4\cdots F = 2.58$ Å) from voluminous second ligand. The calculated energy of stacking interaction between two (2,2'-bipyridyl)dicyanonickel(II) complexes in model systems based on LASXUY structure (Figure 3.12) is -16.1 kcal/mol (Table 3.1).

In the structures that belong to II_b overlap type, only one pyridine fragment is involved in overlap and ion or molecule from the external sphere of the complex packs above *bipy* ring. This type was noticed in 58 interactions. An example of II_b overlap is the crystal structure IROLOQ[408] (bis(2-aminopyridine)-(2,2'-bipyridine)-platinum(II) tetracyanoplatinate(II) dihydrate) (Figure 3.13).
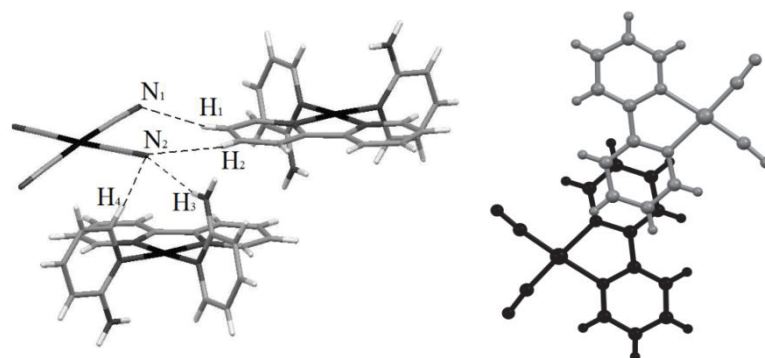
Figure 3.13. The perspective view of crystal fragment of IROLOQ[408] (bis(2-aminopyridine)-(2,2'-bipyridine)-platinum(II) tetracyanoplatinate(II) dehydrate), as a selected example for the structures of type II_b, and view on model system of (2,2'-bipyridyl)dicyanonickel(II) complexes, based on this crystal structure.

In this structure *bipy* ligand interacts with tetracyanoplatinate(II), forming two C-N/H interactions ($H_1 \cdots N_1$=2.64 Å and $H_2 \cdots N_2$=2.84 Å). This Pt complex is located above second *bipy* ligand and simultaneously interacts with other ligands of second *bipy* complex ($H_3 \cdots N_2$=2.36 Å and $H_4 \cdots N_2$=2.53 Å). The calculated energy of stacking interaction in model systems based on IROLOQ structure (Figure 3.13) is -7.3 kcal/mol (Table 3.1). The interaction energy indicates that the interaction in II_b type is the weakest of all overlap types, as can be anticipated based on small overlap area.

The results obtained by calculations show that the most stable model systems have the largest overlap surface, with ligands at third and fourth positions included in the overlap (I_a overlap type). Although the calculated interaction of I_a type is the strongest, I_a type overlaps are not the most numerous in the crystal structures. Namely, model systems used for the calculations have small ligands at third and fourth positions (CN groups), while in most of the crystal structures other ligands coordinated to the metal are voluminous, hence, the overlap type I_a is not possible. This is the reason why the structures with overlap type I_b, I_c, and I_d, in which the ligands at third and fourth coordination position are not included in interaction, are more numerous than those with overlap type I_a (14 interactions) (Table 3.1). The number of structures with overlap type I_b (82 interactions), I_c (46 interactions), and I_d (28 interactions) can be correlated with the results of calculations (Table 3.1), which show that the reduction in the overlap area leads to decrease of the interaction energy.

Weakest interaction, with energy of -7.3 kcal/mol, is calculated in model system of overlap type II_b where only one pair of pyridyl rings overlap. The interaction in model system of overlap type II_a is remarkably stronger, with energy of -16.1 kcal/mol; however, the data from the CSD showed that the contacts with overlap type II_b (58 interactions) are more numerous than the contacts with overlap type II_a (36 interactions). The large number of structures with weaker interaction can be the consequence of additional interactions in supramolecular structures in crystals. Namely, in type II_b, large area of the *bipy* ligand is available for additional contacts; in structure IROLOQ[408] (Figure 3.13) *bipy* ligand forms interaction with *bipy* ligand from the other complex and simultaneously forms interaction with tetracyanoplatinate(II) complex. The loss of energy in structures with overlap type II_b is compensated by the additional stabilization in supramolecular structure due to simultaneous interactions.

Table 3.1. Number of stacking interactions, geometric data[a], and energies of interactions.

Group of structures	N[b]	T_1 (°)	T_2 (°)	Overlap type	N[b]	Limiting parameters	Refcode[c]	ΔE^d (kcal/mol)
I	170	0-10	0-10	I_a	14	$r_{MM} < 3$ Å, $\varphi < 40°$	AREHOU	-31.7
				I_b	82	3 Å $< r_{MM} < 5$ Å, $\varphi < 40°$	GETMIC	-26.1
				I_c	46	5 Å $< r_{MM} < 6$ Å, $\varphi < 30°$	GETMIC	-16.5
				I_d	28	6 Å $< r_{MM} < 8$ Å, $\varphi < 30°$	NEZPIR	-12.6
II	94	0-10	170-180	II_a	36	$r_{MM} < 7$ Å, $\varphi < 40°$	LASXUY	-16.1
				II_b	58	($r_{MM} < 7$ Å, $\varphi > 40°$) + ($r_{MM} > 7$ Å)	IROLOQ	-7.3

[a]Geometric parameters are given in Figure 3.1.
[b]Number of stacking interactions.
[c]*Refcodes* of crystal structures selected as examples of overlap types).
[d]Interaction energies at TPSS-D3/def2-TZVP level were calculated for model systems based on crystal structures selected as examples of overlap types.

Comparison of the interaction energy for overlap type I_d (-12.6 kcal/mol), in which there are two pairs of pyridine-pyridine overlap, with the energy of interaction for overlap type II_a (-6.1 kcal/mol), in which there are two pairs of chelate-pyridine overlap, indicates that chelate-aryl stacking interactions are stronger than aryl-aryl stacking interactions. It is in accordance with findings that chelate-benzene stacking interactions are stronger than benzene-benzene stacking interactions.[91, 92] It is also interesting to compare interaction energy for overlap type II_b (-7.3 kcal/mol), in which only one pair of pyridyl rings overlap, with energy of stacking interactions between pyridine molecules (-4.1 kcal/mol).[50] This indicates that stacking interactions become more favourable when pyridyl rings are coordinated to a metal, which is in accordance with Hunter-Sanders rules.[21]

3.2. Packing in crystal structures

Analysis of packing in crystal structures showed that stacking interactions form stacking chains and dimers. Stacking chains are formed only by overlap of *bipy* ligands. We analysed packing in all structures with all values of torsion angles T_1 and T_2, not only structures belonging to group I and II. In 64% of total interactions, stacked *bipy* ligands form chains, while in 31% of interactions stacked *bipy* ligands form dimers. In some chains the same overlap is permanently repeated (15%), while in most of the structures two types of overlap alternately appear in the chains (49%). Stacking chains with the repeating of the same overlap appear in structures where there is no ion or molecule from the external sphere. Most of the contacts have no voluminous or planar other ligands. If the other ligands are voluminous, their configuration is the same on both sides of the mean plane of *bipy* ring.

An example of the chains with the same overlap is the structure PNIHEP[409] ((2,2'-bipyridyl)-5-nickel-3,3,7,7-tetramethyl-trans-tricyclo(4.1.0.02,4) heptane). In this structure (Figure 3.14), the other ligand is voluminous chelate ring ((2,2'-bipyridyl)-5-nickela-3,3,7,7-tetramethyl-*trans*-tricyclo[4.1.0.0^{2,4}]heptane).

Figure 3.14. The perspective view of crystal fragment of PNIHEP[409] ((2,2'-bipyridyl)-5-nickela-3,3,7,7-tetramethyl-trans-tricyclo (4.1.0.02,4)heptane), as an example of stacking chains with repeating the same overlap; in this case the other ligand is voluminous.

Stacking dimers were found in 31% of interactions. The reasons for forming dimers instead of chains in crystal packing can be voluminosity of the other ligand, but also the possibility of either other ligand or molecule (ion) from the external sphere of the complex to interact with π-system of *bipy* ligand. Example of dimer is crystal structure IVUFAG,[410] shown in Figure 3.15.
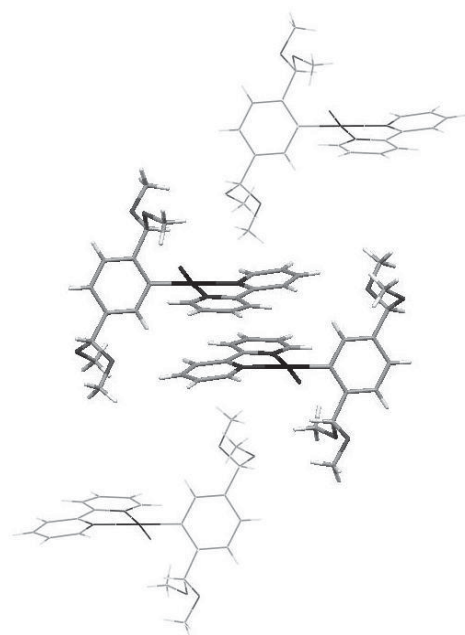
Figure 3.15. The perspective view of crystal fragment of IVUFAG[410] (chloro-(2,2'-bipyridine)-(2,5-bis(dimethoxymethyl)phenyl)-palladium(II)), as an example of stacking dimer.

In this structure both methyl groups of 2,5-*bis*(dimethoxymethyl)phenyl ligand interact with π-system of *bipy* ligand as hydrogen atom donors. However, in 12% of total interactions the other ligand contains aromatic ring, which forms π-π stacking interaction with *bipy* ligand. In this way stacking chains are formed and stacking interactions of two different sorts of molecules alternately appear in the chains. An example of such packing is crystal structure EVEWEH,[411] shown in Figure 3.16. In this case, aryl group of 1,2-benzenediselenolato ligand form π-π stacking interaction with *bipy* ligand of neighbouring complex.
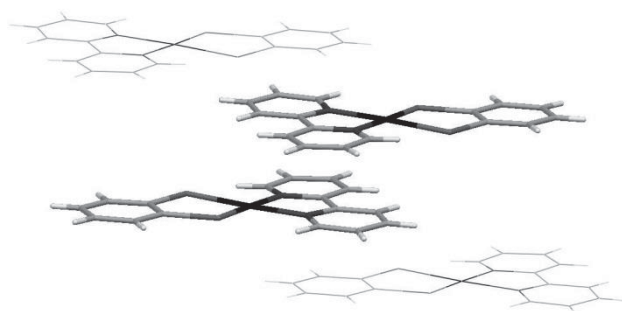
Figure 3.16. The perspective view of crystal fragment of EVEWEH[411] ((2,2'-bipyridine-N,N')-(1,2-benzenediselenolato-Se,Se')-platinum dichloromethane solvate), as an example of stacking dimer.

Recently[62, 63] it was shown that for the *terpy* and *phen* complexes stacking chains with alternating overlaps are the predominant type of packing; the chains occur approximately

three times more often than dimers. Data in this work indicate that *bipy* complexes also show preference for stacking chains. In *bipy* complexes, the chains are nearly two times more frequent than dimers. Since *terpy* and *phen* ligands coordinated to metal ions form planar systems of five and four rings, respectively, the explanation for larger number of chains in case of *terpy* and *phen* complexes can be connected with number of rings that has propensity to form stacking interactions. It is obvious that decrease of number of rings leads to reduction of stacking chains fraction in crystal structures. The probable reasons for this may be that interactions of ligands with environment are stronger than stacking interactions.

3.3. Relationship of calculated interaction energy and overlap surface

Analysis of the data obtained from CSD showed several types of overlap patterns between *bipy* complexes. In previous sections we presented the data on the interaction energies of all overlap types. In order to find relationship between interaction energy and overlap surface of *bipy* complexes, the calculations on several geometries of stacked [Ni(CN)$_2$(*bipy*)] dimers were performed. In all model systems, Ni complexes have *head-to-tail* orientations, which is the most common orientation in crystal structures. Several geometries with different overlap surface are shown in Figure 3.17. By increasing r_{MM}, from geometry **a** to geometry **c**, the overlap surface decreases. In geometry **d** we changed both distance r_{MM} and angle φ, in the way that the distance between centres of interacting pyridine rings is the same as in geometry **c**, offset for two rings is 1.5 Å. The values of optimal normal distance R for geometries in Figure 3.17 were obtained by single-point energy calculations by changing the normal distance R, while the geometries of the monomers were kept rigid. The calculated interaction energies and geometric data are presented in Figure 3.17.

The interaction energy decreases with decreasing overlap surface. The strongest interaction is in geometry **a** (-27.7 kcal/mol)**,** with largest overlap surface, and the weakest in geometry **c** (-12.5 kcal/mol), with smallest overlap surface. Geometry **d** has somewhat smaller overlap surface than geometry **b**, and somewhat smaller interaction energy (Figure 3.17).

r_{MM}= 3.96 Å φ= 0°
R= 3.3 Å
ΔE= **-27.7** kcal/mol

r_{MM}= 5.46 Å φ= 0°
R= 3.3 Å
ΔE= **-18.6** kcal/mol

r_{MM}= 6.96 Å φ= 0°
R= 3.3 Å
ΔE= **-12.5** kcal/mol

r_{MM}= 5.66 Å φ= 15.40°
R= 3.3 Å
ΔE= **-16.8** kcal/mol
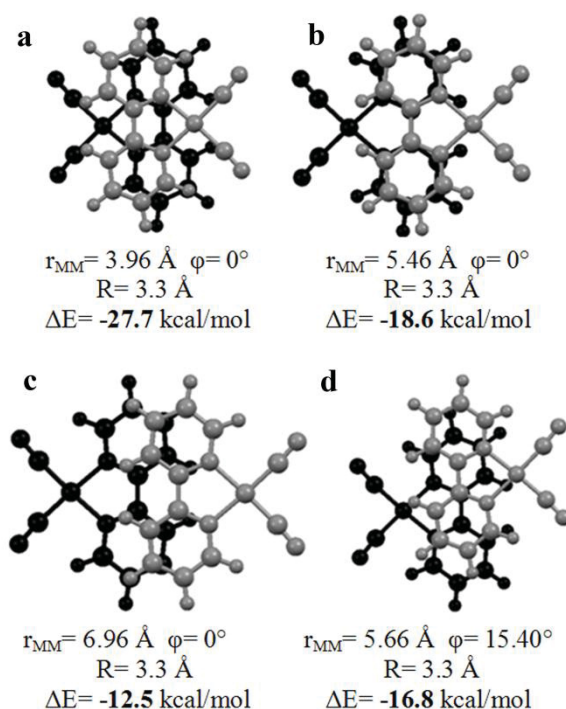
Figure 3.17. Four geometries of [Ni(CN)$_2$*bipy*]$_2$ dimer used for calculations; the geometric parameters and interaction energies are shown. Calculations were done on TPSS-D3/def2-TZVP level of theory, with effective core potential used for metals (SDD).

Previous data on stacking interactions in benzene[43] and pyridine dimers[50] show that displaced geometries are more stable than face-to-face geometries, hence, geometries with larger overlap surface do not have stronger interaction energies. On the other hand, data in this work on *bipy* complexes show that decreasing overlap surface decrease strength of stacking interaction (Figure 3.17 and Table 3.1). This difference between stacking interaction of benzene and pyridine and interactions of *bipy* metal complexes is probably caused by number of nitrogen atoms and metal atom in *bipy* complexes. Namely, nitrogen atoms and metal atoms in complexes make electrostatic interactions more favourable in geometries with large overlap surface. It is also interesting to compare interaction energy in model system in Figure 3.13, where only two pyridine rings overlap, with interaction energy of two uncoordinated pyridines.[50] The interaction energy in model system in Figure 3.13 is remarkably stronger (-7.3 kcal/mol, Table 3.1) than interaction energy between two uncoordinated pyridines (-4.1 kcal/mol). Hence, coordination of pyridine influences stacking interaction energies significantly.

Chapter 4

4. Synthesis and study on oligomerization of new Rh(I) complexes

Oligomerization of the square-planar complexes of Rh(I) is very well documented in the literature, as shown in Chapter 1 of this thesis. In order to study the influence of the chirality on this self-aggregation and potential for chiral recognition, several novel chiral Rh(I) complexes have been synthesized and characterized. Process of oligomerization was followed by UV/Vis spectroscopy and ITC experiments.

4.1. Synthesis

Chiral ligands used in synthesis of the Rh(I) complexes were prepared following the procedure reported by Weber et al.[412] (procedure B), for synthesis of isocyanides from amines. The procedure utilized the phase transfer catalysis method[413] of generating dihalocarbene from chloroform and 50% aqueous sodium hydroxide under reflux, which constitutes a very effective and convenient method for the direct one-step conversion of a primary amine into the corresponding isocyanide. Organic phase was separated by extraction, washed with water and brine, and dried over $MgSO_4$. Resulting products (Figure 4.1) were purified by column chromatography, giving 30-50% yields.
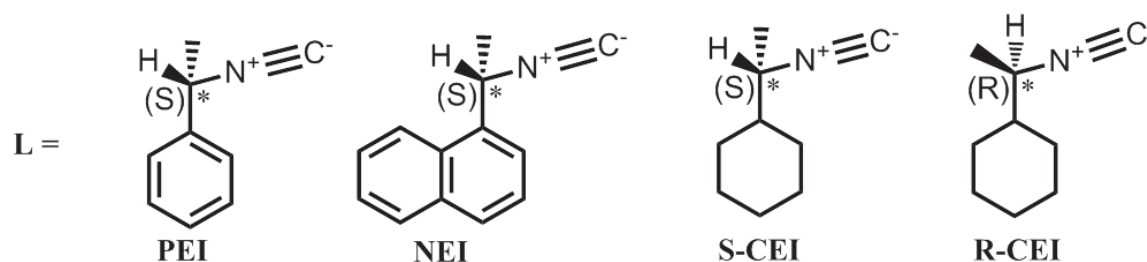
Figure 4.1. Chiral isocyanides ligands; **PEI** - *S*-(-)-1-phenylethylisocyanide; **NEI** - *S*-(-)-1-(1-Naphthyl)ethylisocyanide; *S*-**CEI** - *S*-(+)-1-cyclohexylethylisocyanide; *R*-**CEI** - *R*-(-)-1-cyclohexylethylisocyanide

The tetrakis(isocyanide)Rh(I) complexes were prepared following the procedure reported by Miya et al.,[246] with slight modifications (Figure 4.2). Corresponding isocyanide ligand was added to the solution of [Rh(COD)Cl]$_2$ in toluene under argon and stirred for 1-3 hours. Treating the mixture with n-pentane resulted in precipitation of the purple colored products (shade of purple depending on the ligand used). Products were recrystallized from the CH_2Cl_2/n-pentane giving 35-45% yield for *R*-**CEI** and *S*-**CEI** analogue, and 85-90% yield for complexes with **NEI** and **PEI** ligands.

Figure 4.2. General schematic for the reaction of preparation of the Rh(I) complexes ; L – as shown on Figure 4.1.

All synthesized complexes are soluble in common organic solvents: chloroform, dichloromethane, DMSO, acetonitrile, acetone and moderately in THF and ethanol. They are air-sensitive and decompose in water solution.

Following complexes have been synthesized:

Figure 4.3. tetrakis(S-(-)-1-phenylethylisocyanide) rhodium(I) chloride (**RH1**), tetrakis(S-(-)-1-(1-Naphthyl)ethylisocyanide) rhodium(I) chloride (**RH2**), tetrakis(R-(-)-1-cyclohexylethylisocyanide) rhodium(I) chloride (**RH3**) and tetrakis(S-(+)-1-cyclohexylethylisocyanide) rhodium(I) chloride (**RH4**).

It has to be stressed that the all the attempts to obtain the X-ray crystal structures of synthesized complexes have failed. Various techniques (solvent diffusion, slow evaporation, etc.) under different crystallization conditions (room and low temperature, absence of light, several solvent combinations, etc.) have been tested. We have also tried exchange of the

default, Cl⁻ anion, with few other anions (I⁻, PF_6^-, BF_4^-, BPh_4^-, BARF), but the only crystals we managed to obtain were thin, deep red colored needles, for the **RH1** complex, which were of unsatisfactory quality for X-ray diffraction analysis.

This failure to obtain crystal structures limited our analysis and understanding of the structure and organization of these complexes in solid state.

4.2. Spectroscopic characterization

Infrared spectra of the free ligands and the corresponding Rh(I) complexes were compared in order to gain the preliminary information about the way ligands coordinate to the metal centre. The stretching wave numbers of the most important bands are presented in Table 4.1, spectra for all the compounds can be found in Appendix.

Table 4.1. Stretching wave numbers of **N≡C** bond (cm⁻¹) for synthesized compounds

Compound	υ (N≡C) [cm⁻¹]
PEI	2138
NEI	2133
S-CEI	2134
R-CEI	2133
RH1	2211, 2163
RH2	2198, 2139
RH3	2212, 2165
RH4	2212, 2162

All compounds show the stretching N≡C vibrations in range 2130-2220 cm⁻¹, which falls in the range that is typical for isocyanide group.[414] There are two distinct bands that can be observed in the IR spectra of Rh(I) complexes. First one, sharp and strong, appears at wave numbers from 2170-2160 cm⁻¹ for the **RH1**, **RH3** and **RH4** complexes while the values for the corresponding free ligands range from 2140-2130 cm⁻¹. The difference of 30 cm⁻¹ is the consequence of the coordination of the ligands to the metal centre through carbon atom from isocyanide suggesting square-planar $[Rh(L)_4]^+$ structure. Here, Rh complex with **NEI** ligand differ from the other complexes by showing just a small shift in frequencies (6 cm⁻¹) comparing to the free **NEI** ligand. This suggested different environment around N≡C bond compared to the other complexes.

Second band, sharp and weak, appears at wave numbers from 2210-2195 cm^{-1}. This band corresponds with the IR signals for the stretching N≡C vibrations reported by Balch and Olmstead[241] for the trans-$(C_6H_{11}NC)_4RhI_2$ complex, suggesting partial oxidation of our complexes, and formation of the dimer.

^{1}H NMR proton chemical shifts for all synthesized compounds are summarized in the experimental section in Chapter 8. Comparative spectra between **RH1** complex and its corresponding ligand are shown on Figure 4.4. Spectra for the other compounds can be found in Appendix. Analysis of the chemical shifts and the integration of the peaks gave us further information on the coordination of the ligand to the Rh(I) metal centre.
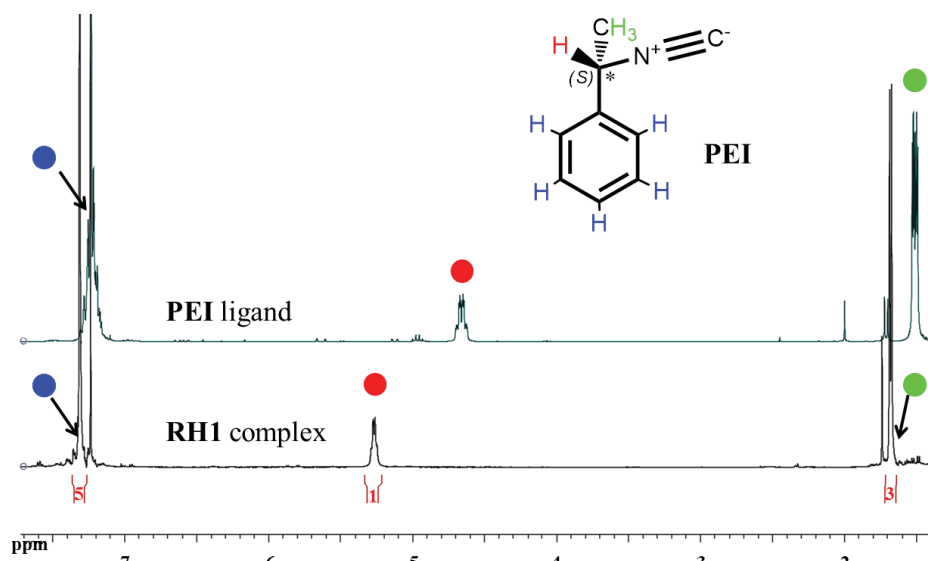
Figure 4.4. Comparative ^{1}H NMR spectra of **RH1** and **PEI** ligand

Signals for the methyl group are shifted to the higher values for about 0.2 ppm upon coordination, while signals for aromatic protons are shifted for about 0.1 ppm. Tertiary H-atom has a distinctive chemical shift, which is not overlapped by other proton signals, designating it as a good candidate to check the coordination of the ligand, and shed more light on possible structure of the complex. The difference in the shifts of the signal for the tertiary H-atom is the consequence of coordination of the ligand to the metal centre. Presence of just one signal for this proton in the spectra of Rh complex, i.e. presence of one distinctive specie, leads to the conclusion that the coordination of the **PEI** ligand to the Rh(I) centre leads to the formation of square-planar tetrakis(isocyanide)Rh(I) complex.

Similar observations can be made for the complexes of **RH3** and **RH4**. For those complexes we can see shift in signal of the tertiary H-atom upon coordination for around 0.4

ppm, and around 0.1 ppm for methyl protons, while the change in the shift for the cyclohexyl protons couldn't be precisely determined, due to the shape of the peaks (multiplets).

For the Rh complex with **NEI** ligand, situation is different. Upon analysis of the spectra we noticed two pairs of signals for methyl protons, and tertiary H-atom. This suggested different kind of coordination (already hinted by IR), and existence of two distinct environments around tertiary proton.

Due to the possibility of free rotation around N-C bond in ligand various conformations of the **NEI** ligands in the complex are possible, forming different oligomers. In order to shed some light on this issue, we performed synthesis of this complex on low and high temperatures. Comparative ^{1}H NMR spectra show rise of the new signals (Figure 4.5). This suggested another change in the environment, but, as already stated before, since we haven't managed to obtain crystal structures, full structural analysis of this Rh complex and the explanation for observations in ^{1}H NMR spectra, stayed outside of our grasp.
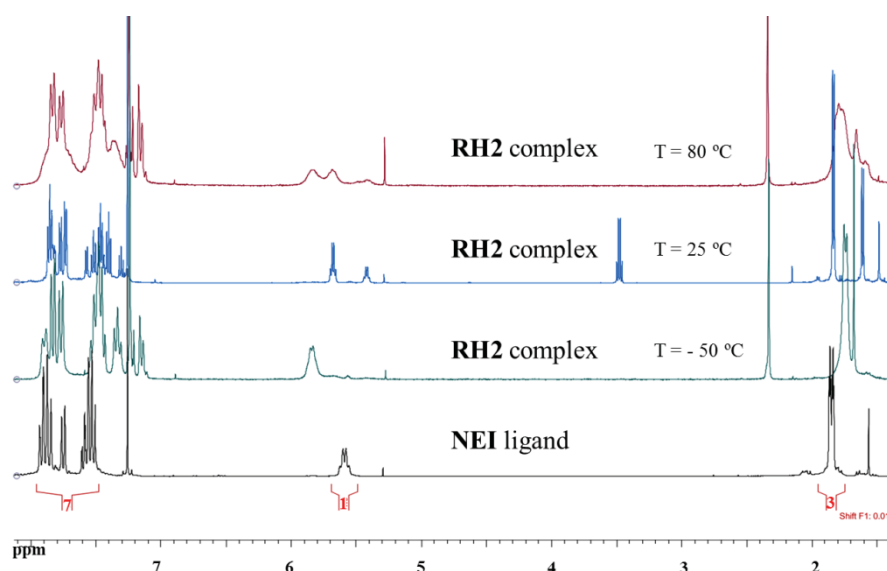
Figure 4.5. Comparative spectra of the **NEI** ligand and **RH2** complex synthesized on different temperatures

The summary of ^{13}C NMR spectra for all complexes can be found in experimental part in Chapter 8. Example of one ^{13}C NMR spectra for **RH1** complex is shown on Figure 4.6.
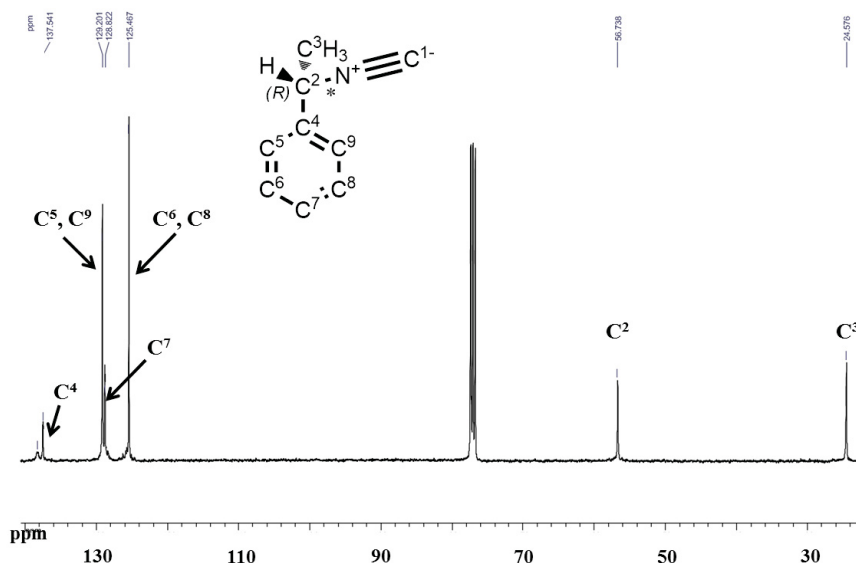
Figure 4.6. ^{13}C NMR spectra for **RH1** complex

The spectra show characteristic signals for methyl (C^3), and tertiary (C^2) carbon atoms with chemical shifts of 24.58 and 56.73 ppm respectively. Signals for the aromatic carbons appear in the range 125-138 ppm. The last expected signal that corresponds to the shift of the carbon atom (C^1) from isocyianide group coordinated to the metal centre cannot be observed in the spectra at room temperature. This is probably due to very slow relaxation time of this particular carbon nucleus upon coordination to the metal. The complexes with **CEI** ligands also show characteristic signals for methyl and tertiary carbon atom with chemical shifts of 18.4-18.7 ppm, and 58.3-58.5 ppm respectively. The rest of the signals that were observed correspond to the chemical shifts of the carbon atoms of cyclohexyl ring in the range 25-43 ppm. Again, signal for the isocyanide carbon couldn't be observed. The ^{13}C spectra of the ligands are very similar to that of the corresponding complexes, with the chemical shifts moved slightly to the lover values, and one distinctive feature. Namely, signal for the carbon atom of the isocyanide group is sharp and clearly distinguishable, giving proof that coordination of the ligand to the metal centre, indeed happens through the terminal carbon atom of the isocyanide. The spectra of the **RH2** showed more signals than it was expected that couldn't be attributed to the appropriate carbon atoms precisely. Again, like in the case of the ^{1}H NMR spectra, it suggested that **NEI** ligands take different conformations in this complex.

All the ligands used in the preparation of the Rh(I) complexes possess chiral centre on the tertiary carbon atom (Figure 4.1). We have measured the optical rotation in dichloromethane and calculated specific rotation for each compound using the relation *eq* 4.1:

$$[\alpha]_D = \frac{\alpha_{obs}}{l \cdot c} \qquad\qquad eq\ 4.1$$

where α_{obs} is the experimentally observed rotation, c is the concentration in g/ml and l is the path length of the cell used expressed in dm (10 cm). The results are summarized in the experimental section in Chapter 8. The peculiar behaviour was observed in case of **RH2** complex. Namely, specific rotation for the **NEI** ligand is -44.24 $°cm^3$/g·dm, which is in accordance with the rotation of the corresponding amine; while for the Rh complex, value for specific rotation, measured under the same conditions, is +66.29 $°cm^3$/g·dm.

Circular dichroism spectra – CDs for the complexes can be found in the Appendix. Summary of the spectra is presented in the Table 4.2.

Table 4.2. Mol. CDs of the synthesized complexes in CH_2Cl_2 and CH_3CN

Compound	Solvent	Lambda (nm)	Mol. CD
RH1	CH_2Cl_2	461, 389	-0.181, -0.669
	CH_3CN	384	-0.774
RH2	CH_2Cl_2	373	2.032
	CH_3CN	372	1.885
RH3	CH_2Cl_2	n/a	n/a
	CH_3CN	382	-0.453
RH4	CH_2Cl_2	n/a	n/a
	CH_3CN	381	0.096

The absorption band of CDs spectra observed at 461 nm in CH_2Cl_2 solution for the **RH1** complex corresponds to the negative Cotton effect, and can be attributed to the absorption in the dimer form of Rh complex, which was confirmed later by the UV/Vis spectra. This band does not appear in the CDs spectra of the CH_3CN solution, due to the low concentration of the complex.

UV/Vis spectra of the complexes proved to be very useful in analysis of the aggregation of synthesized complexes, which will be explained in the next section. Example for the **RH1** in acetonitrile solution at different concentrations is shown on Figure 4.7. The other spectra can be found in Appendix (spectra were not recorded for **RH2** complex).
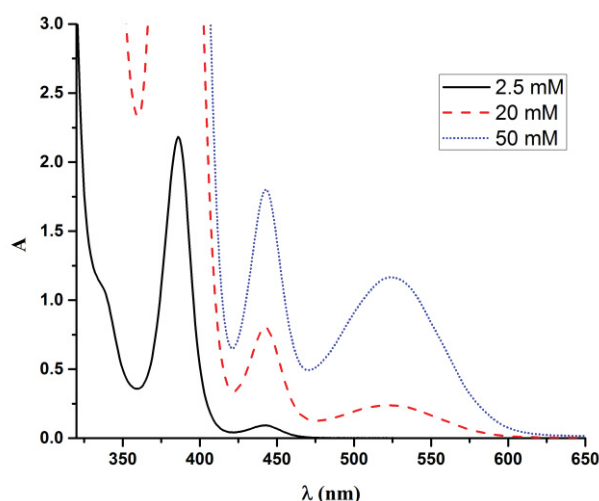
Figure 4.7. UV/Vis spectra of **RH1** complex in 0.1 M solution of n-Bu$_4$NPF$_6$ in CH$_3$CN

Spectra for the **RH1** complex show strong band at 386 nm, which could be ascribed as absorption of monomeric form of complex. Second band, small and broad, appears at 441 nm, which is attributed to the absorption of the dimer form of complex (see below). As can be seen from the Figure 4.7, increase in the concentration lead to the appearance of the new band, at 524 nm, which was shown to be due to the absorption in trimeric form of complex. In case of **RH3** and **RH4** complexes the spectra were recorded in pure acetonitrile. Here, strong band appears at 384 nm, and the second one at 441 nm. The third band is absent from their spectra, due to a lower solubility of these complexes in acetonitrile. As was mentioned before, the band that can be attributed to the trimer only appears at high concentrations.

Mass spectra of the synthesized compounds can be found in Appendix. ESI mass spectra of the **RH1** complex recorded in positive mode, show signal at 627.20 *m/z*, which originates from the [M]$^+$ ion. For the **RH3**, signal originating from [M]+ ion is found at 651.36 *m/z*, for **RH4** on 651.39 *m/z* and for the **RH2** complex is found at 827.45 *m/z*. For all the ligands [M+Na]$^+$ ions have been found at: 160.11 m/z for **R-** and **S-CEI**, and at 204.08 m/z for **NEI**.

4.3.   Analysis of the oligomerization process

Analysis of the UV-Vis spectra of synthesized Rh complexes helped greatly in understanding and describing the process of self-aggregation that these complexes exhibit *in solutio*. We have based our study on the procedure reported by Mann et al.[415] As it was already mentioned, UV-Vis spectra of the **RH1** complex show the rise of the new absorption

bands at 441 and 525 nm with the increase in concentration of the complex. This can be explained in terms of an oligomerization of the complex rhodium cations. We considered the process of oligomerization as shown on Figure 4.8.

$$2M \xrightleftharpoons{K_1} D$$

$$M + D \xrightleftharpoons{K_2} T$$
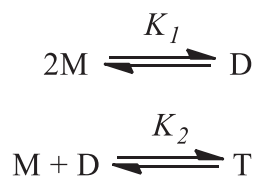
Figure 4.8. Schematic representation of the oligomerization process. M = [Rh(**PEI**)$_4$]$^+$, D = [Rh$_2$(**PEI**)$_8$]$^{2+}$ T = [Rh$_3$(**PEI**)$_{12}$]$^{3+}$.

Using equations *eq* 4.2 and *eq* 4.3 to treat the equilibria, we gained a powerful tool in the confirmation of the oligomerization process.

$$\frac{[Rh]}{\sqrt{A_2}} = \frac{1}{\sqrt{\varepsilon_2 K_1}} + \frac{2\sqrt{A_2}}{\varepsilon_2} + \frac{3 K_2 A_2}{\varepsilon_2 \sqrt{\varepsilon_2 K_1}} \qquad eq\ 4.2$$

$$A_3 = \frac{\varepsilon_3 K_2 \sqrt{A_2^3}}{\varepsilon_2 \sqrt{\varepsilon_2 K_1}} \qquad eq\ 4.3$$

[Rh] is the total concentration of Rh complex in terms of monomer, A$_2$ and A$_3$ are the absorbances due only to dimers and trimers, and ε_2 and ε_3 are the corresponding molar extinction coefficients.

For the complex **RH1** over the range of concentrations from 2.5 mM to 50 mM at constant ionic force strength 0.1 M (n-Bu$_4$N)PF$_6$, the plot of [Rh]/$\sqrt{A_{441nm}}$ *vs.* $\sqrt{A_{441nm}}$ is a straight line (Figure 4.9. left). Here, the absorption peak at 441 nm is attributed to the dimer. In the *eq* 4.2 third term can be omitted because there is no deviation from the linearity even at higher concentrations.
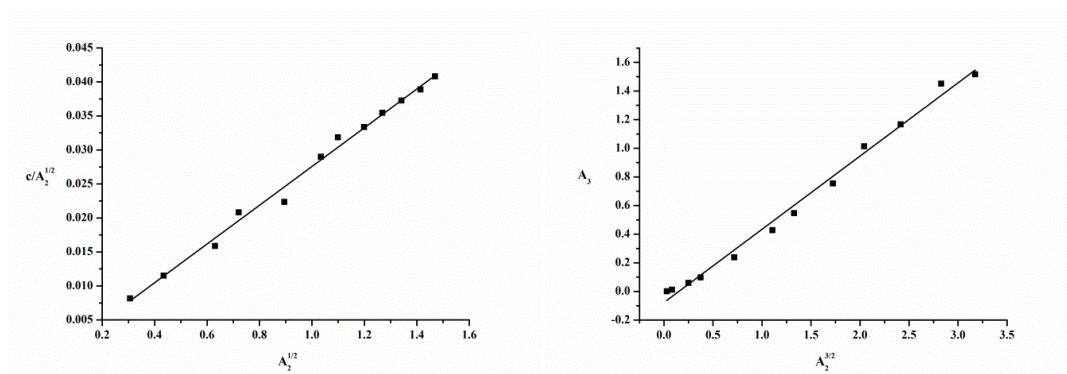
Figure 4.9. Plot of [Rh]/$\sqrt{A_{441nm}}$ *vs.* $\sqrt{A_{441nm}}$ (left) and A_3 *vs.* $\sqrt{A_2^3}$ (right) for **RH1** in 0.1 M solution of n-Bu$_4$N PF$_6$ in CH$_3$CN

From the slope ($\frac{2}{\varepsilon_2}$), and the intercept ($\frac{1}{\sqrt{\varepsilon_2 K_1}}$), we have calculated $K_1 = 1.6 \cdot 10^4$ and $\varepsilon_2 = 70.2$. A plot of A_3 *vs.* $\sqrt{A_2^3}$ is also a straight line (Figure 4.9. right), with the slope $\frac{\varepsilon_3 K_2}{\varepsilon_2 \sqrt{\varepsilon_2 K_1}}$. Substituting K_1 and ε_2 gives $\varepsilon_3 \cdot K_1$. Estimating[415] $\varepsilon_3 = \frac{3}{2} \cdot \varepsilon_2$, gives $K_2 = 366$. From the equilibrium constants, we were able to calculate Gibbs free enthalpy for the processes of dimer and trimer formation. The same procedure was applied for the treatment of the UV-Vis spectra of **RH3** and **RH4**, but only for the process of dimerization. This was due to existence only of absorption band attributed to the dimer. The values of Gibbs free enthalpy are summarized in the Table 4.3. From the values of ΔG for all considered cases we can see that the processes of dimer and trimer formations are favourable in acetonitrile solution.

Table 4.3. Gibbs free enthalpies of the dimer (trimer) formation

Complex	ΔG^{dimer} ; ΔG^{trimer} *(kcal/mol)*
RH1	-5.8 ; -3.5
RH3	-5.7
RH4	-9.7

Extrapolation for the complexes **RH3** and **RH4**, which are enantiomers, have revealed different values for Gibbs free enthalpies of dimer formation. This is not logical because the values should be the same for both complexes due to the symmetry. One possible explanation is that the enantiopurity of the **RH4** complex was questionable, which can be seen from large difference in the value of specific rotation - α_D (see Chapter 8, for RH3 and RH4 characterisation). To further check this we have followed absorption of mixture of **RH3** and **RH4** in different ratios. The UV-Vis spectra (Figure 4.10) show that the intensity of the absorption rises when the ratio moves to the favour of **RH3** at the same concentration.
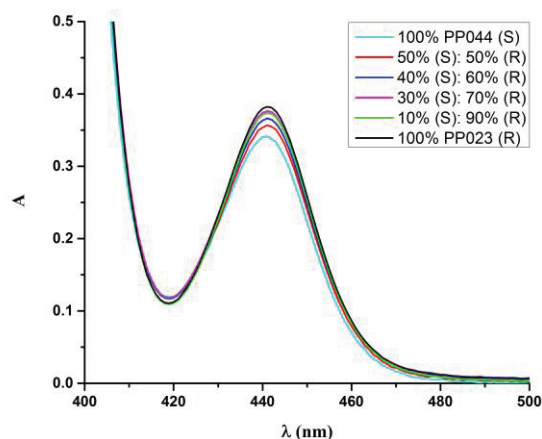
Figure 4.10. UV/Vis spectra of mixture of **RH3** and **RH4** in different ratios (c = 10 mM) in CH$_3$CN

Using the above mentioned method for calculating Gibbs free enthalpy, we have estimated values for the formation of the dimers. What also has to be taken in consideration is that the process of the dimer formation in case of the mixture is not exactly the same as for the pure compounds. Even though the plots of $[Rh]/\sqrt{A_{441nm}}$ *vs.* $\sqrt{A_{441nm}}$ show the same linearity, confirming the absorption attributed to the dimer, we cannot be certain of the exact composition of these dimers. There is equal possibility of existence of both homo-chiral dimers (dimers consisting of one enantiomer) and hetero-chiral dimers (dimers consisting of mixture of two enantiomers), ratio changing in favour of homo-chiral with the increase in percentage of **RH3**. The results are summarized in Table 4.4.

The general trend is the decrease in the value of the ΔG as the percentage of the **RH3** rises, suggesting that the formation of hetero-chiral dimers is favoured more than formation of homo-chiral dimers.

Table 4.4. Gibbs free enthalpies for the dimer formation

RH3 : RH4 (w/w)%	ΔG_f^{dimer} (kcal/mol)
50 : 50	-9.3
60 : 40	-8.7
70 : 30	-8.0
80 : 20	-6.7
90 : 10	-6.5

Another way to follow the process of oligomerization in solution is by Isothermal Titration Calorimetry (ITC). This method proved essential in understanding the process of self-aggregation of cis-platin type complexes, and following thermodynamic of the nucleophilic addition of the several ligands to the complexes of palladium and ruthenium, as will be shown in later chapters of this thesis.

Thermogram of the dilution of concentrated solution of **RH4** (c = 20.4 mM) in chlorobenzene to the pure solution of chlorobenzene show typical endothermic trace (Figure 4.11). We have considered the process of oligomerization as shown of Figure 4.8 . Fitting of the curve provided a value of +21.1 kcal/mol for the enthalpy of dissociation ΔH_{dis} at 298.15 K (the enthalpy of dimer formation ΔH_f has the opposite sign, i.e. -21.1 kcal/mol) and a monomer-dimer association constant K_2 of 91.4. The latter value corresponds to an approximate Gibbs enthalpy ΔG_f^{dimer} of -2.7 kcal/mol. This value was checked by the estimation of the ΔG from UV-Vis spectra as was described above in chlorobenzene. This method afforded a value of -3.9 kcal/mol. As can be seen from these results, tendency of the **RH4** to form dimer in solution of chlorobenzene seems to be less pronounced than in the case of the acetonitrile solution.
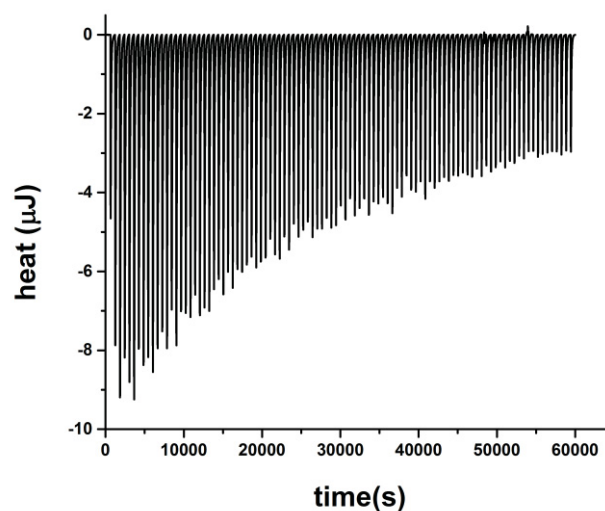
Figure 4.11. Heat released in the reaction: Injection of the solution of **RH4** in chlorobenzene to the pure chlorobenzene. Reaction was performed on 298.15 K. Interval between injections was 600 seconds: **RH4**: $c = 20.4$ mM. There were 100 injections (of 2 μl each).

Chapter 5

5. Understanding the nature and role of the dispersion and other interactions in the stabilization of anti-cancer Pt compounds

Unusual stability and inactivity of the Oxaliplatin and Carboplatin in concentrated solution have been addressed by Dabrowiak and his group. As an explanation they have proposed the oligomerization of these platinum complexes in solution. The core of Dabrowiak's findings is based on the ^{1}H NMR investigations of water solutions of either Carboplatin or Oxaliplatin buffered with HEPES (4-(2-hydroxyethyl)-1-piperazineethanesulfonic acid). Whereas these conditions probably reproduce physiological conditions in term of pH, the use of a potential chelating Lewis base such as HEPES raised our concern about the well documented interactions of this piperazine-based buffer with the considered class of platinum complexes,[416, 417] which could question the reliability of the NMR signal assignment provided by Dabrowiak. For the sake of clarity, we opted for a different methodology that privileged the use of pure polar solvents of high dielectric constants and of either protic (D_2O) or aprotic nature (d_6-dimethylsulfoxide); the aim being to restrict to a minimum the interferences from unwanted processes such as ligand exchange and disruption of chelation. We show further that another buffer such as TRIS (tris(hydroxymethyl)aminomethane), which is also a potential ligand of Pt(II),[416, 417] is far from being innocent when reliable evaluation of the energetics of NCI is at stake. For the purpose of comparison, all experiments carried out with Oxaliplatin were also carried out with its palladium containing analogue - Oxalipalladium,[418] a complex known for being nearly exempt of cytotoxic activity.

5.1. Investigation of the dimerisation of Oxaliplatin and Carboplatin in solution

Diffusion-ordered ^{1}H NMR spectroscopy (^{1}H DOSY NMR)[419] is a tool of choice for the structural analysis of macromolecular systems because in some cases it enables the collection of important structural information on small molecular systems.[292, 420] In the case of solutions of Oxaliplatin (**1**), Oxalipalladium (**2**) and Carboplatin – (**3**) the formation of oligomers could not be established. Large variations in the concentration of analyte within the limits of their solubility did not induce major changes of the measured hydrodynamic diffusion coefficient, which indicated that DOSY was ineffective. It is partly due to the

inaccuracy that resides in the very definition of the hydrodynamic volume included in the Stoke-Einstein equation; this volume is not related directly to analytes volume that one can approximate, for instance, by the solvent-exclusion vdW volume of a molecule.[420]

Practically, if the dynamics of the chemical system are slow with respect to the ^{1}H NMR time-scale, the resulting two-dimensional trace should present one set of signals per analyte ordered by the values of respective translational diffusion coefficients. In the contrary, a system consisting of a fast equilibrium between a monomer and a non-covalently bonded dimer within the time frame of ^{1}H NMR spectroscopy, should lead to an averaged ^{1}H NMR response appearing as a single set of averaged signals. This was typically the behaviour observed for **1-3**, which all displayed a limited solubility in D_2O and in deuterated dry DMSO.

Table 5.1. Hydrodynamic data for compounds **1-3** acquired by two-dimensional ^{1}H DOSY.

cmpd	solvent	c (mM)	D_{exp}^{300K} ($10^{-10}m^2/s$)	r_h^{exp} (Å)	V_s^{exp} (Å^3)	$D^0_{dimer}[D^0_{monomer}]$ ($10^{-10}m^2/s$)
1	D_2O	6.3	5.68	3.55	187.0	6.05[7.63]
	D_2O	12.6	5.96	3.38	162.2	6.05[7.63]
	d_6.DMSO	5.0	2.55	4.10	289.0	3.14[3.96]
	d_6.DMSO	51.8	2.49	4.20	310.4	3.14[3.96]
2	D_2O	6.8	5.17	3.90	248.2	6.05[7.63]
	D_2O	67.7	4.98	4.04	276.8	6.05[7.63]
	d_6.DMSO	9.1	2.20	4.75	448.8	3.14[3.96]
	d_6.DMSO	63.5	1.99	5.27	611.8	3.14[3.96]
3	D_2O	6.7	6.24	3.23	141.0	5.08[7.45]
	D_2O	55.2	6.12	3.29	149.5	5.08[7.45]
	d_6.DMSO	6.5	2.58	4.06	280.6	2.63[3.87]
	d_6.DMSO	53.9	2.39	4.37	349.7	2.63[3.87]

Table 5.1 lists the main relevant data of ^{1}H DOSY experiments that is the millimolar concentration of analyte (c), the measured translational diffusion coefficient (D_{exp}), the experimental hydrodynamic radius (r_h) and the associated spherical volume (V_s).

Calculated translational diffusion coefficient (D^0) for monomers and dimers were obtained by applying the Stoke-Einstein law. This was done by roughly approximating the hydrodynamic volume of the analytes with that of the associated solvent-exclusion volume of

an ideal triaxial ellipsoid. Triaxial ellipsoid is computed from the main dimensions (a, b, c)[421-423] of the structures of either the monomers or the β-stacked dimers produced by COSMO DFT calculations that will be presented later in the text.
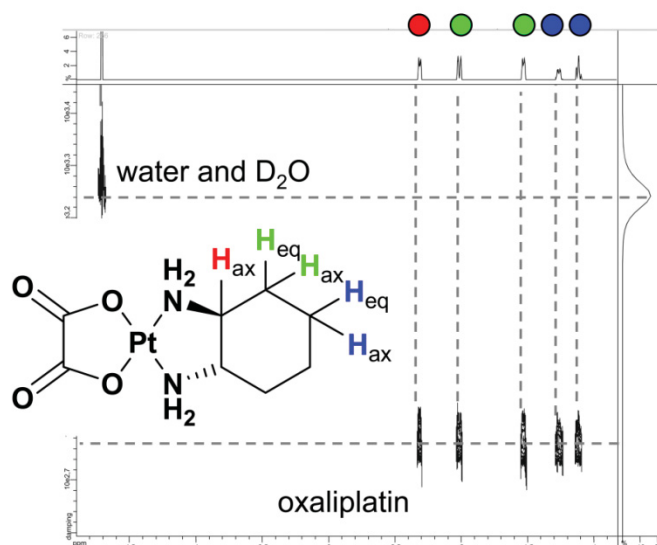
Figure 5.1. Two-dimensional plot of a ^{1}H diffusion-ordered NMR experiment carried out with a solution of **1** in D_2O. Ordinates represent the values of the translational diffusion coefficient.

For each compound a pair of DOSY experiments was carried out by varying the concentration of the analyte: 1) at the highest achievable concentration, which should favour the formation of a dimer, and 2) at a 10 fold lower concentration. Table 5.1 indicates that there is no large influence of the concentration on D_{exp}, the values of which surprisingly remain close to the value computed for a dimer in the case of **1** (Figure 5.1 and Table 5.1 entries 1-4). For d_6-DMSO solutions of **2** the values of D_{exp} also suggested the existence of a dimer. The behaviour of **3** was very similar to that of **1**.

Another attempt to demonstrate the formation of a $[1]_2$ dimer in water was by measuring the variations of absorbance A of the UV/Vis absorption spectrum of **1** as a function of analytes concentration **c**, was inconclusive. Namely, it have failed to provide the expected non-linear variation of the A=f(c) curve generally symptomatic of the formation of a dimer (Figure 5.2), thus confirming early observations by Dabrowiak.[299] Noteworthy, the concentration was constrained within the 1-10 mM domain by the poor solubility of **1** in water.
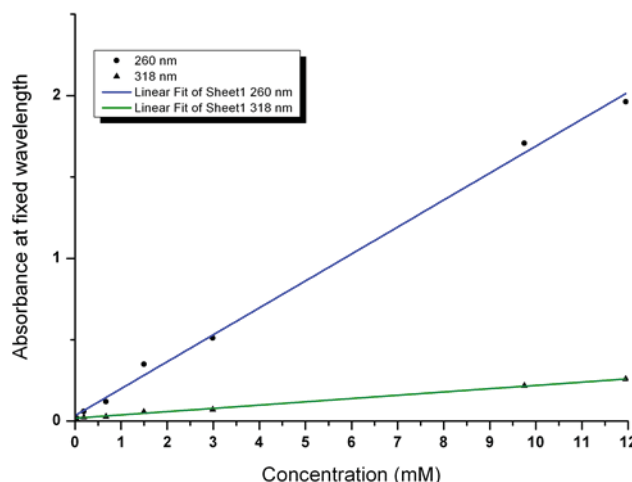
Figure 5.2. Linearity of the relationship between absorbance at 216 nm and 318 nm and the concentration of **1** in pure water at 25°C.

Further investigations of the self-association were consequently restricted to the almost planar complexes **1** and **2** in water using the methods of isothermal titration calorimetry, which allows the accurate determination of thermochemical parameters such as enthalpy of formation/dissociation of oligomers. These parameters are generally produced by the numerical treatment of thermographic traces, applying appropriate thermodynamic models.

For instance, the dissociation of hypothetical dimers [**1**]$_2$ and [**2**]$_2$ was investigated by the dilution of 20 (**2**) to 10 mM (**1**) aqueous solutions of analyte into a relatively large volume of pure water by applying the method of Young et al.[424, 425] Formulation of association constants for these hypothetical processes is shown on Figure 5.3.

For compound **1**, ITC experiments gave no noticeable endothermic heat flow above the dilution background trace, which, in other terms, suggests that either the proportion of oligomer(s) in solution or the enthalpy of dissociation was too low to produce sensible heat flow.

$$2\,\mathbf{1} \rightleftharpoons [\mathbf{1}]_2 \qquad K_1 = \frac{c_{[1]_2}}{c_1^2}$$

$$2\,\mathbf{2} \rightleftharpoons [\mathbf{2}]_2 \qquad K_2 = \frac{c_{[2]_2}}{c_1^2}$$

$$\mathbf{1} + \mathbf{2} \rightleftharpoons [\mathbf{1},\mathbf{2}] \qquad K_{1,2} = \frac{c_{[1,2]}}{c_1 \cdot c_2}$$

$$c_1^0 = c_1^* + c_{[1,2]} \quad c_2^0 = c_2^* + c_{[1,2]} \quad K_{1,2}^* = \frac{c_{[1,2]}}{c_1^* c_2^*}$$

$$c_1^* = c_1 + c_{[1]_2} \quad c_2^* = c_2 + c_{[2]_2}$$
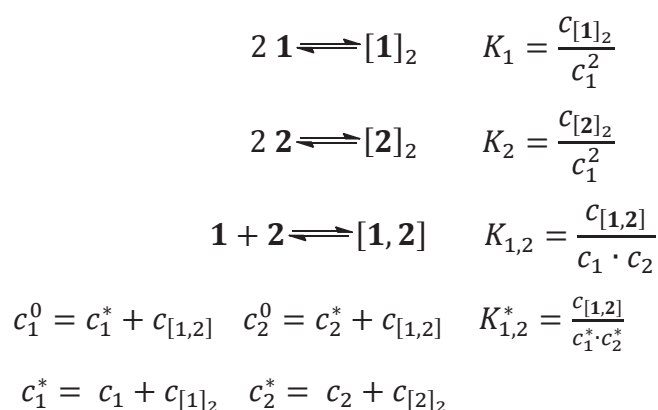
Figure 5.3. Formulations of association constants

For compound **2**, a typical endothermic trace was recorded (Figure 5.4) which matched, assuming dimer dissociation within Young's model,[424, 425] a value of +0.5 ± 0.1 kcal/mol for the enthalpy of dissociation ΔH_{dis} at 298.15 K (the enthalpy of dimer formation ΔH_f has the opposite sign, i.e. -0.5 kcal/mol) and a monomer-dimer association constant K_2 of ca. $3 \cdot 10^{-4}$. The latter value corresponds to an approximate Gibbs enthalpy ΔG_{f2} of ca. +4.6 kcal/mol and a value of entropy change ΔS_{f2} of ca. -17 cal/(K·mol).
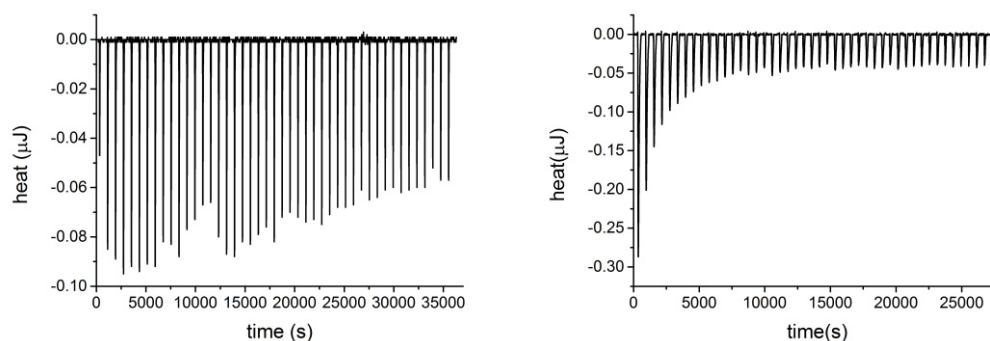
Figure 5.4. Thermographic traces of the dilution by sequential additions of a concentrated aqueous solution of **1** (c = 20 mM, v = 2.06 µL) into pure water at 25 °C (left); and **2** (c = 20 mM, v= 2.06 µL) in pure water at 25 °C (right)

Compounds **1** and **2**, which differ only by the nature of the metal and by few structural features, were probed for their possible mutual interaction. Titration was performed by mixing, in serial microinjections, equimolar solutions (10 mM) of **1** and **2**.

The resulting thermographic trace provided a clear exothermic behaviour (Figure 5.5).
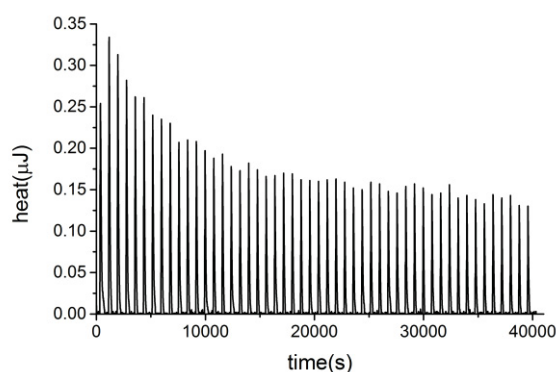
Figure 5.5. Thermograph of the titration of aqueous solution of **1** (c_1^0= 10 mM) by sequential additions of aqueous solution of **2** (c_2^0= 10 mM, v= 4.00 µL) at 25 °C.

Curve fitting assuming an idealized equilibration between **1** and **2** on the one hand and [**1·2**] on the other hand provided an enthalpy of association of -0.6 kcal/mol at 298.15 K and a value of $5.1 \cdot 10^{-4}$ for the apparent constant of association K_{12}^*. The latter is defined as shown in Figure 5.3, and it is associated with a Gibbs enthalpy ΔG_{f12} value of +4.5 kcal/mol at

298.15 K and an entropy change of -17 cal/(K·mol) if one assumes the proportions of $[\mathbf{1}]_2$ and $[\mathbf{2}]_2$ to be negligible.

5.2.   Oligomers in the gas phase

In quite good agreement with earlier reports by other authors, it was found that compounds **1-3** do produce oligomers in the gas phase. Under the mild conditions of electrospray ionization (ESI) in the presence of traces of formic acid and of sodium salts, all three compounds produced complex features in the positive ion mode.

Whether water or DMSO was used as solvent, no difference to the formation of the oligomers could be noticed in the ESI+ mass spectrum. Figure 5.6 and Figure 5.7 show the presence of rather intense signals assigned to oligomeric forms associated to either a proton or a sodium ion.

The variety of "nuclearities", that is the number of monomeric unit per oligomer, that are achieved under such conditions can be deduced from analysis of the isotopic distribution of the main peaks, which reveals that dimers, trimers, tetramers and hexamers readily form in the gas phase with **1-3** (results for **3** are shown in Appendix). Peaks assigned to double cationic tetramers and hexamers of **1** were found hidden behind the isotopic pattern of the respective monocationic dimers and trimers that have identical averaged m/z ratio.

The latter results inform of the obvious propensity of **1-2** to self-assemble in the gas phase into cationic species with sufficient lifetime to allow detection.
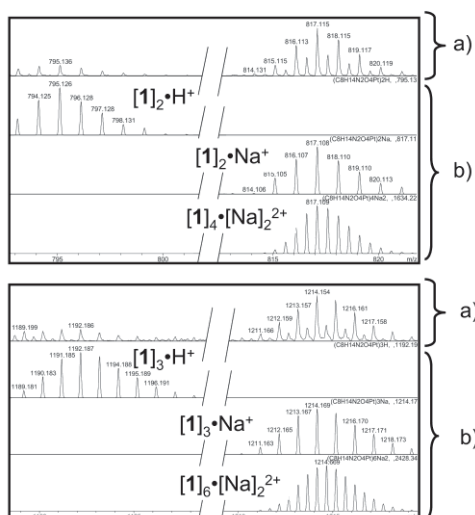
Figure 5.6. Selected regions of the ESI+ mass spectrum of a water solution of **1** containing traces of formic acid and trace contamination by Na$^+$ salts: a) experimental spectrum, b) simulated isotopic patterns.
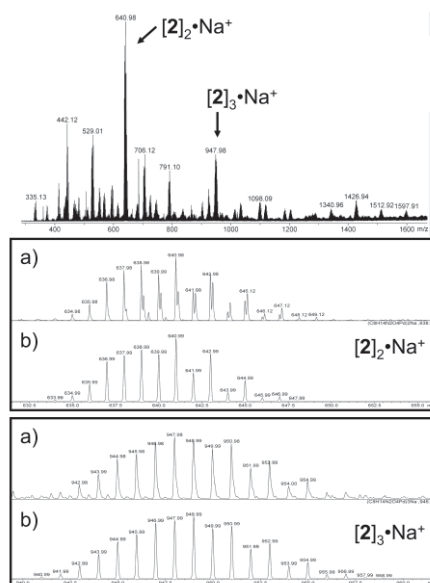
Figure 5.7. Selected regions of the ESI+ mass spectrum of a water solution of **2** containing traces of Na⁺ salts: a) experimental spectrum, b) simulated isotopic patterns.

5.3. *In vacuo* **DFT study of oligomerization**

The aggregation of **1-3** in either the gas phase or solution was modelled by taking advantage of the first-principles-based DFT-D3 approach,[147] which was designed to treat, in a physically correct manner, the attractive contribution of the London force, i.e. dispersion, in addition to all other inter and intramolecular interactions properly treated by conventional DFT. All dispersion corrections reported refer to the zero-damping version of D3 (a.k.a. D3(0)). The differences to the later published so-called Becke-Johnson (BJ) damping approach (a.k.a. D3(BJ))[379, 380] are small and do not affect any of our conclusions. The choice results from technical restrictions we had in the starting phase of work on this thesis.

Models of oligomers of **1-3** were inspired partly by the structures obtained by X-ray diffraction analysis, which are deposited with the CSD.[307] However, whereas most of the experimental crystal structures tend to point a preference for side-to-side γ-type association leading to an organization in parallel strands,[426] theoretical calculations *in vacuo* as well as with a model of solvation (explained later in the text) indicated that the stacked arrangement β observed in one experimental structure of a similar complex by Galanski et al.[307] leads to optimal stabilization. In the following sub-sections three arrangements are considered as they came out of geometry optimizations at the (ZORA) BLYP-D3(0)/all electron-TZP level as local minima. These are the: head-to-tail stack *α*, the head-to-tail shifted-stack *β* and the side-to-side *γ* arrangement (Figure 5.8).
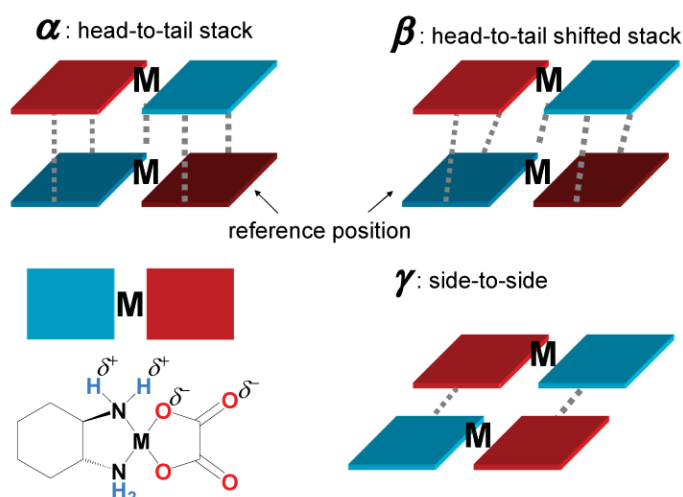
Figure 5.8. Symbolic representations of the arrangements of the aggregates in local energy minima for head-to-tail dimers of **1-3**. The blue colored plate represents the amine ligand and the red colored to the carboxylate ligand. Dotted lines symbolize NCI and H-bonds supposedly intervening in the cohesion of the arrangement.

The α and β arrangements differ by the angle of the normal to the chelate mean plane embodied by the M-M axis, which in the former arrangement (α) is close or equal to 90° and different from this value in the latter arrangement (β).
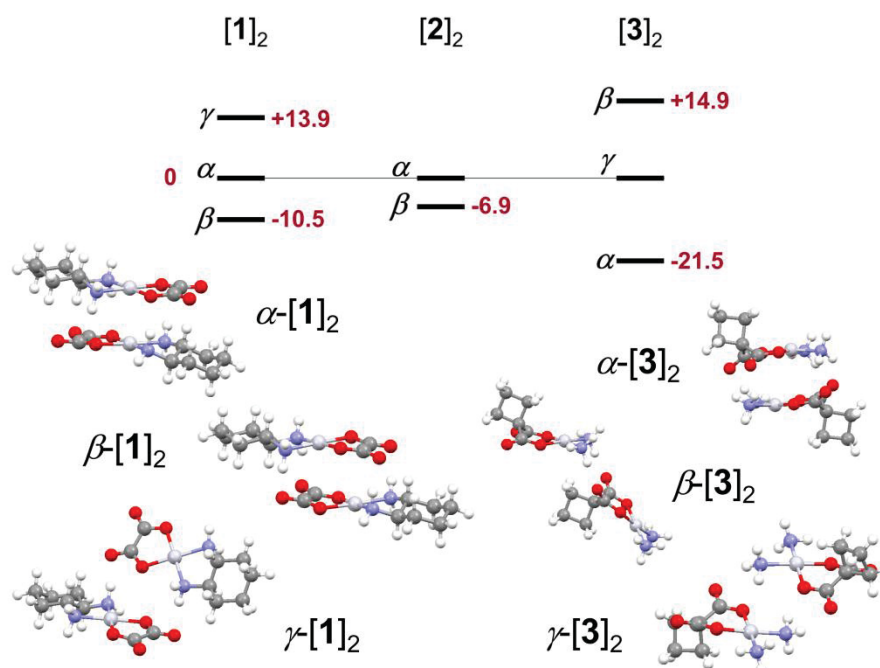
Figure 5.9. Relative energies of the α, β and γ arrangements of the gas-phase dimers of **1-3** (in kcal/mol).

Inspection of the energies of those three types of arrangements indicate that the most favoured one is the β for [**1**]$_2$ and [**2**]$_2$ by ca. 10 and 7 kcal/mol respectively. Formation energies ΔE_f for those two dimers in the gas phase are by ca. 10 and 7 kcal/mol more

favourable to the β arrangement than to the α as can be seen on Figure 5.9. The situation is slightly different in the case of complex 3, partly because of the steric strain induced by the cyclobutyl fragment. In this case, the α arrangement, i.e α-[3]$_2$ appears to be favoured. The β-[3]$_2$ has nothing in common with those of the dimers of 1 and 2 because at least two main N-H···O interactions are missing, which makes it the least favoured arrangement here. This trend is corroborated by Energy Decomposition Analyses (EDA),[427, 428] which indicate (Table 5.2) that the largest intrinsic interaction energies between prepared monomers are found for β-[1]$_2$, β-[2]$_2$ and α-[3]$_2$.

Table 5.2. Components (in kcal/mol) of the EDA for geometries of gas-phase dimers of **1-3** computed at the ZORA-BLYP-D3(0)/all electron TZP.

Complex	ΔE_{def} (kcal/mol)^a	ΔE_{int} (kcal/mol)	ΔE_f (kcal/mol)
α–[**1**]$_2$	+5.4	-60.4	-55.0
β–[**1**]$_2$	+7.9	-73.4	-65.5
γ–[**1**]$_2$	+3.2	-44.2	-41.1
α–[**2**]$_2$	+4.6	-57.6	-52.9
β–[**2**]$_2$	+8.0	-67.9	-59.9
α–[**3**]$_2$	+15.4	-73.9	-58.5
β–[**3**]$_2$	+2.5	-24.6	-22.0
γ–[**3**]$_2$	+4.2	-41.3	-37.0

^{a} within the EDA scheme, ΔE_{def} (>0) corresponds to the deformation energy necessary to prepare each fragment before interaction, ΔE_{int} (generally <0) is the interaction energy, ΔE_f is the formation energy: $\Delta E_f = \Delta E_{int} + \Delta E_{def}$.

Breaking down ΔE_{int} into its main Pauli, orbital, electrostatic and dispersion components informs of the peculiar importance to the latter term, which amounts to 27 %, 39 % and 49 % of the total interaction energy in γ-[1]$_2$ (ΔE_{int} = -44.0 kcal/mol), β-[1]$_2$ (ΔE_{int} = -73.4 kcal/mol) and α-[1]$_2$ (ΔE_{int} = -60.1 kcal/mol) respectively. Particularly in the case of β-[1]$_2$ and β-[2]$_2$, the larger ΔE_{int} value results from more favourable electrostatic and orbital terms, which can be assigned to the H-bonding that constitutes a major effect responsible for the cohesion of those dimers in the gas phase.

The orbital interaction energy term was decomposed in the cases of β−[1]$_2$ and β−[2]$_2$ using the ETS-NOCV method developed by Mitoraj, Michalak and Ziegler.[390] The NOCV are defined as eigenvectors that diagonalize the deformation density matrix ΔP, i.e. $\Delta P = P - P^0$, where P and P^0 correspond to the density matrices of the combined molecule and the fragments considered.

The deformation density, $\Delta\rho = \rho$(**molecule**) - ρ^0(**fragments**), can be expressed in the NOCV representation as a sum of pairs of complementary eigenfunctions (ψ_{-k}, ψ_k) corresponding to the eigenvalues $-\nu_k$ and $+\nu_k$ with the same absolute value but opposite signs. The orbitals with negative eigenvalues exhibit "anti-bonding" character and those corresponding to positive eigenvalues are mostly "bonding".

This analytical method provided a clear picture of the contribution of H-bonding in the cohesion of the gas-phase dimer and confirmed the absence of any significant metal-metal orbital interaction (Figure 5.10). NOCV deformation densities for other arrangements can be found in Appendix.
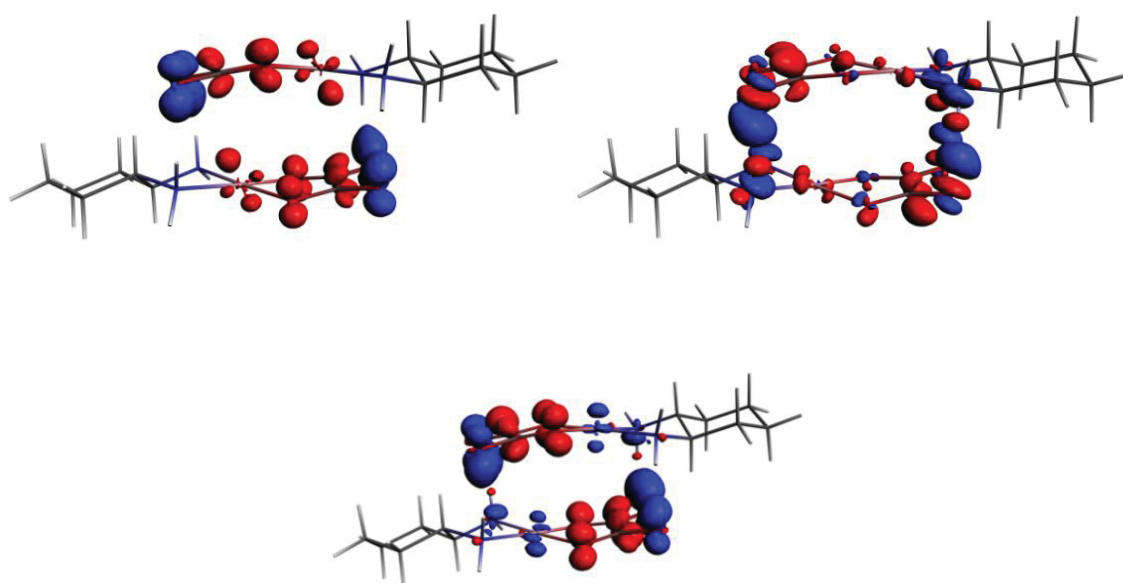
Figure 5.10. NOCV deformation density $\Delta\rho_1$ (left up; ΔE_{orb} = -5.84 kcal/mol; ω = 15%), $\Delta\rho_2$ (right up; ΔE_{orb} = -4.07 kcal/mol; ω = 11%) and $\Delta\rho_5$ (down; ΔE_{orb} = -3.58 kcal/mol; ω = 9%) for $\beta[1]_2$; ΔE_{orb} – orbital stabilization energy for corresponding deformation density ΔE_{torb} – energy of total orbital interactions in the corresponding dimer ω - % of ΔE_{orb} in the ΔE_{torb}

Absence of metal-metal interaction was also confirmed by Wiberg bond indices[429] that were computed from the Natural Atomic Orbital basis for the M-M segment as can be seen in Table 5.3.

Table 5.3. Wiberg bond indices

Molecules	Interacting atoms	Wiberg bond indices
α–[1]$_2$	Pt-Pt	0.02
β–[1]$_2$	Pt-Pt	0.005
α–[2]$_2$	Pd-Pd	0.02
β–[2]$_2$	Pd-Pd	0.004
α–[3]$_2$	Pt-Pt	0.009
β–[3]$_2$	Pt-Pt	0.001
β–[1,2]	Pt-Pd	0.005

Only three orbital interaction terms were found to relate to N-H···O hydrogen bonds with values of ca. 5 kcal/mol, a rather low value consistent with the lack of obvious synaptic basins in between the fragments noted in the analysis of the Electron Localisation Function (ELF).[393] The ELF was introduced by Becke and Edgecombe[430] as a measure of the probability of finding an electron in the neighbourhood of another electron with the same spin, thus being the measure of Pauli repulsion. ELF is formulated as:

$$ELF = \frac{1}{1 + \left[\dfrac{K(r)}{K_h(\rho(r))}\right]^2}$$

Parameter K is the curvature of the electron pair density for electrons of identical spin, $\rho(r)$ the density at (r), and K_h the value of K in a homogeneous electron gas with density ρ. ELF is defined in such way to conveniently take the values between 0 and 1. Values are close to 1 when in the vicinity of one electron, no others with the same spin could be found, e.g. in bonding pairs or lone pairs. Small values of ELF are typical for the region between two electron shells. In a homogeneous electron gas ELF has everywhere the value 0.5.

Figure 5.11 displays two-dimensional (2D) cross section in the plane that contains metals, and split the rest of the molecules nearly through the middle. In this 2D representation ELF values are coded in a colour scale. Savin et al.[393] have shown that in the case of existence of the M-M bond, localization should be found in between metal centres.

Because of the selection of the ELF cross section plane, Pauli repulsion between the metals can clearly be seen, but the hydrogen bond cannot be observed.
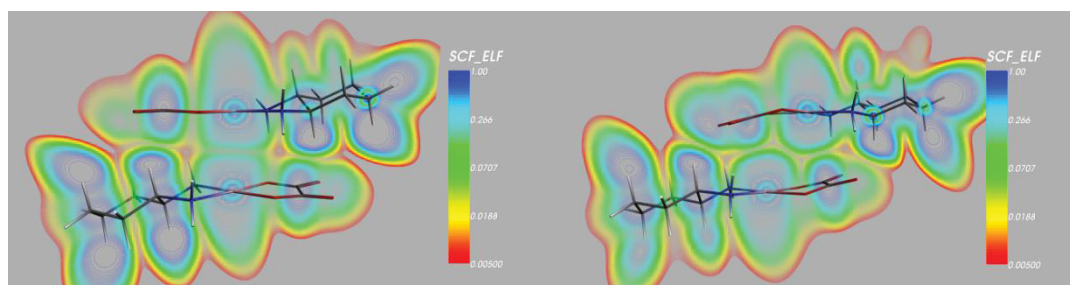
Figure 5.11. ELF for α–[**1**]$_2$ (left and β–[**1**]$_2$ (right)

In the case of both β-[**1**]$_2$ and β-[**2**]$_2$, the anchoring effect of H-bonding can be visualized by Yang's Non-Covalent Interaction (NCI) regions,[391, 392] an intuitive analysis of the electron density topology based on a strict discrimination of the reduced density gradient between covalently bonded and non-covalently interacting atoms. The red coloured isosurfaces materialize the attractive intermolecular amine-carbonyl H bonds (Figure 5.12). Important to mention is that the HOMO-LUMO energy gaps of dimers β−[**1**]$_2$ ($|\Delta E_{\text{monomer-dimer}}|$= 0.35 eV), β−[**2**]$_2$ ($|\Delta E_{\text{monomer-dimer}}|$ = 0.42 eV) and α-[**3**]$_2$ ($|\Delta E_{\text{monomer-dimer}}|$ = 0.16 eV) are only slightly different from those of the parent monomers, which mostly explains why no major changes are observed in the solution UV/Vis spectra upon dilution of concentrated solution of 1 in its supposed dimer forms, which disqualifies UV/Vis titration as a method of characterization.
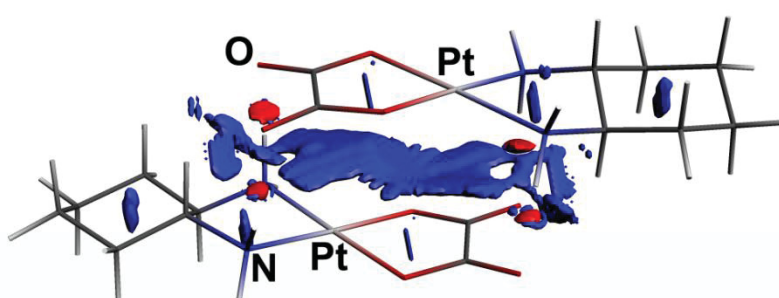
Figure 5.12. ADFview2013 plots of non-covalent interaction (NCI) regions indicated by *reduced density gradient* isosurfaces (cut-off value s= 0.02 a.u., ρ=0.05 a.u.) coloured according to the sign of the signed density $\lambda_2\rho$ (red and blue colours are associated to negatively and positively signed terms) for the gas-phase relaxed singlet ground state model of Pt-containing complexes β-[**1**]$_2$. All calculations were performed with gas phase singlet ground state optimized geometries at the ZORA-BLYP-D3/all electron TZP level. Non-covalent N-H…O bonds are indicated by attractive non-covalent red-coloured isosurfaces. Blue isorsurfaces are assigned to van der Waals interactions or to Pauli repulsion.

Comparison of the BLYP-D3(BJ) energies with those of TPSS-D3(BJ), a notoriously suitable functional for systems with transition metals,[431-433] and of wavefunction-based CCSD(T)/CBS, a "golden standard"[434] were performed on a small model of a Pt chelate dimer devoid of H-bonds of formula $[(NH_3)_2Pt(HC(O)C(O)H)]_2$.

The model system used for the estimation of the CCSD(T)/CBS limit was constructed in such a way as to conserve as much as possible the „original" β-[**1**]$_2$ system. The resulting model system shown on Figure 5.13 has retained the core of the β-[**1**]$_2$ dimer, where two metals and respective chelates are interacting. CCSD(T)/CBS calculations were not possible on the larger system due to computational limitation; the calculations on this model system being done on a supercomputer at Texas A&M at Qatar - the most demanding job lasted for 27 days. In the reduced model system there are no hydrogen bonds; however, interactions of metals with chelate rings are preserved. Our intention was to gauge the BLYP-D3 and TPSS-D3 functionals in their ability to describe NCI between metals and chelates without the interference of H- bonding, which are known to be rather well described anyway by DFT functionals. BLYP–D3(BJ) and TPSS-D3(BJ) methods showed good agreement with CCSD(T)/CBS for this small system; BLYP-D3(BJ) overestimated interaction energy by 0.4 kcal/mol, and TPSS-D3(BJ) by 0.6 kcal/mol compared to the limit estimated by CCSD(T)/CBS (-1 kcal/mol).
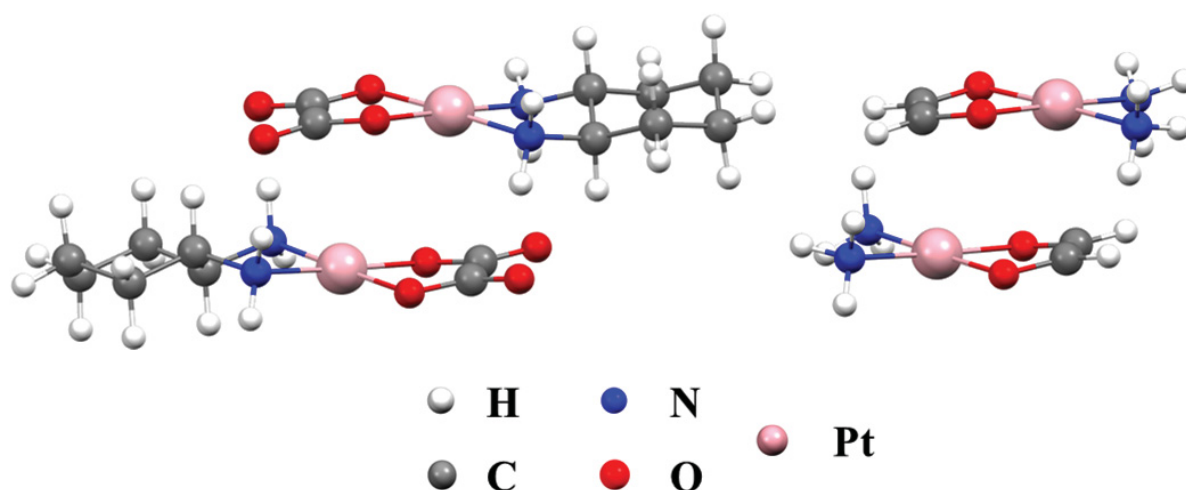
Figure 5.13. β[1]$_2$ (left); model system used for calculations at the CCSD(T)/CBS level (right)

Table 5.4. Interaction energies calculated for model system shown on Figure 5.13.

Method	ΔE_{int} (kcal/mol)
CCSD(T)/CBS	-1
BLYP-D3(0)/TZP	-3
BLYP-D3(BJ)/TZP	-1
TPSS-D3(0)/TZP	-3
TPSS-D3(BJ)/TZP	-1

This result provided stable ground for further use of computationally-light BLYP-D3 method, a conclusion consolidated by comparing the potential energy curves (PECs) computed using an BLYP-D3(0), BLYP-D3(BJ), TPSS, TPSS-D3(BJ) and the non-local density dependent version of TPSS, i.e. TPSS-NL(VV10)[435] in which the dispersion energy is computed from the electron density using the modified approach of Vydrov and van Voorhis.[436] The PECs of α and β arrangements of [**1**]$_2$ and [**2**]$_2$ were computed considering rigid fragments, which were translated along the axes defined by the M-M segment in the energy minimum (Figure 5.14).

a)   **b)**
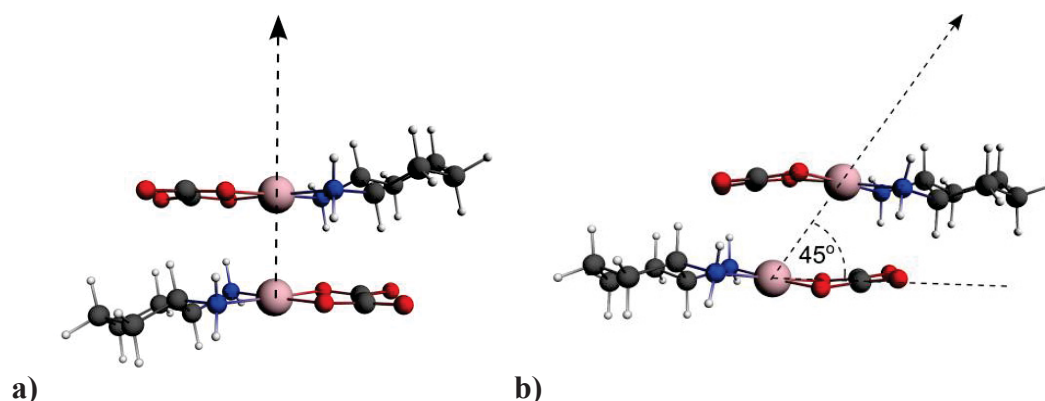
Figure 5.14. Axes along which the position of each fragment was shifted to the potential energy curves on a rigid model of [**1**]$_2$: a) excursion along the normal to the chelate's mean plane in the α configuration ; b) excursion along the axis defined by the Pt-Pt segment that forms an angle of ca. 45° with chelate's mean plane.

The PECs on Figure 5.16 were constructed by normalizing the values of interaction energies for α and β arrangements of [**1**]$_2$ and [**2**]$_2$ in order to compare the stabilization of the different arrangements depending on metal. As stated before, the most favoured is the β arrangements of [**1**]$_2$.
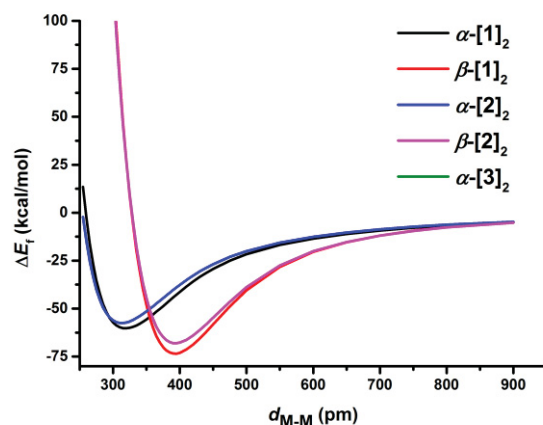
Figure 5.15. Potential energy curves (PEC) based on single point calculations using BLYP-D3(0) with ZORA/AE-TZP level of theory

As shown in Figure 5.16, BLYP-D3(0) and –D3(BJ) functionals produce PECs with minima and asymptotic behaviours very similar to that produced by TPSS-NL, the latter yielding a slightly shorter d_{M-M} value at its energy minimum.
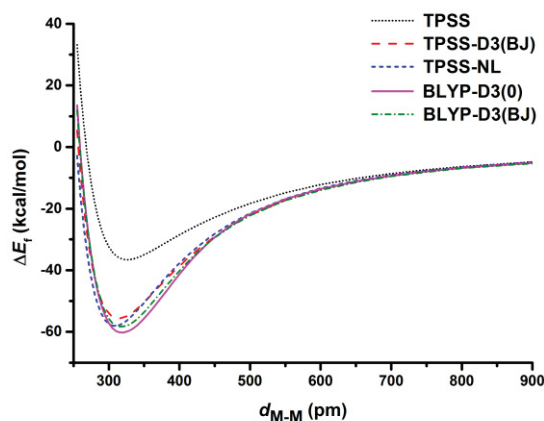
Figure 5.16. PEC for α-[1]$_2$ drawn for a selection of functionals. Computations with TPSS (native, -D3(BJ), -NL) were carried out with a def2-TZVP basis set, and BLYP-D3(0)/D3(BJ) with ZORA/AE-TZP basis set.

As can be seen, adding the dispersion energy to the standard TPSS result has a large and non-negligible effect on the interaction. Moreover, the equilibrium region is lower by around 12 kcal/mol which is about 25 % of the entire interaction even in this polar system involving hydrogen bonding as well. This, once again, demonstrates the importance of dispersion also for systems which are normally not associated with dispersion (van der Waals) type interactions. Worthy to note, the PECs produced by TPSS-D3 and the density dependent TPSS-NL dispersion model (Figure 5.16) are directly comparable regarding the dispersion

effect. As can be seen, both methods agree very well over the entire distance range which strongly supports our overall approach.

Note that this is non-trivial as the dispersion coefficients in D3 for metal atoms are computed from reference molecules (element hydrides). This approach works very well for non-metallic elements but due to larger changes in oxidation state, it may be less accurate in metallo-organic systems. Nevertheless, in this case the dispersion interactions in particular those involving the Pt atoms seem to be described well at both levels of theory. BLYP-D3 results in Figure 5.16 merely demonstrate that the functional dependence of the interaction is relatively weak and that also the choice of the damping function in D3, i.e. (0) or (BJ), is of no importance.
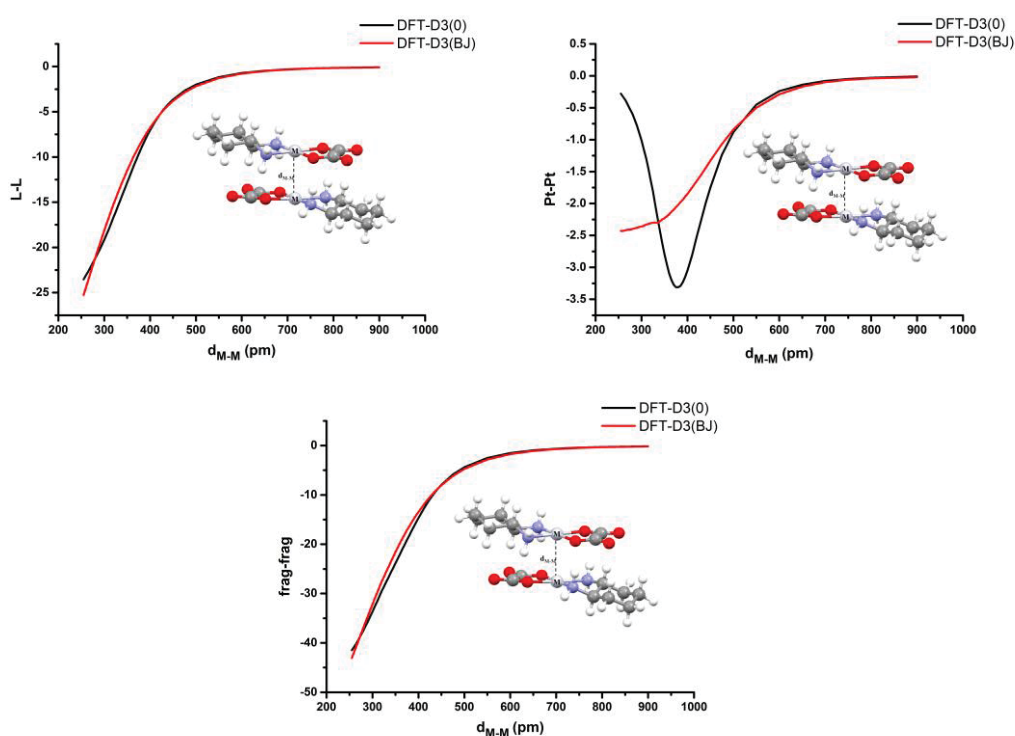
Figure 5.17. DFT-D3 calculated for α-[**1**]$_2$ geometries optimized using BLYP-D3 with (ZORA)/AE-TZP level of theory.

Interfragment dispersion interaction were analysed as follows: frag-frag (contribution for the interaction between monomers), L-L (contribution between monomers without the metals) and M-M (contribution between the metals). L-L contribution to the total dispersion is ca. 55%, and M-M only ca. 5% in the case of α–[**1**]$_2$. Similar results were obtained for the other complexes (Appendix). On the Figure 5.17 for the sake of comparison, schematically is represented the dispersion contribution with "zero-damping" and "BJ-damping".

5.4. *In solutio* DFT study of oligomerization

Modelling the polarity effect of the surrounding solvent was performed using the COSMO solvation model in a first instance. PECs of α and β arrangements (Figure 5.18) where further compared in the solvent continuum of DMSO (COSMO) as a way to discard the arrangements associated with an incorrect asymptotic behaviour.
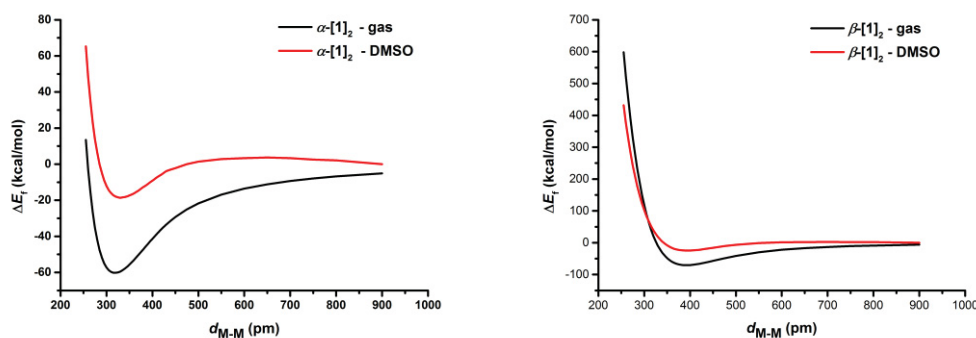
Figure 5.18. PEC for α–[**1**]$_2$ (left) and for β–[**1**]$_2$ (right) in gas phase and DMSO (COSMO)

This study, carried out with α- and β-[**1**]$_2$ revealed that the former arrangement leads to unviable dimers in DMSO, whereas the latter produced better asymptotic behaviour, suggesting persistence of the dimer in solution. Same behaviour was observed for α- and β-[**2**]$_2$ (Appendix). The effect of solvation on the Gibbs enthalpy of formation of those molecular aggregates is important. Table 5.5 lists the main thermochemical parameters for the formation of [**1**]$_2$, [**2**]$_2$ and [**1,2**]. Solvation leads to an absolute decrease of the formation Gibbs enthalpy of about 30 kcal/mol. In all the cases α arrangement leads to positive values of ΔG_f^{298} whereas the β arrangement is generally associated with negative values. The excursion of theoretical data from experimental ones is rather limited and overall acceptable given that BSSE was not accounted for in the values listed in Table 5.5. BSSE calculated by the CP method, which was computed for the (COSMO) relaxed geometries represents about 2.5 % of the computed interaction energy between the two fragments, which brings the corrected ΔG_f^{298} for β-[**2**]$_2$ into a slightly positive value and a decrease in absolute value ΔG_f^{298} for β-[**1**]$_2$. Lack of consideration for the specific interactions of water with the solute by the solvation model used here (COSMO) can also be held responsible for the observed discrepancies between theory and experiment; theory overestimating the propensity of the system to self-assemble.

Table 5.5 Calculated thermochemical parameters for various combinations of monomers, in the gas phase as well as with a COSMO solvation treatment (BSSE was not accounted for).

entry		ΔH_f^{298}	ΔS_f^{298}	ΔG_f^{298}
		kcal/mol	kcal/(K·mol)	kcal/mol
1	exptl [**1**]$_2$ (water)[a]	na[b]	na	na
2	α–[**1**]$_2$	-53.4	-0.054	-37.4
3	β–[**1**]$_2$	-63.3	-0.057	-46.5
4	β–[**1**]$_2$-(DMSO)	-20.0	-0.042	-7.4
5	α–[**1**]$_2$-(water)	-15.6	-0.060	2.2
6	β–[**1**]$_2$-(water)	-18.9	-0.037	-7.7
7	exptl [**2**]$_2$ (water)[a]	-0.5	-0.017	+4.6
8	α–[**2**]$_2$	-50.6	-0.050	-35.6
9	β–[**2**]$_2$	-56.8	-0.042	-44.0
10	β–[**2**]$_2$-(DMSO)	-17.0	-0.053	-1.3
11	β–[**2**]$_2$-(water)	-16.4	-0.051	-1.1
12	exptl [**1·2**] (water)[a]	-0.6	-0.017	+4.5
13	β–[**1·2**]	-60.2	-0.051	-45.1
14	β–[**1·2**] (water)	-18.5	-0.043	-5.6

[a] from ITC experiments. [b] not available

Further observations and conclusions on the behaviour of the Oxaliplatin *in solutio* will be presented in the following, Chapter 6.

Chapter 6

6. Inclusion complexes of organometallic compounds with CB[n] hosts

Results that will be presented here are continuation of the investigation on the behaviour of the complexes Oxaliplatin (**1)** and Oxalipalladium (**2)** *in solutio*, covered in the previous chapter. In this regard we have studied processes of inclusion of the **1** and **2** into the lipophilic cavity of **CB**[7]. Third process we considered was inclusion of the [Cp*Ir(H$_2$O)$_3$](PF$_6$)$_2$ (**4**) complex to the **CB**[7], which was part of the study on the inhibition of water oxidation catalysis. Last considered process was the result of collaboration with Dr. Wissam Iali. Here, we only consider the results of ITC titration for this process and the DFT-D calculations which are the integral part of this thesis.

6.1. Thermochemical data

With complex **1,** for which the inclusion host-guess complex, i.e. **1@CB**[7], was also crystallographically characterized, Kim et al.[325] provided some information on the thermodynamics of the inclusion process by reporting an enthalpy ΔH of -6.3 ± 0.1 kcal/mol at pH= 7.2 in the presence of TRIS buffer at 298.14 K with an association constant K of 2.3×10^5. To this value was also associated an entropy variation ΔS of +3.3 cal/(K·mol). Even though the authors did not indicate the exact concentration of TRIS in their experiments, it is very likely that it acted as a guest competing with **1** for inclusion into **CB**[7]. This introduced, in our opinion, a serious risk of underestimation of the actual affinity of **1** for the considered cavitand.

For the purpose of comparison and in order to show the influence of TRIS on the inclusion process, we performed ITC titrations of a solution of **CB**[7] in a commercially available 200 mM TRIS buffer with a solution of **2** prepared in the same TRIS buffer, as well as titrations with pure water solutions of **1** and **2** and **CB**[7].

In the Table 6.1, values for the enthalpies were obtained using several methods that are denoted by following indices in superscript: *a* - enthalpy of the process computed from the net heat released by the process corrected relative to a blank experiment consisting of an injection of complex into a solvent devoid of **CB**[7]. *b*- the numerical model applied here, i.e. MSCBS, was that of a host-guest interaction between independent molecules. *c*- the numerical model applied here was that of CR, whereby the competing process of inclusion of

TRIS is characterised by ΔH_{TRIS} constant K_2 and ΔS_{TRIS}. d- values of ΔH_{mod} and K_1 determined in pure water were entered as constants for the determination ΔH_{TRIS} and K_2.

Table 6.1. Thermochemical data extracted from isothermal titration calorimetry investigations of the reactions of **1** and **2** with **CB**[7].

compound	**1**	**1**	**2**	**2**
solvent	water	water	water	water + TRIS
T (K)	298.15	313.15	298.15	298.15
$\Delta H_{\text{raw}}{}^{a}$ (kcal/mol)	-7.8(2)	-10	-6.2(3)	-1.62(2)
ΔH_{mod} (kcal/mol)	-8.7(2)^{b}	-10.9^{b}	-6.6(5)^{b}	-6.6(5)^{c}
ΔH_{TRIS} (kcal/mol)	-	-	-	-5.0(2)
K_1	2.4(6)×10^5	9×10^5	0.7(3)×10^5	0.7(3) ×10$^{5\,d}$
K_2	-	-	-	34(6)
ΔS_{mod} (cal/(K·mol))	-4.73(5)	-7.5	0(2)	-
ΔS_{TRIS} (cal/(K·mol))				-10(1)
ΔG_{mod} (kcal/mol)	-7.3(1)	-8.5	-2.1(1)	-

Thermogram for the inclusion of **1** (20 mM) into **CB**[7] (0.7 mM) in pure water show strong exothermic signature (Figure 6.1).
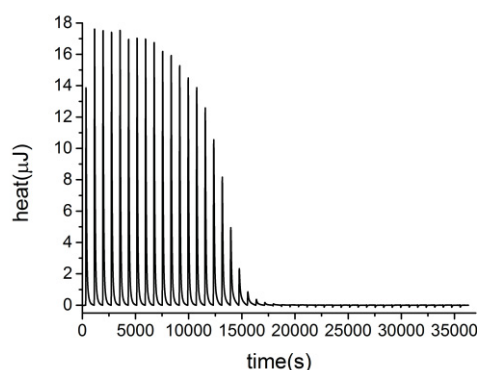
Figure 6.1. Heat released in the reaction: titration of **CB**[7] water solution with **1** complex water solution. Reaction was performed on 298.15 K. Interval between injections was 800 seconds: 1: c = 20mM injected into **CB**[7] : c = 0.7 mM. There were 45 injections (of 2.06 μl each).

Treatment of the ITC data for this process using the MSCBS model, provided an enthalpy of inclusion ΔH_{mod} of -8.7(1) kcal/mol at 298.15 K and an association constant K_1 of 2.4·10^5. Similar treatment of the data related to the inclusion of **2** (17 mM) into **CB**[7] (1 mM) in pure water afforded an enthalpy of inclusion ΔH_{mod} of -6.6(5) kcal/mol at 298.15K and an

association constant K_1 of $7 \cdot 10^4$. Thermogram for this titration can be found in Appendix.

Given the high values of the computed association constants K_1, the self-consistency of the thermochemical model was checked by calculating the raw enthalpy of association ΔH_{raw} by integrating the total molar heat release from the ITC thermograph: the resulting values of -7.8 and -6.2(3) kcal/mol for the formation of **1**@**CB**[7] and **2**@**CB**[7] respectively validated the chosen thermochemical model.

What has to be pointed out is that the experiments with TRIS-buffered solutions (200 mM) revealed the relevant interference of this amine with the inclusion process of **2** (20 mM) into **CB**[7] (1 mM). As a blind test, the above-mentioned MSCBS model was applied and a value of -1.97(6) kcal/mol for ΔH_{mod} was obtained along with a K_1 constant of $1.6(2) \cdot 10^4$. It became obvious that TRIS was playing the role of a competing guest of **CB**[7] and that the effect of its concentration in the medium had to be accounted for. Thermogram for this titration is shown on Figure 6.2).
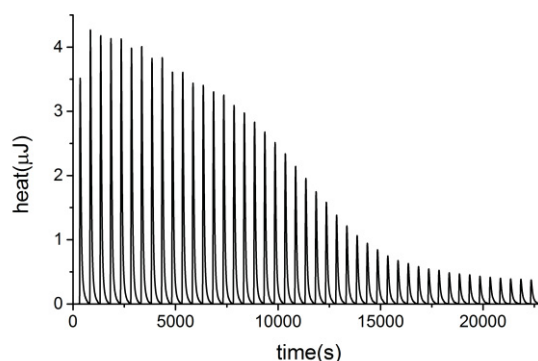
Figure 6.2. Heat released in the reaction: titration of **CB**[7] water solution in TRIS buffer (0,2 M) with water solution of complex **2** in TRIS buffer. Reaction was performed on 298.15 K. Interval between injections was 800 seconds: **2**: c = 20mM injected into **CB**[7] : c = 1mM. There were 45 injections (of 2.06 µl each).

The treatment of ITC data using the CR model, assuming TRIS as a competitor of **2** (for which the enthalpy and constant of association were previously determined) in the binding with **CB**[7], yielded an enthalpy of association of TRIS with **CB**[7], i.e ΔH_{TRIS}, of -5.0(2) kcal/mol and a value of 34(6) for the constant of association of TRIS with **CB**[7]**,** i.e K_2 (Table 6.1).

ITC titration of a 2 mM solution of **CB**[7] in pure water by a 10 mM solution of **4** produced a significant exothermic response, which was found to be largely dependent on the concentration of **CB**[7] (Appendix). The thermograph displayed in Figure 6.3 contains two important contributions that have to be considered here: the first one, on the left hand side, is the exothermic feature corresponding to the host–guest interaction, the second one is the

endothermic feature produced by the dilution of the solution of **4** into the solution of **CB**[7].
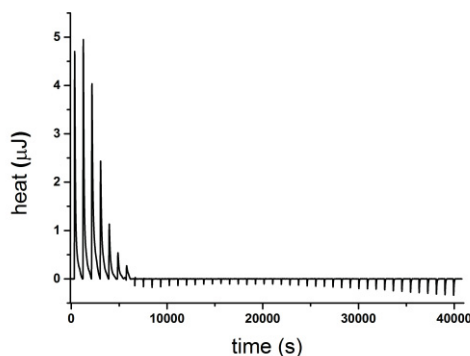
Figure 6.3. Heat released in the reaction: titration of **CB**[7] water solution with water solution of **4** complex. Reaction was performed on 298.15 K. Interval between injections was 900 seconds: **4**: c = 10mM injected into **CB**[7] : c = 2mM. There were 45 injections (of 2.06 μl each). There were 45 injections (of 2.03 μl each).

The net enthalpy of formation of the inclusion complex was approximated by subtracting the thermographic trace of the dilution of the same solution of **4** in pure water. This provided an approximate value of the enthalpy of host–guest complex formation between **CB**[7] and **4** of −3.7(7) kcal/mol at 298.15 K in water, which remains in the typical values for the non-covalent inclusion of coordination complexes within such a class of cavitands.[325] Unfortunately, the exact value of the Gibbs free enthalpy could not be determined by ITC because the impact of the variation of ionic strength during the titration on the association equilibrium constant could not be accounted for in any accurate way.

6.2.   DFT-D calculations: inclusion of 1 and 2 to CB[7]

Our computation of the thermodynamics of inclusion complexes **1** and **2** was carried out with geometries optimized with a COSMO treatment of solvation from the cartesian coordinates of Kim's first structure[325] of **1@CB**[7] which was used here to build also the model of **2@CB**[7] (Figure 6.4).
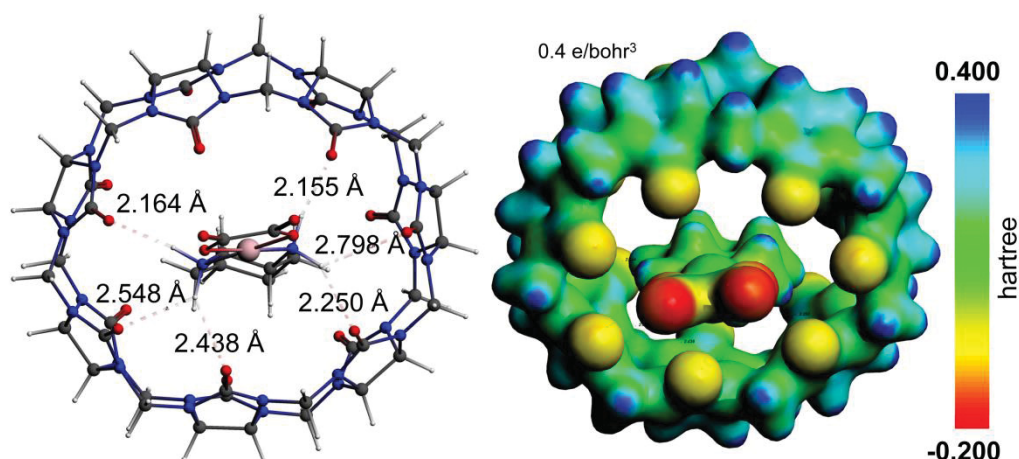
Figure 6.4. The relaxed COSMO (water) geometry of inclusion complex **2@CB**[7]: left, outline of the shortest N-H···O$_{CB[7]}$ contacts within the cucurbit[7]uril's cavity ; right, coulombic potential map drawn over an isosurface of the electron density.

Those geometries were subsequently applied a COSMO-RS treatment to determine the Gibbs free enthalpies of solvation that would yield the ΔG_{solv} parameter used to approximate the values of the Gibbs free enthalpy of formation of the inclusion complex in idealized water from monomers **1-2** and **CB**[7] by applying the following equation:

$$\Delta G_f(water) = \Delta E_g + \Delta G_{RRHO} + \Delta G_{solv} + \Delta E_{disp}^{(3)} + \Delta E_{BBSE}$$

where ΔE_g is the host-guest association energy for COSMO-relaxed geometries taken in the gas phase, ΔG_{RRHO} is the rigid rotor harmonic oscillator energy correction from gas phase energy E to free Gibbs energy G, taken for gas phase calculations, $\Delta E^{(3)}_{disp}$ is the three-body dispersion energy term and ΔE_{BSSE} is the energy correction for the so-called basis set superposition error gathers the values computed in the gas-phase and in idealized water (COSMO-RS).

In the herewith considered model of inclusion complex the role of explicit water was neglected for computational practical reasons. However this was done knowing that, particularly for aqueous solutions of **CB**[7], the inclusion of any guest within the cucurbituril is challenged by the existence, within the cavity itself, of metastable, so-called "high energy water" aggregates[437]. The latter supposedly form, according to the assumptions of Nguyen, Young and Gilson[438], a high density low-entropy water torus that only the interaction with highly hydrophobic guests can displace, provided that an energy toll of ca. 9-15 kcal is paid in the water-displacement free energy. In the case of **1** and **2**, which are both moderately

lipophilic and rather keen to establish specific interactions with bulk water, the values of affinities for **CB**[7] computed by combining DFT-D and COSMO-RS solvation model remain in reasonable agreement with experimental data, particularly if one considers that a negligible energy toll must be paid for the dissociation of portions of dimers [**1**]$_2$ and [**2**]$_2$. Considering that the theoretical ΔG value is a sum of individually large terms of opposite sign, which have been computed without any specific empiricism, the computed correct sign and right order of magnitude for ΔG seems to be a respectable result. Because the ΔH_{solv} values are indirect quantities for which the COSMO-RS model was not developed, enthalpy of solvation was not sought. Calculated thermochemical parameters for the inclusion of the 1 and 2 to CB[7] in gas phase and solution are presented in Table 6.2.

Table 6.2. Estimate of the thermochemical parameters for the inclusion of **1** and **2** into **CB**[7] in the gas-phase (ZORA-BLYP-D3/all electron TZP) and in water (COSMO geometries, treated with COSMO-RS) (energies in kcal/mol; in case of ΔS_f energy is in cal/(K·mol)).

Gas-phase	ΔE_f	ΔH_f	ΔS_f	ΔG_f^{298}	
1@CB7	−49.6	−48.9	−0.065	−29.4	
2@CB7	−48.9	−47.6	−0.058	−30.2	
COSMO-RS (water)	ΔE_g	ΔG_{RRHO}	$\Delta_\delta G_{solv}$	$\Delta E^{(3)}_{disp}$	BSSE	ΔG_f^{298}
1@CB7	-47.4	20.2	8.5	4.6	1.6	-12.3
2@CB7	-47.4	18.7	8.9	4.7	1.5	-13.6

Our approach provides an insight that differs fundamentally from another recently published report[439] in which the inclusion of cis-platin type complexes into **CB**[7] was carried out using the hybrid B3LYP functional[440] in spite of the notorious tendency of this dispersion correction-devoid hybrid functional to raise major BSSE issues.[441,442, 443]

6.3. DFT-D calculations: inclusion of 4 to CB[7]

Because all our attempts to crystallize an inclusion complex of **4** to **CB**[7] have failed, we resorted to molecular modelling to gain some understanding of the interaction between the iridium moiety and the cavitand **CB**[7]. A model system consisting of the biscation [Cp*Ir^{III}(H$_2$O)$_3$]$^{2+}$ of **4**, named here **IV**$^{2+}$, **CB**[7] and the corresponding host–guest complex **IV**@**CB**[7] $^{2+}$ was considered. The geometry of **IV**$^{2+}$ was faithfully reproduced[444] at the chosen level of theory, which offered rather reliable reproduction of H-bonding for an

acceptable computational time-strain.

Possible chelation of the Ir centre by a pair of carbonyl oxygen atoms of **CB**[7] was first considered (Figure 6.5).
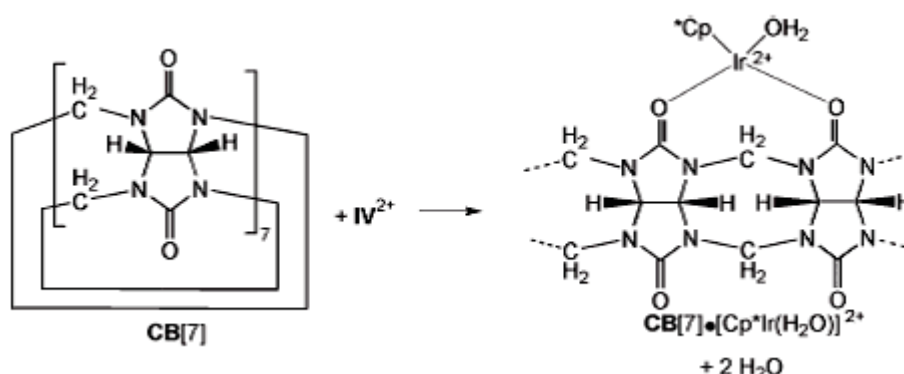
Figure 6.5. Possible mechanism of the chelation of the Ir center

The thermochemistry of this chelation reaction, that entails the release of two molecules of water from model **IV**$^{2+}$, was evaluated in the gas phase, assuming that the remaining aquo ligand at Ir was oriented towards the inner side of the cavitand to favour H-bonding stabilization. The resulting energy of formation of adduct **CB**[7]·[Cp*Ir^{III}(H$_2$O)]$^{2+}$, i.e. $\Delta E_f = -93.9$ kcal/mol, was computed from singlet ground state-relaxed geometries in the gas phase (Figure 6.6). This formation energy is significantly less favourable by ca. 33 kcal/mol than that obtained for the non-covalent inclusion of **IV**$^{2+}$ into the cavity of **CB**[7].
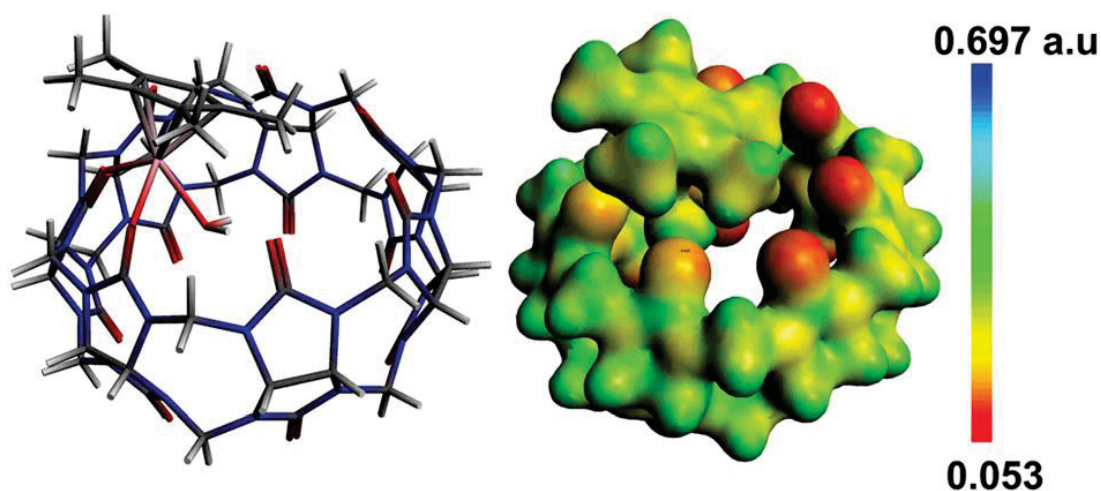
Figure 6.6. Left: Stick-representation of the singlet ground state geometry of **CB**[7]·[Cp*Ir^{III}(H$_2$O)]$^{2+}$. Right: Coulombic potential map of the latter cation drawn over an isosurface of the SCF electron density (isosurface: 0.03 e·bohr^{-3}).
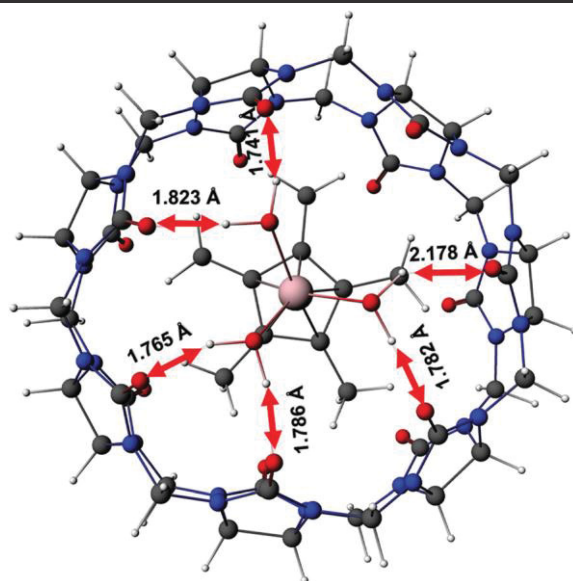
Figure 6.7. Gas phase ground state structure of inclusion complex **IV@CB**[7]$^{2+}$ computed at the (ZORA)BLYP-D3(0)/all-electron TZP level. H-bond interactions partly contribute to the stabilization of the host–guest complex; according to ETS-NOCV analysis the shortest O-H···O distances of ca. 1.75 Å are related to the most efficient H-bonding between the guest and the host.

Gas phase calculations on the ground state relaxed geometry (Figure 6.7) indicate that formation of the host–guest complex is promoted by dispersion (London force), which makes about 50% of the interaction energy (ΔE_{int} = −160.5 kcal/mol, ΔE_{disp} = −86.8 kcal/mol) between "prepared structures" of **IV**$^{2+}$ and **CB**[7] in the inclusion complex. It was found that about 79% of the attractive dispersion energy term arises from the **CB**[7] –Cp* interaction and that the remaining 21% was provided by the **CB**[7]–[Ir^{III} (H$_2$O)$_3$] interaction. This exemplifies well the stabilizing "lipophilic" character of the cucurbit[n]uril cavity, which is advantageously complemented by the two outer "crowns" of 7 oxygen atoms each that may provide further stabilisation of an inclusion complex such as **IV@CB**[7]$^{2+}$ by 5-to-6 additional H-bonds. ETS-NOCV analysis of the interaction between **IV**$^{2+}$ and **CB**[7] indicated that the strongest orbital interactions are between the terminal H atoms of the coordinated water ligands of Ir and 5 oxygen atoms located on a flank of the cavitand with individual orbital interaction energies spanning −7.4 to −5.9 kcal/mol.

The gas-phase value of the formation energy ΔE_f^{gas} = −127.5 kcal/mol (Table 6.3) for host–guest complex formation suggests a thermodynamically favoured formation of inclusion complex **IV@CB**[7]$^{2+}$ in the gas phase. However this result does not account for the effect of water solvation, which challenges the formation of the inclusion complex according to the calorimetric measurements. A more realistic value of energy may be approached addressing the issue of solvation by the use of the COSMO-RS approach.

Table 6.3. Thermodynamic data (in kcal/mol) related to the formation of inclusion complex **IV@CB[7]**$^{2+}$ and **IV@CB[7]Cl$_2$** at T = 298.15 K

Gas-phase		ΔE_f	ΔH_f	ΔG_f^{gas}
IV@CB[7]$^{2+}$		−127.5	−117.5	−96.3
COSMO-RS (water)	ΔG_{RRHO}	ΔE_f^{COSMO}	$\Delta G_{solv}^{COSMO\text{-}RS}$	ΔG_f^{water}
IV@CB[7]Cl$_2$^{a}	+23.3	−69.2	+50.1	+4.2
IV@CB[7]Cl$_2$^{b}		−85.7	+71.9	+9.5
IV@CB[7]Cl$_2$^{c}		−136.8	+121.5	+8.0

Corrections for solvation Gibbs free enthalpy were computed with COSMO-RS for geometries optimized with COSMO; $\Delta G_f^{water} = \Delta E_f^{COSMO} + \Delta G_{RRHO} + \Delta G_{solv}^{COSMO\text{-}RS}$.

However, in test calculations for multiply charged complexes we found, not unexpectedly, a degradation of accuracy due to very large solvation energies (large compensating surface charges). This problem can be solved by including counter-ions which greatly diminishes the electrostatic potential on the COSMO surface thereby reducing the solvation energies to reasonable values. By this technique good agreement between experimental and theoretical Gibbs free association enthalpies could be obtained even for a quadruply-charged porphyrine dimer complex recently.[445] The Gibbs free solvation enthalpy (G_{solv}) is the primary quantity in COSMO-RS and solvation enthalpies can only be obtained indirectly (by the temperature dependence of G_{solv}). Therefore, computed enthalpies, even when including counterions, are inaccurate and consequently not reported (Table 6.3).
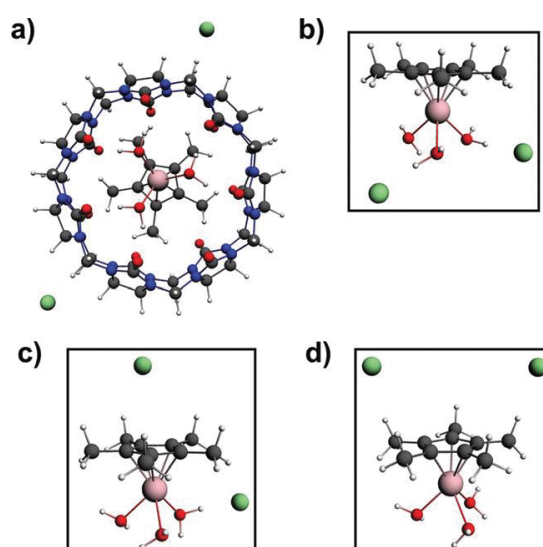
Figure 6.8. COSMO (water) geometries of **IV@CB[7]Cl$_2$** (a) and **[IV]Cl$_2$**: (b) two chlorides at aquo ligands; (c) one Cl$^-$ at an aquo ligand, one Cl$^-$ above the Cp* ligand; (d) two chlorides on the side opposite to aquo ligands. Atom colour code: dark grey, C; light grey, H; blue, N; red, O; green, Cl; pink, Ir.

To improve the accuracy of the treatment of solvation, the system was converted into a neutral version consisting of the same structures associated with two chloride atoms (mimicking the PF_6^- anion) that were located away from the aquo ligands and in areas of low charge density of local energy minima geometries. The Cl$^-$ ions indicated in the Table 6.3 by the letters in superscript correspond to the geometries defined in a following way: a – Two chlorides at aquo ligands (Figure 6.8.b), b - One chloride at the aquo ligand and one above the Cp* ligand (Figure 6.8.c), c - Two chlorides above the Cp* ligand (Figure 6.8.d).

Geometry optimizations of those neutral ion pair structures as local minima with a COSMO treatment of solvation were followed by a new treatment using the COSMO-RS platform to extract the enthalpy and Gibbs free enthalpy corrections for solvation. This treatment led to values of Gibbs free enthalpy for the formation of the host–guest complex **IV@CB**[7]Cl$_2$, that is ΔG_f (T = 298.15 K) that were found to depend greatly on the relative position of the chloride anion relative to the aquo ligands. Although the gas phase complexation energies for the three systems with different locations of the counter ions greatly vary between −69 and −137 kcal/mol, the corresponding complexation free enthalpies ΔG_f^{water} in water show only small variations. This demonstrates the accuracy of the COSMOS-RS model which compensates an unfavourable cation–chloride interaction by a corresponding better solvation Gibbs enthalpy and thus provides realistic values for ΔG_f^{water}.

Chapter 7

7. Synthesis and thermochemistry of new palladium(II) and ruthenium(II) complexes

Reactions of halogen bridge cleavage shown in Chapter 1 have proven to be chemically clean and suitable for the ITC experiments, giving clear thermochemical signature. These reactions fulfilled main objective in finding appropriate process for which accurate thermochemical data could be obtained. These data could then be subsequently used in benchmarking the latest DFT-D methods.

In this chapter, synthesis and characterization of new palladium(II) and reuthenium(II) complexes will be presented. Thermochemistry of the halogen bridge cleavage in the cyclometallated Pd(II) and Ru(II) complexes by addition of nucleophilic ligands, accompanied with the preliminary DFT calculations will be presented as well.

7.1. Synthesis

Precursors for the palladium complexes, [Pd(tBpTP)Cl]$_2$[343] and [Pd(dmba)Cl]$_2$[446] were synthesized using previously reported procedure from the literature. We have synthesized palladium complexes by following simple procedure. Schematic representation of the reaction taking place is shown on Figure 7.1.
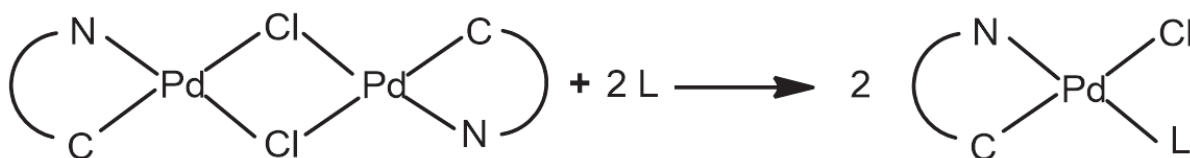
Figure 7.1. General schematic for preparation of Pd(II) complexes. L = pyridine (**Pyr**), 4-(t-butyl)pyridine (**tBPyr**), triphenylphosphine (**PPh$_3$**), tricyclohexylphosphine (**PCy$_3$**)

For the complexes made from [Pd(tBpTP)Cl]$_2$ precursor procedure was as follows. To the stirred solution of the Pd(II) dimer in chloroform, slight excess of the ligand solution in chloroform was added in drops. Opaque yellow solution of the dimer (due to low solubility in solvent) quickly changed to transparent, clear yellow colour. Stirring was continued for another 30 min to 1 hour (depending on the ligand) on room temperature. Solution was then concentrated under vacuum, and product was precipitated by addition of freshly distilled n-pentane. Dirty yellow powder was then rinsed with fresh n-pentane and dried under vacuum affording 50-90% yields. All the reactions took place under argon atmosphere.

Procedure for the complex made from [Pd(dmba)Cl]$_2$ was slightly different. Excess of 4-t-butylpyridine was added in drops to the stirred solution of the Pd dimer in dichloromethane. Stirring was continued during 4 hours on room temperature. Solution was then concentrated, and product precipitated with diethyl ether giving pale yellow-white powder. Drying under vacuum afforded 84% yield.

We have synthesized following complexes with [Pd(tBpTP)Cl]$_2$ precursor: chloro(pyridine)-[4-(t-Butyl)-2-(p-tolyl)pyridine]palladium(II) **(PD1)**, chloro(4-(t-Butyl)pyridine)-[4-(t-Butyl)-2-(p-tolyl)pyridine]palladium(II) **(PD2)**, chloro-[4-(t-Butyl)-2-(p-tolyl)pyridine]-(triphenylphosphane)palladium(II) **(PD3)**, and chloro-[4-(t-Butyl)-2-(p-tolyl)pyridine]-(tricyclohexylphosphane)palladium(II) **(PD4)**. From the [Pd(dmba)Cl]$_2$ precursor chloro(N,N-dimethylbenzylamine)(4-(t-Butyl)pyridine)palladium(II) **(PD5)** was synthesized.

PD1   **PD2**   **PD3**

PD4   **PD5**   **RU1**
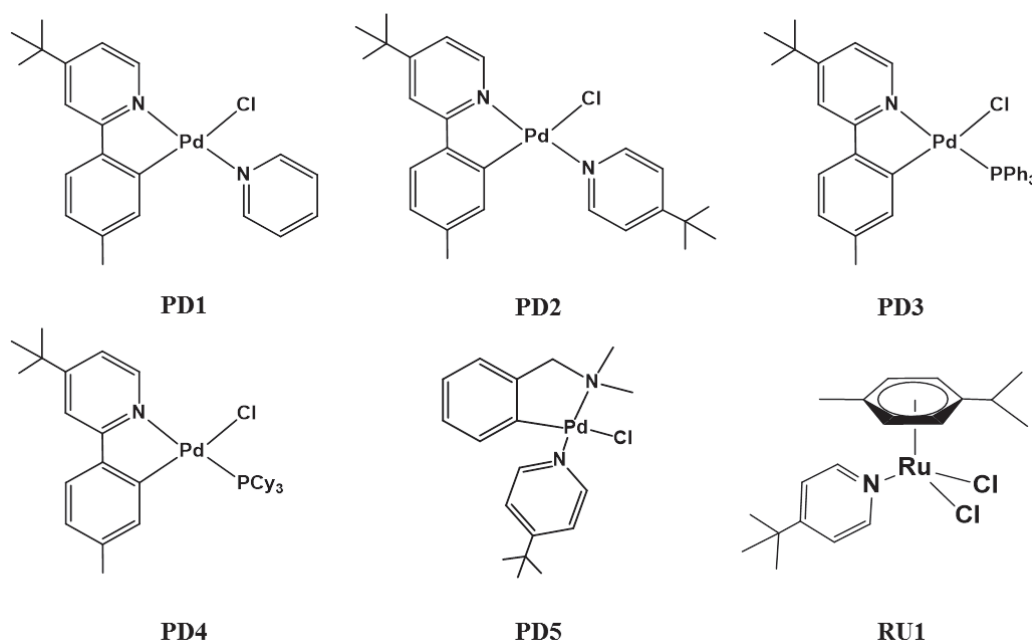
Figure 7.2. Chloro(pyridine)-[4-(t-Butyl)-2-(p-tolyl)pyridine]palladium(II) **(PD1)**, chloro-[4-(t-Butyl)-2-(p-tolyl)pyridine]-(triphenylphosphane)palladium(II) **(PD3)**, chloro(4-(t-Butyl)pyridine)-[4-(t-Butyl)-2-(p-tolyl)pyridine]palladium(II) **(PD2)** and chloro-[4-(t-Butyl)-2-(p-tolyl)pyridine]-(tricyclohexylphosphane)palladium(II) **(PD4)**, chloro(N,N-dimethylbenzylamine)(4-(t-Butyl)pyridine)palladium(II) **(PD5)**, chloro(η^6-1-isopropyl-4-methylbenzene)(4-(t-Butyl)pyridine)ruthenium(II) **(RU1)**

All synthesized complexes are soluble in common organic solvents. **PD4** complex seems to be slightly soluble in n-pentane, thus the final yield upon synthesis was smaller than for the other complexes.

We have synthesized one more complex, made from the [Ru(p-cym)Cl$_2$]$_2$ (prepared following reported procedure).[447, 448] The schematic for the reaction is shown on Figure 7.3.
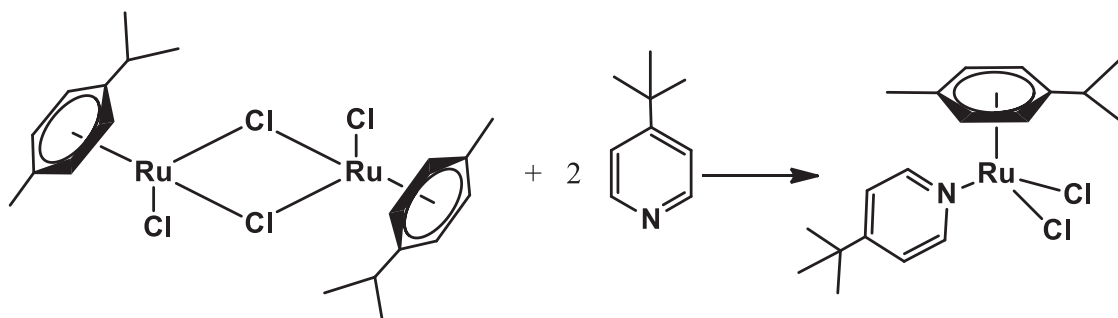
Figure 7.3. Schematic representation of the **RU1** complex synthesis

Procedure for the synthesis of this ruthenium complex is following. To the stirred solution of [Ru(p-cym)Cl$_2$]$_2$ in ethanol, 4-t-butylpyridine was added in drops. Mixture was stirred until solution became transparent, and then continued overnight. Solution was concentrated and dark orange product precipitated with n-pentane. Drying under vacuum afforded 58% yield. Complex is soluble in common organic solvents.

7.2. Spectroscopic characterization

Analysis of the ^{1}H and ^{13}C NMR spectra provided us with the analysis of the structure of complexes and validation of the mono-addition of the ligands in the above mentioned reactions. ^{1}H NMR proton chemical shifts for all synthesized compounds are summarized in the experimental section in Chapter 8. On Figure 7.4 example of the proton spectra for the complex **PD1** is shown.
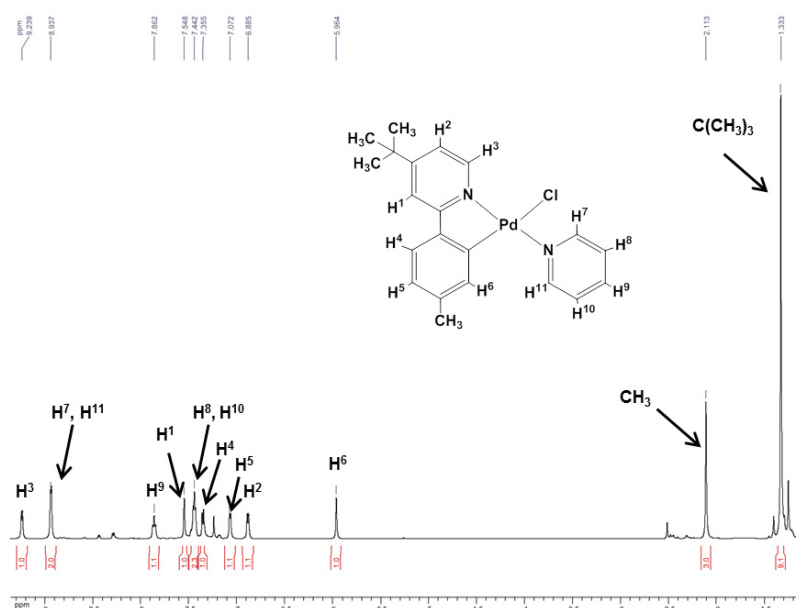
Figure 7.4. ^{1}H NMR spectra of **PD1** in CDCl$_3$

^{1}H NMR spectra of the complexes **PD1** - **PD4** in CDCl$_3$ show characteristic chemical shifts originating from singlets of methyl (1.55 - 2.28 ppm) and t-butyl (1.17 - 1.33 ppm) protons from the 4-(t-Butyl)-2-(p-tolyl)pyridine (**tBpTP**). Also, common for all of these complexes are signals originating from the six aromatic protons of the **tBpTP** appearing on chemical shifts between 5.83 - 9.47 ppm. The rest of the signals that can be observed in the spectra of the complexes belong to the protons located on the ligands (**Pyr**, **tBPyr**, **PPh$_3$** and **PCy$_3$**). The chemical shifts of these protons appear in the part of the spectra expected for the coordinated ligands. For **PD1**, three set of signals corresponding to the Pyr are observed (7.44, 8.94 and 9.28 ppm); **PD3** contain two set of signals for aromatic protons from PPh$_3$ (7.2 - 7.3 and 7.6 ppm); **PD2** shows three set of signals for **tBPyr** (1.16, 7.23 and 8.62 ppm); **PD4** have two set of signals for **PCy$_3$** (1.51-2.10 and 2.64 ppm).

^{1}H NMR spectra of the complex **PD5** in CDCl$_3$ show signals originating from the dmba: signal for two methyl groups (2.90 ppm), methylene group (3.95 ppm), and four signals from aromatic protons (6.02 - 6.96 ppm). The rest of the signals originate from the **tBPyr** ligand: singlet for t-Butyl group (1.30 ppm), and two sets of signals for aromatic protons (7.30, 8.70 ppm).

For the complex **RU1** ^{1}H NMR spectra in C$_6$D$_6$ show signals characteristic for *p*-cymene: singlet for methyl group (1.75 ppm), doublet for -CH(CH$_3$)$_2$ from *i*-propyl group (1.13 ppm), multiplet for -CH(CH$_3$)$_2$ from *i*-propyl group (3.03 ppm) and two set of signals for aromatic protons (5.63, 5.96 ppm). The remaining signals found at the spectra belong to the t-BPyr ligand: singlet for t-Butyl group (0.90 ppm), and two sets of signals for aromatic protons (6.69, 9.03 ppm).

Integration of the proton signals for all complexes provided us with conformation that only mono-addition of the ligands occurred.

In the ^{13}C NMR spectra of the **PD1** - **PD4** in CDCl$_3$, typical signals for the **tBpTP**: signal for carbon from methyl group (21.84 - 21.90 ppm), signal for -C(**C**H$_3$)$_3$ (30.37 - 30.45 ppm), signal for -**C**(CH$_3$)$_3$ (35.29 - 34.03 ppm), and the signals for aromatic carbons (114.40 - 165.03 ppm). The rest of the signals that can be observed in the spectra of the complexes originate from the carbons located on the ligands (**Pyr**, **tBPyr**, **PPh$_3$** and **PCy$_3$**). The chemical shifts appear at the expected positions for coordinated ligands. For complex **PD1** signals originate from aromatic carbons of **Pyr** ligand (125.51, 138.05, 153.33 ppm); for complex **PD3** signals are from aromatic carbons of **PPh$_3$** ligand (128.05, 130.58, 135.49 ppm); for complex **PD2** signals are from t-Butyl group and aromatic carbons of **tBuPyr** ligand (30.38,

35.22, 122.35, 152.68 ppm); for complex **PD4** originate from **PCy₃** ligand (26.47, 27.82, 30.42 ppm).

^{13}C NMR spectra of the complex **PD5** in CDCl₃ (Figure 7.5) show signals originating from the **dmba**. There are signals from two methyl carbons (52.76 ppm), signal from methylene carbon (74.17 ppm), and signals from aromatic carbons (121.76 - 149.13 ppm). The remaining signals correspond to the shift of the carbons from **tBPyr** ligand: two signals from t-Butyl group (30.49, 35.30ppm) and three signals from aromatic carbons (122.50, 153.11, 162.58 ppm).
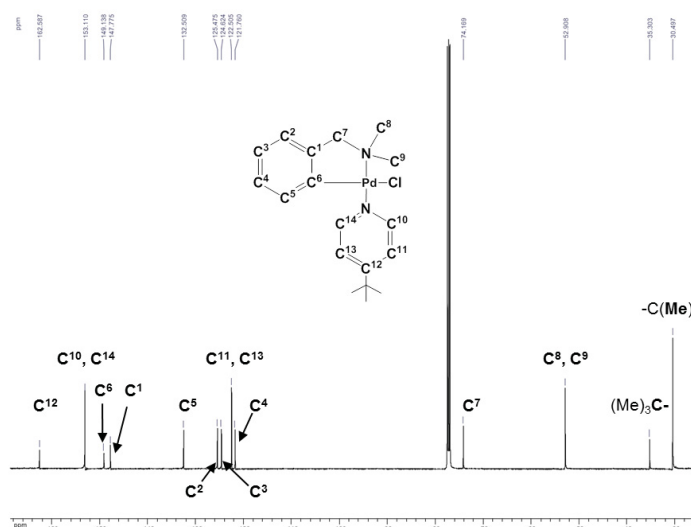
Figure 7.5. ^{13}C NMR spectra of the complex **PD5** in CDCl₃

For the complex **RU1** ^{13}C NMR spectra show characteristic chemical shifts that corresponds to the p-cymene. Signals that were observed are from methyl carbon (18.31 ppm), -CH(**C**H₃)₂ (22.32 ppm), -**C**H(CH₃)₂ (30.66 ppm), and aromatic carbons (82.37, 82.49, 96.89, 103.58 ppm). Remaining signals originate from the **tBPyr** ligand: signal from -CH(**C**H₃)₃ (30.34 ppm), -**C**H(CH₃)₃ (34.92ppm) and aromatic carbons (121.87, 154.27, 162.28 ppm).

Mass spectra of the synthesized compounds can be found in Appendix. ESI mass spectra of the **PD1** complex recorded in positive mode, show signal at 445.064 *m/z*, which originate from the [M+H]$^+$ ion. For the **PD3** signal originating from [M-Cl]$^+$ ion is found at 592.131 *m/z*; for **PD2** on 465.146 *m/z* for [M-Cl]$^+$ ion; for the **PD4** complex signal is found at 610.275 *m/z* for [M-Cl]$^+$ ion; for the **PD5** complex at 411.082 *m/z* corresponding to the [M+H]$^+$ ion; and for complex **RU1** at 442.061 *m/z* for [M+H]$^+$ ion.

7.3. X-ray structural analysis
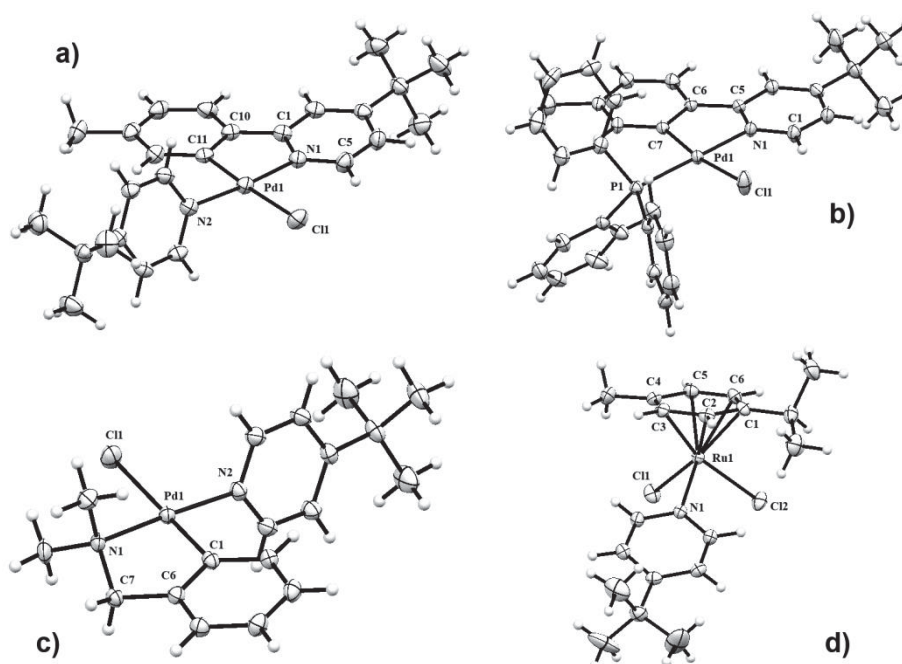
Figure 7.6. Ellipsoid-type plots of the structures (ORTEP style), of **PD2** (a), **PD3** (b), **PD5** (c) and **RU1** (d) drawn at the 50% probability level with partial atom numbering. Molecules of solvents were omitted for the sake of clarity.

Structural characterization by means of X-ray diffraction analysis was successful for complexes **PD3**, **PD2**, **PD5** and **RU1** (Figure 7.6). Crystals of sufficient quality were obtained by solvent diffusion technique from CH_2Cl_2/n-heptane binary system. Crystals were pale yellow color for **PD3**, **PD2** and **PD5** while the orange crystals were obtained for **RU1** complex. Acquisition and Refinement Data for the solved structures can be found in the Appendix. The crystal structures for said complexes were obtained thanks to the efforts of Dr. Christophe Werlé.

All the structures show mono addition of the ligand to the complex, which confirmed the conclusions made by analysis of NMR spectra. Selected geometrical parameters for all complexes are summarized in the Table 7.1 where most important distances and angles are presented.

Table 7.1. Selected distances (in Å) and angles for taken from structural X-ray diffraction analysis

Compound	Distance	Value (Å)	Angle	Value (º)
PD2	Pd1-Cl1	2.415	N1-Pd1-C11	81.78
	Pd1-N1	2.032	C1-N1-C5	118.21
	Pd1-N2	2.032	C17-N2-C21	116.32
	Pd1-C11	1.986	C1-N1-Pd1	115.14
PD3	Pd1-Cl1	2.380	N1-Pd1-C7	81.10
	Pd1-N1	2.091	C1-N1-C5	119.11
	Pd1-P1	2.262	C5-N1-Pd1	114.49
	Pd1-C7	2.019	C23-P1-C29	101.73
			C23-P1-C17	109.76
			C29-P1-C17	103.51
PD5	Pd1-Cl1	2.411	N1-Pd1-C1	82.89
	Pd1-N1	2.087	N1-C7-C6	108.94
	Pd1-N2	2.039	C14-N2-C10	117.30
	Pd1-C1	1.987	C7-N1-Pd1	106.81
RU1	Ru1-Cl1	2.412	Cl1-Ru1-N1	84.01
	Ru1-Cl2	2.417	N1-Ru1-Cl2	87.73
	Ru1-N1	2.123	Cl1-Ru1-Cl2	87.85
	Ru1-C1	2.195	C11-N1-C15	116.82
	Ru1-C2	2.178		
	Ru1-C3	2.181		
	Ru1-C4	2.204		
	Ru1-C5	2.196		
	Ru1-C6	2.179		

Complex **PD2** crystalizes in $P2_1/c$ space group, complex **PD3** in P-1 space group, complex **PD5** in P-1 space group and complex **RU1** in $C2/c$ space group. In the **PD3** complex the interatomic distance between Pd-L distance (Pd1-P1 = 2.262 Å) is slightly longer than Pd-L distance in **PD2** (Pd1-N2 = 2.032 Å), most probably due to the greater steric hindrance of the **PPh₃** compared to the **tBPyr** ligand. The Pd-Cl distance is slightly shorter for the **PD3** complex (2.380 Å) compared to the other complexes (2.411-2.417 Å), again due to the steric reasons. The angle Pd builds with the atoms of the bidentate ligand it is coordinated to, does not change much through the complexes. It remains around the value of 80º.

The geometry complex **RU1** take is so called "piano-stool", typical for large number of ruthenium(II) arene complexes, with π-bonded η^6 aromatic ring as a seat, and two chlorine and the **tBPyr** ligand as legs. The characteristic distances and angles for **RU1** are close to those of the structurally similar complex that can be found in the literature (LARHIX).[449]

Analysis of the packing in the crystal structures of the complexes showed existence of the CH-π (**PD3**, **PD2**, and **PD5**) and CH-X interactions (all complexes). The example for these interactions is shown on Figure 7.7. Detailed analysis of these interactions in the synthesized complexes falls away from the scope of this thesis, and it won't be mentioned further. Another feature noticed in the crystal structures of **PD5** complex is the stacking interaction between chelate of one complex and aromatic ring of the other complex. This arrangement is possible due to the almost planar and sterically free area on the complex around the chelate, enabling the complexes to come close and interact. Similar interactions weren't observed in the structures of other complexes, because steric crowding was too great.
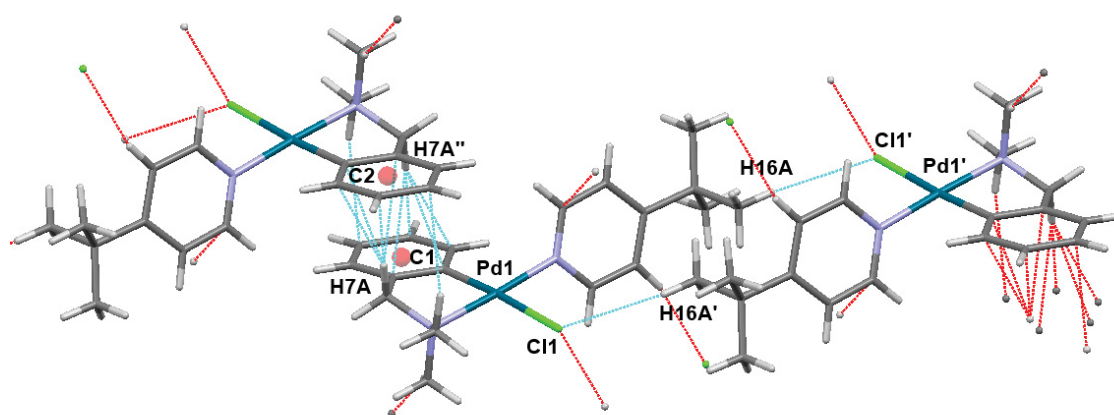
Figure 7.7. CH-π, CH-X, and stacking interactions observed in the complex **PD5**. Distances in Å: H7A···C2 2.486; H7A'···C1 2.486; Cl1···H16A' 2.877; Cl1'···H16A 2.877.

Analysis of the structural and spectroscopic data for the synthesized complexes showed evidence that the reactions presented in Figure 7.1 and Figure 7.3 indeed took place as defined, i.e. mono addition of the ligand to the complex take place. During the study on this topic, we have considered another complex as a precursor for the reaction [Cp*IrCl]$_2$. This complex exhibits the same type of nucleophilic addition of the ligand and μ-Cl bridge cleavage as in the case of Pd(II) and Ru(II) complexes. Still, test reactions with different equivalents of the **tBPyr** ligand showed formation of the mixture of mono- and di- ligand adducts, which was confirmed by ^{1}H NMR spectroscopy. This feature didn't fit in the requirements we have set for the study on the thermochemistry of the nucleophilic addition of

the selected ligands to the bridged organometallic complexes. The results of this study will be presented in following section.

7.4. Thermochemical study

The accurate data obtained by ITC experiments can provide significant help in dealing with the issue of how to make reliable thermochemical predictions for reactions involving larger transition metal complexes where intra-molecular London dispersion interactions are suspected to be essential to their stabilization.

In order to run a successful ITC experiment, and obtain meaningful results for the above mentioned reactions, certain conditions have to be fulfilled. Reactions taking place in the calorimeter have to be energetic enough that the resulting thermogram shows significant thermal signature. The reaction should be able to take place by titrating one component in the solution of the other. Stoichiometry of the reaction should be clearly defined, with the reaction taking place in one step, resulting in one product.

The reactions for the synthesis of the palladium(II) and ruthenium(II) complexes were selected because they fitted the requirements we have set. Mono addition of the ligand to the metal complex in these reactions occurred even when there was larger excess of the ligand.

The ITC experiments were conducted by titrating concentrated solutions of the ligands (**Pyr**, **tBPyr**, **PPh₃** and **PCy₃**) in chlorobenzene to the solution of the Pd/Ru dimer. Summary for the conditions and amounts of all compounds, accompanied by its corresponding thermogram can be found in the Appendix.

All the titration reactions showed significant exothermic response, with the amount of released heat depending on the ligands and complexes used. Example of thermogram for titration of the **PPh₃** ligand (c = 26.3 mM) to the solution of [Pd(**tBpTP**)Cl]$_2$ complex (c = 1 mM) in chlorobenzene is shown on Figure 7.8.
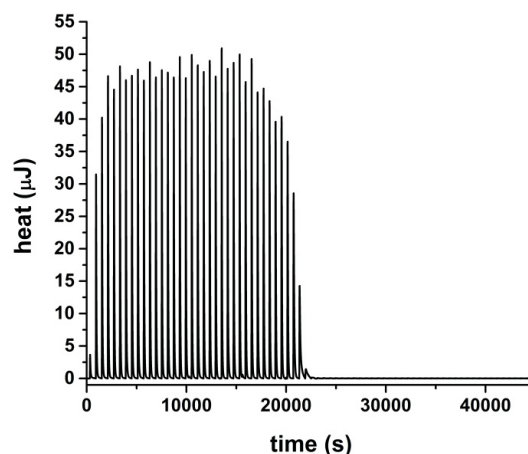
Figure 7.8. Heat released in the reaction: titration of [Pd(**tBpTP**)Cl]$_2$ solution in Chlorobenzene with Triphenylphosphine solution in Chlorobenzene. Reaction was performed on 298.15 K. Interval between injections was 600 seconds – **PPh$_3$**: c = 26.3 mM injected into [Pd(**tBpTP**)Cl]$_2$: c = 1mM. There were 90 injections (of 2 μl each).

Treatment of the data obtained by ITC afforded the values for enthalpy, Gibbs free enthalpy, entropy and constant of the reactions. Values for the enthalpies and constant of the reactions were obtained using the MSCBS numerical model. ΔG and ΔS of the reactions were subsequently calculated from the values of ΔH and K for each ITC experiment. The values for the calculated parameters that correspond to the reaction with the stoichiometry shown on Figure 7.1 are summarized in Table 7.2.

Table 7.2. Thermochemical parameters for selected reactions obtained by ITC experiments in chlorobenzene

Complex	Ligand	ΔH	K^a	ΔG	ΔS	N^{ob}
		kcal/mol		kcal/mol	$\cdot 10^{-3}$ kcal/(K·mol)	
[Pd(**tBpTP**)Cl]$_2$	**Pyr**	-12.11(7)^c	2.52(5)·10^4	-12.00(2)	-4(3)	(1$_a$)
	tBPyr	-15.4(3)	1.00(3)·10^5	-13.63(4)	-6(1)	(2$_a$)
	PPh$_3$	-24(1)	6.4(6)·10^6	-18.6(1)	-17(4)	(3$_a$)
	PCy$_3$	-25.3(3)	5(1)·10^7	-20.9(4)	-15(2)	(4$_a$)
[Pd(**dmba**)Cl]$_2$	**Pyr**	-15.1(1)	2.9(2)·10^4	-12.18(7)	-10.0(7)	(1$_b$)
	tBPyr	-20.1(2)	1.3(2)·10^5	-13.9(2)	-20.5(8)	(2$_b$)
	PPh$_3$	-26.5(3)	8(3)·10^7	-21.6(5)	-16(3)	(3$_b$)
	PCy$_3$	-32.8(4)	2(3)·10^7	-19.7(4)	-44(2)	(4$_b$)
[Ru(**p-cym**)Cl$_2$]$_2$	**Pyr**	-16.2(1)	9(2)·10^5	-16.3(2)	0(4)	(1$_c$)
	tBPyr	-19.0(7)	4(1)·10^6	-17.8(4)	-4(1)	(2$_c$)
	PPh$_3$	-28.4(3)	3.7(3)·10^7	-20.62(8)	-26(1)	(3$_c$)
	PCy$_3$	-23.3(4)	1(6)·10^8	-22.1(4)	-4(8)	(4$_c$)

^{a} The value of K were obtained by fitting for the stoichiometry of 2; ^{b} designated number for the titration reactions; ^{c} values in parenthesis are the standard errors of experimental measurements.

The values for the enthalpies and Gibbs free enthalpies show the trend of increase in value, going from reactions 1 to 4. This trend is observed in titration reactions of all three complexes.

The aim of this study was to gather the accurate experimental data that will be subsequently used as a reference to evaluate the ability of theoretical models to predict the thermochemistry of reactions involving larger transition metal complexes in solution. To this extent we have started collaboration with the group of Dr. Grimme from Mulliken Center for Theoretical Chemistry at University of Bonn, Germany. We have also performed preliminary calculations on the model systems in gas phase and using COSMO approach for treating the solvation. Since this work is still in progress, only part of the results will be presented in following section.

7.5. DFT studies

All geometry optimizations were done on the (ZORA)PBE-D3(BJ)/all electron/TZP level of theory as local minima. In the first approximation we have treated the solvation in chlorobenzene using COSMO model. The starting geometries for the optimizations were constructed from the crystal structures deposited in the Cambridge structural database (CSD), or if the exact structures were not available, they have been modelled from the similar available structures. For the ruthenium complexes we have used LARHIX,[449] HESHAP[450] and ROHPEK[451] geometries, and for palladium complexes we have constructed most probable geometries using intuition. Figures showing optimized geometries can be found in Appendix.

Since we managed to obtain crystal structures for some of the synthesized complexes, we have compared geometrical parameters of **PD2**, **PD3** and **RU1** complex with the geometries obtained by DFT-D optimizations. Comparison of the geometrical parameters is summarized in the Table 7.3.

Table 7.3. Comparison of the geometrical parameters obtained by X-ray diffraction and DFT calculations

Compound	Distance	X-ray/calc.^{a} (Å)	Angle	X-ray/calc. (º)
PD2	Pd1-Cl1	2.415/2.444	N1-Pd1-C11	81.78/81.01
	Pd1-N1	2.032/2.046	C1-N1-C5	118.21/119.19
	Pd1-N2	2.032/2.047	C17-N2-C21	116.32/118.00
	Pd1-C11	1.986/2.004	C1-N1-Pd1	115.14/115.42
PD3	Pd1-Cl1	2.380/2.434	N1-Pd1-C7	81.10/80.31
	Pd1-N1	2.091/2.110	C1-N1-C5	119.11/119.32
	Pd1-P1	2.262/2.277	C5-N1-Pd1	114.49/114.47
	Pd1-C7	2.019/2.018	C23-P1-C29	101.73/100.93
			C23-P1-C17	109.76/106.77
			C29-P1-C17	103.51/105.94
RU1	Ru1-Cl1	2.412/2.408	Cl1-Ru1-N1	84.01/85.12
	Ru1-Cl2	2.417/2.411	N1-Ru1-Cl2	87.73/85.79
	Ru1-N1	2.123/2.118	Cl1-Ru1-Cl2	87.85/88.98
	Ru1-C1	2.195/2.232	C11-N1-C15	116.82/117.72
	Ru1-C2	2.178/2.181		
	Ru1-C3	2.181/2.199		
	Ru1-C4	2.204/2.232		
	Ru1-C5	2.196/2.215		
	Ru1-C6	2.179/2.200		

^{a} geometries were optimized in gas phase using PBE-D3(BJ)/TZP level of theory

As can be seen from the Table 7.3, geometric parameters obtained by calculations don't differ very much from the geometrical parameters in crystal structures. The enthalpies, Gibbs free enthalpies and entropies of formation were calculated in gas phase and in chlorobenzene by using COSMO model. Results are summarized in the Table 7.4.

Table 7.4. Thermochemical parameters obtained by gas-phase[a] and COSMO[b] calculations on PBE-D3(BJ)/TZP level of theory

Compound	T	ΔH_f	ΔS_f	ΔG_f
	K	kcal/mol	$\cdot 10^{-2}$ kcal/molK	kcal/mol
[Pd(**tBPyr**)(**tBpTP**)Cl][a]	298.15	-47.6	-5.9	-30.1
[Pd(**PPh₃**)(**tBpTP**)Cl][a]	298.15	-37.2	-5.8	-19.9
[Pd(**PCy₃**)(**tBpTP**)Cl][a]	298.15	-46.7	-4.9	-32.1
[Ru(**p-cym**)(**Pyr**)Cl₂][a]	298.15	-14.5	-4.1	-2.1
[Ru(**p-cym**)(**Pyr**)Cl₂] (PhCl)[b]	298.15	-23.7	-4.8	-9.5
[Ru(**p-cym**)(**PPh₃**)Cl₂][a]	298.15	-44.8	-6.0	-26.9
[Ru(**p-cym**)(**PPh₃**)Cl₂] (PhCl)[b]	298.15	-42.9	-5.3	-27.2

The thermochemical parameters obtained by our calculations cannot be directly compared to the parameters obtained by ITC experiments. The solvation model used in the calculations is not sufficient to reproduce the experimental results. As was shown in previous chapters, COSMO-RS have proved to be good model for treatment of small organometallic complexes in solution. But, even this model is not successful in prediction of the thermochemical parameters in the reactions involving larger transition metal complexes with significant dispersion interactions. As a step in this direction we have provided the geometries optimized by COSMO to Dr Grimme, who used some of them in developing the benchmark set for latest dispersion corrected DFT-D3 and local CCSD(T)[452, 453] methods and the treatment of solvation using COSMO-RS and SMD[454] continuum solvation models.

The ITC measurements in solution revealed that the reaction with R=Cy ($\Delta H = -25.3$ kcal/mol) is slightly more exothermic than that with R=Ph ($\Delta H = -23.6$ kcal/mol). This is in agreement with chemical intuition since PCy₃ is a stronger Lewis base than PPh₃. Moreover, there is no strong steric cluttering around the palladium center and thus it is easily accessible for both ligands. The measured reaction enthalpies are, however, not directly comparable to results from a standard calculation since the single point energies (SPEs) of the molecules in question represent pure electronic energies in the gas phase at 0 K. Hence, solvent and ro-vibrational effects as well as their temperature dependence have to be properly taken into account.

Calculating reaction enthalpies from reaction energies, seemingly the most straightforward way of comparing the experimental and calculated values, is not advisable

since continuum solvation models are usually parametrized for the description of Gibbs free energies and not for enthalpies. Hence, a different approach was used, based on 'backcorrection' of the Gibbs free reaction energies to pure electronic energies (Eq. 7.1) which then can be directly compared to calculated reaction energies. In this scheme, the thermo-statistical (ro-vibrational) corrections from energy to Gibbs free energy (ΔG^T_{RRHO}) are calculated from analytic PBE-D3(BJ)/def2-TZVP frequencies within a modified RRHO approximation to avoid large errors for low-frequency modes.[369] The Gibbs free solvation energy contributions ($\Delta G^T_{solv}(X)$) are determined using two different continuum solvation models (COSMO-RS and SMD) for the solvent X=PhCl (at T = 298.15 K).

$$\Delta E(exp., gas) \approx \Delta E(exp., X) - \Delta G^T_{RHHO} - \Delta G^T_{solv}(X) \qquad \text{eq 7.1}$$

ΔE(exptl.,gas) denotes the zero-point-vibrational exclusive 'experimental' reaction energy for the isolated molecules. Since this 'back-correction' scheme is based on Gibbs free energies, the measured reaction enthalpies had to be converted to Gibbs free energies by applying a fitting procedure (as mentioned above).
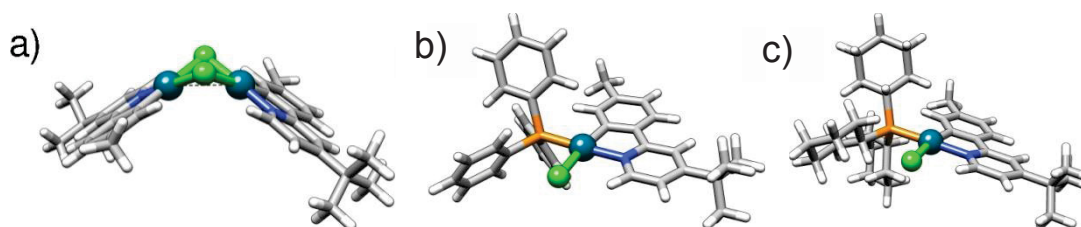
Figure 7.9. Optimized structures (PBE-D3(BJ)/def2-TZVP of a) the investigated dipalladium complex (**P1**), b) the adduct with the PPh$_3$ ligand (**P2a**), and c) the product with the PCy$_3$ ligand (**P2b**). Color code: green Cl, blue N, emerald Pd, grey C, white H.

The theoretical corrections (as the single point energies itself) also depend on how well the optimized structures represent the actual geometries of the molecules in solution. The dimer **P1** in the solvent cavity as well as in the gas phase is not planar but shows a slightly folded C$_2$ symmetric structure. The geometry optimizations were performed at the PBE-D3(BJ)/def2-TZVP level and for comparison also with plain PBE and the same basis set. While the structures of the ligands and monopalladium complexes **P2a** and **P2b** do not change significantly due to the dispersion correction, the Pd-Pd distance in the dimer **P1** is shortened due to dispersion by about 5% from 3.32 Å to 3.14 Å. Furthermore, the ligand moieties are folded stronger in the PBE-D3(BJ) structure (the closest C-N distance between

Table 7.5. 'Back-corrected' experimental reference values in kcal/mol.

	R = Ph	R = Cy
$\Delta G(exp., \text{PhCl})$ (fitted ITC values)	−18.6	−20.9
$\Delta E(exp., gas)$ ($E \to G$ (COSMO-RS, PhCl))	−30.8	−36.1
$\Delta E(exp., gas)$ ($E \to G$ (SMD, PhCl))	−32.5	−37.9
$\Delta E(exptl.\ reference)$ (best estimate)	−32 ±3	−36 ±3

In the case of metals, the electron density around the metal atom in these model systems will be larger than it is the case for typical organometallic compounds. This leads to too large C_6 coefficients and to a systematic overestimation of the related dispersion energy. However, it is not well known how large this physical effect in typical organometallic compounds is and how well it is described by e.g. density based dispersion correction schemes like VV10. Due to the importance of dispersion forces in the Pd complexes discussed in this work, new C_6 coefficients were calculated based on model hydrides with a net charge of +1.

Table 7.6. Coordination number (CN) dependent C_6 coefficients (in atomic units) for homogeneous atom pairs. The C_6(Pd-Pd) coefficients refer to London dispersion interactions between two Pd atoms with the same coordination number. The difference between D3 and D3M+ concerning the coordination numbers results from the use of different hydride compounds.

	CN	C_6(Pd-Pd)	CN	C_6(Pd-Pd)	CN	C_6(Pd-Pd)
D3	0	608.5	1.863	287.0	5.710	265.9
D3M+	0	67.5	1.618	133.1	2.945	99.7

For the free atom (CN = 0), the neutral and ionic values of the C_6 (Pd-Pd) differ by about an order of magnitude and thus already much less than for alkaline metals. For more realistic coordinations typically found in molecules, the neutral and ionic coefficients differ even less (only by a factor of two to three, compare 5th column in Table 7.6). It shall be pointed out that only the C_6 coefficients of atom pairs containing Pd are modified here, i.e. the dispersion forces between e.g. two carbon atoms remain identical in D3 and D3M+ and the same BJ damping scheme is applied. However, from the results given in Table 7.6 a sizeable effect on computed reaction energies is expected when the overall change of the dispersion energy is large and the metal atom(s) contribute significantly to the latter.

Since the investigated reactions differ only by the phosphane ligand used to quench the dimer (**P1**), the difference of their reaction energies ($\approx$ 10%) is rather small. Hence, it

poses a challenging test case for computational thermochemistry as consistency for varying ligands can be extremely important in practice. Investigation of two similar reactions also provides an internal consistency check of our theoretical procedures.

Both reaction energies are predicted qualitatively wrong at the HF level which is expected since the reactions are driven by electron correlation and in particular, long-range London dispersion interactions as discussed above. Hence, not surprisingly, DFT methods without dispersion correction are also not able to reproduce the experimental reference values. All tested uncorrected DFT functionals underestimate the reaction energies although the ligand effect is predicted correctly.

Comparing the (meta-)GGA functionals TPSS and PBE with the hybrid-(meta) functionals PBE0, PW6B95 and B3LYP there is no systematic improvement visible and the latter even shows the largest deviations of 17.2 kcal/mol and 20.3 kcal/mol for R=Ph and R=Cy, respectively. Although the medium-range NCI energy is already included in the highly parameterized M06-2X and M06 functionals by construction, they still underbind due to the missing long-range part. The better performance of the latter agrees with the recommendation by Zhao and Truhlar that M06 is fitted for systems involving both NCI and transition metals while the M06-2X functional was proposed to be accurate for aromatic stacking interactions of main group chemistry.[455] A similar observation is made for the double hybrid B2PLYP which includes nonlocal correlation through its scaled MP2 contribution. Since the latter is strongly overestimated for the investigated reactions the underbinding of B2PLYP is less pronounced. The long-range London dispersion interaction is, however, missing in all functionals and fortuitous agreement with the experimental reference values would be just a matter of uncontrollable error cancellation.

The atom-pairwise D3 dispersion correction (with Becke-Johnson damping) corrects for a large part of the error. It yields a sizeable contribution to the reaction energies and for TPSS and B3LYP the D3 contribution is even larger than that of the functional itself (e.g. −30.5 kcal/mol for R=Cy with B3LYP). The TPSS-D3(BJ), PBE-D3(BJ), PBE0-D3(BJ), B3LYP-D3(BJ), and B2PLYP-D3(BJ) reaction energies differ much less from each other than for the plain functional which is a very positive result. The values are all too large (about 5-7 kcal/mol) but the R=Ph reaction is still correctly predicted as being less exothermic. Besides the intrinsic errors of the functionals, the overbinding on the product side (which involves the larger dispersion energy) also indicates a slight overshooting of the D3 correction. The PW6B95-D3(BJ) results, however, are already within the error bars of the experimental

reference values thus indicating that this functional shows clearly smaller errors for the investigated molecules and that the overestimation of the D3 dispersion energy is only a small part of the remaining error for the other functionals. The M06 and M06-2X energies can be improved by adding the missing long-range part of the dispersion energy via a D3 correction with 'zero'-damping to avoid double counting of medium-range contributions (D3(0)) and only after correcting for this missing physics, the reaction energies are approaching the experimental reference value for the right reason, at least with the M06 functional.

As discussed above the slight overestimation of the D3 correction can be attributed to the too large C_6 coefficients of the Pd atoms. The new C_6 coefficients (denoted D3M+) based on positively charged model systems are assumed to be more appropriate to describe the partially positive charged metal in the complexes. This is proven by the systematic improvement of all DFT results with D3M+ correction compared to the D3 results. The overestimation of the reaction energies is reduced by up to 10 % (3.1 kcal/mol for R=Cy with B3LYP) and consequently all tested DFT functionals combined with D3M+ deviate by less than 5 kcal/mol from the experimental reaction energies. Moreover, the PW6B95-D3M+(BJ) results perfectly agree with the experimental reference (similar for M06-D3M+(0)). Only the B2PLYP-D3M+(BJ) reaction energy for R=Ph is still too large by ca. 6 kcal/mol but this can be attributed to the strong overestimation of the MP2 correlation energy for molecules with significant p-p interactions and potentially also to problems associated with perturbation theory applied to metal containing systems. Although scaled down in double hybrids, these MP2 related errors directly show up in the B2PLYP results and deteriorate the usually superior performance of double hybrid functionals in this case. As a check for D3M+, the non-local van der Waals functional approach by Vydrov and van Voorhis (VV10[104], DFT-NL[105]) was employed for PBE, PBE0, and B3LYP. The results obtained with the density dependent dispersion correction are in good agreement with the D3M+ results thus indicating that the new C_6 coefficients for the palladium atoms are physically sound. This argument can be reversed by stating that the local dipole polarizability model in VV10 seems to reflect the change in the electronic environment in the reaction quite well. Moreover, the B3LYP-NL reaction energies are within the error bound of the experimental reference.

Adding dispersion contributions to the plain HF reaction energies via the D3M+ method leads to remarkably accurate results which are within the error bars of the experimental reference values and only the energetic difference between the two reactions is predicted slightly too large.

This again emphasizes that the investigated reactions are driven by London dispersion interactions which can be accurately estimated by the atom-pairwise correction scheme. Notably, the D3M+ contributions for the HF method (−36.6 kcal/mol and −41.9 kcal/mol for R=Ph and R=Cy, respectively) are even larger than the reaction energies itself.

Besides the already discussed basis set and metal related issues, the MP2 method and to a much lesser extent, SCS-MP2, suffer from strong overestimation of π-π and CH-π dispersion interactions[456] which is most evident for the monopalladium complex 2a. Consequently, the R=Ph reaction energy is spuriously identical to that of the R=Cy reaction and about 20 kcal/mol too exothermic. Notably, SCS-MP2 reduces the overbinding by 13 kcal/mol compared to standard MP2 but the difference between the two ligands is still not described correctly. Obviously, correlated methods beyond MP2 such as the 'gold standard' CCSD(T) are mandatory in this case to get accurate results with WFT methods but their unfavourable scaling of the computational demands with system size necessitates further approximations. One promising approach in this direction is the recently published DLPNO scheme which allows CCSD(T) calculations of larger molecules with only minor loss of accuracy.[457] The DLPNO-CCSD(T) reaction energies are slightly too large if the default value for the pair cut-off ($T_{CutPairs} = 10^{-4}$ Eh) is applied. Tightening this threshold by one order of magnitude, however, yields reaction energies which are in excellent agreement with the experimental reference values. A closer inspection reveals that the difference of the reaction energy obtained with the two threshold values is significantly larger for R=Ph (4.2 kcal/mol) than for R=Cy (2.9 kcal/mol) which furthermore underlines that the reaction with the PPh3 ligand is more problematic for MP2.

Chapter 8

8. Experimental part

8.1. General

Experiments were carried out under an argon atmosphere using a vacuum line using standard Schlenk techniques. Pure water was obtained by reverse osmosis using a Millipore RiOs-v5 water purification system. Deuterated solvents were dried over sodium or CaH_2 and purified by trap-to-trap techniques, degassed by freeze-pump-thaw cycles and stored under argon. Diethyl ether and pentane were distilled over sodium/benzophenone, dichloromethane and acetonitrile over calcium hydride and methanol and ethanol over magnesium under argon immediately before use. Chromatography columns were carried out on Merk aluminium oxide 90 standardized.

8.2. Materials

Oxaliplatin (**1**) and Carboplatin (**3**) were purchased from TCI Europe, and were used as received without further purification. Compound **2**,[426, 458] cucurbit[7]uril (**CB**[7]),[459] [Rh(COD)Cl]$_2$,[460] [Pd(tBpTP)Cl]$_2$,[343] [Pd(dmba)Cl]$_2$,[446] [Ru(p-cym)Cl$_2$]$_2$[447, 448] were prepared and purified according to the literature procedures.

8.3. Analytical instruments

The NMR spectra were obtained at room temperature on Brucker spectrometers. ^{1}H NMR spectra were recorded at 300.13 MHz (AC-300), 400.13 MHz (AM-400), 500.13 MHz (AM-500) and referenced to SiMe$_4$. ^{13}C{^{1}H} NMR spectra were recorded at 75.48 MHz (AC-300) or 100.62 MHz (AC-400) and referenced to SiMe$_4$. The chemical shifts are referenced to the residual solvent peak. Chemical shifts (δ) and coupling constants (J) are expressed in ppm and Hz respectively. Multiplicity: s = singlet, d = doublet, t = triplet, q = quadruplet, sept = septuplet, m = multiplet.

The infra-red spectra powdered amorphous samples were recorded on an alpha ATR spectrometer from Brucker Optics and analysed with OPUS software. UV/Vis spectra

(absorption spectroscopy) were recorded with a Kontron Instruments UVIKON 860 spectrometer at RT. Circular dichroism absorption spectropolarimetry was carried out with a UV−visible Jasco J-810 CD spectrometer using a 0.1 mm optical path quartz cell at 20.0 ± 0.1 °C. The determination of specific rotations [α] was performed with a Perkin-Elmer 341 polarimeter at 589 nm (Na) using a thermostatted (20.0 ± 0.1 °C) 10 cm optical path quartz cell.

Measures of self-diffusion coefficients were performed on a BRUKER 600 MHz spectrometer - Avance III, equipped with a high strength z gradient probe DOTY Scientific. Diffusion NMR data were acquired using a Stimulated Echo pulse sequence with bipolar z gradients. DOSY spectra were generated by the DOSY module of the software NMRNotebook, using Inverse Laplace Transform (ILT) driven by maximum entropy, to build the diffusion dimension.

All ITC measures were carried out with a Waters-SAS nanoITC device equipped with two stainless steel hastealloy cells of 1 mL volume each. All aqueous solutions were prepared by sonication of suspensions of the complexes in pure water and were thoroughly degassed under reduced pressure. Organic solvents were freshly distilled and subsequently degassed prior to the use.

ESI-MS experiments were performed on a Bruker Daltonik GmgH (Bremen, Germany) microTOF spectrometer equipped with an orthogonal electrospray (ESI) interface. Calibration was performed using Tuning mix (Agilent Technologies). Sample solutions were introduced into the spectrometer source with a syringe pump (Harvard type 55 1111: Harvard Apparatus Inc., South Natick, MA, USA) with a flow rate of 5 $\mu L^{.}min^{-1}$. An external multi-point calibration was carried out before each measurement using the singly charged peaks of a standard peptide mixture (0.4 μM, in water acidified with 1% HCOOH). Scan accumulation and data processing were performed with FlexAnalysis 3.0 software. α-Cyano-4-hydroxy-cinnamic acid (CHCA) was obtained from Sigma (St Louis, MO, USA), 1,8,9-anthracenetriol (dithranol) from Alfa Aesar (Karlsruhe, Germany). Matrix solutions were freshly prepared: CHCA was dissolved to saturation in a $H_2O/CH_3CN/HCOOH$ solution and dithranol to saturation in THF. Typically, a 1/1 mixture of the sample solution in CH_2Cl_2 was mixed with the matrix solution and 0.5 μL of the resulting mixture was deposited on the stainless steel plate. MALDI-TOF mass spectra were acquired on a time-of-flight mass spectrometer equipped with a nitrogen laser.

Reflections were collected with a Nonius KappaCCD and with an APEX diffractometers equipped with an Oxford Cryosystem liquid N_2 device, using Mo K_α radiation

(λ =0.71073 Å). The crystal-detector distance was 38 mm. The cell parameters were determined (APEX2 software[461]) from reflections taken from three sets of 12 frames, each at 10 s exposure. The structures were solved by direct methods using the program SHELXS-97.[462] The refinement and all further calculations were carried out using SHELXL-97.[463] The crystal structures acquired with the Nonius Kappa CCD were solved using SIR-97[464] and refined with SHELXL-97.[463] The refinement and all further calculations were carried out using SHELXL-97. The H-atoms were included in calculated positions and treated as riding atoms using SHELXL default parameters. The non-H atoms were refined anisotropically, using weighted full-matrix least-squares on F2. A semiempirical absorption correction was applied using SADABS in APEX2.

8.4. Synthesis and characterization

8.4.1. Rhodium complexes

RH1: Tetrakis(S-(-)-1-phenylethylisocyanide)rhodium(I) chloride

[Rh(COD)Cl]$_2$ (0.49 g, 1 mmol), was dissolved in freshly distilled toluene (20 ml) in a Schlenk tube under argon. While stirring, ligand S-PEI (1 ml, 8 mmol) was added slowly. After 1 h, distilled n-pentane was added in excess to precipitate the product. Solution was removed, and resulting solid washed couple of times with n-pentane, and then dried under vacuum. During drying, green solid changed the colour to purple. (1.21 g, 91 %)

Calculated for $C_{36}H_{36}N_4RhCl \cdot 1/10C_5H_{12} \cdot 1/2CH_2Cl_2$: C 62.35; H 5.40; N 7.86; found: C 62.35; H 5.68; N 7.68

ESI–MS (m/z): calc for $C_{36}H_{36}N_4Rh^+$ 627.199; found: 627.201 [M]$^+$

IR (cm^{-1}): 2211 (medium, v N≡C), 2163 (strong, v N≡C); [α]$_{589nm, 20°C}$ = -10.85 (1.3 mM, CH$_2$Cl$_2$)

^{1}H NMR (500 MHz, CDCl$_3$): δ 7.34 (m, 5 H), 5.29 (dd, 1 H, J = 13.4 Hz, 6.6 Hz), 1.7 (d, 3 H, J = 6.8 Hz)

^{13}C{^{1}H}-NMR (400 MHz, CDCl$_3$): δ = 138.3, 137.5, 129.2 (2C), 128.8, 125.5 (2C), 56.7, 24.6

NEI: S-(-)-1-(1-Naphthyl)ethylisocyanide

S-(-)-1-(1-Naphthyl)ethylisocyanide (3 g, 17.5 mmol) was placed in round bottom flask with three necks equipped with stirring bar, thermometer and condenser. Excess of distilled CHCl$_3$

(4.2 ml), tetrabuthyl ammonium chloride (0.22 g, 0.8 mmol) and distilled CH_2Cl_2 (50 ml) were then added to the flask with the amine, and the mixture stirred vigorously. NaOH in water (50 % : 50 %, 10.7 g) was then slowly added in portions to the stirring mixture resulting in exothermic reaction. When total amount of $NaOH/H_2O$ was added, mixture was heated to ca. 50 ºC during 3 h. After that time, mixture was allowed to cool, and water (100 ml) was added to the flask. Organic phase was extracted, washed with brine, dried over $MgSO_4$, and filtered through Celite. Solvents were then removed under vacuum and resulting brown oil purified by column chromatography. (1.2 g, 38 %)

IR (cm^{-1}): 2137 (strong, v N≡C); $[\alpha]_{589nm,\ 25ºC}$ = -44.24 (6.1 mM, CH_2Cl_2)

ESI–MS (m/z): calc for $C_{13}H_{11}NNa^+$: 204.08, found: 204.08 [M+Na]$^+$

^{1}H NMR (300 MHz, CDCl$_3$): δ 7.83-7.95 (m, 3 H), 7.75 (d, 1H, J=7.3 Hz), 7.49-7.62 (m, 3 H), 5.59 (m, 1 H), 1.85 (dt, 3 H, J = 6.8 Hz, 2.1 Hz)

^{13}C{^{1}H}-NMR (500 MHz, CDCl$_3$): δ = 156.8, 133.8, 129.3 (2C), 129.1, 126.8, 126.0, 125.5, 123.1, 121.9, 51.0, 24.2

RH2: Tetrakis(*S*-(-)-1-(1-Naphthyl)ethylisocyanide)rhodium(I) chloride

[Rh(COD)Cl]$_2$ (0.51 g, 1.03 mmol), was dissolved in freshly distilled toluene (20 ml) in a Schlenk tube under argon. While stirring, ligand *S*-PEI (1.5 g, 8.3 mmol) was added slowly. After 3 h, distilled n-pentane was added in excess to precipitate the product. Solution was removed, and resulting solid washed couple of times with n-pentane, and then dried under vacuum resulting in dark purple solid. Product was recrystallized from CHCl$_3$/n-pentane. (1.51 g, 84 %)

Calculated for $C_{52}H_{44}N_4RhCl·CHCl_3$: C 64.78; H 4.62; N 5.70; found: C 64.88; H 4.75; N 6.02

ESI–MS (m/z): calc for $C_{52}H_{44}N_4Rh^+$: 827.26, found: 827.45 [M]$^+$

IR (cm^{-1}): 2192 (medium, v N≡C), 2139 (strong, v N≡C); $[\alpha]_{589nm,\ 25ºC}$ = +66.29 (1 mM, CH_2Cl_2)

^{1}H NMR (500 MHz, CDCl$_3$) : δ 7.69-7.88 (m, 11 H), 7.35-7.60 (m, 10 H), 5.69 (dd, 2 H, J = 13.4 Hz, 6.7 Hz), 5.42 (dd, 1 H, J = 13.4 Hz, 6.7 Hz), 1.82 (d, 6 H, J = 6.7 Hz), 1.59 (d, 6 H, J = 6.7 Hz)

^{13}C{^{1}H}-NMR (500 MHz, CDCl$_3$): δ = 134.6, 133.8, 133.5, 129.2, 129.1, 128.9, 126.8, 126.66, 125.9, 125.6, 125.4, 123.3, 122.9, 122.1, 121.9, 65.9, 53.2, 23.9, 23.9, 15.3

***R*-CEI:** *R*-(-)-1-cyclohexylethylisocyanide

R-(-)-1-cyclohexylethylamine (5 g, 39 mmol) was placed in round bottom flask with three necks equipped with stirring bar, thermometer and condenser. Excess of distilled CHCl$_3$ (9.4 ml), tetrabuthyl ammonium chloride (0.49 g, 1.8 mmol) and distilled CH$_2$Cl$_2$ (40 ml) were then added to the flask with the amine, and the mixture stirred vigorously. NaOH in water (50 % : 50 %, 17 g) was then slowly added in portions to the stirring mixture resulting in exothermic reaction. When total amount of NaOH/H$_2$O was added, mixture was heated to ca. 50ºC during 4 h. After that time, mixture was allowed to cool, and water (100 ml) was added to the flask. Organic phase was extracted, washed with brine, dried over MgSO$_4$, and filtered through Celite. Solvents were then removed under vacuum and resulting brown oil purified by column chromatography. (1.8 g, 33%)

Calculated for C$_9$H$_{15}$N·1/10C$_5$H$_{12}$: C 79.00; H 11.31; N 9.70; found: C 79.81; H 11.25; N 10.29

ESI–MS (m/z): calc for C$_9$H$_{15}$NNa$^+$: 160.11, found: 160.11 [M+Na]$^+$

IR (cm^{-1}): 2133 (strong, v N≡C); [α]$_{589nm, 25ºC}$ = -36.08 (7.1 mM, CH$_2$Cl$_2$)

^{1}H NMR (400 MHz, CDCl$_3$): δ 3.45 (m, 1 H), 1.64-1.92 (m, 5 H), 1.35-1.45 (m, 1 H), 1.33 (dt, 3 H, J = 6.7 Hz, 2.1 Hz), 1.02-1.29 (m, 5 H)

^{13}C{^{1}H}-NMR (300 MHz, CDCl$_3$): δ = 154.4, 55.5, 42.4, 29.3, 27.8, 26.0, 25.8, 25.7, 22.3, 18.9

***S*-CEI:** *S*-(+)-1-cyclohexylethylisocyanide

This ligand was prepared in same manner as ***R*-CEI**. (2.5g, 46 %)

Calculated for C$_9$H$_{15}$N·1/20C$_5$H$_{12}$: C 78.89; H 11.17; N 9.95; found: C 79.38; H 11.08; N 10.40

ESI–MS (m/z): calc for C$_9$H$_{15}$NNa$^+$: 160.110, found: 160.109 [M+Na]$^+$

IR (cm^{-1}): 2134 (strong, v N≡C); [α]$_{589nm, 25ºC}$ = +9.65 (6.3 mM, CH$_2$Cl$_2$)

^{1}H NMR (400 MHz, CDCl$_3$): δ 3.45 (m, 1 H), 1.64-1.92 (m, 5 H), 1.35-1.45 (m, 1 H), 1.33 (dt, 3 H, J = 6.7 Hz, 2.1 Hz), 1.02-1.29 (m, 5 H)

^{13}C{^{1}H}-NMR (300 MHz, CDCl$_3$): δ = 154.4, 55.5, 42.4, 29.3, 27.8, 26.0, 25.8, 25.7, 22.3, 18.9

RH3: Tetrakis(*R*-(-)-1-cyclohexylethylisocyanide)rhodium(I) chloride

[Rh(COD)Cl]$_2$ (0.6 g, 1.22 mmol), was dissolved in freshly distilled toluene (20 ml) in a Schlenk tube under argon. While stirring, ligand *R*-CEI (1.33 g, 9.7 mmol) was added slowly. After 2 h, distilled n-pentane was added in excess to precipitate the product. Solution was

removed, and resulting solid washed couple of times with n-pentane, and then dried under vacuum resulting in purple powder. (0.49 g, 29 %)

Calculated for $C_{36}H_{60}N_4RhCl \cdot 1/2CHCl_3 \cdot 1/10C_5H_{12}$: C 58.93; H 8.25; N 7.43; found: C 59.05; H 7.96; N 7.69

ESI–MS (m/z): calc for $C_{36}H_{60}N_4Rh^+$: 651.39, found: 651.36 $[M]^+$

IR (cm^{-1}): 2212 (medium, v N≡C), 2162 (strong, v N≡C); $[\alpha]_{589nm, \ 25°C}$ = -63.01 (1.2 mM, CH_2Cl_2)

^{1}H NMR (400 MHz, CDCl$_3$): δ 3.83 (m, 1 H, J = 6.2 Hz), 1.69-1.89 (m, 5 H), 1.47-1.57 (m, 1 H), 1.41 (d, 3 H, J = 6.8 Hz), 0.99-1.33 (m, 5 H)

^{13}C{^{1}H}-NMR (500 MHz, CDCl$_3$): δ = 137.3, 58.3, 42.4, 29.4, 27.8, 25.9, 25.7, 25.6, 18.6

RH4: Tetrakis(*S*-(+)-1-cyclohexylethylisocyanide)rhodium(I) chloride

[Rh(COD)Cl]$_2$ (0.5 g, 1.01 mmol), was dissolved in freshly distilled toluene (15 ml) in a Schlenk tube under argon. While stirring, ligand *S*-CEI (1.11 g, 8.11 mmol) was added slowly. After 2 h, distilled n-pentane was added in excess to precipitate the product. Solution was removed, and resulting solid washed couple of times with n-pentane, and then dried under vacuum resulting in purple powder. (0.6 g, 43 %)

Calculated for $C_{36}H_{60}N_4RhCl \cdot 1/2CHCl_3$: C 59.08; H 8.22; N 7.56; found: C 58.90; H 8.67; N 7.40

ESI–MS (m/z): calc for $C_{36}H_{60}N_4Rh^+$: 651.387, found: 651.389 $[M]^+$

IR (cm^{-1}): 2212 (medium, v N≡C), 2165 (strong, v N≡C) $[\alpha]_{589nm, \ 25°C}$ = +56.63 (1.2 mM, CH_2Cl_2)

^{1}H NMR (400 MHz, CDCl$_3$): δ 3.81 (m, 1 H, J = 6.3 Hz), 1.69-1.89 (m, 5 H), 1.47-1.57 (m, 1 H) 1.40 (d, 3 H, J = 6.8 Hz), 0.99-1.33 (m, 5 H)

^{13}C{^{1}H}-NMR (300 MHz, CDCl$_3$): δ = 137.1, 58.4, 42.2, 29.2, 27.6, 25.7, 25.5, 25.4, 18.4

8.4.2.   Palladium(II) complexes

PD1: chloro(pyridine)[4-(t-Butyl)-2-(p-tolyl)pyridine]palladium(II) [Pd(Pyr)(tBpTP)Cl]

Pd dimer (0.3 g, 0.4 mmol) was dissolved in 20 ml of distilled CHCl$_3$ and stirred. Slight excess of pyridine (0.070 g, 0.89 mmol) was dissolved in 3 ml of CHCl$_3$, and added dropwise to the stirring solution of dimer. Dirty yellow suspension changed colour to transparent yellow almost instantly. Stirring was continued for additional 1 hour and then solution was

concentrated to ca. 3 ml and product precipitated with n-pentane. Dirty yellow powder was washed with fresh n-pentane and dried under vacuum. (0.321 g, 88 % yield).

Calculated for $C_{21}H_{23}ClN_2Pd \cdot 1/20CHCl_3$: C 56.03; H 5.15; N 6.12; found: C 56.14; H 5.44; N 5.86

ESI–MS (m/z): calc for $C_{21}H_{24}ClN_2Pd$: 445.066, found: 445.064 $[M+H]^+$

^1H NMR (500 MHz, $CDCl_3$) : δ = 9.28 (d, 1 H, J = 5.9 Hz), 8.94 (dt, 2 H, J = 5.00 Hz, 1.5 Hz), 7.86 (t, 1 H, J = 7.2 Hz), 7.54 (s, 1 H), 7.44 (t, 2 H, J = 5.9 Hz), 7.35 (d, 1 H, J = 7.6 Hz), 7.07 (d, 1 H, J = 5.0 Hz), 6.88 (d, 1 H, J = 7.6 Hz), 5.96 (s, 1 H), 2.11 (s, 3 H, CH_3), 1.33 (s, 9 H, CMe_3)

$^{13}C\{^1H\}$-NMR (500 MHz, $CDCl_3$): δ = 165.0, 163.3, 154.3, 153.3 (2 C), 151.4, 143.4, 139.4, 138.0, 133.3, 125.5, 125.5 (2 C), 122.9, 119.1, 114.8, 35.3 (-C-Me_3), 30.4 (3C, -CH_3), 21. 8 (-CH_3)

PD3: chloro-[4-(t-Butyl)-2-(p-tolyl)pyridine]-(triphenylphosphane)palladium(II) [Pd(PPh_3)(tBpTP)Cl]

Pd dimer $[Pd(tBpTP)Cl]_2$ (0.3 g, 0.4 mmol) was dissolved in 20 ml of distilled $CHCl_3$ and stirred. Slight excess of triphenylphosphine (0.22 g, 0.84 mmol) was dissolved in 5 ml of $CHCl_3$, and added dropwise to the stirring solution of dimer. Dirty yellow suspension changed colour to transparent dark yellow almost instantly. Stirring was continued for additional 30 min and then solution was concentrated to ca. 3 ml and product precipitated with n-pentane. Dirty yellow powder was washed with fresh n-pentane and dried under vacuum. (0.346 g, 67 % yield).

Calculated for $C_{34}H_{33}ClNPPd \cdot 1/3CHCl_3$: C 61.74; H 5.03; N 2.10; found: C 61.57; H 5.35; N 2.00

ESI–MS (m/z): calc for $C_{34}H_{33}NPPd$: 592.139, found: 592.131 $[M-Cl]^+$

$^{31}P\{^1H\}$ NMR (161.97 MHz, $CDCl_3$): δ = 39.97.

^1H NMR (500 MHz, $CDCl_3$): δ = 9.33 (dd, 1 H, J = 5.8 Hz, 3.6 Hz), 7.67 (dd, 6 H, J = 11.4 Hz, 7.8 Hz), 7.53 (s, 1H), 7.3-7.2 (m, 9 H), 7.13 (s, 1 H), 7.06 (d, 1 H, J = 6.1 Hz), 6.63 (d, 1 H, J = 7.8 Hz), 6.16 (d, 1 H, J = 7.1 Hz), 1.55 (s, 3 H, CH_3), 1.24 (s, 9 H, CMe_3)

$^{13}C\{^1H\}$-NMR (125.77 MHz, $CDCl_3$): δ = 164.3, 163.3, 154.8, 150.0, 144.8, 140.2 (d, J = 11.7 Hz), 138.5 (d, J = 5.8 Hz), 135.5 (d, 6C, J = 11.7 Hz), 135.1 (t, J = 6.1 Hz), 131.6, 131.3, 130.6(3C), 128.0 (d, 6C, J = 10.9 Hz), 124.9, 123.2, 119.1, 114.6, 35.3 (-C-Me_3), 30.4 (3C, -CH_3), 21.3 (-CH_3)

PD2: chloro[4-(t-Butyl)pyridine]-[4-(t-Butyl)-2-(p-tolyl)pyridine]palladium(II) [Pd(tBPyr)(tBpTP)Cl]

Pd dimer (0.3 g, 0.4 mmol) was dissolved in 20 ml of distilled $CHCl_3$ and stirred. Excess of 4-tert-bytilpyridine (0.16 g, 1.2 mmol) was dissolved in 5 ml of $CHCl_3$, and added dropwise to the stirring solution of dimer. Dirty yellow suspension changed colour to transparent yellow almost instantly. Stirring was continued for additional 30 minutes and then solution was concentrated to ca. 3 ml and product precipitated with n-pentane. Dirty yellow powder was washed with fresh n-pentane and dried under vacuum. (0.367 g, 89 % yield).

Calculated for $C_{25}H_{31}ClN_2Pd·1/5CHCl_3$: C 57.62; H 5.99; N 5.33; found: C 57.75; H 6.18; N 5.18

ESI–MS (m/z): calc for $C_{25}H_{31}N_2Pd$: 465.153, found: 465.146 $[M-Cl]^+$

^1H NMR (500 MHz, $CDCl_3$) : δ = 9.08 (d, 1 H, J = 6 Hz), 8.62 (dd, 2 H, J = 5.6 Hz, 1.4 Hz), 7.37 (d, 1 H, J = 2.0 Hz), 7.23 (dd, 2 H, J = 5.6 Hz, 1.4 Hz), 7.19 (d, 1 H, J = 7.8 Hz), 6.89 (dd, 1 H, J = 6 Hz, 1.4 Hz), 6.71 (d, 1 H, J = 7.7 Hz), 5.83 (s, 1H), 1.96 (s, 3 H, CH_3), 1.17 (s, 9 H, CMe_3), 1.16 (s, 9 H, CMe_3)

$^{13}C\{^1H\}$-NMR (500 MHz, $CDCl_3$): δ = 165.0, 163.2, 162.6, 154.3, 152.6 (2C), 151.4, 143.4, 139.4, 133.4, 125.5, 122.9, 122.6 (2C), 119.1, 114.8, 35.3 ($-C-Me_3$), 35.2 ($-C-Me_3$), 30.4 (6C, $-CH_3$), 21.9 ($-CH_3$)

PD4: chloro[4-(t-Butyl)-2-(p-tolyl)pyridine](tricyclohexylphosphane)palladium (II) [Pd(tBpTP)(PCy_3)Cl]

Pd dimer $[Pd(tBpTP)Cl]_2$ (0.24 g, 0.3 mmol) was dissolved in 15 ml of distilled $CHCl_3$ and stirred. Slight excess of tricyclohexylphosphine (0.18 g, 0.66 mmol) was dissolved in 5 ml of $CHCl_3$, and added dropwise to the stirring solution of dimer. Dirty yellow suspension changed colour to transparent dark yellow almost instantly. Stirring was continued for additional 45 min and then solution was concentrated to ca. 3 ml and product precipitated with n-pentane. Dirty yellow powder was washed with fresh n-pentane and dried under vacuum. (0.210 g, 49 % yield).

Calculated for $C_{34}H_{51}ClNPPd·H_2O·CHCl_3$: C 53.62; H 6.94; N 1.79; found: C 53.50; H 7.27; N 2.04

ESI–MS (m/z): calc for $C_{34}H_{51}NPPd$: 610.280, found: 610.275 $[M-Cl]^+$

^{1}H NMR (300.17 MHz, CDCl$_3$): δ = 9.47 (dd, 1 H, J = 6.1 Hz, 3.1 Hz), 7.60 (s, 1 H), 7.41 (d, 1 H, J = 7.8 Hz), 7.21 (d, 1 H, J = 4.2 Hz), 7.12 (dq, 1 H, J = 6.3 Hz, 1.1 Hz), 6.87 (d, 1 H, J = 7.8 Hz), 2.64 (dd, 3 H, -Cy, J = 23.5 Hz, 11.9 Hz), 2.28 (s, 3 H, CH$_3$), 2.10-1.51 (m, 30 H, -Cy), 1.33 (s, 9 H, CMe$_3$)

^{13}C{^{1}H}-NMR (125.77 MHz, CDCl$_3$): δ = 164.0, 162.6, 149.6, 139.2, 125.8, 124.8, 123.5, 122.9, 118.9, 115.1, 114.4, 34.0 (-C-Me$_3$), 30.4 (12 C, -Cy), 30.4 (3 C, -Me$_3$), 27.8 (3 C, -Cy), 26.5 (3 C, -Cy), 21.8 (1 C, Me)

PD5: chloro(N,N-dimethylbenzylamine)(4-(t-Butyl)pyridine)palladium(II) [Pd(dmba)(tBPyr)Cl]

[Pd(μ-Cl)(dmba)]$_2$ (0.25 g, 0.45 mmol) was dissolved in 10 ml of freshly distilled CH$_2$Cl$_2$. 4-tert-butylpyridine (0.12 g, 0.9 mmol) was then added to the stirring solution of Pd dimer in drops and previously opaque solution turned transparent yellow. Stirring was continued for additional 4 hours on room temperature. After this time, solution was concentrated, and product precipitated with Et$_2$O giving pale yellow-white powder. (0.322 g, 86 % yield)

Calculated for C$_{18}$H$_{25}$ClN$_2$Pd: C 52.57; H 6.13; N 6.81; found: C 52.23; H 6.16; N 6.52

ESI–MS (m/z): calc. for C$_{18}$H$_{26}$ClN$_2$Pd: 411.081, found: 411.082 [M+H]$^{+}$

^{1}H NMR (500 MHz, CDCl$_3$) : δ = 8.70 (dd, 2 H, J = 5.4, 1.3 Hz), 7.30 (dd, 2 H, J = 5.4, 1.3 Hz), 6.96 (d, 1 H, J = 1.5 Hz), 6.95 (s, 1 H), 6.74-6.79 (m, 1 H), 6.02 (d, 1 H, J = 7.7 Hz), 3.95 (s, 2 H, CH$_2$), 2.90 (s, 6 H, CH$_3$), 1.30 (s, 9 H, CMe$_3$)

^{13}C{^{1}H}-NMR (500 MHz, CDCl$_3$): δ = 162.6, 153.1, 149.1, 147.7, 132.5, 125.4 (2 C), 124.6 (2 C), 122.5 (2 C), 121.7, 74.2 (1C, -CH$_2$-), 52.9 (2C, -CH$_3$), 35.3 (1C, -C-Me$_3$), 30.5 (3C, -CH$_3$)

8.4.3. Ruthenium(II) complexes

RU1: chloro(η^{6}-1-isopropyl-4-methylbenzene)(4-(t-Butyl)pyridine)ruthenium(II) [Ru(p-cym)(tBPyr)Cl$_2$]

[Ru(p-cym)Cl$_2$]$_2$ (0.3 g, 0.49 mmol) was dissolved in 40 ml of ethanol and then 4-tert-butylpyridine (0.140 g, 1 mmol) was added to the stirring solution in drops. Mixture was stirred until solution became transparent, and then continued for 12 more hours. After this time, solution was concentrated and product precipitated with n-pentane. Dark orange powder was washed with n-pentane and dried under vacuum. (0.25 g, 58 % yield)

C$_{19}$H$_{27}$Cl$_2$NRu·1/5CH$_2$Cl$_2$: C 50.31; H 6.02; N 3.06; found: C 50.55; H 6.09; N 3.06

ESI–MS (m/z): calc for $C_{19}H_{28}Cl_2NRu$: 442.063, found: 442.061 $[M+H]^+$

^1H NMR (400 MHz, C_6D_6): δ = 9.03 (dd, 2 H, J = 5.0 Hz, 1.4 Hz), 6.69 (dd, 2 H, J = 5.0 Hz, 1.4 Hz), 5.96 (d, 2 H, J = 5.7 Hz), 5.63 (d, 2 H, J = 5.7 Hz), 3.03 (m, 1 H, J = 7.0 Hz), 1.75 (s, 3 H), 1.13 (d, 6 H, J = 7 Hz), 0.90 (s, 9 H, CMe_3)

$^{13}C\{^1H\}$-NMR (500 MHz, $CDCl_3$): δ = 162.3, 154.3 (2 C), 121.8 (2 C), 103.6, 96.9, 82.5 (2 C), 82.4 (2 C), 34.9, 30.7, 30.3 (3 C), 22.3 (2 C), 18.3 (1 C)

Chapter 9

9. Conclusions

Recent years have shown emergence of the new methods, both experimental and theoretical, that have been used to study NCI. In this thesis, we have used several theoretical (density functional theory - DFT and *ab initio* calculations, analysis of CSD), and experimental methods (synthesis and characterizations of new complexes, ITC, etc.) to address the questions and concepts that were previously not fully studied in the manner that we have used. It is our belief that the new knowledge on NCI in coordination chemistry and organometallic systems can only be acquired by using theoretical chemistry as a complement to the experiment. This is only possible with the creation of a "new type of experimental chemists" who are both able to build their own objects of research and to study their intimate electronic structures and properties with modern theoretical methods.

Even though some of the questions we addressed in our studies were not fully answered, one thing is clear. It has been shown that the use of latest theoretical methods in complement to the experimental investigations is crucial in understanding the processes in which it was shown that dispersion forces play major role. Especially, ITC proved to be the method that was extremely useful in our studies. It gave us an insight in the thermochemistry of the processes we addressed, and the data we have obtained, compared to those that were calculated, made a basis for most of our conclusions.

The study of the square-planar *bipy* complexes have shown that the strength of the stacking interactions rises with the increase in the overlapping area between the two *bipy* ligands. The results of this study also indicate that chelate-aryl interactions are stronger than aryl-aryl interactions and that interaction of pyridine rings coordinated to the metal is stronger than interaction of non-coordinated pyridines. The manner of organization of square-planar *bipy* complexes in crystal structures depends, besides the overlapping area, on the nature of the other two ligands coordinated to the metal.

The next step in the understanding of the stacking interactions of bipy complexes is to study the role of the chelate rings in the interactions and the stabilization of the complexes. Preliminary studies have shown that the specific interactions of the chelate rings with other chelate and aromatic rings, as well as with the metal will play important role in the way the complexes overlap. To this extent further DFT-calculations will be performed, and the data analysed in the light of the results we obtained during the work on the subject. Given the

various applications of this family of complexes in different area of chemistry and biochemistry, it is our hope that the results of this study will help in understanding some of the issues encountered in these fields.

We have synthesised and characterized several novel tetrakis(isocyanide) rhodium(I) complexes. Analysis of spectroscopic data suggests that the chiral isocyanide ligands coordinate to the rhodium forming square-planar complex of the general formula $[Rh(L)_4]Cl$. All complexes retain the absolute configuration of their respective ligands and turn the plane of polarized light in the same direction, except the **RH2** complex which changes the sign of the specific rotation comparing to the **NEI** ligand. This suggested peculiarities in the structure of **RH2** complex but since all attempts to obtain crystal structures failed, the clarification of noticed features remains to be discovered.

Study on the oligomerization process of synthesized rhodium complexes *in solutio* was conducted by analysing the UV-Vis spectra in acetonitrile. Oligomerization of this type of complexes was already well documented in the literature. The absorption bands that rise with the increase in concentration of the complex have confirmed formation of the dimer (or trimer). Treatment of the obtained data provided estimation of the K_2 and ΔG_f. Values for the Gibbs free enthalpy show that the process of dimer (trimer) formation in solution is thermodynamically favoured. The thermochemistry of the oligomerization process was checked with the ITC experiment in the case of the one Rh complex, where the results show agreement between thermochemical parameters obtained from UV/Vis extrapolation and ITC experiment. One of the issues that have to be taken in to consideration here is the fact that in solution of these complexes ion pair cannot be fully dissociated, so the dilution enthalpy should play a role as well. In our studies we have not addressed this issue, so the thermochemical parameters we obtained represent just the rough estimate for the processes of the self-aggregation we have considered.

Given the nature of the theoretical calculations and the technical limitations we encountered, we were not able to address the problems of self-assembly of the Rh(I) complexes, and to compare the experimentally obtained data with theory. Experiments showed that the forming of the oligomers in concentrated solution is favoured process, but this was still not addressed by theoretical analysis. Like in the previously published results of theoretical calculations for this class of complexes, dispersion should probably play an important role in the oligomerization process. So, in that regard, theoretical calculations in gas phase, and in solution using solvation models, would provide valuable information concerning

oligomerization for our complexes. This data could help in evaluation of the theoretical methods by comparing the experimentally obtained data with results of the calculations.

Another important issue that could be addressed using newly synthesised chiral Rh complexes is a perspective for the chiral recognition. Since all synthesised complexes are cations, there is a possibility of the stabilization of large anionic species and resolving the mixtures by specific interactions with Rh complexes. Further theoretical investigations of this issue could provide valuable information on the energetics of the chiral recognition processes.

Interesting stability of the cis-platin type of complexes in concentrated solutions and the possible answer given by Dabrowiak et al. was addressed studying their behaviour in gas phase and solution. Experimental and theoretical methods have given clear confirmation to the propensity of these molecules to form oligomers in gas phase. This propensity to self-aggregate is primarily due to the ability of the compounds in question to establish H-bonds, which is challenged by the specific interactions of bulk water in solution. Hence, the non-local attractive dispersion force most likely assists H-bonding in the dimerization process in solution by counter balancing the entropic penalty induced by hydration. This contribution of dispersion is particularly obvious in the interfragment interaction energy of dimers $[1]_2$ and $[2]_2$. The fact that the shifted stacked β arrangement seems to be particularly favoured in solution for **1** and **2**, questions the role of electron correlation-based metal-metal attractive interactions, which was not explicitly addressed here. It has to be mentioned though, that our results indicate absence of direct metal-metal interactions. This study outlined the performance of DFT-D in producing rather realistic thermochemical parameters. Our investigations suggest that monomeric Oxaliplatin tends to be rather predominant at least in solution in pure water. In the scope of the development of anti-cancer drugs that can withstand storage over long periods of time in aqueous media, the correlation of resistance towards hydrolysis with self-aggregation still remains an open question.

Investigation on the behaviour of the cisplatin-type drugs in solution was continued by studying the inclusion of the **1** and **2** to the **CB**[7] cavitand. Inclusion of the host-guess complex **1@CB**[7] studied previously by Kim et al. provided some information on the thermodynamics of the inclusion process by reporting an enthalpy ΔH of the process and the association constant in the presence of TRIS buffer. In our opinion, this introduced a serious risk of underestimation of the actual affinity of **1** for the considered cavitand. To validate this, we have performed ITC measurements by titrating the concentrated solution of **2** in presence of TRIS buffer to the **CB**[7], as well as titrations with pure water solutions of **1** and **2** and

CB[7]. The results show that TRIS play the role of a competing guest of **CB**[7] and that the effect of its concentration in the medium had to be accounted for.

Inclusion of **4** to the **CB**[7] by means of ITC method was considered in order to obtain data on energetic of the inclusion process of this host-guest system, all with a goal to shed some light on the way complex **4** interacts with the host cavitand.

We have then proceeded with DFT calculations with a goal to assess the ability of the DFT-D calculations with COSMO-RS solvation model to reproduce experimentally obtained thermochemical data. In the case of **1** and **2**, which are both moderately lipophilic and rather keen to establish specific interactions with bulk water, the values of affinities for **CB**[7] remain in reasonable agreement with experimental data, particularly if one considers that a negligible energy toll must be paid for the dissociation of portions of dimers [**1**]$_2$ and [**2**]$_2$. Calculations for the inclusion of complex **4** to **CB**[7] suggest that the non-covalent concealment is way more favourable thermodynamically than the trapping of the Ir complex by chelation at the cavitand.

Finally, we have synthesised and structurally and spectroscopically characterized several new palladium(II) and ruthenium(II) complexes. Complexes and their respective synthesis reactions were chosen in a way to be suitable for the ITC experiments. All reactions have clearly defined stoichiometry resulting in one product. Reactions showed strong exothermic signature, and the subsequent treatment of data afforded thermochemical parameters of the reactions (ΔH_f, ΔS_f, ΔG_f). Thermochemical data obtained by the ITC reactions was collected in order to give accurate experimental data for the reactions in solution involving larger palladium and ruthenium complexes where long-range intramolecular London dispersion forces are suspected to be essential to their stabilization. These data was used to benchmark the latest dispersion corrected DFT and WFT theoretical methods in collaboration with the group of Dr. Grimme from Mulliken Center for Theoretical Chemistry at University of Bonn, Germany, where said theoretical methods were developed.

First benchmark calculations have shown very promising results, but also the limitations of the solvation models available today. Since experimental results are not directly comparable to the calculations, raw experimental values have been "back-corrected" to account for entropic effects as well as solvation contribution. The calculation of the Gibbs free solvation energy contribution to a reaction using continuum solvation models show uncertainties of ca. 2 kcal/mol, while the reaction entropies calculated through RRHO model show uncertainties of ca. 1 kcal/mol for large systems. Even though accuracy of the calculated

parameters is quite good, improvement for the Gibbs free solvation energy would be better, which could be achieved by developing new explicit solvation models. From the standpoint of accepted "chemical accuracy" "back-corrected" experimental reaction energies for large molecules have higher error estimates.

The calculations performed with modern dispersion corrected density functionals have shown that an accuracy of 2-3 kcal/mol (which is around 5–10% of interaction energy) for our systems differ from standard notion of 'chemical accuracy' of 1 kcal/mol. If all of the physical interactions are accounted for and described correctly, the modern DFT and WFT methods give results very close to the experimental reference and are able to predict the thermochemistry of larger transition metal complexes where long-range London dispersion interactions play significant role.

Some results of this study have been published, but the investigations are still in progress and will be continued in the future as part of collaboration, with the work that will be basis of the new PhD thesis in our groups.

10. References

1. E. Frieden, *J. Chem. Edu.*, 1975, **52**, 754-756.
2. P. Hobza, R. Zahradnik and K. Muller-Dethlefs, *Collect. Czech. Chem. Commun.*, 2006, **71**, 443-531.
3. J. D. Watson and F. H. C. Crick, *Nature*, 1953, **171**, 737-738.
4. L. M. Brown, A. Pais, B. Pippard, *Twentieth Century Physics*, Institute of Physics Pub. ; American Institute of Physics Press, Bristol; Philadelphia; New York, 1995.
5. F. London, *Z. Physik. Chem.*, 1930, **11**, 222-251.
6. H. Hellmann, *Acta Physicochim. URSS*, 1935, **2**, 273-290.
7. P. Debye, *Phys. Z.*, 1921, **22**, 302-308.
8. I. E. Dzyaloshinskii, E. M. Lifshitz and P. P. Lev, *Sov. Phys. Usp.,* 1961, **4**, 153.
9. H. C. Hamaker, *Physica*, 1937, **4**, 1058-1072.
10. D. Langbein, *Phys. Rev. B*, 1970, **[3]2**, 3371-3383.
11. F. London, *Trans. Faraday Soc.*, 1937, **33**, 8-26.
12. Y. Zheng and A. Narayanaswamy, *Phys. Rev. A*, 2011, **83**, 042504.
13. F. London, *Z. Phys.*, 1930, **63**, 245-279.
14. A. D. McNaught and A. Wilkinson, *IUPAC. Compendium of Chemical Terminology, 2nd ed. (the "Gold Book")*, Blackwell Scientific Publications, Oxford, 1997, doi:10.1351/goldbook.H02907.
15. C. Bissantz, B. Kuhn and M. Stahl, *J. Med. Chem.*, 2010, **53**, 5061-5084.
16. M. Ma, Y. Kuang, Y. Gao, Y. Zhang, P. Gao and B. Xu, *J. Am. Chem. Soc.*, 2010, **132**, 2719-2728.
17. L. M. Salonen, M. Ellermann and F. Diederich, *Angew. Chem., Int. Ed.*, 2011, **50**, 4808-4842.
18. H.-J. Schneider, *Angew. Chem., Int. Ed.*, 2009, **48**, 3924-3977.
19. M. O. Sinnokrot, E. F. Valeev and C. D. Sherrill, *J J. Am. Chem. Soc.*, 2002, **124**, 10887-10893.
20. F. Cozzi, M. Cinquini, R. Annunziata, T. Dwyer and J. S. Siegel, *J. Am. Chem. Soc.*, 1992, **114**, 5729-5733.
21. C. A. Hunter and J. K. M. Sanders, *J. Am. Chem. Soc.*, 1990, **112**, 5525-5534.
22. E.-i. Kim, S. Paliwal and C. S. Wilcox, *J. Am. Chem. Soc.*, 1998, **120**, 11192-11193.
23. S. Grimme, *Angew. Chem., Int. Ed.*, 2008, **47**, 3430-3434.
24. M. O. Sinnokrot and C. D. Sherrill, *J. Phys. Chem. A*, 2003, **107**, 8377-8379.
25. M. O. Sinnokrot and C. D. Sherrill, *J. Am. Chem. Soc.*, 2004, **126**, 7690-7697.
26. S. E. Wheeler and K. N. Houk, *J. Am. Chem. Soc.*, 2008, **130**, 10854-10855.
27. F. Cozzi, R. Annunziata, M. Benaglia, K. K. Baldridge, G. Aguirre, J. Estrada, Y. Sritana-Anant and Jay S. Siegel, *Phys. Chem. Chem. Phys.,* 2008, **10**, 2686-2694.
28. S. L. Cockroft and C. A. Hunter, *Chem. Soc. Rev.*, 2007, **36**, 172-188.
29. J. C. Ma and D. A. Dougherty, *Chem. Rev.*, 1997, **97**, 1303-1324.
30. S. D. Zarić, *Eur. J. Inorg. Chem.*, 2003, **2003**, 2197-2209.
31. C. Rapp, E. Goldberger, N. Tishbi and R. Kirshenbaum, *Proteins: Struct., Funct., Bioinf.*, 2014, 82, 7, 1494–1502.
32. K. K. Bania, A. K. Guha, P. K. Bhattacharyya and S. Sinha, *Dalton Trans.*, 2014, **43**, 1769-1784.
33. D. A. Dougherty, *Science*, 1996, **271**, 163-168.
34. D. A. Dougherty, *J. Nutr.*, 2007, **137**, 1504S-1508S; discussion 1516S-1517S.

35.   S. A. Pless, A. P. Hanek, K. L. Price, J. W. Lynch, H. A. Lester, D. A. Dougherty and S. C. Lummis, *Mol. Pharmacol.*, 2011, **79**, 742-748.

36.   J. P. Gallivan and D. A. Dougherty, *J. Am. Chem. Soc.*, 2000, **122**, 870-874.

37.   S. Tsuzuki, M. Yoshida, T. Uchimaru and M. Mikami, *J. Phys. Chem. A*, 2001, **105**, 769-773.

38.   C. D. Sherrill, T. Takatani and E. G. Hohenstein, *J. Phys. Chem. A*, 2009, **113**, 10146-10159.

39.   S. Mecozzi, A. P. West, Jr. and D. A. Dougherty, *Proc. Nat. Acad. Sci. U.S.A.*, 1996, **93**, 10566-10571.

40.   S. Mecozzi, A. P. West, Jr. and D. A. Dougherty, *J. Am. Chem. Soc.*, 1996, **118**, 2307-2308.

41.   S. E. Wheeler and K. N. Houk, *J. Am. Chem. Soc.*, 2009, **131**, 3126-3127.

42.   D. B. Ninkovic, J. M. Andric and S. D. Zaric, *ChemPhysChem*, 2013, **14**, 237-243.

43.   D. B. Ninkovic, G. V. Janjic, D. Z. Veljkovic, D. N. Sredojevic and S. D. Zaric, *ChemPhysChem*, 2011, **12**, 3511-3514.

44.   R. Chelli, F. L. Gervasio, P. Procacci and V. Schettino, *J. Am. Chem. Soc.*, 2002, **124**, 6133-6143.

45.   U. Samanta and P. Chakrabarti, *Protein Eng.*, 2001, **14**, 7-15.

46.   S. K. Burley and G. A. Petsko, *Science*, 1985, **229**, 23-28.

47.   V. L. Malinovskii, F. Samain and R. Haner, *Angew. Chem., Int. Ed.*, 2007, **46**, 4464-4467.

48.   S. A. Arnstein and C. D. Sherrill, *Phys. Chem. Chem. Phy.s*, 2008, **10**, 2646-2655.

49.   W. Wang and P. Hobza, *ChemPhysChem*, 2008, **9**, 1003-1009.

50.   D. B. Ninkovic, G. V. Janjic and S. D. Zaric, *Cryst. Growth Des.*, 2012, **12**, 1060-1063.

51.   S. T. Mutter and J. A. Platts, *Chemistry*, 2010, **16**, 5391-5399.

52.   H. Masui, *Coord. Chem. Rev.*, 2001, **219-221**, 957-992.

53.   M. K. Milcic, B. D. Ostojic and S. D. Zaric, *Inorg. Chem.* , 2007, **46**, 7109-7114.

54.   G. A. Bogdanovic, V. Medakovic, M. K. Milcic and S. D. Zaric, *Int. J. Mol. Sci.*, 2004, **5**, 174-185.

55.   G. A. Bogdanovic, A. Spasojevic-de Bire and S. D. Zaric, *Eur. J. Inorg. Chem.* , 2002, 1599-1602.

56.   V. B. Medakovic, M. K. Milcic, G. A. Bogdanovic and S. D. Zaric, *J. Inorg. Biochem.*, 2004, **98**, 1867-1873.

57.   M. K. Milcic, V. B. Medakovic, D. N. Sredojevic, N. O. Juranic and S. D. Zaric, *Inorg. Chem.*, 2006, **45**, 4755-4763.

58.   M. K. Milcic, V. B. Medakovic and S. D. Zaric, *Inorg. Chim. Acta*, 2006, **359**, 4427-4430.

59.   S. Đ. Stojanović, V. B. Medaković, G. Predović, M. Beljanski and S. D. Zarić, *J. Biol. Inorg. Chem.*, 2007, **12**, 1063-1071.

60.   T. J. Anderson, G. D. Jones and D. A. Vicic, *J. Am. Chem. Soc.*, 2004, **126**, 8100-8101.

61.   B. C. De Pater, H.-W. Fruehauf, K. Vrieze, R. De Gelder, E. J. Baerends, D. McCormack, M. Lutz, A. L. Spek and F. Hartl, *Eur. J. Inorg. Chem.* , 2004, 1675-1686.

62.   G. Janjic, J. Andric, A. Kapor, Z. D. Bugarcie and S. D. Zaric, *CrystEngComm*, 2010, **12**, 3773-3779.

63.   G. V. Janjic, P. V. Petrovic, D. B. Ninkovic and S. D. Zaric, *J. Mol. Mod.*, 2011, **17**, 2083-2092.

64. D. N. Sredojević, Z. D. Tomić and S. D. Zarić, *Cryst. Growth Des.*, 2010, **10**, 3901-3908.

65. D. N. Sredojevic, D. Z. Vojislavljevic, Z. D. Tomic and S. D. Zaric, *Acta Crystallogr., Sect. B: Struct. Sci.*, 2012, **68**, 261-265.

66. C. A. Eckert, D. L. Bergmann, D. L. Tomasko and M. P. Ekart, *Acc. Chem. Res.*, 1993, **26**, 621-627.

67. O. Schuster, U. Monkowius, H. Schmidbaur, R. S. Ray, S. Krueger and N. Roesch, *Organometallics*, 2006, **25**, 1004-1011.

68. T. R. Ward, J. Collot, J. Gradinaru, A. Loosli, M. Skander, C. Letondor, E. Joseph and G. Klein, *Chimia*, 2003, **57**, 586-588.

69. D. B. Amabilino and J. Veciana, *Top. Curr. Chem.*, 2006, **265**, 253-302.

70. S. M. Benito, M. Sauer and W. Meier, *Nanocontainers*, in *Encyclopedia of Nanoscience and Nanotechnology*, ed. H. S. Nalwa, American Scientific Publishers, 2004, Vol. 6, 301-319.

71. C. G. Claessens and J. F. Stoddart, *J. Phys. Org. Chem.*, 1997, **10**, 254-272.

72. J. A. A. W. Elemans, A. E. Rowan and R. J. M. Nolte, *J. Mater. Chem.*, 2003, **13**, 2661-2670.

73. A. S. Borovik, *Comments Inorg. Chem.*, 2002, **23**, 45-78.

74. L. H. Doerrer, *Comments Inorg. Chem.*, 2008, **29**, 93-127.

75. C. A. Hunter, *Chem. Soc. Rev.*, 1994, **23**, 101-109.

76. J. K. Klosterman, Y. Yamauchi and M. Fujita, *Chem. Soc. Rev.*, 2009, **38**, 1714-1725.

77. S. Li, Y. Xu, Q. Shen, X. Liu, J. Lu, Y. Chen, T. Lu, C. Luo, X. Luo, M. Zheng and H. Jiang, *Curr. Pharm. Des.*, 2013, **19**, 6522-6533.

78. A. K. Patri, J. F. Kukowska-Latallo and J. R. Baker, Jr., *Adv. Drug Delivery Rev.*, 2005, **57**, 2203-2214.

79. P. Zhou, J. Huang and F. Tian, *Curr. Med. Chem.*, 2012, **19**, 226-238.

80. J. M. Pollino and M. Weck, *Chem. Soc. Rev.*, 2005, **34**, 193-207.

81. S. Zhang, D. M. Marini, W. Hwang and S. Santoso, *Curr. Opin. Chem. Biol.*, 2002, **6**, 865-871.

82. T. L. Brown, *Chemistry: the central science*, Prentice Hall, Boston, 2012.

83. D. H. Guston, *Encyclopedia of nanoscience and society*, Sage, Thousand Oaks, Calif., 2010.

84. K. Autumn, Y. A. Liang, S. T. Hsieh, W. Zesch, W. P. Chan, T. W. Kenny, R. Fearing and R. J. Full, *Nature*, 2000, **405**, 681-685.

85. K. Autumn, M. Sitti, Y. A. Liang, A. M. Peattie, W. R. Hansen, S. Sponberg, T. W. Kenny, R. Fearing, J. N. Israelachvili and R. J. Full, *Proc. Natl. Acad. Sci. U. S. A.*, 2002, **99**, 12252-12256.

86. B. I. N. Chen and H. Gao, *Int. J. App. Mech.*, 2010, **02**, 1-9.

87. P. Y. Hsu, L. Ge, X. Li, A. Y. Stark, C. Wesdemiotis, P. H. Niewiarowski and A. Dhinojwala, *J. R. Soc. Interface*, 2012, **9**, 657-664.

88. M. S. Prowse, M. Wilkinson, J. B. Puthoff, G. Mayer and K. Autumn, *Acta Biomater.*, 2011, **7**, 733-738.

89. A. Rajput and R. Mukherjee, *Coord. Chem. Rev.*, 2013, **257**, 350-368.

90. C. Janiak, *Dalton Trans.*, 2000, 3885-3896.

91. D. P. Malenov, D. B. Ninković, D. N. Sredojević and S. D. Zarić, *ChemPhysChem*, 2014, 15(12), 2458–2461.

92. D. N. Sredojevic, D. B. Ninkovic, G. V. Janjic, J. Zhou, M. B. Hall and S. D. Zaric, *ChemPhysChem*, 2013, **14**, 1797-1800.

93. D. N. Sredojevic, Z. D. Tomic and S. D. Zaric, *Cryst. Growth Des.*, 2010, **10**, 3901-3908.

94.   Z. D. Tomic, S. B. Novakovic and S. D. Zaric, *Eur. J. Inorg. Chem.*, 2004, 2215-2218.

95.   Z. D. Tomic, D. Sredojevic and S. D. Zaric, *Cryst. Growth Des.*, 2006, **6**, 29-31.

96.   A. C. Buchholz and D. A. Schoeller, *Am. J. Clin. Nutr.*, 2004, **79**, 899s-906s.

97.   M. Kleiber, *in The fire of life : an introduction to animal energetics*, R. E. Krieger Pub. Co, Huntington, N.Y., 1987.

98.   J. J. Christensen, R. M. Izatt, L. D. Hansen and J. A. Partridge, *J. Phys. Chem.*, 1966, **70**, 2003-2010.

99.   L. D. Hansen, J. J. Christensen and R. M. Izatt, *Chem. Commun.*, 1965, 36-38.

100.   J. J. Christensen, R. M. Izatt and D. Eatough, *Inorg. Chem.*, 1965, **4**, 1278-1280.

101.   D. Eatough, *Anal. Chem.*, 1970, **42**, 635-639.

102.   N. V. Beaudette and N. Langerman, *Anal. Biochem.*, 1978, **90**, 693-704.

103.   R. L. Biltonen and N. Langerman, *Methods Enzymol.*, 1979, **61**, 287-318.

104.   N. Langerman and R. L. Biltonen, *Methods Enzymol.*, 1979, **61**, 261-286.

105.   T. Wiseman, S. Williston, J. F. Brandts and L. N. Lin, *Anal. Biochem.*, 1989, **179**, 131-137.

106.   A. Velazquez Campoy and E. Freire, *Biophys. Chem.*, 2005, **115**, 115-124.

107.   G. A. Holdgate, *BioTechniques*, 2001, **31**, 164-184.

108.   I. Jelesarov and H. R. Bosshard, *J. Mol. Recognit.*, 1999, **12**, 3-18.

109.   J. E. Ladbury, *Thermochim. Acta*, 2001, **380**, 209-215.

110.   E. A. Lewis and K. P. Murphy, *Methods Mol. Biol.,* 2005, **305**, 1-15.

111.   F. P. Schmidtchen, in *Macrocyclic Chemistry*, ed. K. Gloe, Springer Netherlands, 2005, ch. 19, 291-302.

112.   P. C. Weber and F. R. Salemme, *Curr. Opin. Chem. Biol.*, 2003, **13**, 115-121.

113.   E. Freire, O. L. Mayorga and M. Straume, *Anal. Chem.*, 1990, **62**, 950A-959A.

114.   M. W. Freyer and E. A. Lewis, in *Methods in Cell Biology*, eds. J. C. Dr. John and Dr. H. William Detrich, III, Academic Press, 2008, vol. 84, 79-113.

115.   C. Spink and I. Wadso, *Methods Biochem. Anal.*, 1976, **23**, 1-159.

116.   M. J. Todd and J. Gomez, *Anal. Biochem.*, 2001, **296**, 179-187.

117.   B. A. Williams and E. J. Toone, *J. Org. Chem.*, 1993, **58**, 3507-3510.

118.   N. A. Demarse, M. C. Killian, L. D. Hansen and C. F. Quinn, *Methods Mol. Biol.*, 2013, **978**, 21-30.

119.   T. Ehtezazi, U. Rungsardthong and S. Stolnik, *Langmuir*, 2003, **19**, 9387-9394.

120.   M. Keller, M. R. Jorgensen, E. Perouzel and A. D. Miller, *Biochemistry*, 2003, **42**, 6067-6077.

121.   M. Keller, T. Tagawa, M. Preuss and A. D. Miller, *Biochemistry*, 2002, **41**, 652-659.

122.   D. Matulis, I. Rouzina and V. A. Bloomfield, *J. Am. Chem. Soc.*, 2002, **124**, 7331-7342.

123.   C. K. Nisha, S. V. Manorama, M. Ganguli, S. Maiti and J. N. Kizhakkedathu, *Langmuir*, 2004, **20**, 2386-2396.

124.   E. Pozharski and R. C. MacDonald, *Biophys. J.*, 2002, **83**, 556-565.

125.   U. Rungsardthong, T. Ehtezazi, L. Bailey, S. P. Armes, M. C. Garnett and S. Stolnik, *Biomacromolecules*, 2003, **4**, 683-690.

126.   D. R. Bundle and B. W. Sigurskjold, *Methods Enzymol.*, 1994, **247**, 288-305.

127.   P. Puja and K. S. Gopinatha, *Photochem. Photobiol. Sci.*, 2014,13, 1192-1202.

128.   E. Freire, *Drug Discovery Today: Technol.*, 2004, **1**, 295-299.

129.   L. Indyk and H. F. Fisher, *Methods Enzymol.*, 1998, **295**, 350-364.

130.   A. Ababou and J. E. Ladbury, *J. Mol. Recognit.*, 2007, **20**, 4-14.

131.   M. J. Cliff, A. Gutierrez and J. E. Ladbury, *J. Mol. Recognit.*, 2004, **17**, 513-523.

132.   J. E. Ladbury, *Biochem. Soc. Trans.*, 2010, **38**, 888-893.

133.   P. Hohenberg and W. Kohn, *Phys. Rev.*, 1964, **136**, B864-B871.

134. W. Kohn and L. J. Sham, *Phys. Rev.*, 1965, **140**, A1133-A1138.
135. A. D. Becke, *J. Chem. Phys*, 1993, **98**, 1372-1377.
136. O. Gunnarsson and B. I. Lundqvist, *Phys. Rev. B*, 1976, **13**, 4274-4298.
137. J. Harris, *Phys. Rev. A*, 1984 29, 1648.
138. P. M. W. Gill, R. D. Adamson and J. A. Pople, *Mol. Phys.*, 1996, **88**, 1005-1009.
139. A. Savin, *Theoretical and Computational Chemistry*, ed. J. M. Seminario, Elsevier, 1996, vol. 4, 327-357.
140. G. A. DiLabio and A. Otero-de-la-Roza, *arXiv:1405.1771 [physics.chem-ph]*, 2014.
141. P. W. Atkins, R. S. Friedman, *Molecular quantum mechanics*, Oxford University Press, New York, 2005.
142. H. B. G. Casimir and D. Polder, *Phys. Rev.*, 1948, **73**, 360-372.
143. Q. Wu and W. Yang, *J. Chem. Phys.*, 2002, **116**, 515-524.
144. T. A. Halgren, *J. Am. Chem. Soc.,* 1992, **114**, 7827-7843.
145. S. Grimme, *J. Comput. Chem.*, 2004, **25**, 1463-1473.
146. S. Grimme, *J. Comput. Chem.*, 2006, **27**, 1787-1799.
147. S. Grimme, J. Antony, S. Ehrlich and H. Krieg, *J. Chem. Phys.*, 2010, **132**, 154104.
148. A. Tkatchenko and M. Scheffler, *Phys. Rev. Lett.*, 2009, **102**, 073005/073001-073005/073004.
149. A. Otero-de-la-Roza and E. R. Johnson, *J. Chem. Phys.*, 2013, **138**, 054103.
150. J. Tao, J. P. Perdew and A. Ruzsinszky, *Proc. Nat. Acad. Sci.*, 2012, **109**, 18-21.
151. J. Tomasi, B. Mennucci and R. Cammi, *Chem. Rev.*, 2005, **105**, 2999-3093.
152. A. Klamt, *J. Phys. Chem.*, 1995, **99**, 2224-2235.
153. M. Born, *Z. Phys.*, 1920, **1**, 45-48.
154. J. G. Kirkwood, *J. Chem. Phys.*, 1934, **2**, 351-361.
155. L. Onsager, *J. Am. Chem. Soc.*, 1936, **58**, 1486-1493.
156. A. Bondi, *J. Phys. Chem.*, 1964, **68**, 441-451.
157. L. Pauling, *The chemical bond: a brief introduction to modern structural chemistry*, Cornell University Press, Ithaca, N.Y., 1967.
158. A. K. Rappe, C. J. Casewit, K. S. Colwell, W. A. Goddard, III and W. M. Skiff, *J. Am. Chem. Soc.*, 1992, **114**, 10024-10035.
159. M. L. Connolly, *Science*, 1983, **221**, 709-713.
160. M. L. Connolly, *J. Mol. Graph.*, 1993, **11**, 139-141.
161. A. Klamt and G. Schueuermann, *J. Chem. Soc., Perkin Trans. 2*, 1993, 799-805.
162. A. Klamt, V. Jonas, T. Bürger and J. C. W. Lohrenz, *J. Phys. Chem. A*, 1998, **102**, 5074-5085.
163. R. Putnam, R. Taylor, A. Klamt, F. Eckert and M. Schiller, *Ind. Eng. Chem. Res.*, 2003, **42**, 3635-3641.
164. COSMOlogic GmbH & Co. KG, Leverkusen, Germany, C3.0 Release 14.01 edn., December 2013.
165. E. Cances, B. Mennucci and J. Tomasi, *J. Chem. Phys.*, 1997, **107**, 3032-3041.
166. B. Mennucci, E. Cances and J. Tomasi, *J. Phys. Chem. B*, 1997, **101**, 10506-10517.
167. D. M. Chipman, *J. Chem. Phys.*, 1999, **110**, 8012-8018.
168. D. M. Chipman, *J. Chem. Phys.*, 2000, **112**, 5558-5565.
169. D. M. Chipman, *J. Chem. Phys.*, 2002, **116**, 10129-10138.
170. C.-G. Zhan, J. Bentley and D. M. Chipman, *J. Chem. Phys.*, 1998, **108**, 177-192.
171. J. G. Kirkwood, *J. Chem. Phys.*, 1939, **7**, 911-919.
172. K. V. Mikkelsen, H. Aagren, H. J. A. Jensen and T. Helgaker, *J. Chem. Phys.*, 1988, **89**, 3086-3095.
173. J. L. Rivail and D. Rinaldi, *Chem. Phys.*, 1976, **18**, 233-242.

174. M. W. Wong, M. J. Frisch and K. B. Wiberg, *J. Am. Chem. Soc.*, 1991, **113**, 4776-4782.

175. M. W. Wong, K. B. Wiberg and M. J. Frisch, *J. Am. Chem. Soc.*, 1992, **114**, 523-529.

176. D. Bashford and D. A. Case, *Annu. Rev. Phys. Chem.*, 2000, **51**, 129-152.

177. A. Onufriev, D. Bashford and D. A. Case, *J. Phys. Chem. B*, 2000, **104**, 3712-3720.

178. F. B. Sheinerman, R. Norel and B. Honig, *Curr. Opin. Struct. Biol.*, 2000, **10**, 153-159.

179. V. Tsui and D. A. Case, *Biopolymers*, 2001, **56**, 275-291.

180. T. Sato, T. Tsuneda and K. Hirao, *J. Chem. Phys.*, 2005, **123**, 104307/104301-104307/104310.

181. E. Yurtsever, *J. Phys. Chem. A*, 2009, **113**, 924-930.

182. M. Rubes, O. Bludsky and P. Nachtigall, *ChemPhysChem*, 2008, **9**, 1702-1708.

183. E. C. Lee, D. Kim, P. Jurecka, P. Tarakeshwar, P. Hobza and K. S. Kim, *J. Phys. Chem. A*, 2007, **111**, 3446-3457.

184. M. O. Sinnokrot and C. D. Sherrill, *J. Phys. Chem. A*, 2006, **110**, 10656-10668.

185. R. Podeszwa, R. Bukowski and K. Szalewicz, *J. Phys. Chem. A*, 2006, **110**, 10345-10354.

186. M. Pitonak, P. Neogrady, J. Rezac, P. Jurecka, M. Urban and P. Hobza, *J. Chem. Theory Comput.*, 2008, **4**, 1829-1834.

187. A. K. Tewari and R. Dubey, *Bioor. Med. Chem.*, 2008, **16**, 126-143.

188. J. Sponer, K. E. Riley and P. Hobza, *Phys.Chem. Chem. Phys.*, 2008, **10**, 2595-2610.

189. R. J. Terryn, H. W. German, T. M. Kummerer, R. R. Sinden, J. C. Baum and M. J. Novak, *Toxicol. Mech. Meth.*, 2014, **24**, 73-79.

190. P. Li, C. Zhao, M. D. Smith and K. D. Shimizu, *J. Org. Chem.*, 2013, **78**, 5303-5313.

191. H. Robson Marsden, J. G. E. M. Fraaije and A. Kros, *Angew. Chem., Int. Ed.*, 2010, **49**, 8570-8572.

192. W. B. Motherwell, J. Moise, A. E. Aliev, M. Nie, S. J. Coles, P. N. Horton, M. B. Hursthouse, G. Chessauri, C. A. Hunter and J. G. Vinter, *Angew. Chem., Int. Ed.*, 2007, **46**, 7823-7826.

193. W. B. Schweizer and J. D. Dunitz, *J. Chem. Theory Comput.*, 2006, **2**, 288-291.

194. J. Rezac and P. Hobza, *J. Chem. Theory Comput.*, 2008, **4**, 1835-1840.

195. S. Tsuzuki, K. Honda, T. Uchimaru, M. Mikami and K. Tanabe, *J. Am. Chem. Soc.*, 2002, **124**, 104-112.

196. M. O. Sinnokrot, E. F. Valeev and C. D. Sherrill, *J. Am. Chem. Soc.*, 2002, **124**, 10887-10893.

197. O. Bludsky, M. Rubes, P. Soldan and P. Nachtigall, *J. Chem. Phys.*, 2008, **128**, 114102/114101-114102/114108.

198. T. Janowski and P. Pulay, *Chem. Phys. Lett.*, 2007, **447**, 27-32.

199. H. F. Bettinger, T. Kar and E. Sanchez-Garcia, *J. Phys. Chem. A*, 2009, **113**, 3353-3359.

200. C. D. Sherrill, T. Takatani and E. G. Hohenstein, *J. Phys. Chem. A*, 2009, **113**, 10146-10159.

201. E. G. Hohenstein and C. D. Sherrill, *J. Phys. Chem. A*, 2009, **113**, 878-886.

202. I. Geronimo, E. C. Lee, N. J. Singh and K. S. Kim, *J. Chem. Theory Comput.*, 2010, **6**, 1931-1934.

203. P. Mignon, S. Loverix, F. De Proft and P. Geerlings, *J. Phys. Chem. A*, 2004, **108**, 6038-6044.

204. B. K. Mishra, J. S. Arey and N. Sathyamurthy, *J. Phys. Chem. A*, 2010, **114**, 9606-9616.

205. B. K. Mishra and N. Sathyamurthy, *J. Phys. Chem. A*, 2005, **109**, 6-8.

206. M. Piacenza and S. Grimme, *ChemPhysChem*, 2005, **6**, 1554-1558.
207. S. E. Wheeler, *J. Am. Chem. Soc.*, 2011, **133**, 10262-10274.
208. D. Sredojević, G. A. Bogdanović, Z. D. Tomić and S. D. Zarić, *CrystEngComm*, 2007, **9**, 793-798.
209. D. N. Sredojević, Z. D. Tomić and S. D. Zarić, *Cent. Eur. J. Chem.*, 2007, **5**, 20-31.
210. G. V. Janjic, D. Z. Veljkovic and S. D. Zaric, *Cryst. Growth Des.*, 2011, **11**, 2680-2683.
211. B. D. Ostojic, G. V. Janjic and S. D. Zaric, *Chem. Comm.*, 2008, 6546-6548.
212. Z. D. Tomic, V. M. Leovac, S. V. Pokorni, D. Zobel and S. D. Zaric, *Eur. J. Inorg. Chem.*, 2003, 1222-1226.
213. D. N. Sredojevic, Z. D. Tomic and S. D. Zaric, *Cent. Eur. J. Chem.*, 2007, **5**, 20-31.
214. H. Yuge, Y. Noda and T. Iwamoto, *Inorg. Chem.*, 1996, **35**, 1842-1848.
215. U. Abram, A. Castineiras, I. Garcia-Santos and R. Rodriguez-Riobo, *Eur. J. Inorg. Chem.*, 2006, 3079-3087.
216. P. D. W. Boyd and A. Hosseini, *Acta Crystallogr., Sect. E: Struct. Rep. Online*, 2006, **E62**, o2081-o2083.
217. J. Granifo, M. Vargas, M. T. Garland, A. Ibanez, R. Gavino and R. Baggio, *Inorg. Chem. Comm.*, 2008, **11**, 1388-1391.
218. Y.-F. Jiang, C.-J. Xi, Y.-Z. Liu, J. Niclos-Gutierrez and D. Choquesillo-Lazarte, *Eur. J. Inorg. Chem.*, 2005, 1585-1588.
219. V. Philip, V. Suni, M. R. P. Kurup and M. Nethaji, *Polyhedron*, 2004, **23**, 1225-1233.
220. S. D. Stojanovic, V. B. Medakovic, G. Predovic, M. Beljanski and S. D. Zaric, *J. Biol. Inorg. Chem.*, 2007, **12**, 1063-1071.
221. H. Tsubaki, S. Tohyama, K. Koike, H. Saitoh and O. Ishitani, *Dalton Trans.*, 2005, 385-395.
222. D. Sredojevic, G. A. Bogdanovic, Z. D. Tomic and S. D. Zaric, *CrystEngComm*, 2007, **9**, 793-798.
223. M. Chandrasekharam, M. A. Reddy, S. P. Singh, B. Priyanka, K. Bhanuprakash, M. L. Kantam, A. Islam and L. Han, *J. Mater. Chem.*, 2012, **22**, 18757-18760.
224. J. G. Cordaro, J. K. McCusker and R. G. Bergman, *Chem. Comm.*, 2002, 1496-1497.
225. M. E. Hagerman, S. J. Salamone, R. W. Herbst and A. L. Payeur, *Chem. Mater.*, 2003, **15**, 443-450.
226. Y. Ma, Y. Gao, Y. Wang, Y. Li and X. Yang, *Mod. Appl. Sci.*, 2011, **5**, 232-235.
227. G. R. Newkome, A. K. Patri, E. Holder and U. S. Schubert, *Eur. J. Org. Chem.*, 2004, 235-254.
228. M. J. Scott, J. J. Nelson, S. Caramori, C. A. Bignozzi and C. M. Elliott, *Inorg. Chem.*, 2007, **46**, 10071-10078.
229. B. Zhang, S. Shi, W. Shi, Z. Sun, X. Kong, M. Wei and X. Duan, *Electrochim. Acta*, 2012, **67**, 133-139.
230. U. S. Schubert, C. Eschbaumer and G. Hochwimmer, *Tetrahedron Lett.*, 1998, **39**, 8643-8644.
231. U. S. Schubert, J. L. Kersten, A. E. Pemp, C. D. Eisenbach and G. R. Newkome, *Eur. J. Org. Chem.*, 1998, 2573-2581.
232. A. Luetzen, M. Hapke, H. Staats and J. Bunzen, *Eur. J. Org. Chem.*, 2003, 3948-3957.
233. Y. Sato and K. Uosaki, *J. Electroanal. Chem.*, 1995, **384**, 57-66.
234. M. Su and S. Liu, *Anal. Biochem.*, 2010, **402**, 1-12.
235. F. Dimiza, F. Perdih, V. Tangoulis, I. Turel, D. P. Kessissoglou and G. Psomas, *J. Inorg. Biochem.*, 2011, **105**, 476-489.
236. X.-L. Hong, Z.-H. Liang and M.-H. Zeng, *J. Coord. Chem.*, 2011, **64**, 3792-3807.
237. M. N. Patel, P. A. Dosi and B. S. Bhatt, *J. Coord. Chem.*, 2012, **65**, 3833-3844.

238.   A. L. Balch and J. Miller, *J. Organomet. Chem.*, 1971, **32**, 263-268.

239.   P. R. Branson and M. Green, *J. Chem. Soc., Dalton Trans.*, 1972, 1303-1310.

240.   J. W. Dart, M. K. Lloyd, J. A. McCleverty and R. Mason, *J. Chem. Soc. D*, 1971, 1197-1198.

241.   A. L. Balch and M. M. Olmstead, *J. Am. Chem. Soc.*, 1976, **98**, 2354-2356.

242.   N. S. Lewis, K. R. Mann, J. G. Gordon, II and H. B. Gray, *J. Am. Chem. Soc.*, 1976, **98**, 7461-7463.

243.   K. R. Mann, J. G. Gordon, II and H. B. Gray, *J. Am. Chem. Soc.*, 1975, **97**, 3553-3555.

244.   J. A. McCleverty and J. Williams, *Transition Met. Chem.*, 1978, **3**, 205-211.

245.   V. M. Miskowski, G. L. Nobinger, D. S. Kliger, G. S. Hammond, N. S. Lewis, K. R. Mann and H. B. Gray, *J. Am. Chem. Soc.*, 1978, **100**, 485-488.

246.   S. Miya, Y. Yamamoto and H. Yamazaki, *Inorg. Chem.*, 1982, **21**, 1486-1488.

247.   I. S. Sigal and H. B. Gray, *J. Am. Chem. Soc.*, 1981, **103**, 2220-2225.

248.   A. L. Balch and V. J. Catalano, *Inorg. Chem.*, 1992, **31**, 3934-3942.

249.   V. M. Miskowski, T. P. Smith, T. M. Loehr and H. B. Gray, *J. Am. Chem. Soc.*, 1985, **107**, 7925-7934.

250.   S. F. Rice and H. B. Gray, *J. Am. Chem. Soc.*, 1981, **103**, 1593-1595.

251.   C.-K. Koo, K.-L. Wong, K.-C. Lau, W.-Y. Wong and M. H.-W. Lam, *Chem. Eur. J.*, 2009, **15**, 7689-7697.

252.   K. R. Mann, J. A. Thich, R. A. Bell, C. L. Coyle and H. B. Gray, *Inorg. Chem.*, 1980, **19**, 2462-2468.

253.   G. S. Rodman and K. R. Mann, *Inorg. Chem.,* 1988, **27**, 3338-3346.

254.   A. E. Stiegman, S. F. Rice, H. B. Gray and V. M. Miskowski, *Inorg. Chem.* , 1987, **26**, 1112-1116.

255.   J. R. Winkler, J. L. Marshall, T. L. Netzel and H. B. Gray, *J. Am. Chem. Soc.*, 1986, **108**, 2263-2266.

256.   G. L. Geoffroy, M. S. Wrighton, G. S. Hammond and H. B. Gray, *J. Am. Chem. Soc.*, 1974, **96**, 3105-3108.

257.   S. F. Rice, S. J. Milder, H. B. Gray, R. A. Goldbeck and D. S. Kliger, *Coord. Chem. Rev.*, 1982, **43**, 349-354.

258.   S. K. Doorn, K. C. Gordon, R. B. Dyer and W. H. Woodruff, *Inorg. Chem.*, 1992, **31**, 2284-2285.

259.   S. J. Milder, *Inorg. Chem.,* 1985, **24**, 3376-3378.

260.   S. J. Milder and D. S. Kliger, *J. Phys. Chem.*, 1985, **89**, 4170-4171.

261.   S. Oberneder and G. Gliemann, *J. Phys. Chem.*, 1989, **93**, 4487-4489.

262.   P. V. Yaneff and J. Powell, *J. Organomet. Chem.* , 1979, **179**, 101-113.

263.   S. Fukuzumi, N. Nishizawa and T. Tanaka, *Bull. Chem. Soc. Jpn.*, 1982, **55**, 2892-2897.

264.   S. Fukuzumi, N. Nishizawa and T. Tanaka, *Bull. Chem. Soc. Jpn.*, 1982, **55**, 3482-3490.

265.   M. G. Hill, W. M. Lamanna and K. R. Mann, *Inorg. Chem.*, 1991, **30**, 4687-4690.

266.   M. G. Hill, J. P. Bullock, T. Wilson, P. Bacon, C. A. Blaine and K. R. Mann, *Inorg. Chim. Acta*, 1994, **226**, 61-68.

267.   M. G. Hill and K. R. Mann, *Catal. Lett.*, 1991, **11**, 341-347.

268.   M. R. Rhodes and K. R. Mann, *Inorg. Chem.*, 1984, **23**, 2053-2058.

269.   A. L. Balch and M. M. Olmstead, *J. Am. Chem. Soc.*, 1979, **101**, 3128-3129.

270.   H. B. Gray, V. M. Miskowski, S. J. Milder, T. P. Smith, A. W. Maverick, J. D. Buhr, W. L. Gladfelter, I. S. Sigal and K. R. Mann, *Fundamental Research in Homogeneous Catalysis*, ed. M. Tsutsui, Springer US, 1979, 819-834.

271.   K. R. Mann, R. A. Bell and H. B. Gray, *Inorg. Chem.*, 1979, **18**, 2671-2673.

272. K. R. Mann, M. J. DiPierro and T. P. Gill, *J. Am. Chem. Soc.*, 1980, **102**, 3965-3967.

273. I. S. Sigal, K. R. Mann and H. B. Gray, *J. Am. Chem. Soc.*, 1980, **102**, 7252-7256.

274. A. W. Maverick, T. P. Smith, E. F. Maverick and H. B. Gray, *Inorg. Chem.*, 1987, **26**, 4336-4341

275. X. Shen, Y. Yamaguchi, K. Sakata and M. Hashimoto, *Anal. Sci.: X-Ray Struct. Anal. Online*, 2005, **21**, x75-x76.

276. H. Endres, N. Gottstein, H. J. Keller, R. Martin, W. Rodemer and W. Steiger, *Zeitschrift Fur Naturforschung, Section Ba, J. Chem. Sci.*, 1979, **34**, 827-833.

277. M. M. Olmstead and A. L. Balch, *J. Organomet. Chem.*, 1978, **148**, C15-C18.

278. N. T. Tran, J. R. Stork, D. Pham, C. J. Chancellor, M. M. Olmstead, J. C. Fettinger and A. L. Balch, *Inorg. Chem.*, 2007, **46**, 7998-8007.

279. N. T. Tran, J. R. Stork, D. Pham, M. M. Olmstead, J. C. Fettinger and A. L. Balch, *Chem. Comm.*, 2006, 1130-1132.

280. D. T. Plummer, B. A. Karcher, R. A. Jacobson and R. J. Angelici, *J. Organomet. Chem.* , 1984, **260**, 347-362.

281. Y. Yamamoto, K. Aoki and H. Yamazaki, *Inorg. Chem.*, 1979, **18**, 1681-1687.

282. P. Coppens, O. Gerlits, I. I. Vorontsov, A. Y. Kovalevsky, Y.-S. Chen, T. Graber, M. Gembicky and I. V. Novozhilova, *Chem. Comm.*, 2004, 2144-2145.

283. I. V. Novozhilova, A. V. Volkov and P. Coppens, *Inorg. Chem.*, 2004, **43**, 2299-2307.

284. C. L. Exstrom, D. Britton, K. R. Mann, M. G. Hill, V. M. Miskowski, W. P. Schaefer, H. B. Gray and W. M. Lamanna, *Inorg. Chem.*, 1996, **35**, 549-550.

285. M. Fetterolf, A. E. Friedman, Y. Y. Yang, H. Offen and P. C. Ford, *J. Phys. Chem.*, 1988, **92**, 3760-3763.

286. R. F. Dallinger, M. J. Carlson, V. M. Miskowski and H. B. Gray, *Inorg. Chem.*, 1998, **37**, 5011-5013.

287. O. Gerlits, A. Y. Kovalevsky and P. Coppens, *Dalton Trans.*, 2004, 3955-3962.

288. V. M. Miskowski, S. F. Rice, H. B. Gray, R. F. Dallinger, S. J. Milder, M. G. Hill, C. L. Exstrom and K. R. Mann, *Inorg. Chem.*, 1994, **33**, 2799-2807.

289. M. G. Hill and K. R. Mann, *Inorg. Chim. Acta*, 1996, **243**, 219-228.

290. D. C. Smith, V. M. Miskowski, W. R. Mason and H. B. Gray, *J. Am. Chem. Soc.*, 1990, **112**, 3759-3767.

291. J. J. Novoa, G. Aullon, P. Alemany and S. Alvarez, *J. Am. Chem. Soc.*, 1995, **117**, 7169-7171.

292. S. Grimme and J.-P. Djukic, *Inorg. Chem.*, 2011, **50**, 2619-2628.

293. B. Lippert, *Cisplatin: Chemistry and Biochemistry of a leading anticancer drug*, Verlag Helvetica Chimica Acta, Zurich, 1999.

294. M. E. Alberto, V. Butera and N. Russo, *Inorg. Chem.*, 2011, **50**, 6965-6971.

295. S. G. Chaney, S. L. Campbell, E. Bassett and Y. Wu, *Crit. Rev. Oncol. Hematol.*, 2005, **53**, 3–11.

296. I. Ott and R. Gust, *Anticancer Agents Med. Chem.*, 2007, **7**, 95-110.

297. J. Peng, R. Mandal, M. Sawyer and X.-F. Li, *Clin. Chem.*, 2005, **51**, 2274–2281.

298. D. M. Kweekel, H. Gelderblom and H. J. Guchelaar, *Cancer Treatment Rev.*, 2005, **31**, 90-105.

299. A. J. Di Pasqua, D. J. Kerwood, Y. Shi, J. Goodisman and J. C. Dabrowiak, *Dalton Trans.*, 2011, **40**, 4821-4825.

300. M. Lederer and E. Leipzig-Pagani, *Int. J. Pharmaceutics*, 1998, **167**, 223–228.

301. M. F. A. Lucas, M. Pavelka, M. E. Alberto and N. Russo, *J. Phys. Chem. B*, 2009, **113**, 831-838.

302. M. Pavelka, M. F. A. Lucas and N. Russo, *Chem. Eur. J.*, 2007, **13**, 10108 - 10116.

303. P. Videhult, J. Yachnin, E. Jerremalm, R. Lewensohn and H. Ehrsson, *Cancer Lett.*, 2002, **180**, 191-194.

304. R. B. Burns, R. W. Burton, S. P. Albon and L. Embree, *J. Pharm. Biomed. Anal.*, 1996, **14**, 367-372.

305. M. A. Bruck, R. Bau, M. Noji, K. Inagaki and Y. Kidani, *Inorg. Chim. Acta*, 1984, **92**, 279-284.

306. M. Galanski, A. Yasemi, S. Slaby, M. A. Jakupec, V. B. Arion, M. Rausch, A. A. Nazarov and B. K. Keppler, *Eur. J. Med. Chem.*, 2004, **39**, 707-714.

307. T. Schwabe, S. Grimme and J.-P. Djukic, *J. Am. Chem. Soc.*, 2009, **131**, 14156-14157.

308. C. Werle, M. Hamdaoui, C. Bailly, G. X.-F. Le, L. Brelot and J.-P. Djukic, *J. Am. Chem. Soc.*, 2013, **135**, 1715-1718.

309. D. R. Alston, T. H. Lilley and J. F. Stoddart, *J. Chem. Soc., Chem. Commun.*, 1985, 1600-1602.

310. G. Hettiarachchi, D. Nguyen, J. Wu, D. Lucas, D. Ma, L. Isaacs and V. Briken, *PLoS ONE*, 2010, **5**, e10514.

311. K. Uekama, F. Hirayama and T. Irie, *Chem. Rev.*, 1998, **98**, 2045-2076.

312. A. D. McNaught and A. Wilkinson, *IUPAC. Compendium of Chemical Terminology, 2nd ed. (the "Gold Book")*, Blackwell Scientific Publications, Oxford, 1997, doi:10.1351/goldbook.I02998.

313. K. Kim and H.-J. Kim*, Encyclopedia of Supramolecular Chemistry,* ed. A. Steed, Marcel Dekker Inc., New York, 2004, 390.

314. W. L. Mock, *Comperhensive Supramolecular Chemistry*, Pergamon, Oxford, 1996, *Vol **2**.,* 477.

315. H. J. Buschmann, E. Cleve and E. Schollmeyer, *Inorg. Chim. Acta*, 1992, **193**, 93-97.

316. Y.-M. Jeon, J. Kim, D. Whang and K. Kim, *J. Am. Chem. Soc.*, 1996, **118**, 9790-9791.

317. C. Márquez, R. R. Hudgins and W. M. Nau, *J. Am. Chem. Soc.*, 2004, **126**, 5806-5816.

318. O. A. Gerasko, D. G. Samsonenko and V. P. Fedin, *Russian Chem. Rev.* 2002, **71**, (9), 741–760.

319. K. Kim, *Chem. Soc. Rev.*, 2002, **31**, 96-107.

320. A. Day, A. P. Arnold, R. J. Blanch and B. Snushall, *J. Org. Chem.*, 2001, **66**, 8094-8100.

321. S. Kim, H.-J. Song, T.-L. Choi and J.-Y. Yoon, *Angew. Chem., Int. Ed.*, 2001, **40**, 2524-2526.

322. J. W. Lee, S. Samal, N. Selvapalam, H.-J. Kim and K. Kim, *Acc. Chem. Res.*, 2003, **36**, 621-630.

323. S. Yi, W. Li, D. Nieto, I. Cuadrado and A. E. Kaifer, *Org. Biomol. Chem.*, 2013, **11**, 287-293.

324. R. J. Blanch, A. J. Sleeman, T. J. White, A. P. Arnold and A. I. Day, *Nano Lett.*, 2002, **2**, 147-149.

325. Y. J. Jeon, S.-Y. Kim, Y. H. Ko, S. Sakamoto, K. Yamaguchi and K. Kim, *Org. Biomol. Chem.*, 2005, **3**, 2122-2125.

326. V. J. Catalano, B. L. Bennett and B. C. Noll, *Chem. Commun.*, 2000, 1413-1414.

327. C.-M. Che and S.-W. Lai, *Coord. Chem. Rev.*, 2005, **249**, 1296-1309.

328. E. Fernandez, K. Maeda, M. W. Hooper and J. M. Brown, *Chem. Eur. J.*, 2000, **6**, 1840-1846.

329. P. Pyykkö and F. Mendizabal, *Inorg. Chem.*, 1998, **37**, 3018-3025.

330. S. Sharma, R. S. Baligar, H. B. Singh and R. J. Butcher, *Angew. Chem., Int. Ed.*, 2009, **48**, 1987-1990.

331. B. Assadollahzadeh and P. Schwerdtfeger, *Chem. Phys. Lett.*, 2008, **462**, 222-228.

332. R. Jószai, I. Beszeda, A. C. Bényei, A. Fischer, M. Kovács, M. Maliarik, P. Nagy, A. Shchukarev and I. Tóth, *Inorg. Chem.*, 2005, **44**, 9643-9651.

333. A. Otero-de-la-Roza, J. D. Mallory and E. R. Johnson, *J. Chem. Phys.*, 2014, **140**, 18A504.

334. P. Pyykkö, *Chem. Rev.*, 1997, **97**, 597-636.

335. S.-G. Wang and W. H. E. Schwarz, *J. Am. Chem. Soc.*, 2004, **126**, 1266-1276.

336. E. J. Fernández, A. Laguna, J. M. López-de-Luzuriaga, M. Monge, M. Montiel, M. E. Olmos and M. Rodríguez-Castillo, *Dalton Trans.*, 2009, 7509-7518.

337. J.-M. Poblet and M. Bénard, *Chem. Commun.*, 1998, 1179-1180.

338. J.-P. Zhang, Y.-B. Wang, X.-C. Huang, Y.-Y. Lin and X.-M. Chen, *Chem. Eur. J.*, 2005, **11**, 552-561.

339. S. Grimme and J.-P. Djukic, *Inorg. Chem.*, 2010, **49**, 2911-2919.

340. I. Hyla-Kryspin, S. Grimme and J.-P. Djukic, *Organometallics*, 2009, **28**, 1001-1013.

341. W. Iali, P. Petrovic, M. Pfeffer, S. Grimme and J.-P. Djukic, *Dalton Trans.* 2012, **41**, 12233-12243.

342. N. Marom, A. Tkatchenko, M. Scheffler and L. Kronik, *J. Chem. Theory Comput.*, 2010, **6**, 81-90.

343. C. Werlé, C. Bailly, L. Karmazin-Brelot, X.-F. Le Goff, L. Ricard and J.-P. Djukic, *J. Am. Chem. Soc.*, 2013, **135**, 17839-17852.

344. E. C. Constable, *Polyhedron*, 1984, **3**, 1037-1057.

345. J. Dehand and M. Pfeffer, *Coord. Chem. Rev.*, 1976, **18**, 327-352.

346. V. V. Dunina, O. A. Zalevskaya and V. M. Potapov, *Russian Chem. Rev.*, 1988, **57**, 250-269.

347. D. W. Evans, G. R. Baker and G. R. Newkome, *Coord. Chem. Rev.*, 1989, **93**, 155-183.

348. G. R. Newkome, W. E. Puckett, V. K. Gupta and G. E. Kiefer, *Chem. Rev.*, 1986, **86**, 451-489.

349. A. D. Ryabov, V. A. Polyakov and A. K. Yatsimirsky, *J. Chem. Soc., Perkin Trans. 2*, 1983, 1503-1509.

350. A. D. Ryabov, R. Van Eldik, G. Le Borgne and M. Pfeffer, *Organometallics*, 1993, **12**, 1386-1393.

351. A. D. Ryabov, *Synthesis*, 1985, **1985**, 233-252.

352. A. J. Deeming, I. P. Rothwell, M. B. Hursthouse and L. New, *J. Chem. Soc., Dalton Trans.*, 1978, 1490-1496.

353. L. I. Elding and L. F. Olsson, *Inorg. Chem.* , 1977, **16**, 2789-2794.

354. M. M. Muir and E. M. Cancio, *Inorg. Chim. Acta*, 1970, **4**, 565-567.

355. R. G. Pearson and M. M. Muir, *J. Am. Chem. Soc.*, 1966, **88**, 2163-2166.

356. M. Pfeffer, J. P. Sutter, A. DeCian and J. Fischer, *Organometallics*, 1993, **12**, 1167-1173.

357. P. S. Pregosin, R. Rüedi and C. Anklin, *Magn. Reson. Chem.*, 1986, **24**, 255-258.

358. D. Brown and B. McMahon, *Acta Crystallogr.*, 2002, 317-324.

359. S. R. Hall, F. H. Allen and I. D. Brown, *Acta Crystallogr. Sect. A*, 1991, **47**, 655-685.

360. F. H. Allen, *Acta Crystallogr. Sect. B: Struct. Sci.*, 2002, **B58**, 380-388.

361. A. G. Orpen, *Acta Crystallogr. Sect. B: Struct. Sci.*, 2002, **58**, 398-406.

362. M. Taylor, S. Menzer, J. Wall, S. Bates and G. Fraser, *Acta Crystallogr. Sect. A*, 2002, **58**, c185.

363. J. Lj. Dragelj, G. V. Janjić, D. Ž. Veljković, S. D. Zarić, *CrystEngComm*, 2013, 15, 10481-10489.

364. M. Nishio, *CrystEngComm*, 2004, **6**, 130-158.

365. F. H. Allen, J. E. Davies, J. J. Galloy, O. Johnson, O. Kennard, C. F. Macrae, E. M. Mitchell, G. F. Mitchell, J. M. Smith and D. G. Watson, *J. Chem. Inform. Comput. Sci.*, 1991, **31**, 187-204.

366. J.-D. Chai and M. Head-Gordon, *Phys. Chem. Chem. Phys.*, 2008, **10**, 6615-6620.

367. B. M. Axilrod and E. Teller, *J. Chem. Phys.*, 1943, **11**, 299-300.

368. Y. Muto, *J. Phys.-Math. Soc. Japan.*, 1943, **17**, 629-631.

369. S. Grimme, *Chem. Eur. J.*, 2012, **18**, 9955-9964.

370. M. J. Frisch, G. W. Trucks, H. B. Schlegel, G. E. Scuseria, M. A. Robb, J. R. Cheeseman, G. Scalmani, V. Barone, B. Mennucci, G. A. Petersson, H. Nakatsuji, M. Caricato, X. Li, H. P. Hratchian, A. F. Izmaylov, J. Bloino, G. Zheng, J. L. Sonnenberg, M. Hada, M. Ehara, K. Toyota, R. Fukuda, J. Hasegawa, M. Ishida, T. Nakajima, Y. Honda, O. Kitao, H. Nakai, T. Vreven, J. A. Montgomery, Jr., J. E. Peralta, F. Ogliaro, M. Bearpark, J. J. Heyd, E. Brothers, K. N. Kudin, V. N. Staroverov, R. Kobayashi, J. Normand, K. Raghavachari, A. Rendell, J. C. Burant, S. S. Iyengar, J. Tomasi, M. Cossi, N. Rega, N. J. Millam, M. Klene, J. E. Knox, J. B. Cross, V. Bakken, C. Adamo, J. Jaramillo, R. Gomperts, R. E. Stratmann, O. Yazyev, A. J. Austin, R. Cammi, C. Pomelli, J. W. Ochterski, R. L. Martin, K. Morokuma, V. G. Zakrzewski, G. A. Voth, P. Salvador, J. J. Dannenberg, S. Dapprich, A. D. Daniels, Ö. Farkas, J. B. Foresman, J. V. Ortiz, J. Cioslowski and D. J. Fox, *Gaussian, Inc., Wallingford CT, 2009*.

371. J. Tao, J. P. Perdew, V. N. Staroverov and G. E. Scuseria, *Phys. Rev. Lett.,* 2003, **91**, 146401/146401-146401/146404.

372. F. Weigend and R. Ahlrichs, *Phys. Chem. Chem. Phys.,* 2005, **7**, 3297-3305.

373. M. Dolg, U. Wedig, H. Stoll and H. Preuss, *J. Chem. Phys.*, 1987, **86**, 866-872.

374. S. F. Boys and F. Bernardi, *Mol. Phys.*, 1970, **19**, 553-566.

375. S. F. Sousa, P. A. Fernandes and M. J. Ramos, *J. Phys. Chem. A*, 2007, **111**, 10439-10452.

376. X. Yang and M. B. Hall, *J. Am. Chem. Soc.*, 2010, **132**, 120-130.

377. A. D. Becke, *Phys. Rev. A Gen. Phys.*, 1988, **38**, 3098-3100.

378. C. Lee, W. Yang and R. G. Parr, *Phys. Rev. B: Condens. Matter Mater. Phys.*, 1988, **37**, 785-789.

379. A. D. Becke and E. R. Johnson, *J. Chem. Phys.*, 2005, **122**, 154104.

380. E. R. Johnson and A. D. Becke, *J. Chem. Phys.*, 2006, **124**, 174104.

381. J. P. Perdew, K. Burke and M. Ernzerhof, *Phys. Rev. Lett.*, 1996, **77**, 3865-3868.

382. J. P. Perdew, K. Burke and M. Ernzerhof, *Phys. Rev. Lett.*, 1997, **78**, 1396.

383. C. F. Guerra, J. G. Snijders, G. Te Velde and E. J. Baerends, *Theo. Chem. Acc.*, 1998, **99**, 391-403.

384. E. J. Baerends, T. Ziegler, J. Autschbach, D. Bashford, A. Bérces, F. M. Bickelhaupt, C. Bo, P. M. Boerrigter, L. Cavallo, D. P. Chong, L. Deng, R. M. Dickson, D. E. Ellis, M. vanFaassen, L. Fan, T. H. Fischer, C. F. Guerra, A. Ghysels, A. Giammona, S. J. A. vanGisbergen, A. W. Götz, J. A. Groeneveld, O. V. Gritsenko, M. Grüning, S. Gusarov, F. E. Harris, P. vandenHoek, C. R. Jacob, H. Jacobsen, L. Jensen, J. W. Kaminski, G. vanKessel, F. Kootstra, A. Kovalenko, M. V. Krykunov, E. vanLenthe, D. A. McCormack, A. Michalak, M. Mitoraj, J. Neugebauer, V. P. Nicu, L. Noodleman, V. P. Osinga, S. Patchkovskii, P. H. T. Philipsen, D. Post, C. C. Pye, W. Ravenek, J. I. Rodríguez, P. Ros, P. R. T. Schipper, G. Schreckenbach, J. S. Seldenthuis, M. Seth, J. G. Snijders, M. Solà, M. Swart, D. Swerhone, G. teVelde, P. Vernooijs, L. Versluis, L. Visscher, O. Visser, F. Wang, T. A. Wesolowski, E. M. vanWezenbeek, G. Wiesenekker, S. K. Wolff, T. K. Woo and A. L. Yakovlev,

Amsterdam Density Functional, 2012, SCM, Theoretical Chemistry, Vrije Universiteit, Amsterdam, The Netherlands.

385. E. van Lenthe, A. Ehlers and E.-J. Baerends, *J. Chem. Phys.*, 1999, **110**, 8943-8953.
386. E. van Lenthe and E. J. Baerends, *J. Comput. Chem.*, 2003, **24**, 1142-1156.
387. A. Klamt and V. Jonas, *J. Chem. Phys.*, 1996, **105**, 9972-9981.
388. C. C. Pye, T. Ziegler, E. van Lenthe and J. N. Louwen, *Can. J. Chem.*, 2009, **87**, 790-797.
389. E. D. Glendening, J. K. Badenhoop, A. E. Reed, J. E. Carpenter, J. A. Bohmann, C. M. Morales and F. Weinhold, NBO 5.0, *Theoretical Chemistry Institute, University of Wisconsin, Madison, WI*, 2001.
390. M. P. Mitoraj, A. Michalak and T. Ziegler, *J. Chem. Theory Comput.*, 2009, **5**, 962-975.
391. J. Contreras-García, E. R. Johnson, S. Keinan, R. Chaudret, J.-P. Piquemal, D. N. Beratan and W. Yang, *J. Chem. Theory Comput.*, 2011, **7**, 625-632.
392. E. R. Johnson, S. Keinan, P. Mori-Sánchez, J. Contreras-García, A. J. Cohen and W. Yang, *J. Am. Chem. Soc.*, 2010, **132**, 6498-6506.
393. A. Savin, R. Nesper, S. Wengert and T. F. Fassler, *Angew. Chem., Int. Ed. Engl.*, 1997, **36**, 1808-1832.
394. C. Møller and M. S. Plesset, *Phys. Rev.*, 1934, **46**, 618-622.
395. J. Čížek, *J. Chem. Phys.*, 1966, **45**, 4256-4266.
396. J. Čížek and J. Paldus, *Int. J. Quantum Chem.*, 1971, **5**, 359-379.
397. J. Paldus, J. Čížek and I. Shavitt, *Phys. Rev. A*, 1972, **5**, 50-67.
398. R. J. Bartlett and M. Musiał, *Rev. Mod. Phys.*, 2007, **79**, 291-352.
399. K. Raghavachari, G. W. Trucks, J. A. Pople and M. Head-Gordon, *Chem. Phys. Lett.*, 1989, **157**, 479-483.
400. I. D. Mackie and G. A. DiLabio, *J. Chem. Phys.*, 2011, **135**.
401. R. A. Kendall, T. H. D. Jr and R. J. Harrison, *J. Chem. Phys.*, 1992, **96**, 6796-6806.
402. D. E. Woon and T. H. D. Jr, *J. Chem. Phys.*, 1993, **98**, 1358-1371.
403. M. O. Sinnokrot and C. D. Sherrill, *J. Phys. Chem. A*, 2004, **108**, 10200-10207.
404. S. Kishi and M. Kato, *Inorg. Chem.*, 2003, **42**, 8728-8734.
405. T. N. Fedotova, G. G. Aleksandrov and G. N. Kuznetsova, *Zh. Neorg. Khim.*, 2006, **51**, 601-608.
406. E. H. de Oliveira, G. E. A. Medeiros, C. Peppe, M. A. Brown and D. G. Tuck, *Can. J. Chem.*, 1997, **75**, 499-506.
407. G. M. Kapteijn, D. M. Grove, G. van Koten, W. J. J. Smeets and A. L. Spek, *Inorg. Chim. Acta*, 1993, **207**, 131-134.
408. K. Sakai, M. Mizota and N. Akiyama, *Acta Crystallogr., Sect. E: Struct.Rep. Online*, 2004, **E60**, m88-m90.
409. P. Binger, M. J. Doyle, J. McMeeking, C. Krueger and Y.-H. Tsay, *J. Organomet. Chem.*, 1977, **135**, 405-414.
410. J. Vicente, J.-A. Abad, F. S. Hernandez-Mata, B. Rink, P. G. Jones and M. C. Ramirez de Arellano, *Organometallics*, 2004, **23**, 1292-1304.
411. S. M. Dibrov and R. E. Bachman, *Inorg. Chim. Acta*, 2004, **357**, 1198-1204.
412. W. P. Weber, G. W. Gokel and I. K. Ugi, *Angew. Chem., Int. Ed. Engl.*, 1972, **11**, 530-531.
413. C. M. Starks, *J. Am. Chem. Soc.*, 1971, **93**, 195-199.
414. R. W. Stephany, M. J. A. d. Bie and W. Drenth, *Org. Mag. Res.*, 1974, **6**, 45-47.
415. K. R. Mann, N. S. Lewis, R. M. Williams, H. B. Gray and J. G. Gordon, II, *Inorg. Chem.*, 1978, **17**, 828-834.

416. S. J. Berners-Price and T. G. Appleton, *Platinum-Based Drugs in Cancer Therapy*, eds. L. R. Kheland and N. P. Farrell, Humana Press, Totowa, New Jersey, 1999, 3-35.
417. P. D. Prenzler and W. D. McFadyen, *J. Inorg. Biochem.*, 1997, **68**, 279-282.
418. B. Petrovic, Z. D. Bugarcic and R. vanEldik, *Dalton Trans.*, 2008, 807-813.
419. K. F. Morris and C. S. Johnson, *J. Am. Chem. Soc.*, 1992, **114**, 3139-3141.
420. S. E. Harding, *Biophys. Chem.*, 1995, **55**, 69-93.
421. L. Allouche, A. Marquis and J.-M. Lehn, *Chem. Eur. J.*, 2006, **12**, 7520 - 7525.
422. S. Hansen, *J. Chem. Phys.*, 2004, **121**, 9111-9115.
423. F. Perrin, *J. Phys. Radium*, 1934 **5**, 497-511.
424. S. D. Burrows, M. L. Doyle, K. P. Murphy, S. G. Franklin, J. R. White, I. Brooks, D. E. McNulty, M. O. Scott, J. R. Knutson, D. Porter, P. R. Young and P. Hensley, *Biochemistry*, 1994, **33**, 12741-12745.
425. G. M. K. Poon, *Anal. Biochem.*, 2010, **400**, 229-236.
426. A. S. Abu-Surrah, T. A. K. Al-Allaf, M. Klinga and M. Ahlgren, *Polyhedron* 2003, **22**, 1529-1534.
427. F. M. Bickelhaupt and E. J. Baerends, *Rev. Comput. Chem.*, 2000, **15**, 1-86.
428. T. Ziegler and A. Rauk, *Inorg. Chem.*, 1979, **18**, 1558-1565.
429. K. B. Wiberg, *Tetrahedron*, 1968, **24**, 1083-1096.
430. A. D. Becke and K. E. Edgecombe, *J. Chem. Phys.*, 1990, **92**, 5397-5403.
431. M. Bühl, C. Reimann, D. A. Pantazis, T. Bredow and F. Neese, *J. Chem. Theory Comput.*, 2008, **4**, 1449-1459.
432. Y. Minenkov, Å. Singstad, G. Occhipinti and V. R. Jensen, *Dalton Trans.,* 2012, **41**, 5526-5541.
433. K. K. Pandey, S. K. Patidar, P. Patidar, R. Vishwakarma and P. K. Bariya, *Z. Anorg. Allg. Chem.*, 2014, **640**, 370-379.
434. J. Řezáč and P. Hobza, *J. Chem. Theory Comput.*, 2013, **9**, 2151-2155.
435. W. Hujo and S. Grimme, *Phys. Chem. Chem. Phys.*, 2011, **13**, 13942-13950.
436. O. A. Vydrov and T. Van Voorhis, *J. Chem. Phys.*, 2010, **133**, 44103-44103.
437. F. Biedermann, V. D. Uzunova, O. A. Scherman, W. M. Nau and A. De Simone, *J. Am. Chem. Soc.*, 2012, **134**, 15318-15323.
438. C. N. Nguyen, T. K. Young and M. K. Gilson, *J. Chem. Phys.*, 2012, **137**, 044101.
439. N. S. Venkataramanan, S. Ambigapathy, H. Mizuseki and Y. Kawazoe, *J. Phys. Chem. B*, 2012, **116**, 14029-14039.
440. A. Suvitha, N. S. Venkataramanan, H. Mizuseki, Y. Kawazoe and N. Ohuchi, *J. Inclusion Phenom. Macrocyclic Chem.*, 2010, **66**, 213-218.
441. H. Kruse, L. Goerigk and S. Grimme, *J. Org. Chem.*, 2012, **77**, 10824-10834.
442. S. Grimme, *J. Phys. Chem. A*, 2005, **109**, 3067-3077.
443. S. Grimme, *Angew. Chem., Int. Edit*, 2006, **45**, 4460-4464.
444. S. Ogo, N. Makihara and Y. Watanabe, *Organometallics*, 1999, **18**, 5470-5474.
445. S. Ehrlich, J. Moellmann and S. Grimme, *Acc. Chem. Res.*, 2013, **46**, 916-926.
446. A. Mentes, R. D. W. Kemmitt, J. Fawcett and D. R. Russell, *J. Mol. Struct.*, 2004, **693**, 241-246.
447. M. A. Bennett, T. N. Huang, T. W. Matheson, A. K. Smith, S. Ittel and W. Nickerson, *Inorganic Syntheses*, ed. J. P. F. Jr, John Wiley & Sons, Inc., 1982, 74-78.
448. E. Hodson and S. J. Simpson, *Polyhedron*, 2004, **23**, 2695-2707.
449. J. Grau, V. Noe, C. Ciudad, M. J. Prieto, M. Font-Bardia, T. Calvet and V. Moreno, *J. Inorg. Biochem.*, 2012, **109**, 72-81.
450. M. R. J. Elsegood, M. B. Smith and N. M. Sanchez-Ballester, *Acta Crystallogr. Sect. E*, 2006, **62**, m2838-m2840.

451. J. Wolf, K. Thommes, O. Briel, R. Scopelliti and K. Severin, *Organometallics*, 2008, **27**, 4464-4474.

452. L. Goerigk and S. Grimme, *Phys. Chem. Chem. Phys.*, 2011, **13**, 6670-6688.

453. R. Huenerbein, B. Schirmer, J. Moellmann and S. Grimme, *Phys. Chem. Chem. Phys.*, 2010, **12**, 6940-6948.

454. A. V. Marenich, C. J. Cramer and D. G. Truhlar, *J. Phys. Chem. B*, 2009, **113**, 6378-6396.

455. Y. Zhao and D. G. Truhlar, *Acc. Chem. Res.*, 2008, **41**, 157-167.

456. S. Grimme, L. Goerigk and R. F. Fink, *Wiley Interdiscip. Rev.: Comput. Mol. Sci.*, 2012, **2**, 886-906.

457. C. Riplinger, B. Sandhoefer, A. Hansen and F. Neese, *J. Chem. Phys.*, 2013, **139**, 134101/134101-134101/134113.

458. T. A. K. Al-Allaf, L. J. Rashan, G. Ketler, H.-H. Fiebig and A. H. Al-Dujaili, *App. Organom. Chem.,* 2009, **23**, 173-178.

459. D. Bardelang, K. A. Udachin, D. M. Leek, J. C. Margeson, G. Chan, C. I. Ratcliffe and J. A. Ripmeester, *Cryst. Growth Des.*, 2011, **11**, 5598-5614.

460. J. Chatt and L. M. Venanzi, *J. Chem. Soc.*, 1957, 4735-4741.

461. M86-E01078 APEX2, Bruker AXS Inc., Madison, USA, 2006.

462. G. M. Sheldrick, *Acta Crystallogr. Sect. A*, 1990, **46**, 467-473.

463. G. M. Sheldrick and T. R. Schneider, *Methods in enzymology*, ed. R. M. S. Charles W. Carter Jr, Academic Press, 1997, vol. 277, 319-343.

464. A. Altomare, M. C. Burla, M. Camalli, G. L. Cascarano, C. Giacovazzo, A. Guagliardi, A. G. G. Moliterni, G. Polidori and R. Spagna, *J. Appl. Crystallogr.*, 1999, **32**, 115-119.

Appendix

IR spectra
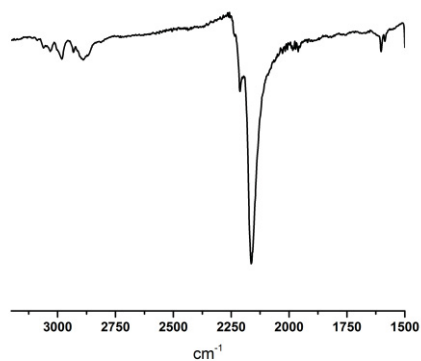
Figure A. 1. IR spectrum of **RH1**
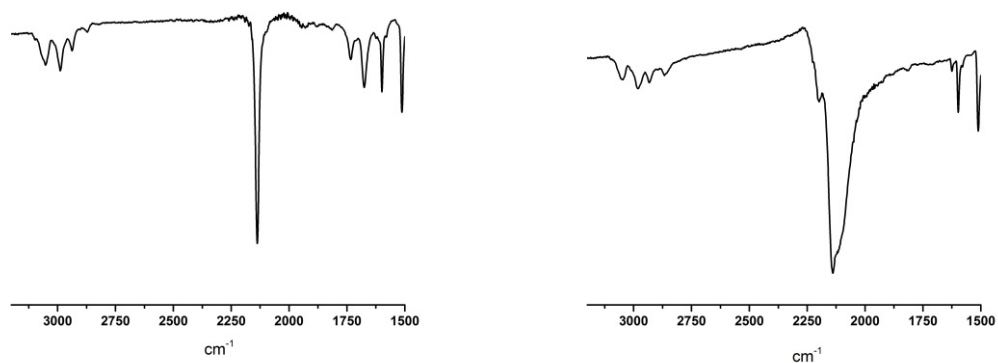
Figure A. 2. IR spectra of **NEI** (left) and **RH2** (right)
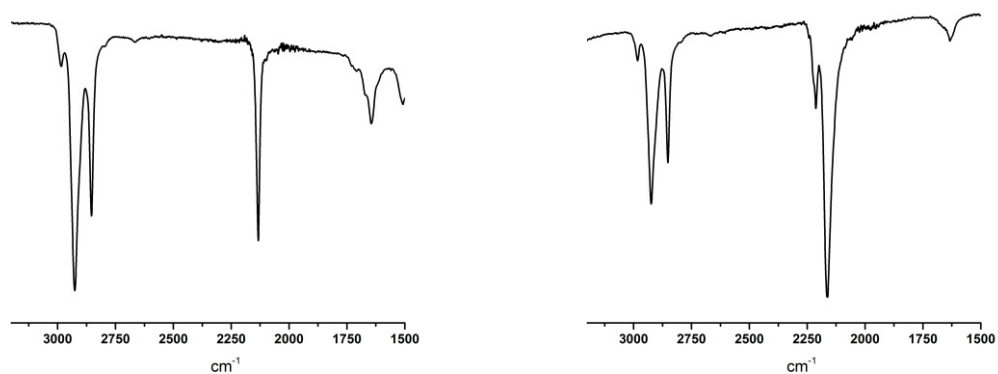
Figure A. 3. IR spectra of **R-CEI** (left) and **RH3** (right)
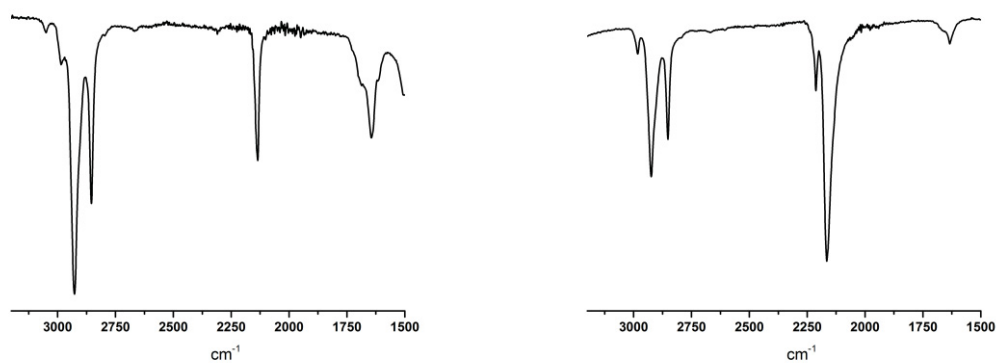
Figure A. 4. IR spectra of **S-CEI** (left) and **RH4** (right)

CDs Spectra
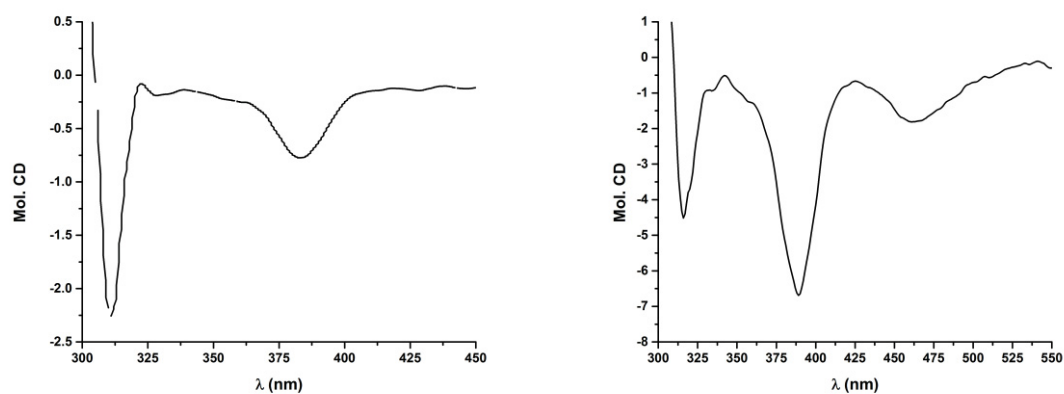
Figure A. 5. Mol. CDs spectra of **RH1** in acetonitrile (left) and dichloromethane (right)
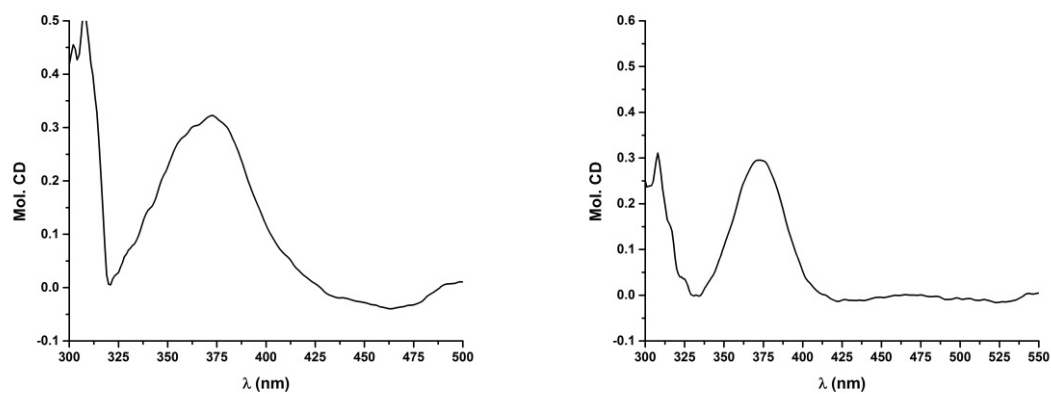
Figure A. 6. Mol. CDs spectra of **RH2** in acetonitrile (left) and dichloromethane (right)
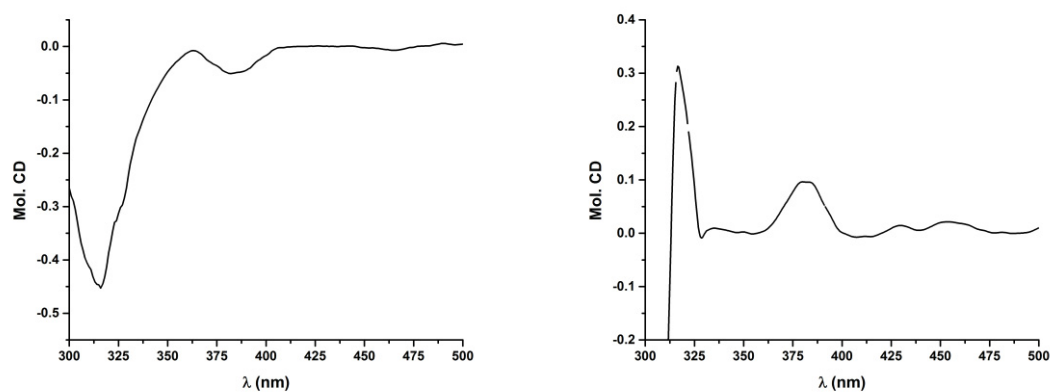
Figure A. 7. Mol. CDs spectra of **RH3** (left) and **RH4** (right) in acetonitrile

UV-Vis spectra
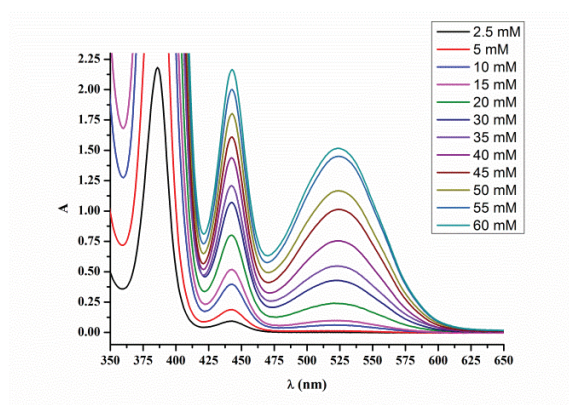
Figure A. 8. UV-Vis spectra of **RH1** in 0.1 M solution of n-Bu$_4$N PF$_6$ in CH$_3$CN for several concentrations
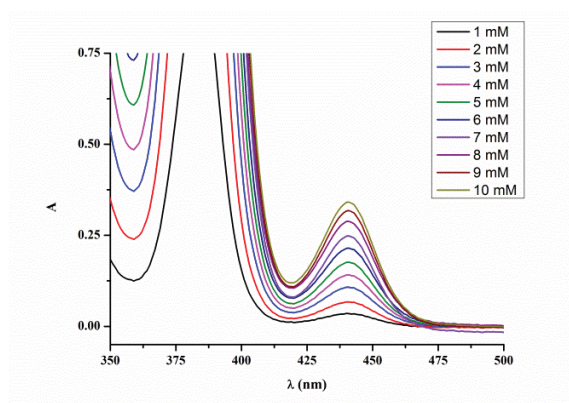
Figure A. 9. UV-Vis spectra of **RH4** in CH$_3$CN for several concentrations
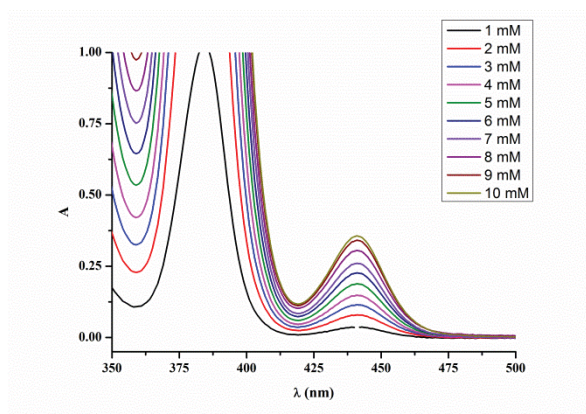
Figure A. 10. UV-Vis spectra of 50% **RH3** + 50% RH4 mixture in CH$_3$CN for several concentrations
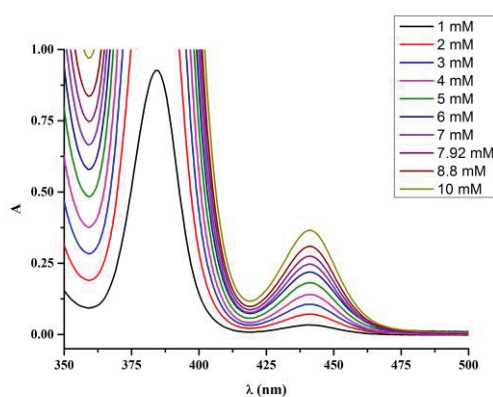
Figure A. 11. UV-Vis spectra of 60% **RH3** + 40% RH4 mixture in CH$_3$CN for several concentrations
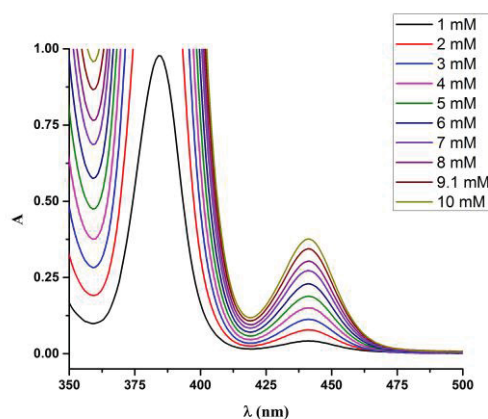
Figure A. 12. UV-Vis spectra of 70% **RH3** + 30% RH4 mixture in CH$_3$CN for several concentrations
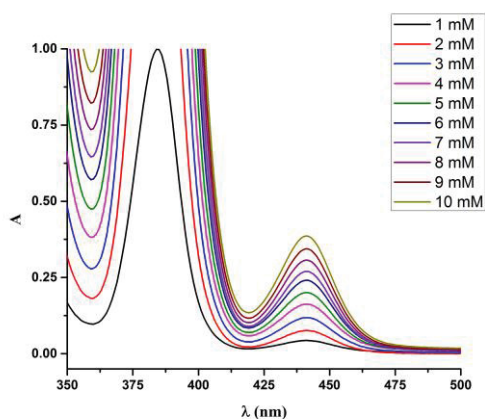
Figure A. 13. UV-Vis spectra of 80% **RH3** + 20% RH4 mixture in CH$_3$CN for several concentrations
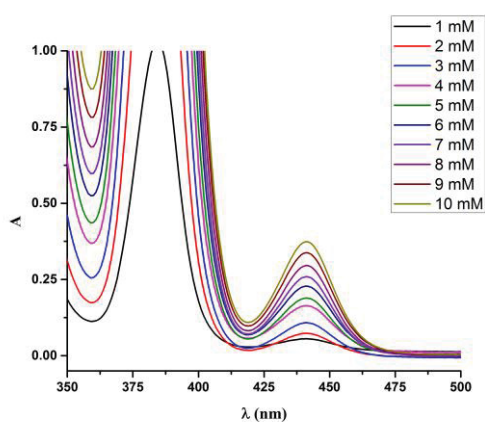
Figure A. 14. UV-Vis spectra of 90% **RH3** + 10% RH4 mixture in CH$_3$CN for several concentrations
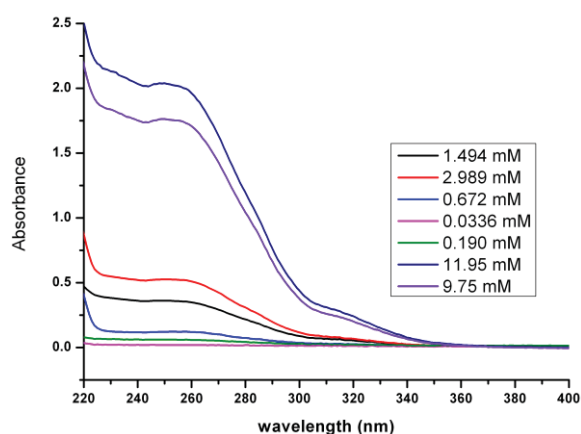
Figure A. 15. Stacked UV-visible spectra of aqueous solutions of oxaliplatin (**1**) measured at different concentrations in a 1 mm optical path quartz cell at 25°C. The large absorption band at 260 nm (λ= 16.4·10^4) and the weaker shoulder at 318 nm (λ= 2.1·10^4) display perfect linearity with respect to concentration, in good accord with Beer Lambert law, which suggest the apparent absence of a second analyte in the concentrated solution.

Mass spectra
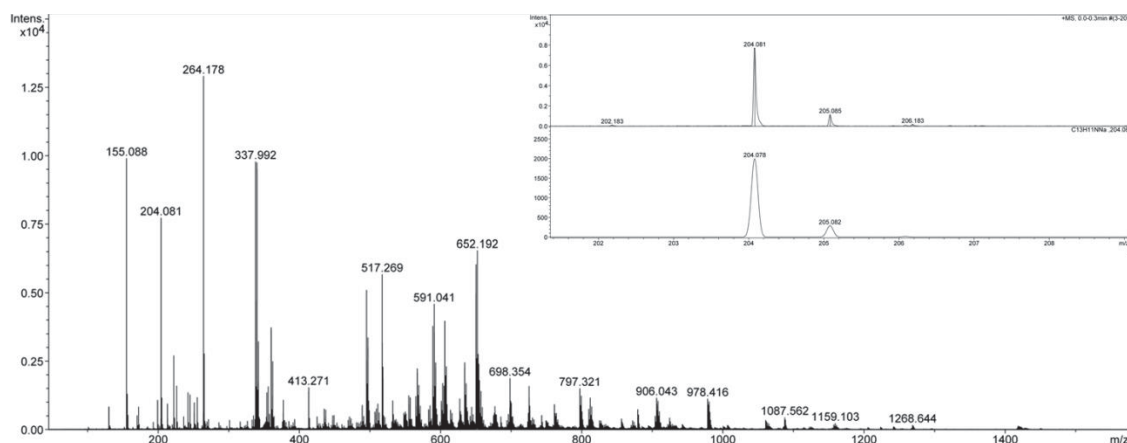
Figure A. 16. ESI$^+$ mass spectrum of **NEI** with zoomed signal for [M+Na]$^+$ ion
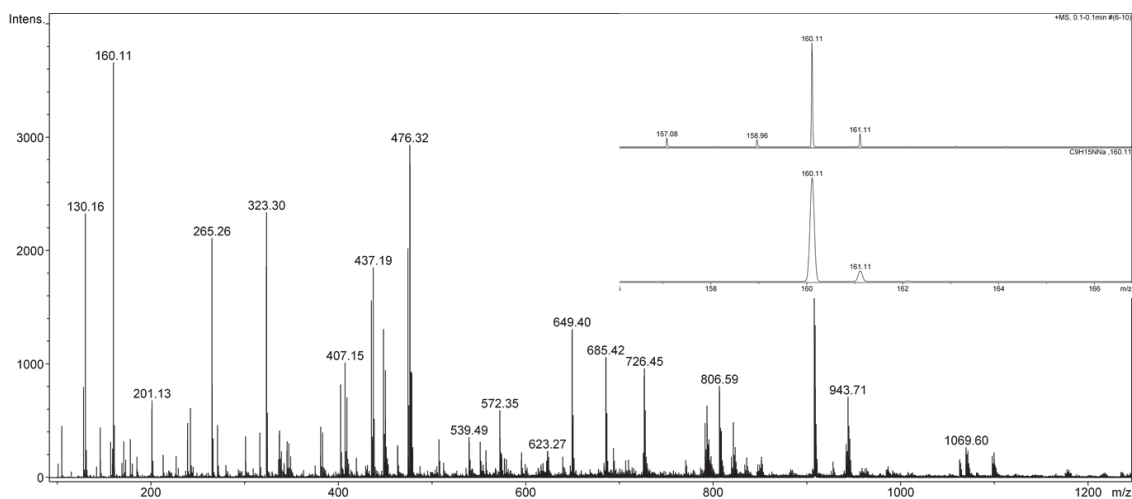
Figure A. 17. ESI$^+$ mass spectrum of **R-CEI** with zoomed signal for [M+Na]$^+$ ion
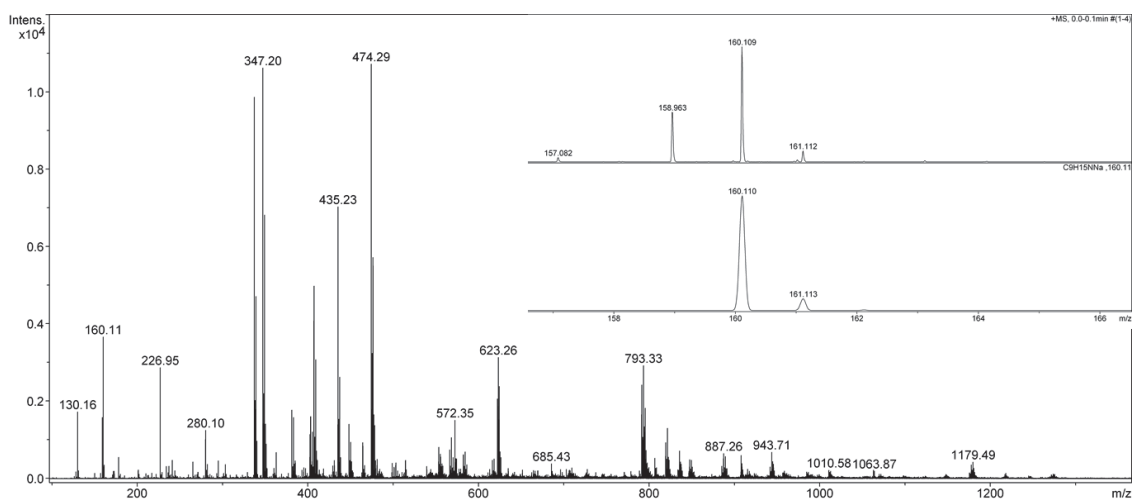
Figure A. 18. ESI$^+$ mass spectrum of **S-CEI** with zoomed signal for [M+Na]$^+$ ion
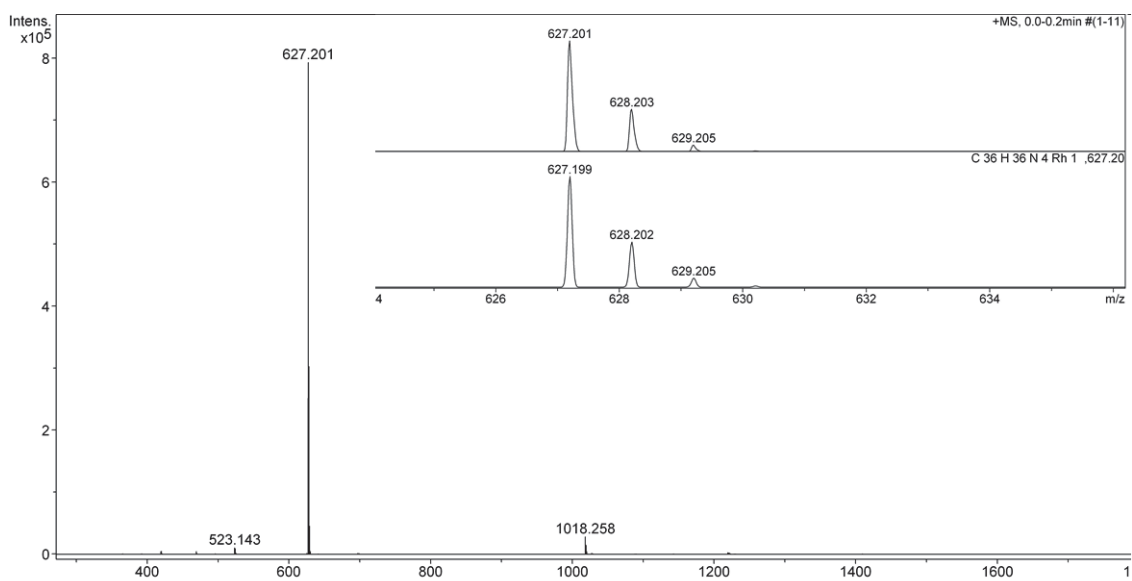
Figure A. 19. ESI$^+$ mass spectrum of **RH1** with zoomed signal for [M]$^+$ ion
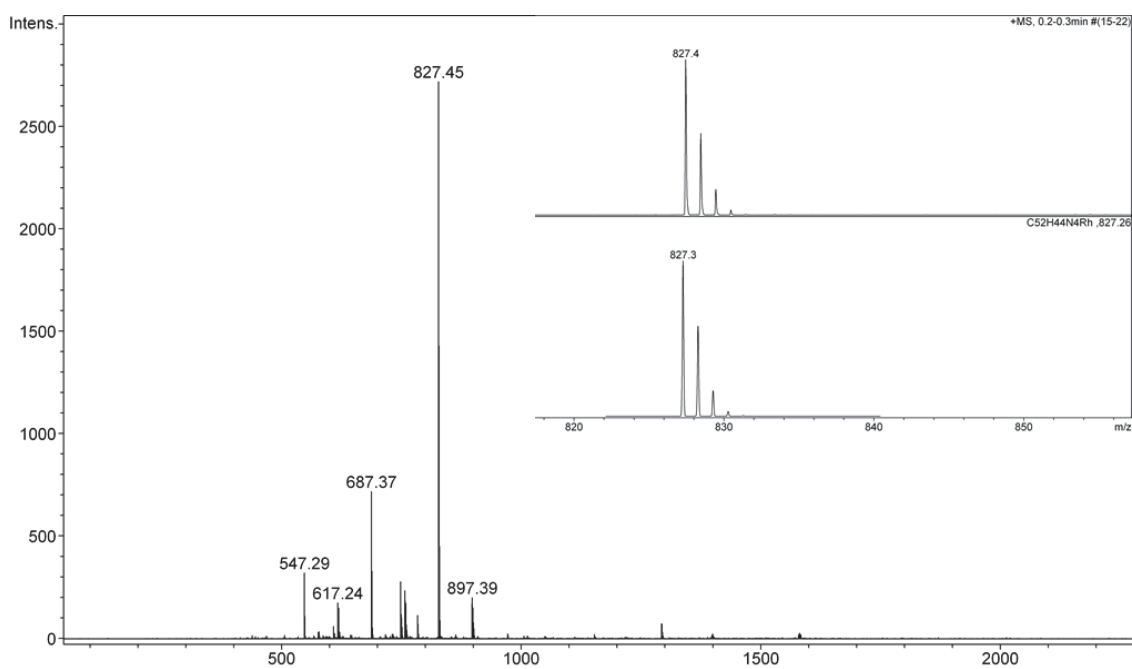
Figure A. 20. ESI$^+$ mass spectrum of **RH2** with zoomed signal for [M]$^+$ ion
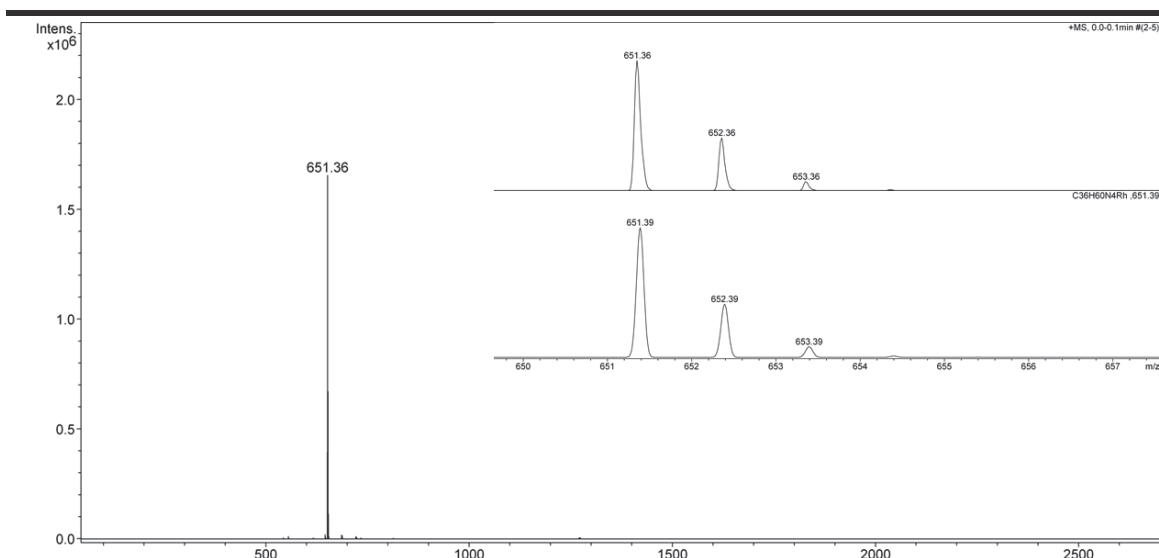
Figure A. 21. ESI$^+$ mass spectrum of **RH3** with zoomed signal of [M]$^+$
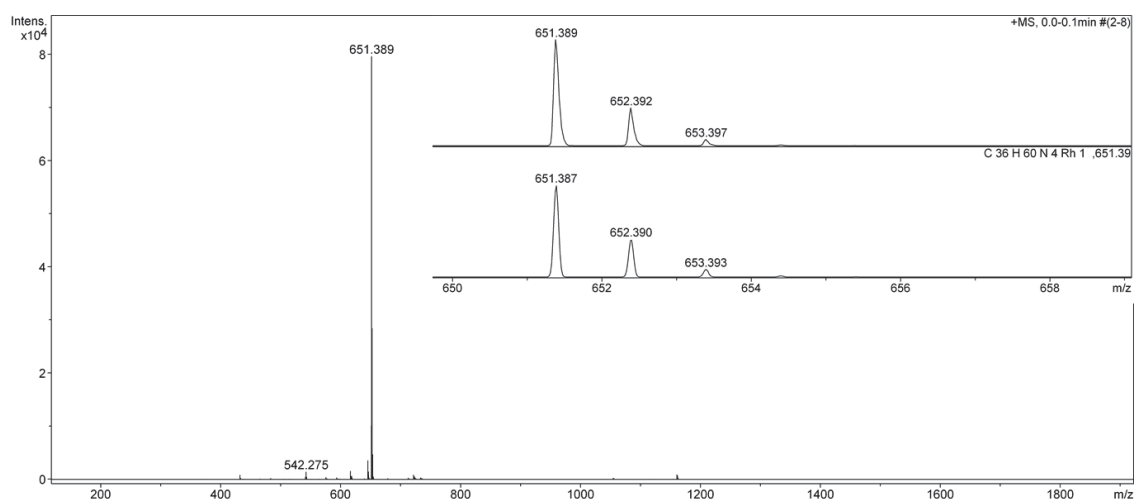
Figure A. 22. ESI$^+$ mass spectrum of **RH4** with zoomed signal for [M]$^+$ ion
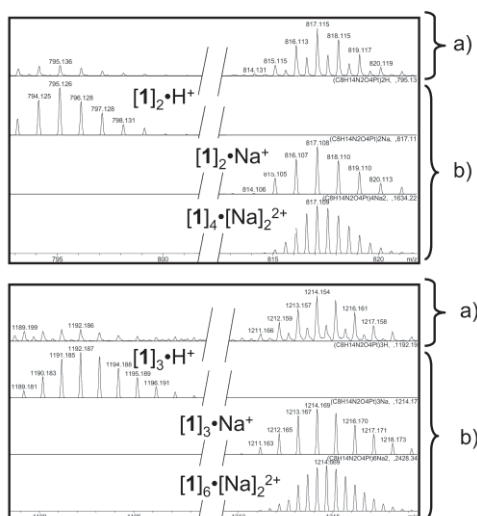
Figure A. 23. Selected regions of the ESI+ mass spectrum of a water solution of **1** containing

traces of formic acid and trace contamination by Na$^+$ salts: a) experimental spectrum, b) simulated isotopic patterns.
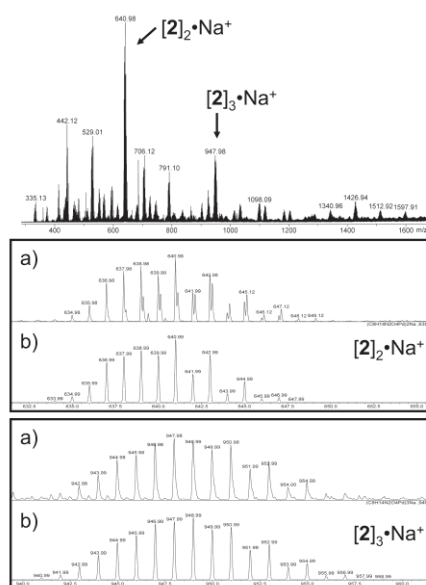
Figure A. 24. Selected regions of the ESI+ mass spectrum of a water solution of oxalipaladium (**2**) containing traces of Na$^+$ salts: a) experimental spectrum, b) simulated isotopic patterns.
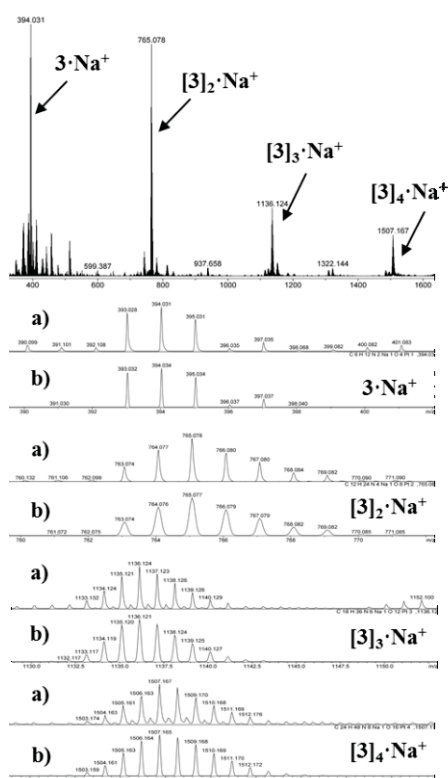
Figure A. 25. Selected regions of the ESI$^+$ mass spectrum of a DMSO solution of carboplatin (**3**) containing traces of Na$^+$ salts: a) experimental spectrum, b) simulated isotopic patterns.
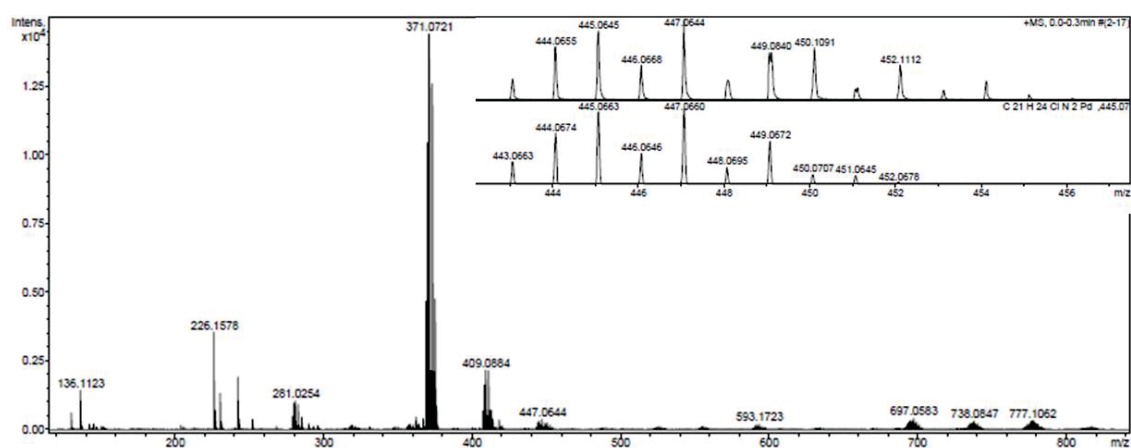
Figure A. 26. ESI$^+$ mass spectrum of **PD1** with zoomed signal for [M-H]$^+$ ion
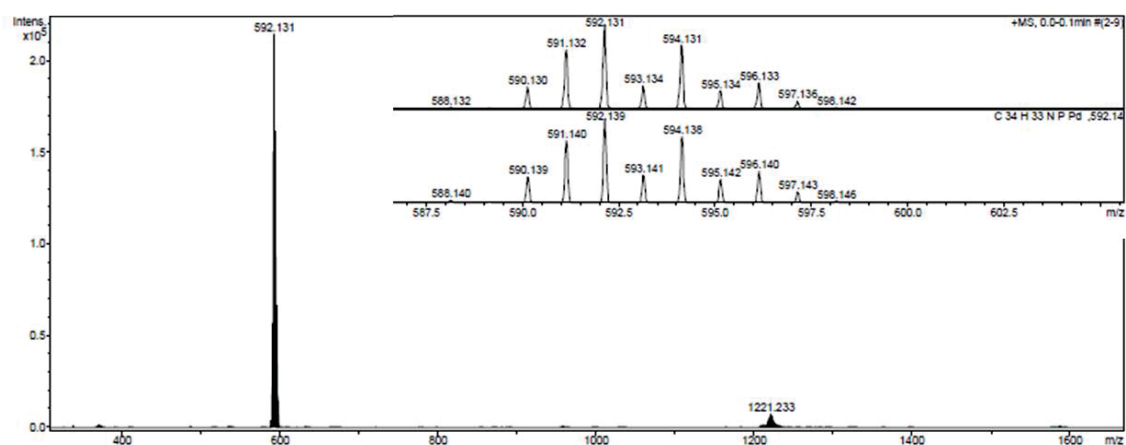
Figure A. 27. ESI$^+$ mass spectrum of **PD3** with zoomed signal for [M-Cl]$^+$ ion
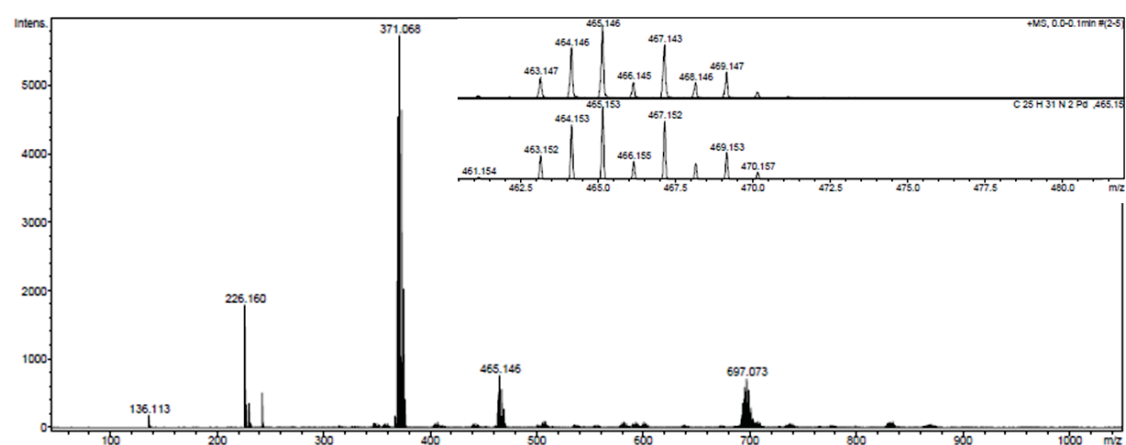
Figure A. 28. ESI$^+$ mass spectrum of **PD2** with zoomed signal for [M-Cl]$^+$ ion
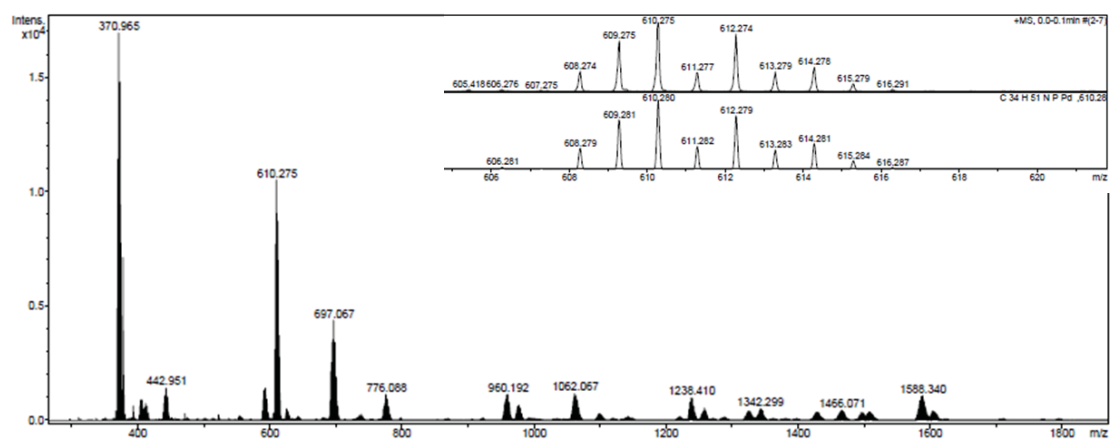
Figure A. 29. ESI⁺ mass spectrum of **PD4** with zoomed signal for [M-Cl]⁺ ion
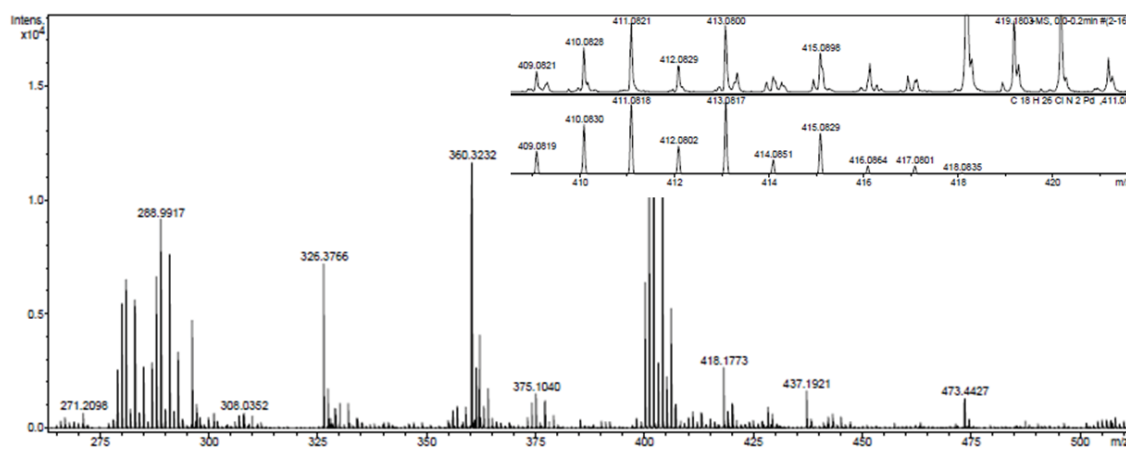
Figure A. 30. ESI⁺ mass spectrum of **PD5** with zoomed signal for [M-H]⁺ ion
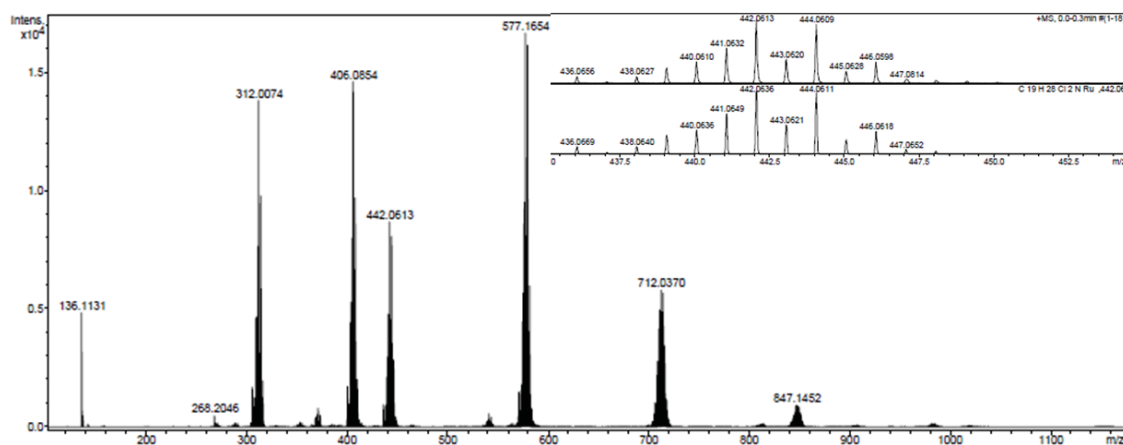
Figure A. 31. ESI⁺ mass spectrum of **RU1** with zoomed signal for [M-H]⁺ ion

^{1}H Spectra
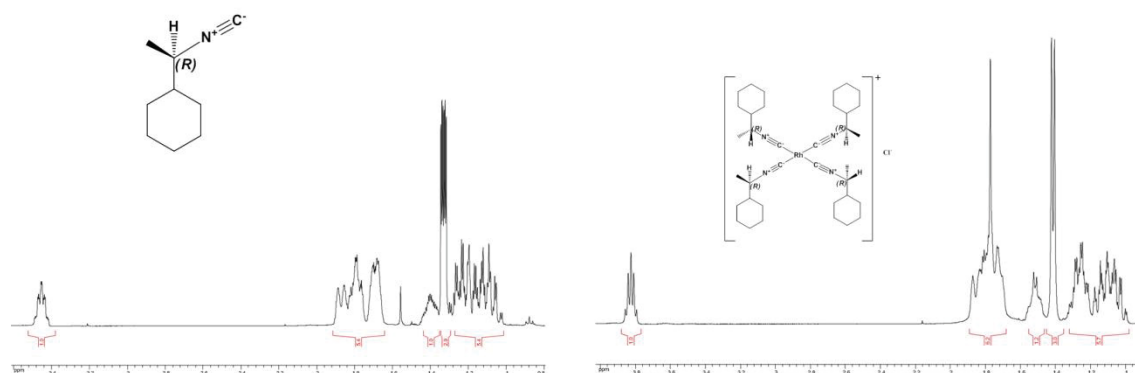
Figure A. 32. ^{1}H spectra of **R-CEI** ligand (left) and **RH3** (right) in CDCl$_3$
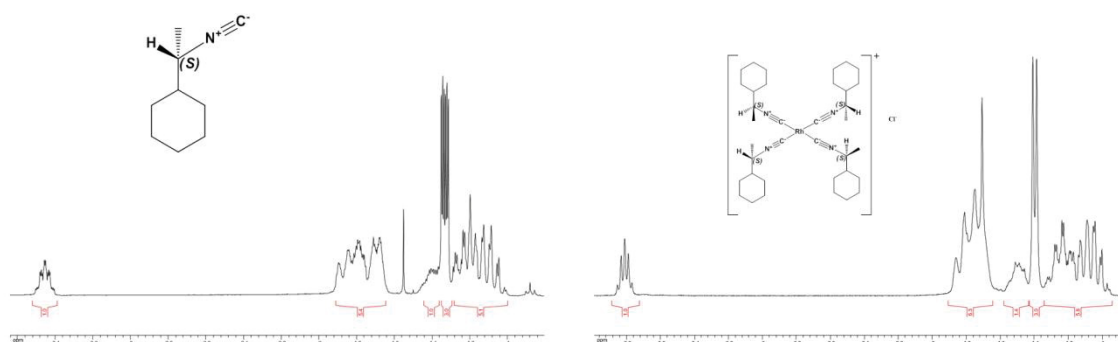
Figure A. 33. ^{1}H spectra of **S-CEI** ligand and **RH4** (right) in CDCl$_3$
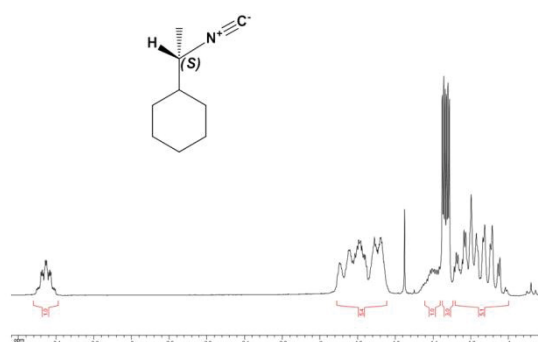
Figure A. 34. ^{1}H spectra of **NEI** ligand in CDCl$_3$
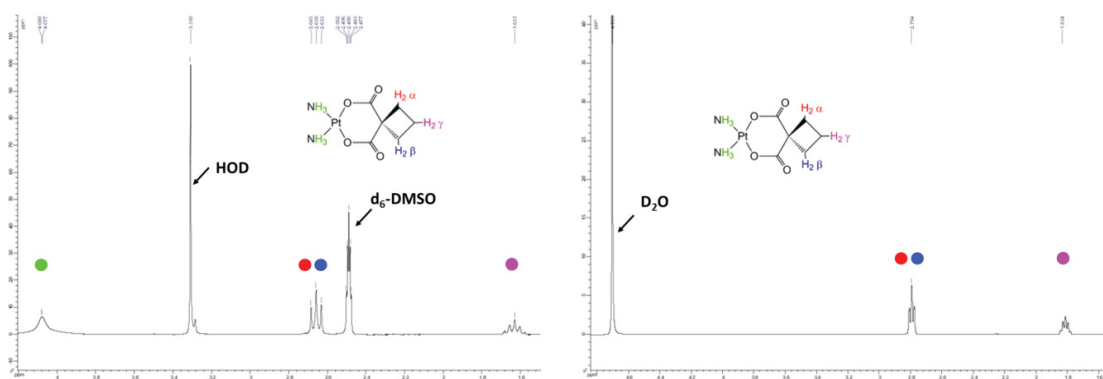
Figure A. 35. ^{1}H NMR spectra of **3** in d$_6$-DMSO(left), in D$_2$O (right)
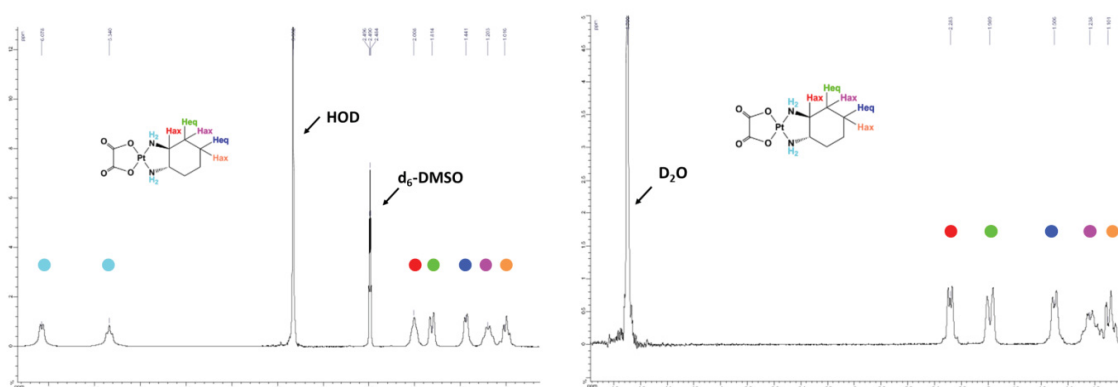
Figure A. 36. ^{1}H NMR spectra of **1** in d$_6$-DMSO (left), in D$_2$O (right)
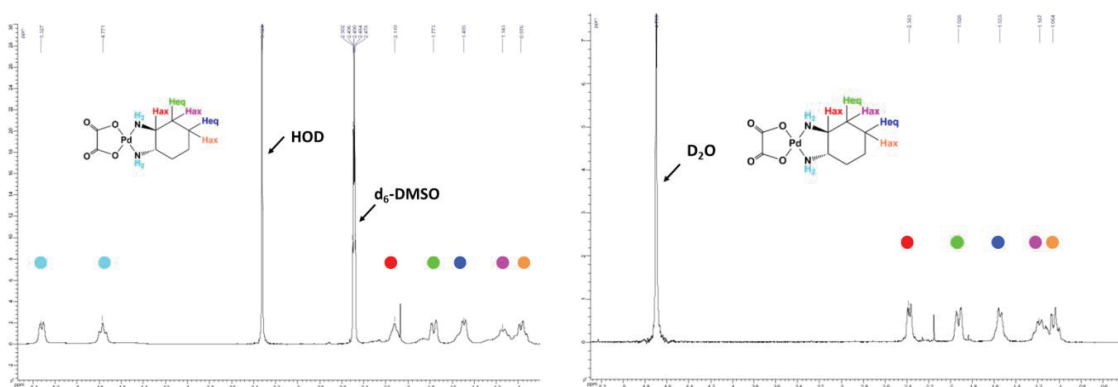
Figure A. 37. ^{1}H NMR spectra of **2** in d$_6$-DMSO (left), in D$_2$O (right)
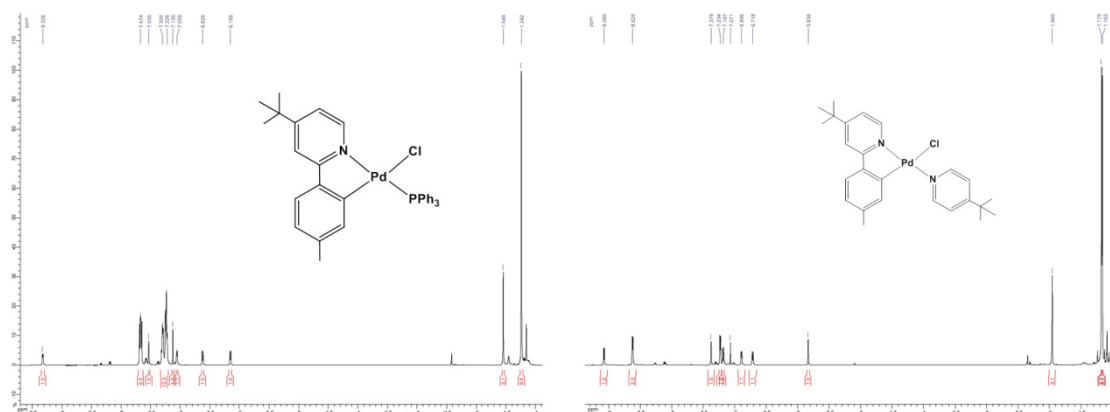
Figure A. 38. ^{1}H NMR spectra of **PD3** (left) and **PD2** (right) in CDCl$_3$
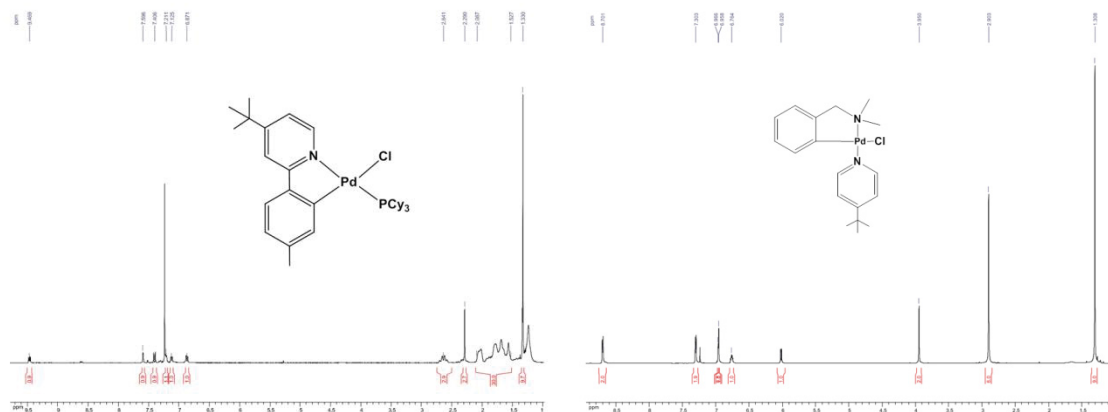
Figure A. 39. ^{1}H NMR spectra of **PD4** (left) and **PD5** (right) in CDCl$_3$
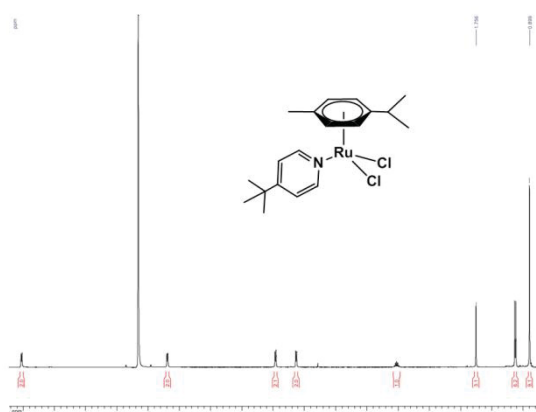
Figure A. 40. ^{1}H NMR spectra of **RU1** in C$_6$D$_6$

^{13}C spectra
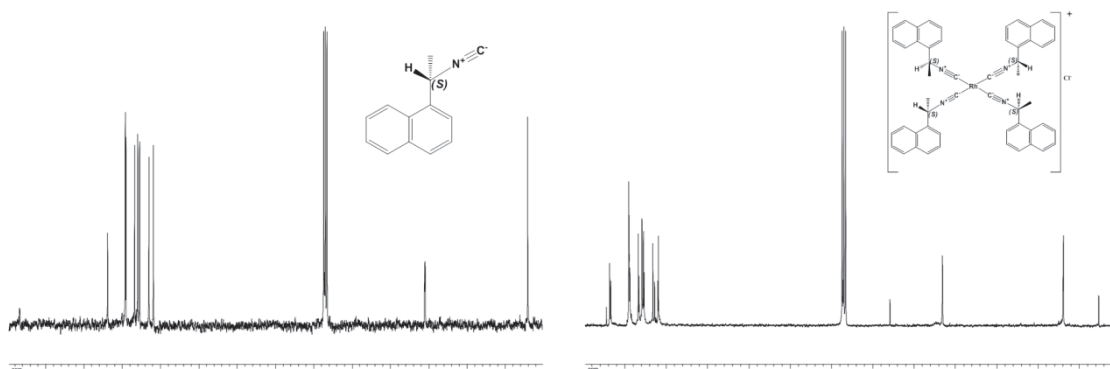
Figure A. 41. ^{13}C spectra of **NEI** ligand (left) and **RH2** (right) in CDCl$_3$
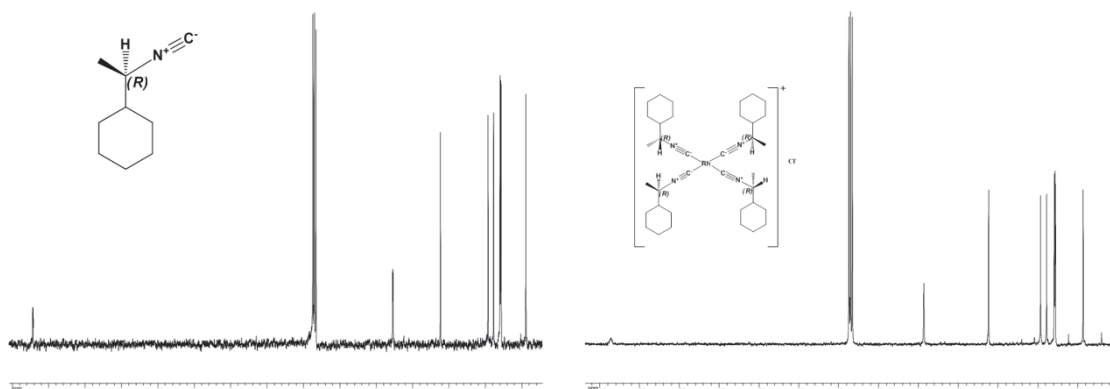
Figure A. 42. ^{13}C spectra of **R-CEI** ligand (left) and **RH3** (right) in CDCl$_3$
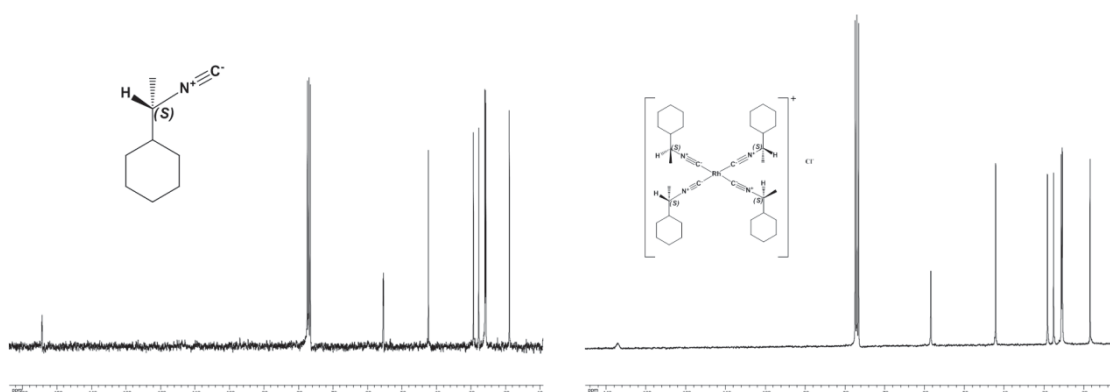
Figure A. 43. ^{13}C spectra of **S-CEI** ligand (left) and **RH4** (right) in CDCl$_3$
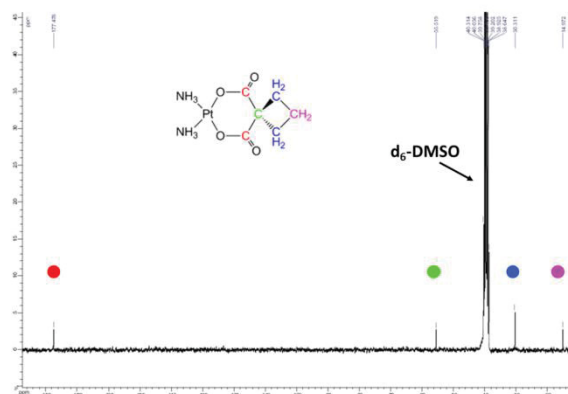
Figure A. 44. ^{13}C NMR spectra for **3** in d$_6$-DMSO
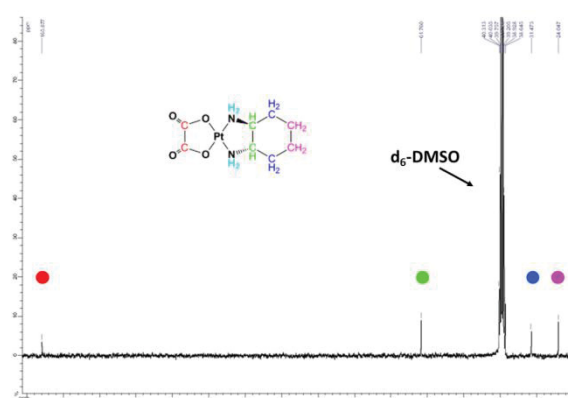
Figure A. 45. ^{13}C NMR spectra for **1** in d$_6$-DMSO
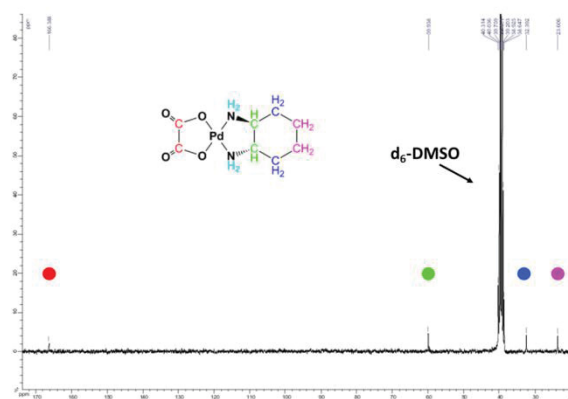
Figure A. 46. ^{13}C NMR spectra for **2** in d$_6$-DMSO
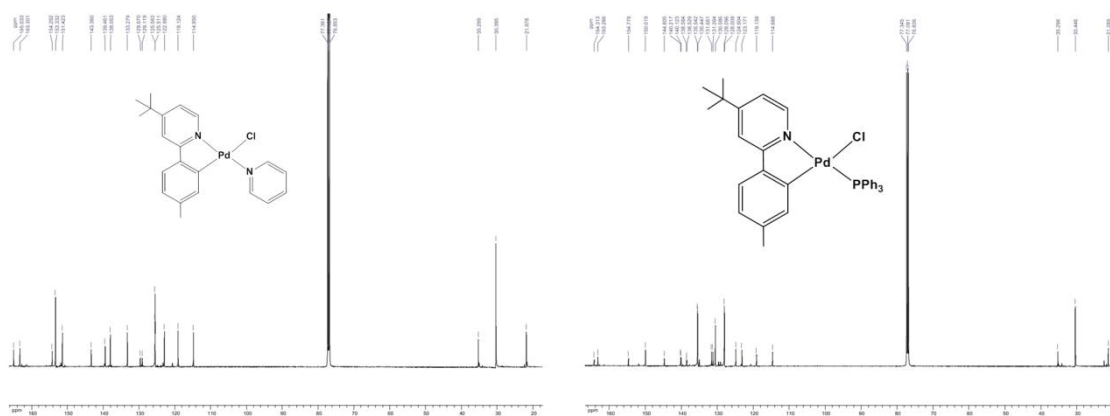
Figure A. 47. ^{13}C spectra of **PD1** (left) and **PD3** (right) in CDCl$_3$
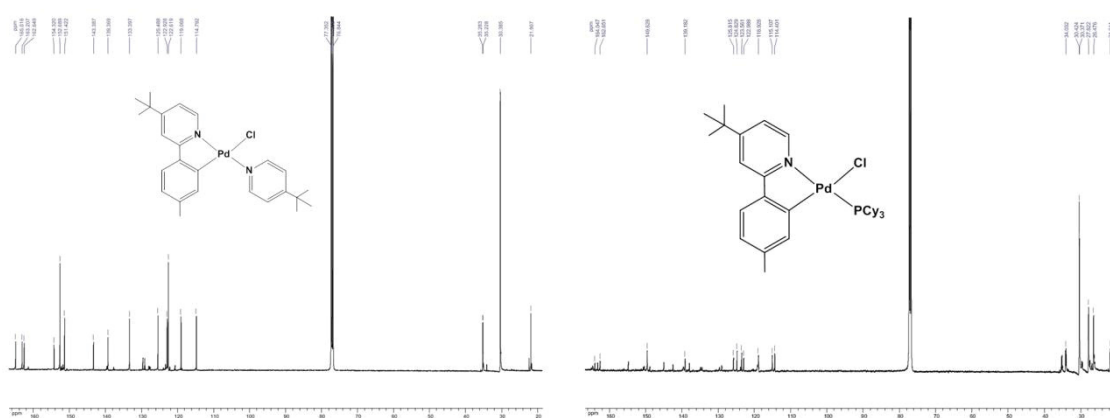
Figure A. 48. ^{13}C spectra of **PD2** (left) and **PD4** (right) in CDCl$_3$
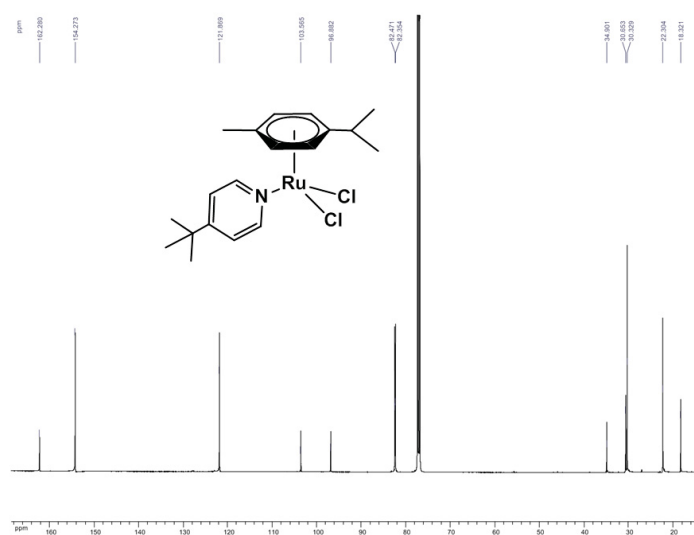
Figure A. 49. ^{13}C spectra of **RU1** in CDCl$_3$

^{1}H DOSY
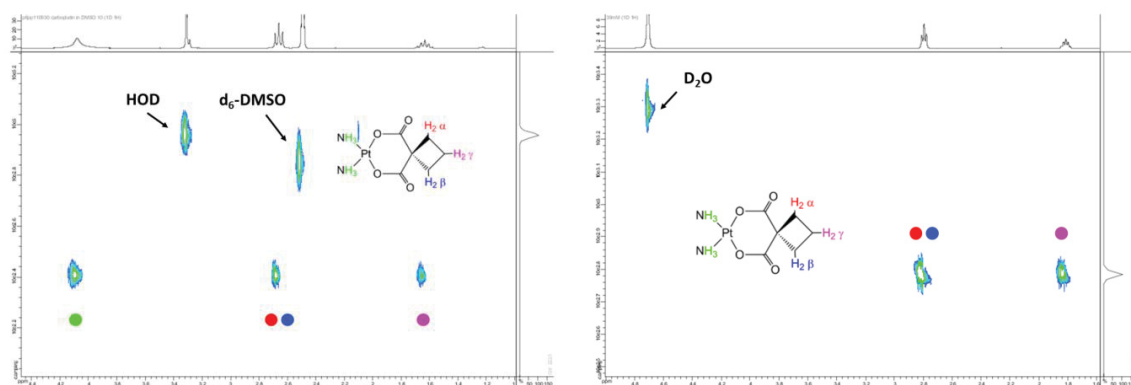
Figure A. 50. ^{1}H DOSY spectra for **3** in d$_6$-DMSO(left), in D$_2$O (right)
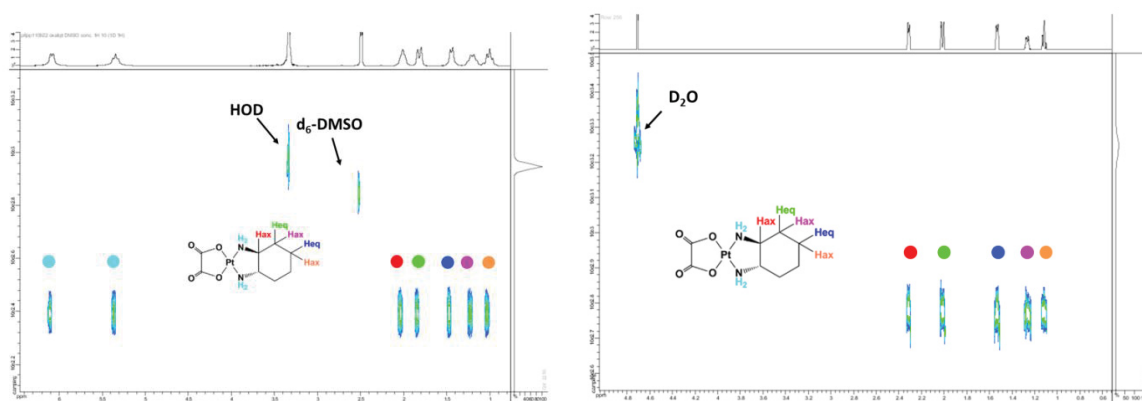
Figure A. 51. ^{1}H DOSY spectra for **1** in d$_6$-DMSO(left), in D$_2$O (right)
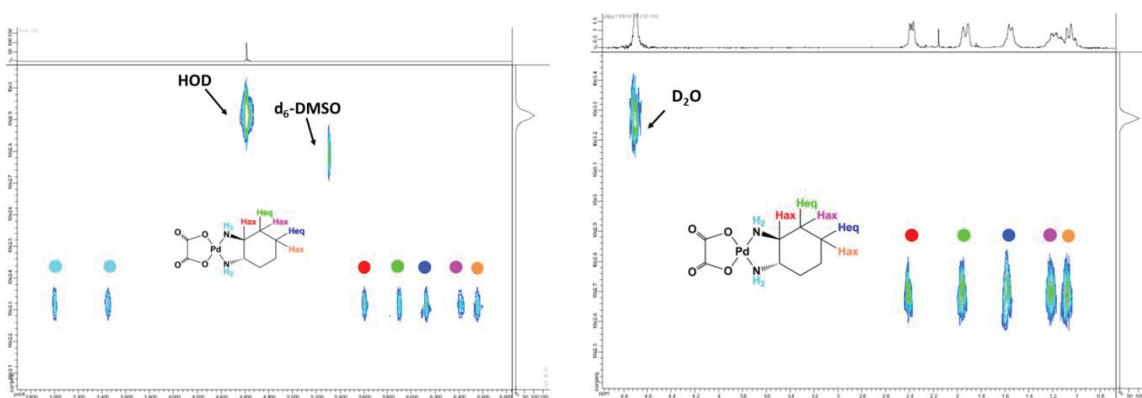
Figure A. 52. ^{1}H DOSY spectra for **2** in d$_6$-DMSO(left), in D$_2$O (right)

Calorimetry
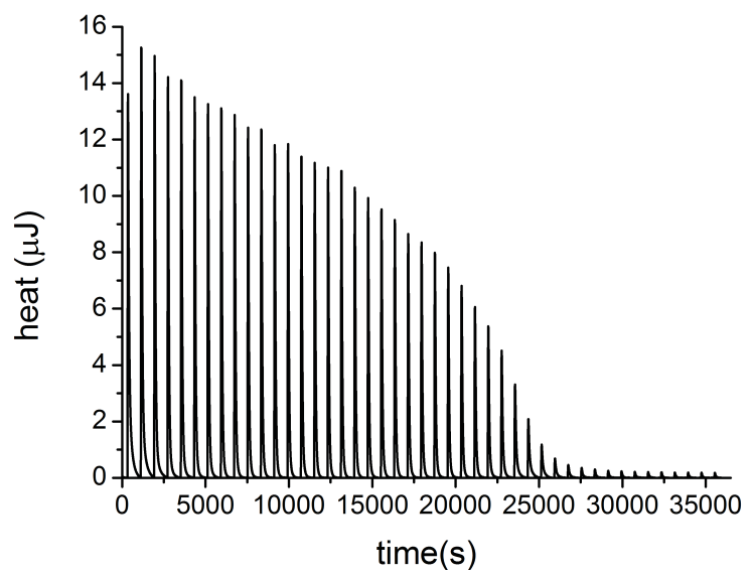
Figure A. 53. Heat released in the reaction: titration of **CB**[7] water solution with water solution of complex **2**. Reaction was performed on 298.15 K. Interval between injections was 800 seconds: **2**: c = 20mM injected into **CB**[7] : c = 2mM. There were 45 injections (of 2.06 µl each).
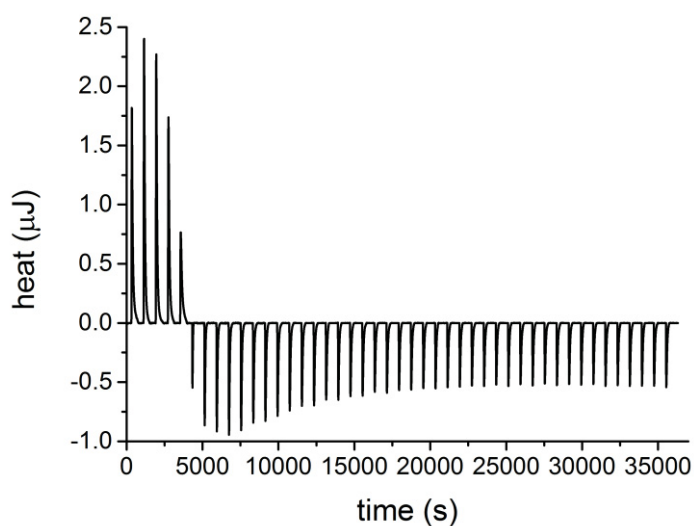
Figure A. 54. Heat released in the reaction: titration of **CB**[7] water solution with water solution of **4** complex. Reaction was performed on 298.15 K. Interval between injections was 900 seconds: **4**: c = 10mM injected into **CB**[7] : c = 0.5 mM. There were 45 injections (of 2.06 µl each). There were 45 injections (of 2.03 µl each).
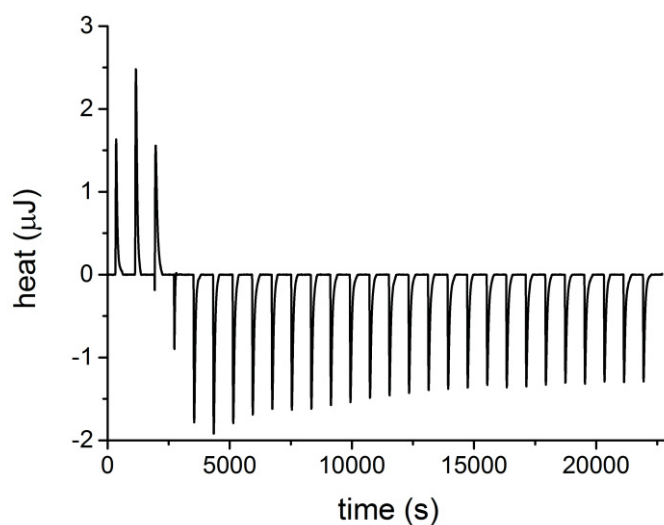
Figure A. 55. Thermographic trace of the dilution by sequential additions of a concentrated aqueous solution of IrCp*(H$_2$O)$_3$(PF$_6$)$_2$ (c = 10 mM, v = 2.06 µL) into pure water at 298.15 K
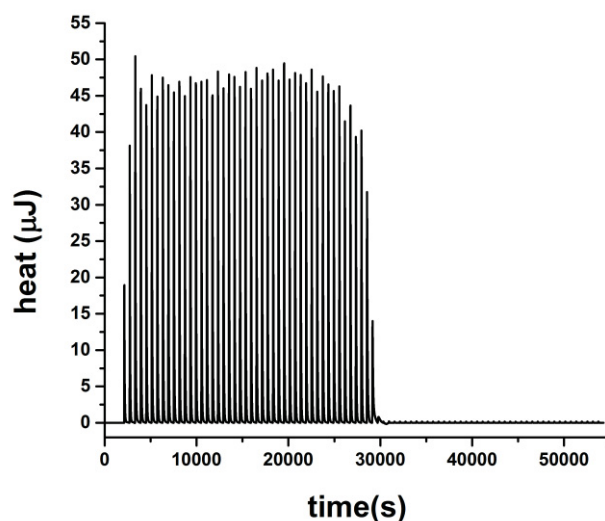
Figure A. 56. Heat released in the reaction: titration of [Pd(**tBpTP**)Cl]$_2$ solution in Chlorobenzene with Tricylohexylphosphine solution in Chlorobenzene. Reaction was performed on 298.15 K. Interval between injections was 600 seconds - **PCy$_3$**: c = 23.3 mM injected into [Pd(**tBpTP**)Cl]$_2$: c = 1 mM. There were 90 injections (of 2 µl each).
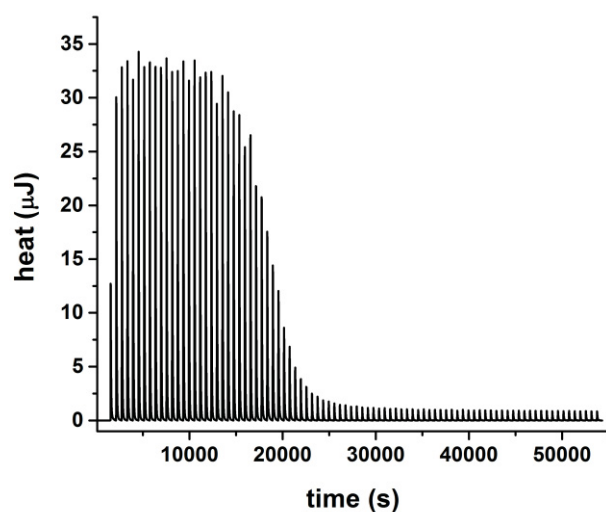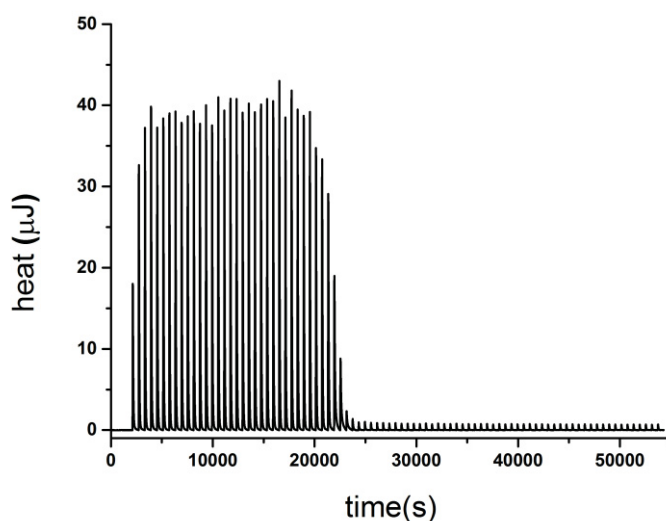
Figure A. 57. Heat released in the reaction: titration of [Pd(**tBpTP**)Cl]$_2$ dimer solution in Chlorobenzene with 4-tert-Butylpyridine solution in Chlorobenzene. Reaction was performed on 298.15 K. Interval between injections was 600 seconds: **tBPyr**: c = 30.5 mM injected into [Pd(**tBpTP**)Cl]$_2$: c = 1mM. There were 90 injections (of 2 μl each).
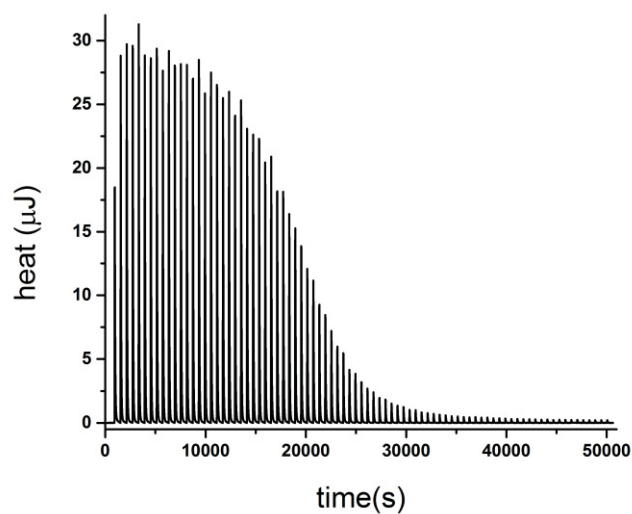
Figure A. 58. Heat released in the reaction: titration of [Pd(**tBpTP**)Cl]$_2$ dimer solution in Chlorobenzene with pyridine solution in Chlorobenzene. Reaction was performed on 298.15 K. Interval between injections was 600 seconds: **Pyr**: c = 39.54 mM injected into [Pd(**tBpTP**)Cl]$_2$: c = 1mM. There were 90 injections (of 2 μl each).
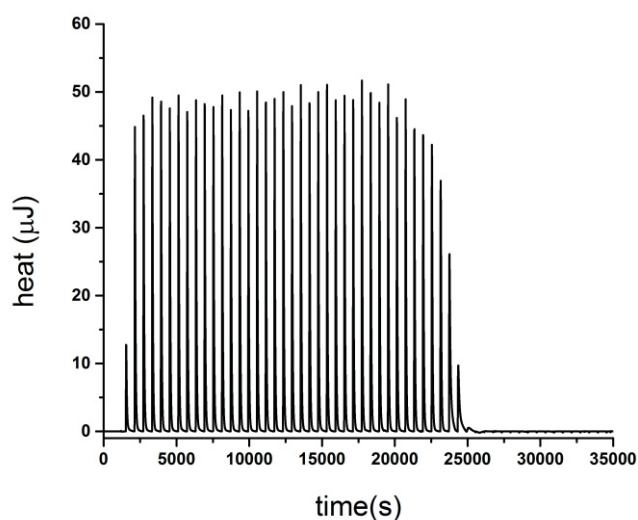
Figure A. 59. Heat released in the reaction: titration of [Pd(**dmba**)Cl]$_2$ dimer solution in Chlorobenzene with triphenylphospine solution in Chlorobenzene. Reaction was performed on 298.15 K. Interval between injections was 600 seconds: **PPh$_3$**: c = 23.79 mM injected into [Pd(**dmba**)Cl]$_2$: c = 1mM. There were 60 injections (of 2 μl each).
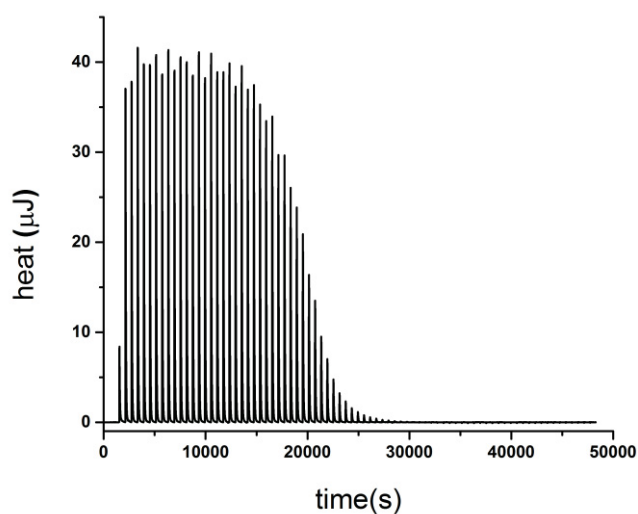
Figure A. 60. Heat released in the reaction: titration of [Pd(**dmba**)Cl]$_2$ dimer solution in Chlorobenzene with 4-tert-Butylpyridine solution in Chlorobenzene. Reaction was performed on 298.15 K. Interval between injections was 600 seconds: **tBuPyr**: c = 24.94 mM injected into [Pd(**dmba**)Cl]$_2$: c = 1mM. There were 80 injections (of 2 μl each).
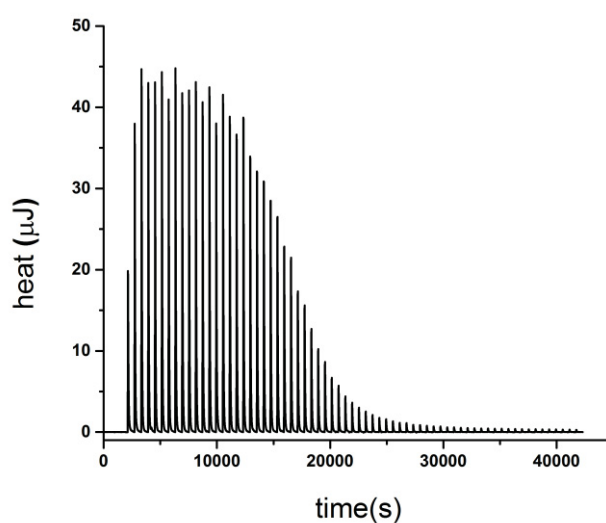
Figure A. 61. Heat released in the reaction: titration of [Pd(**dmba**)Cl]$_2$ dimer solution in Chlorobenzene with pyridine solution in Chlorobenzene. Reaction was performed on 298.15 K. Interval between injections was 600 seconds: **Pyr**: $c = 37.93$ mM injected into [Pd(**dmba**)Cl]$_2$: $c = 1$mM. There were 70 injections (of 2 μl each).
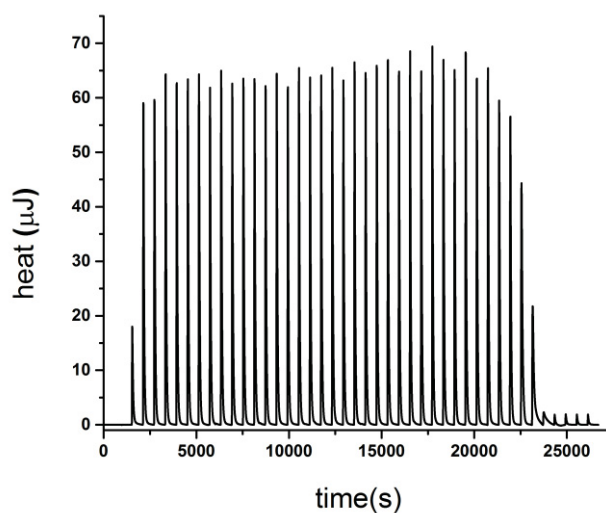
Figure A. 62. Heat released in the reaction: titration of [Pd(**dmba**)Cl]$_2$ dimer solution in Chlorobenzene with tricyclohexylphosphine solution in Chlorobenzene. Reaction was performed on 298.15 K. Interval between injections was 600 seconds: **PCy$_3$**: $c = 24.52$ mM injected into [Pd(**dmba**)Cl]$_2$: $c = 1$mM. There were 44 injections (of 2 μl each).
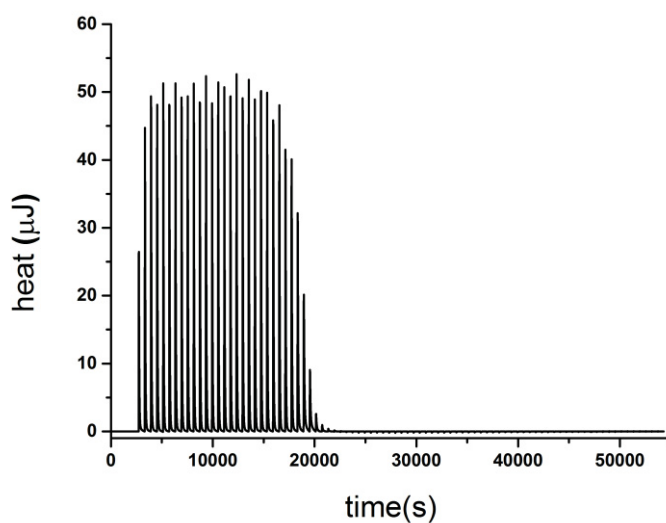
Figure A. 63. Heat released in the reaction: titration of [Ru($\textbf{p-cym}$)Cl$_2$]$_2$ dimer solution in Chlorobenzene with pyridine solution in Chlorobenzene. Reaction was performed on 298.15 K. Interval between injections was 600 seconds: **Pyr**: c = 39.54 mM injected into Ru($\textbf{p-cym}$)Cl$_2$]$_2$: c = 1mM. There were 90 injections (of 2 μl each).
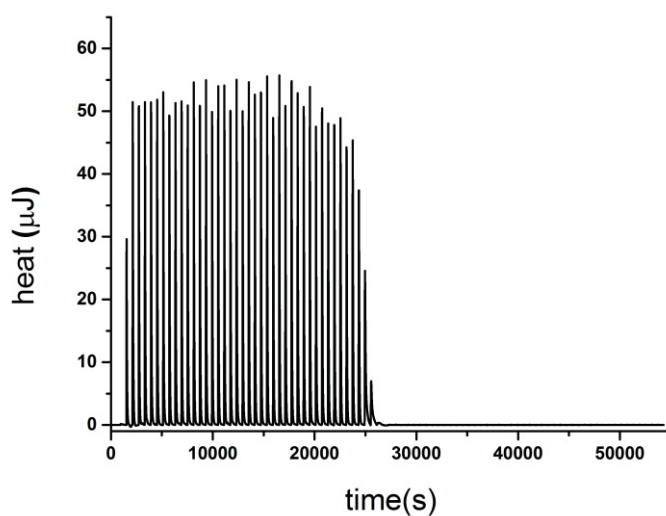
Figure A. 64. Heat released in the reaction: titration of [Ru($\textbf{p-cym}$)Cl$_2$]$_2$ dimer solution in Chlorobenzene with triphenylphosphine solution in Chlorobenzene. Reaction was performed on 298.15 K. Interval between injections was 600 seconds: **PPh$_3$**: c = 23.27 mM injected into Ru($\textbf{p-cym}$)Cl$_2$]$_2$: c = 1mM. There were 90 injections (of 2 μl each).

Figure A. 65. Heat released in the reaction: titration of [Ru($\textbf{p-cym}$)Cl$_2$]$_2$ dimer solution in Chlorobenzene with 4-tert-Butylpyridine solution in Chlorobenzene. Reaction was performed on 298.15 K. Interval between injections was 600 seconds: **tBuPyr**: c = 27.50 mM injected into Ru($\textbf{p-cym}$)Cl$_2$]$_2$: c = 1mM. There were 90 injections (of 2 µl each).
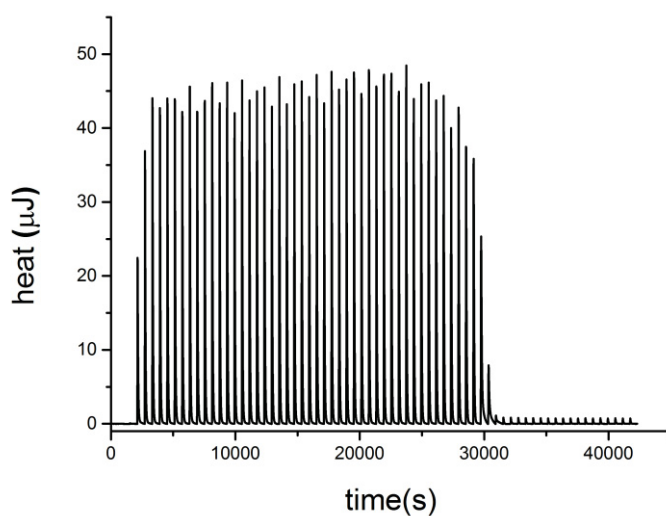
Figure A. 66. Heat released in the reaction: titration of [Ru($\textbf{p-cym}$)Cl$_2$]$_2$ dimer solution in Chlorobenzene with trycyclohexylphoshine solution in Chlorobenzene. Reaction was performed on 298.15 K. Interval between injections was 600 seconds: **PCy$_3$**: c = 23.35 mM injected into Ru($\textbf{p-cym}$)Cl$_2$]$_2$: c = 1mM. There were 70 injections (of 2 µl each).

X-ray diffraction parameters

Table A. 1. Acquisition and Refinement Data for the Structures **PD3**, **PD2**, **PD5** and **RU1**

Compound	**PD3**	**PD2**	**PD5**	**RU1**
Molecular formula	$2 \cdot (C_{34}H_{33}ClNPPd)$, $C_2H_4Cl_2$	$C_{25}H_{31}ClN_2Pd$	$C_{18}H_{25}ClN_2Pd$	$C_{19}H_{27}Cl_2NRu$
Molecular weight	1355.82	501.37	411.25	441.38
Crystal habit	colorless block	colorless plate	colorless prism	orange prism
Crystal dimensions(mm)	0.24x0.22x0.16	0.14x0.08x0.08	0.50x0.30x0.20	0.30x0.25x0.20
Crystal system	triclinic	monoclinic	Triclinic	monoclinic
Space group	P -1	P2$_1$/c	P -1	C 2/c
a(Å)	9.682(1)	8.504(1)	7.2762(3)	22.6755(6)
b(Å)	13.353(1)	12.042(1)	10.3768(3)	14.2314(4)
c(Å)	25.421(1)	23.6434(10)	12.5143(5)	12.9185(3)
α(°)	83.19	90.00	76.248(2)	90
β(°)	83.58	109.107(3)	87.493(2)	111.6020(10)
γ(°)	73.82	90.00	77.164(2)	90
V(Å^3)	3123.3(4)	2287.8(3)	894.81(6)	3876.05(18)
Z	2	4	2	8
d(g-cm^{-3})	1.442	1.456	1.526	1.513
F(000)	1388	1032	420	1808
μ(cm^{-1})	0.841	0.941	1.185	1.084
Absorption corrections	multi-scan ; 0.8236 min, 0.8771 max	multi-scan ; 0.8795 min, 0.9285 max	multi-scan ; 0.57686 min, 0.80608 max	multi-scan ; 0.6376 min, 0.7463 max
Diffractometer	KappaCCD	KappaCCD	KappaCCD	Bruker APEX-II CCD
X-ray source	MoKα	MoKα	MoKα	MoKα
λ(Å)	0.71069	0.71069	0.71073	0.71073
Monochromator	graphite	graphite	graphite	/
T (K)	150.0(1)	150.0(1)	173(2)	173(2)
Scan mode	phi and omega scans	phi and omega scans	phi and omega scans	phi and omega scans
Maximum θ	30.02	27.49	27.485	31.98
HKL ranges	-13 13 ; -18 18 ; -35 35	-7 11 ; -9 15 ; -29 26	-9 9; -13 13; -13 16	-33 33; -21 15; -19 15
Reflections measured	31497	7989	8801	20407
Unique data	17235	4661	4098	6712
R$_{int}$	0.0433	0.0530	0.0385	0.0205
Reflections used	15301	3787	3801	5514
Criterion	I > 2σ(I)	I > 2σ(I)	I > 2σ(I)	I > 2σ(I)
Refinement type	Fsqd	Fsqd	Fsqd	Fsqd
Hydrogen atoms	constr	constr	constr	constr
Parameters refined	739	269	204	214
Reflections / parameter	20	14	18	31
wR$_2$	0.1173	0.1408	0.0771	0.0544
R$_1$	0.0558	0.0616	0.0276	0.0247
Weights a, b	0.0146; 13.787	0.0528; 11.579	0.0445; 0.4878	0.0214; 5.9695
GoF	1.073	1.071	1.158	1.048
difference peak / hole (eÅ^{-3})	0.949(0.111) / -1.040(0.111)	0.935(0.126) / -1.186(0.126)	0.594(0.144)/ -1.217(0.144)	0.699(0.078)/ -0.676(0.078)

Computational details

Table A. 2.Energies obtained by geometry optimization for **1**, **2** and **3**

Molecule	Symmetry	Theory level	Tot. Pauli repulsion	Electrostatic	Orbital interactions	Dispersion	Solvation	Tot. Bonding
			kcal/mol	kcal/mol	kcal/mol	kcal/mol	kcal/mol	kcal/mol
1	C_1	BLYP-D3, TZP	14396.39	-3131.26	-15033.05	-25.23	--	-3793.15
1	C_1	BLYP-D3BJ, TZP	14466.71	-3149.07	-15085.48	-47.01	--	-3814.85
1 water	C_1	BLYP-D3, TZP	14411.85	-3135.14	-15028.45	-25.16	-56.67	-3833.56
1 DMSO	C_1	BLYP-D3, TZP	14409.35	-3134.2	-15027.74	-25.16	-55.09	-3832.84
α[**1**]$_2$	C_2	BLYP, TZP	28901.03	-6286.22	-30178.69	--	--	-7563.87
α[**1**]$_2$	C_1	BLYP, QZ4P	29129.38	-6335.67	-30420.29	--	--	-7626.56
α[**1**]$_2$	C_1	BLYP-D3, TZP	29023.61	-6325.36	-30259.87	-79.69	--	-7641.3
α[**1**]$_2$	C_2	BLYP-D3, TZP	29032.46	-6327.68	-30266.44	-79.63	--	-7641.28
α[**1**]$_2$	C_2	BLYP-D3, QZ4P	29280.76	-6384.39	-30519.67	-79.91	--	-7703.21
α[**1**]$_2$ Na	C_1	BLYP-D3, TZP	29137.58	-6373.6	-30264.9	-80.04	--	-7580.96
α[**1**]$_2$ water	C_2	BLYP-D3, TZP	28998.45	-6312.37	-30234.03	-75.91	-58.87	-7682.73
α[**1**]$_2$ water	C_1	BLYP-D3, TZP	28995.74	-6311.39	-30232.19	-75.88	-58.9	-7682.61
β[**1**]$_2$	C_1	BLYP, TZP	29008.8	-6320.35	-30262.84	--	--	-7574.39
β[**1**]$_2$	C_1	BLYP-D3, TZP	29089.5	-6346.27	-30316.18	-78.86	--	-7651.82
β[**1**]$_2$	C_1	BLYP-D3BJ, TZP	29240.79	-6385.64	-30428.1	-118.87	--	-7691.83
β[**1**]$_2$	C_1	BLYP-D3, TZ2P	29241.79	-6379.61	-30474.76	-78.96	--	-7691.56
β[**1**]$_2$	C_1	BLYP-D3, QZ4P	29335.2	-6393.6h3	-30576.74	-79.21	--	-7714.38
β[**1**]$_2$ Na	C_1	BLYP-D3, TZP	29181.65	-6392.71	-30294.8	-81.22	--	-7587.07
β[**1**]$_2$ DMSO	C_1	BLYP-D3, TZP	29021.55	-6323.71	-30258.64	-77.95	-49.19	-7687.94
β[**1**]$_2$ water	C_1	BLYP-D3, TZP	29020.79	-6324.02	-30256.52	-77.9	-51.46	-7689.1
γ[**1**]$_2$	C_1	BLYP-D3, TZP	28971.08	-6307.49	-30228.52	-62.44	--	-7627.37
γ[**1**]$_2$	C_1	BLYP-D3BJ, TZP	29120.02	-6347	-30337.59	-105.59	--	-7670.15
2	C_1	BLYP-D3, TZP	14054.17	-3029.13	-14750.92	-22.8	--	-3748.68
2	C_1	BLYP-D3BJ, TZP	14116.12	-3043.84	-14798.25	-45.71	--	-3771.69
2 DMSO	C_1	BLYP-D3, TZP	14070.45	-3036.86	-14743.35	-22.75	-54.93	-3787.43
2 water	C_1	BLYP-D3, TZP	14072.04	-3037.63	-14743.07	-22.75	-57.1	-3788.52
α[**2**]$_2$	C_1	BLYP, TZP	28199.45	-6084.78	-29594.27	--	--	-7479.58

α[**2**]₂	C₂	BLYP, TZP	28205.25	-6086.35	-29598.45	--	--	-7479.54
α[**2**]₂	C₂	BLYP-D3, TZP	28332.76	-6127.11	-29683.55	-72.43	--	-7550.32
α[**2**]₂ Na	C₁	BLYP-D3, TZP	28435.5	-6173.86	-29678	-73.16	--	-7489.52
α[**2**]₂ water	C₁	BLYP-D3, TZP	28312.39	-6120.19	-29655.89	-69.29	-57.48	-7590.46
β[**2**]₂	C₁	BLYP, TZP	28199.45	-6084.78	-29594.27	--	--	-7479.58
β[**2**]₂	C₁	BLYP-D3, TZP	28384.37	-6140.49	-29731.91	-69.25	--	-7557.28
β[**2**]₂	C₁	BLYP-D3BJ, TZP	28534.22	-6179.72	-29842.16	-115.11	--	-7602.77
β[**2**]₂	C₁	BLYP-D3, TZ2P	28544.64	-6176.73	-29894.33	-69.15	--	-7595.57
β[**2**]₂ Na	C₁	BLYP-D3, TZP	28475.6	-6187.88	-29709.29	-71.96	--	-7493.52
β[**2**]₂ DMSO	C₁	BLYP-D3, TZP	28296.25	-6114.9	-29657.54	-67.34	-49.23	-7592.76
β[**2**]₂ water	C₁	BLYP-D3, TZP	28311.26	-6120.01	-29665.56	-68.39	-51.74	-7594.45
3	C₁	BLYP-D3, TZP	12036.35	-2609.73	-12633.33	-21.99	--	-3228.7
3	C₁	BLYP-D3BJ, TZP	12097.01	-2626.44	-12677.12	-39.42	--	-3245.97
3 water	C₁	BLYP-D3, TZP	12025.6	-2610.41	-12602.81	-22.43	-57.85	-3267.9
α[**3**]₂	C₁	BLYP-D3, TZP	24394.7	-5308.19	-25528.87	-73.54	--	-6515.88
α[**3**]₂	C₁	BLYP-D3BJ, TZP	24541.02	-5343.64	-25645.02	-101.19	--	-6548.84
α[**3**]₂ Na	C₁	BLYP-D3, TZP	24404.3	-5324.36	-25456.42	-56.37	--	-6432.84
α[**3**]₂ water	C₁	BLYP-D3, TZP	24351.83	-5297.72	-25481.86	-74.29	-49.11	-6551.15
β[**3**]₂	Cₛ	BLYP-D3, TZP	24224.62	-5242.3	-25405.19	-53.56	--	-6479.43
β[**3**]₂	C₁	BLYP-D3BJ, TZP	24354.99	-5280.66	-25500.15	-87.87	--	-6513.7
γ[**3**]₂	C₁	BLYP-D3, TZP	24228.71	-5262.58	-25410.17	-54.69	--	-6494.38
γ[**3**]₂	C₁	BLYP-D3BJ, TZP	24346.01	-5294.55	-25490.92	-88.36	--	-6527.83
β[**1,2**]	C₁	BLYP-D3, TZP	28735.26	-6243.16	-30022.8	-74.23	--	-7604.94
β[**1,2**]	C₁	BLYP-D3BJ, TZP	28887.88	-6283.48	-30134.65	-117.22	--	-7647.46
β[**1,2**] water	C₁	BLYP-D3, TZP	28667.38	-6222.43	-29962.19	-73.23	-51.38	-7641.83
α,α[**1**]₃	C₁	BLYP-D3, TZP	43672.01	-9509.08	-45508.12	-132.93	--	-11478.12
α,α[**1**]₃ Na	C₁	BLYP-D3, TZP	43836.6	-9586.38	-45551.47	-134.46	--	-11435.71
α,α[**1**]₃ Na middle	C₁	BLYP-D3, TZP	43830.46	-9580.48	-45523.71	-136.9	--	-11410.62
α,β[**1**]₃	C₁	BLYP-D3, TZP	43666.73	-9518.75	-45502.2	-132.98	--	-11487.19
β,β[**1**]₃	C₁	BLYP-D3, TZP	43687.98	-9532.63	-45512.5	-135.88	--	-11493.02
CB[7]	C₁	BLYP-D3, TZP	87740.17	-19339.74	-87016.91	-159.26	--	-18775.61
CB[7] water	C₁	BLYP-D3, TZP	87508.92	-19253.89	-86809.05	-160.14	-201.45	-18915.67

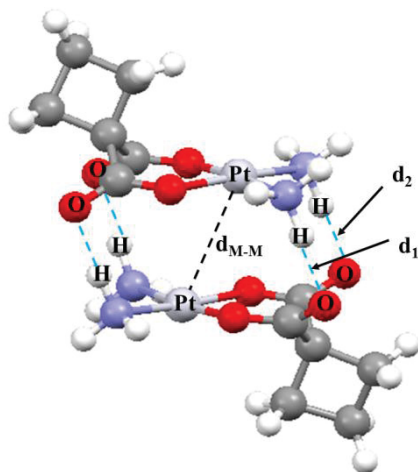|								
1@CB[7]	C_1	BLYP-D3, TZP,	102540.86	-22550.67	-102382	-226.55	--	-22618.37
2@CB[7]	C_1	BLYP-D3, TZP	102201.19	-22450.9	-102099.7	-223.77	--	-22573.18

Optimized geometries of 1 and 3

Figure A. 67. α-[**3**]$_2$; d_1 = 1.798 Å; d_2 = 1.805 Å; d_{MM} = 3.5 Å

Figure A. 68. β-[**3**]$_2$; d_1 = d_2 = 1.877 Å; d_{MM} = 7.238 Å

Figure A. 69. γ-[**3**]$_2$; d_1 = 1.944 Å; d_2 = 2.134 Å; d_{MM} = 5.429 Å

Figure A. 70. α-[**1**]$_2$; d$_1$ = 2.143Å; d$_2$ = 2.487 Å; d$_{MM}$ = 3.202 Å

Figure A. 71. β-[**1**]$_2$; d$_1$ = 1.951 Å ;d$_2$ = 2.016 Å; d$_{MM}$ = 3.945 Å

Figure A. 72. γ-[**1**]$_2$; d$_1$ = 2.255 Å; d$_2$ = 2.298 Å; d$_{MM}$ = 5.182 Å
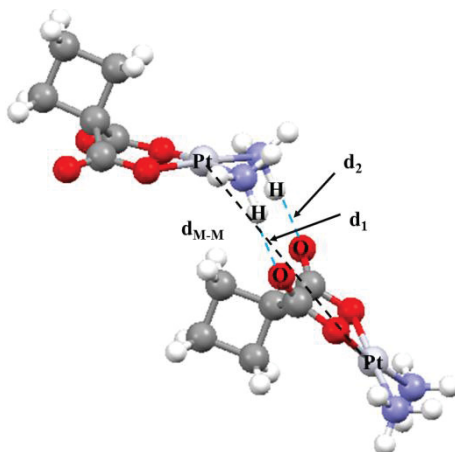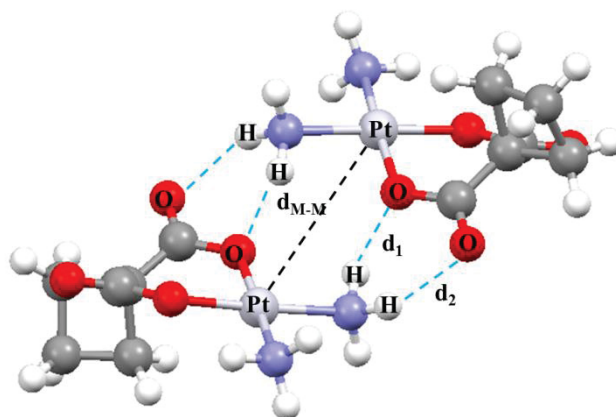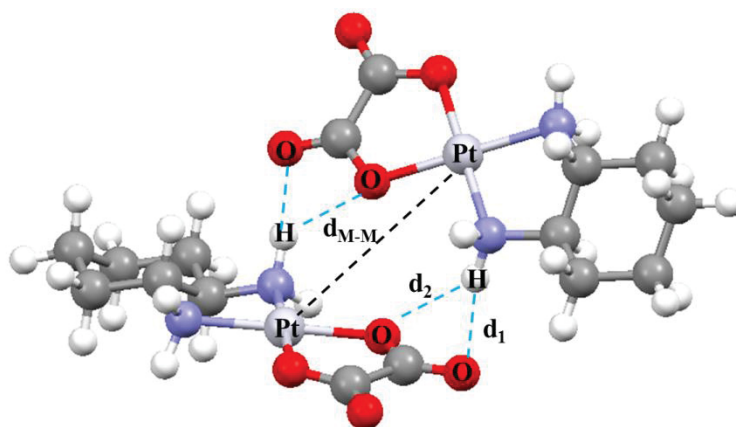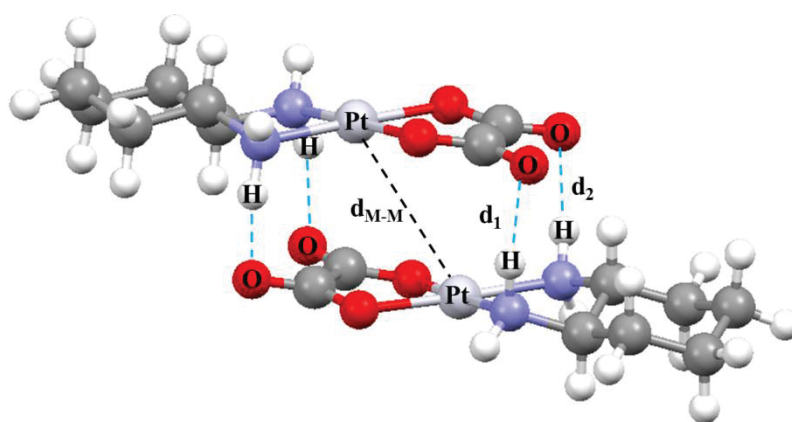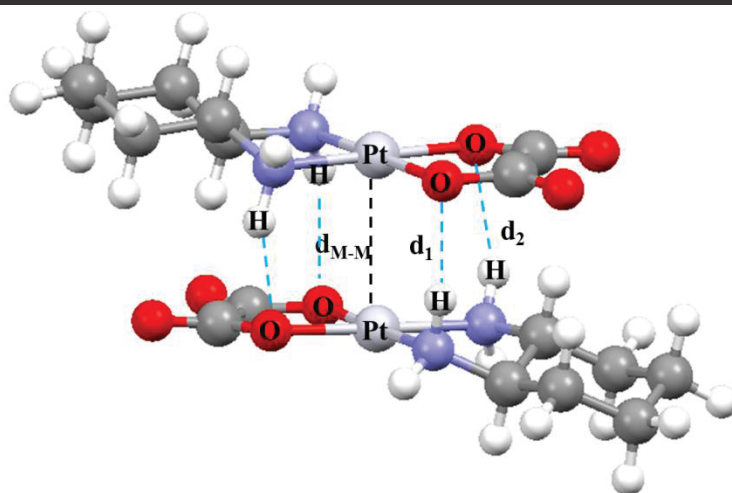
Table A. 3. BSSE for selected systems

Molecule	BSSE	TBE(ΔE_{int})	% BSSE in TBE
	kcal/mol	kcal/mol	
α-[**1**]$_2$	-2.22	-60.13	3.7
β-[**1**]$_2$	-2.02	-73.41	2.7
α-[**2**]$_2$	-1.72	-57.48	3.0
β-[**2**]$_2$	-1.52	-67.63	2.2
1@CB[7]	-1.57	-51.71	3.0
2@CB[7]	-1.48	-50.64	3.0
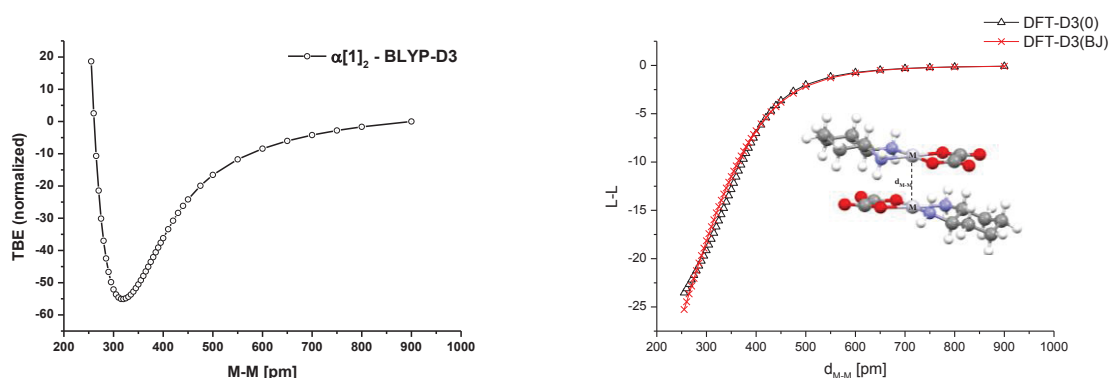
Figure A. 73. PEC for α-[1]$_2$ without (left) and with BJ-damping (right)
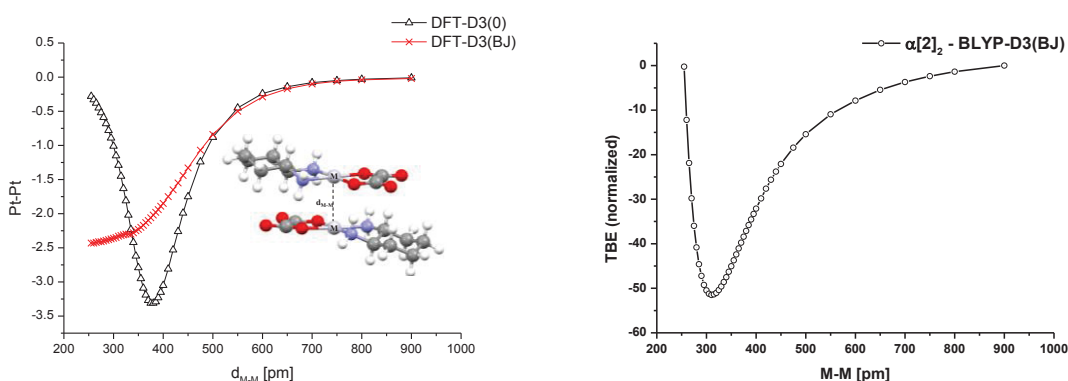
Figure A. 74. PEC for α-[2]$_2$ without (left) and with BJ-damping (right)
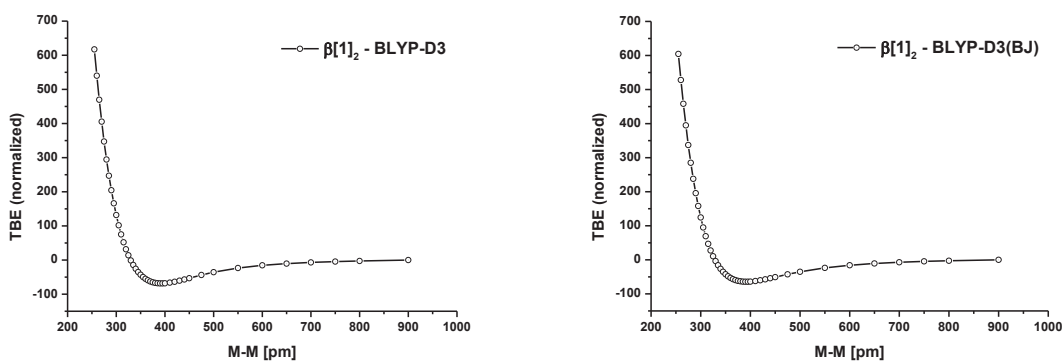
Figure A. 75. PEC for β-[1]$_2$ without (left) and with BJ-damping (right)
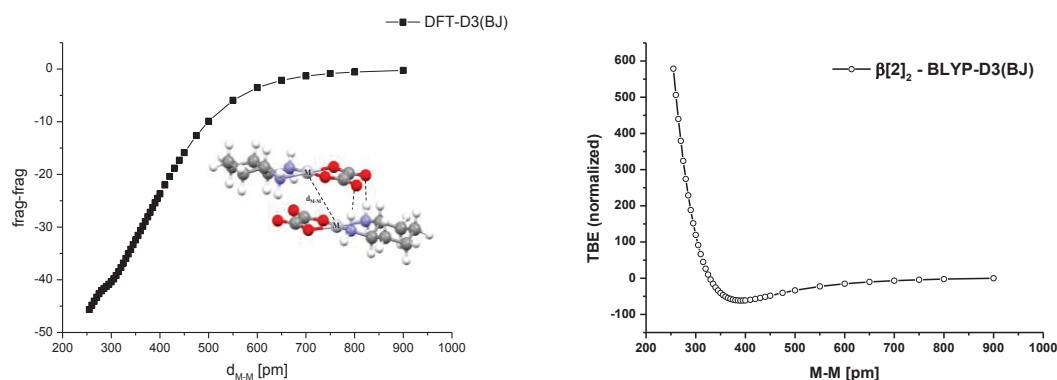
Figure A. 76. PEC for β-[2]₂ without (left) and with BJ-damping (right)
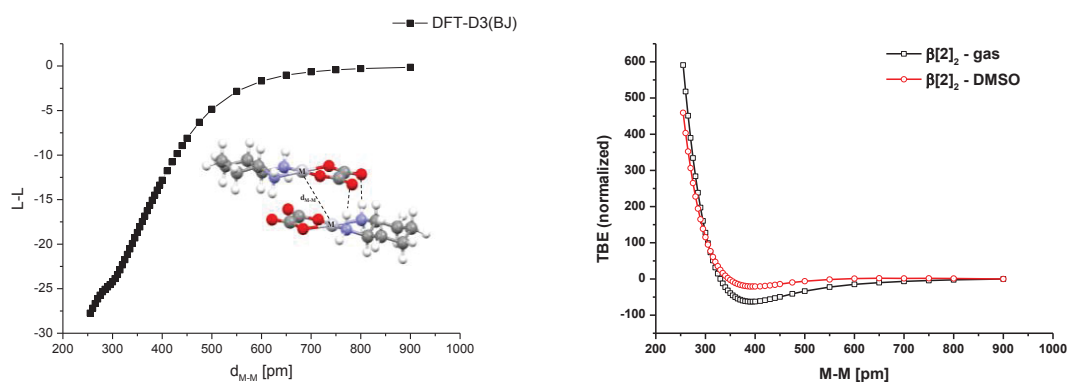
Figure A. 77.PEC for α-[2]₂ (left) and for β-[2]₂ (right) in gas phase and DMSO(COSMO)

Dispersion energy curves
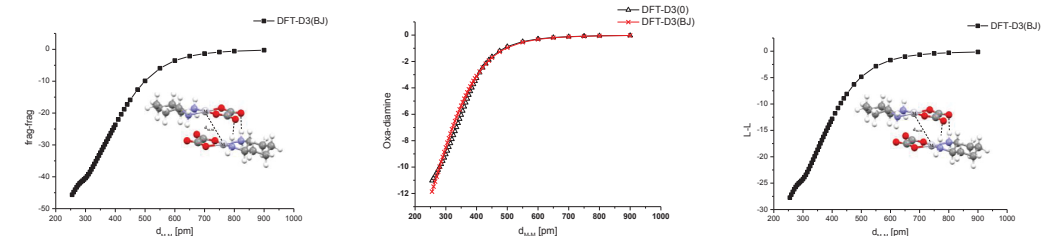
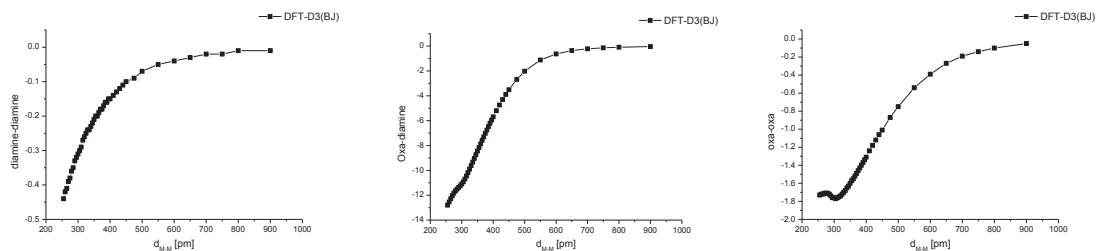Figure A. 78. DFT-D3 calculated for geometries optimized using BLYP-D3 with (ZORA)/AE-TZP level of theory for β-[1]₂
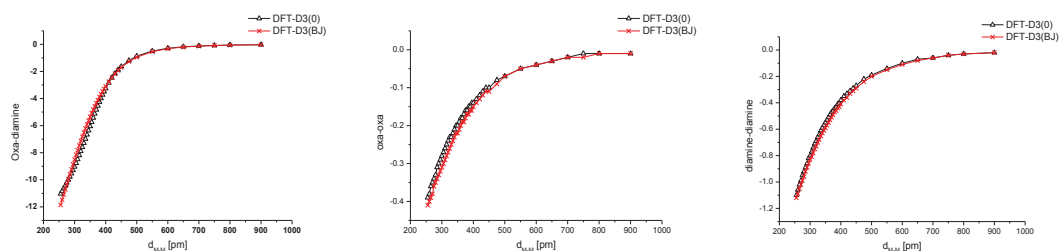
Figure A. 79. Dispersion energy contribution for interactions of predefined α–[1]₂ fragments: between oxalate and diamine ligand of different fragments, between two oxalates, between two diamine ligands.

Figure A. 80. Dispersion energy contribution for interactions of predefined β-[1]₂ fragments: between diamine ligands, between oxalate and diamine ligand of two different fragments, between two different oxalates.
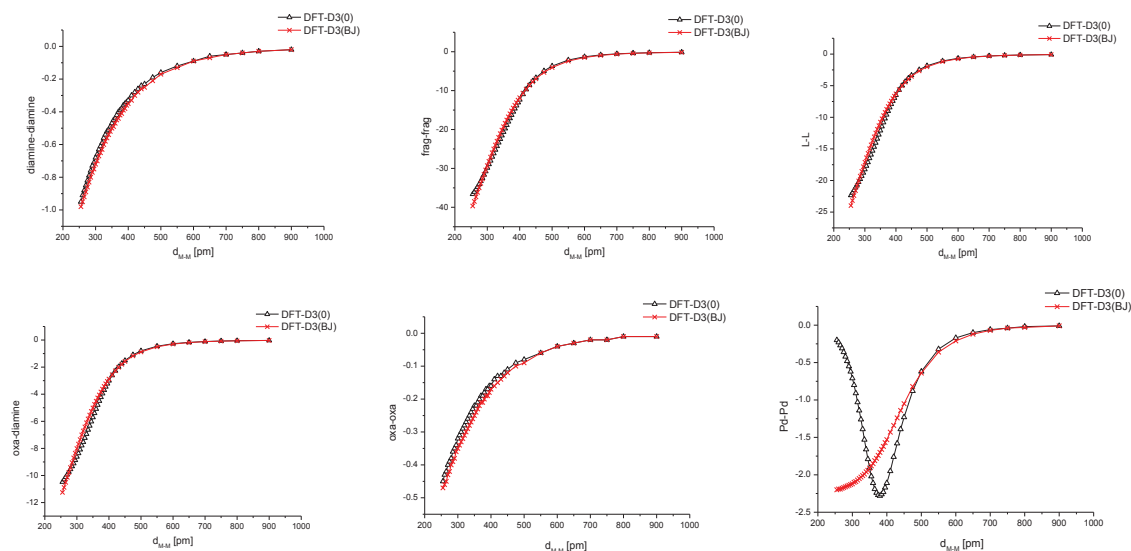
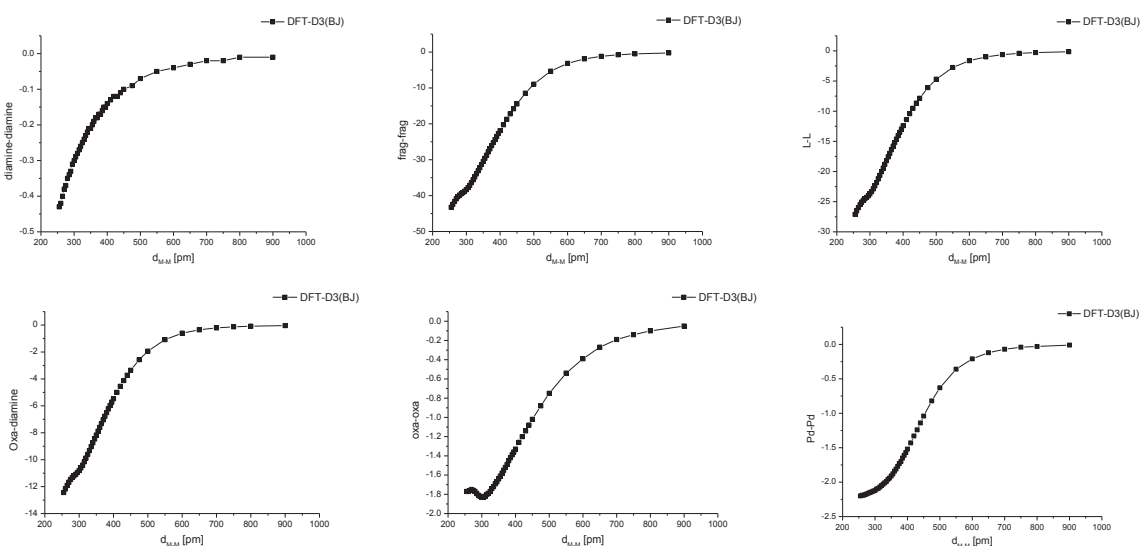Figure A. 81. Dispersion energy contribution for interactions of predefined α–[2]₂ fragments

Figure A. 82. Dispersion energy contribution for interactions of predefined β-[2]₂ fragments
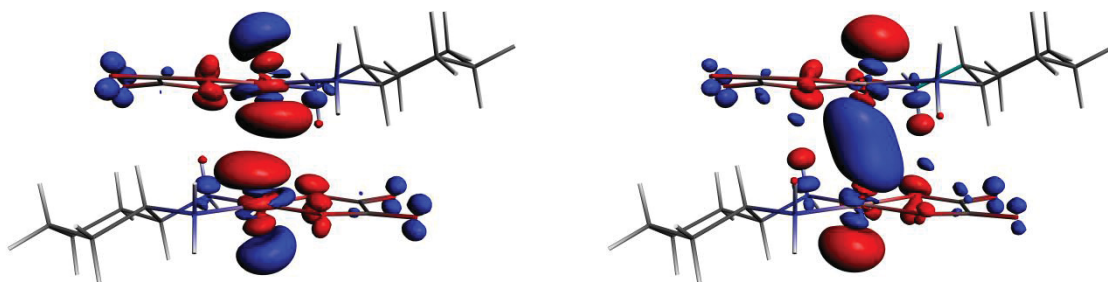
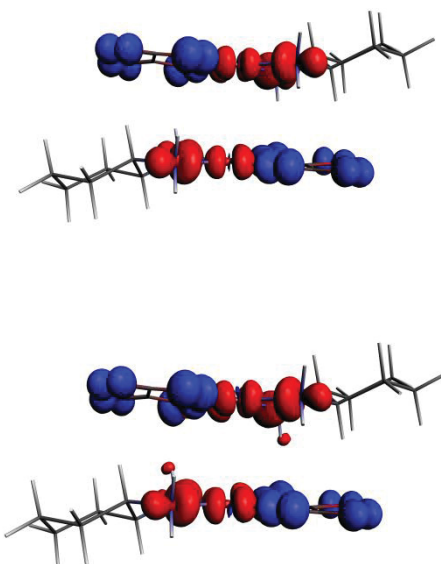**Analysis of the bonding interaction**

NOCV deformation densities

Figure A. 83. NOCV deformation density $\Delta\rho_1$ (left; ΔE_{orb} = -3.76 kcal/mol; ω = 14%) and $\Delta\rho_2$ (right; ΔE_{orb} = -2.94 kcal/mol; ω = 11%) for α–[**1**]$_2$

Figure A. 84. NOCV deformation density $\Delta\rho_1$ (left; ΔE_{orb} = -2.45 kcal/mol; ω = 10%) and $\Delta\rho_2$ (right; ΔE_{orb} = -2.47 kcal/mol; ω = 10%) for α–[**2**]$_2$
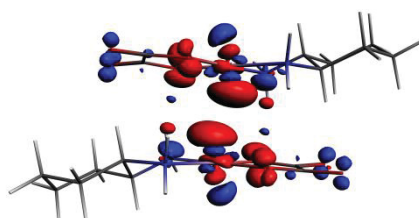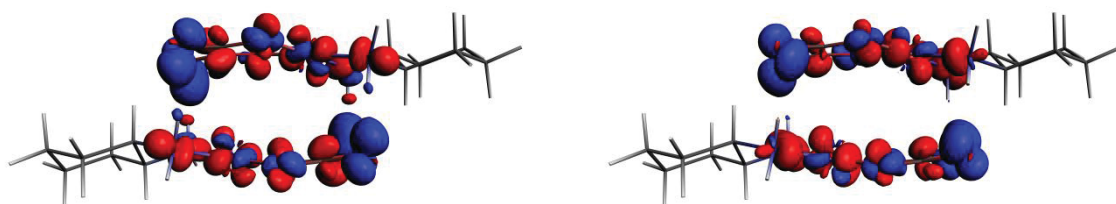

Figure A. 85. NOCV deformation density $\Delta\rho_3$ (ΔE_{orb} = -2.71 kcal/mol; ω = 11%) for α-[**2**]$_2$

Figure A. 86.NOCV deformation density $\Delta\rho_1$ (left; ΔE_{orb} = -4.87 kcal/mol; ω = 13%) and $\Delta\rho_3$ (right; ΔE_{orb} = -3.89 kcal/mol; ω = 10%) for β–[**2**]$_2$

Figure A. 87. NOCV deformation density $\Delta\rho_4$ (left; ΔE_{orb} = -4.13 kcal/mol; ω = 11%) and $\Delta\rho_5$ (right; ΔE_{orb} = -3.76 kcal/mol; ω = 10%) for β–[**2**]$_2$

Figure A. 88. NOCV deformation density $\Delta\rho_1$ (left; ΔE_{orb} = -7.63 kcal/mol; ω = 19%) and $\Delta\rho_2$ (right; ΔE_{orb} = -6.18 kcal/mol; ω = 15%) for α–[3]$_2$
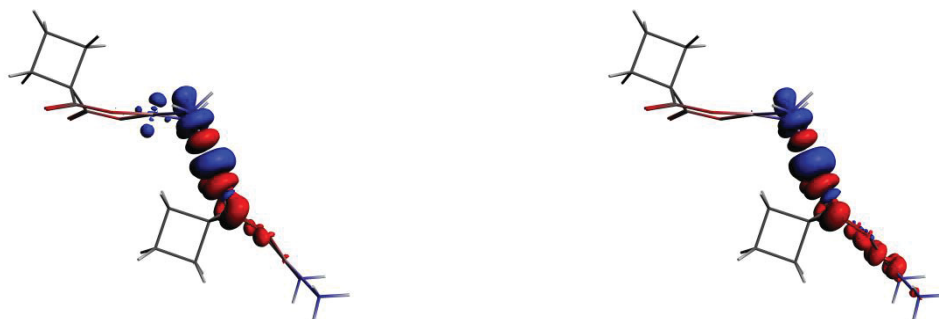

Figure A. 89. NOCV deformation density $\Delta\rho_1$ (left; ΔE_{orb} = -4.50 kcal/mol; ω = 30%) and $\Delta\rho_2$ (right; ΔE_{orb} = -4.19 kcal/mol; ω = 28%) for β–[**3**]$_2$
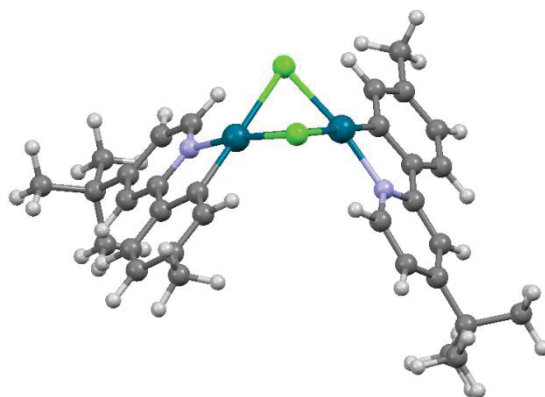
Figure A. 90. Optimized geometry for the [Pd(tBpTP)Cl]₂ complex in gas phase. Color code: Pd- blue; Cl- green; N- purple; C- gray; H- white
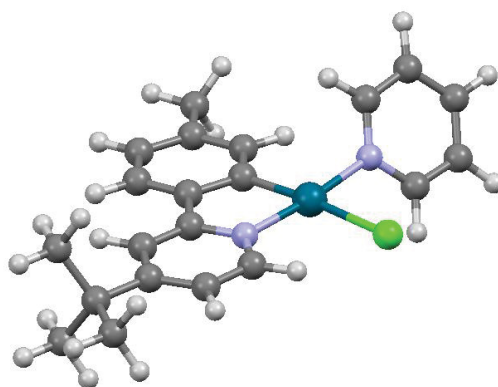

Figure A. 91. Optimized geometry for the [Pd(Pyr)(tBpTP)Cl] complex in gas phase. Color code: Pd- blue; Cl- green; N- purple; C- gray; H- white
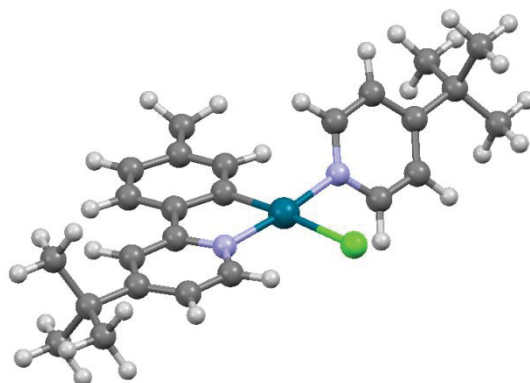

Figure A. 92. Optimized geometry for the [Pd(tBPyr)(tBpTP)Cl] complex in gas phase. Color code: Pd- blue; Cl- green; N- purple; C- gray; H- white

Figure A. 93. Optimized geometry for the [Pd(PPh₃)(tBpTP)Cl] complex in gas phase. Color code: Pd- blue; Cl- green; P- orange; N- purple; C- gray; H- white

Figure A. 94. Optimized geometry for the [Pd(PCy₃)(tBpTP)Cl] complex in gas phase. Color code: Pd- blue; Cl- green; P- orange; N- purple; C- gray; H- white
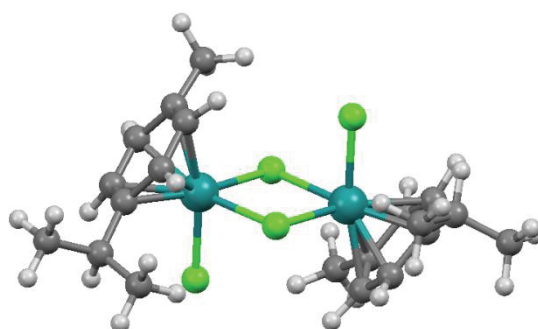
Figure A. 95. Optimized geometry for the [Ru(p-cym)Cl₂]₂ complex in gas phase. Color code: Ru- blue; Cl- green; C- gray; H- white
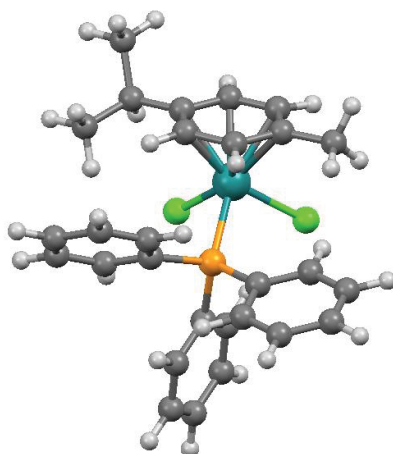
Figure A. 96. Optimized geometry for the [Ru(p-cym)(PPh$_3$)Cl$_2$] complex in gas phase. Color code: Ru- blue; Cl- green; P- orange; C- gray; H- white

Figure A. 97. Optimized geometry for the [Ru(p-cym)(Pyr)Cl$_2$] complex in gas phase. Color code: Ru- blue; Cl- green; N- purple; C- gray; H- white
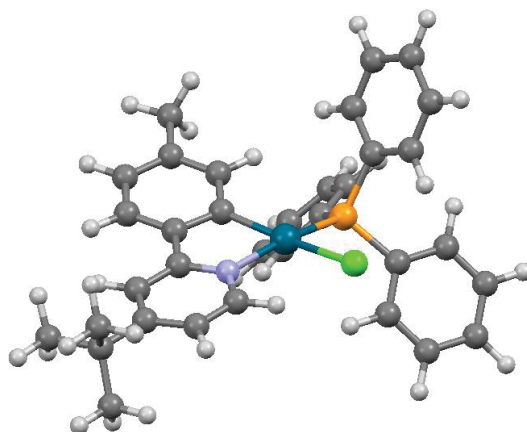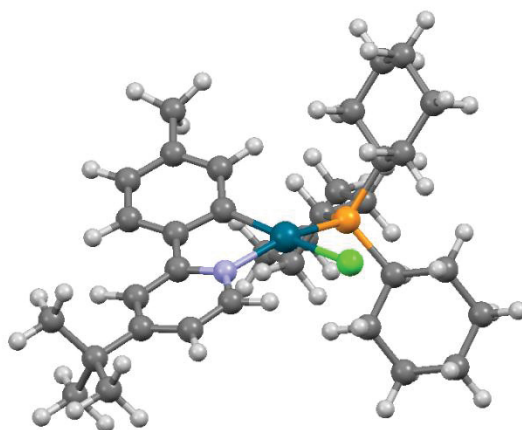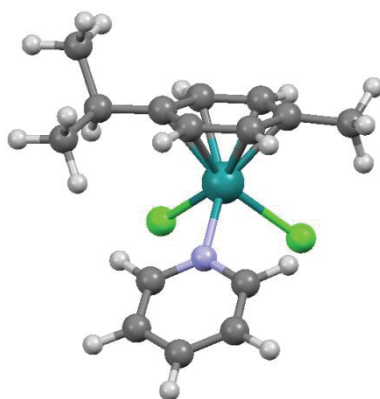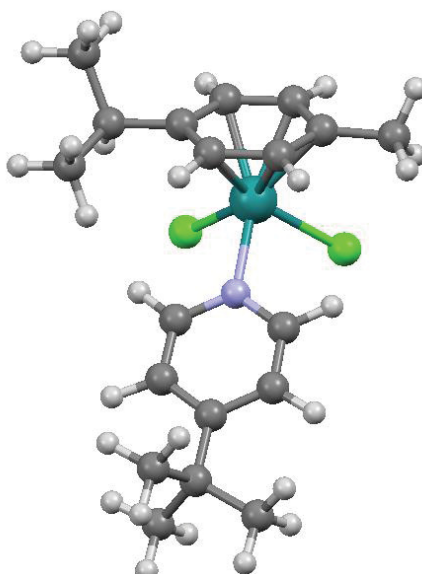

Figure A. 98. Optimized geometry for the [Ru(p-cym)(tBPyr)Cl$_2$] complex in gas phase. Color code: Ru- blue; Cl- green; N- purple; C- gray; H- white

Appendix

Publications:

A1. P. V. Petrović, G. V. Janjić, S. D. Zarić, *Stacking Interactions between Square-Planar Metal Complexes with 2,2'-Bipyridine Ligands. Analysis of Crystal Structures and Quantum Chemical Calculations*, Cryst. Growth Des., 2014, 14(8), 3880–3889.

A2. P. V. Petrović, S. Grimme, S. D. Zarić, M. Pfeffer and J.-P. Djukic, *Experimental and theoretical investigations of the self-association of oxaliplatin*, Phys. Chem. Chem. Phys., 2014, 16(28), 14688-14698.

A3. W. Iali, P. Petrovic, M. Pfeffer, S. Grimme and J.-P. Djukic, *The inhibition of iridium-promoted water oxidation catalysis (WOC) by cucurbit[n]urils*, Dalton Trans., 2012, 41, 12233-12243.

A4. A. Hansen, C. Bannwarth, S. Grimme, P. Petrović, C. Werlé and J.-P. Djukic, *The Thermochemistry of London Dispersion-Driven Transition Metal Reactions: Getting the 'Right Answer for the Right Reason'*, ChemistryOpen 2014, accepted, DOI: 10.1002/open.201402017

Predrag PETROVIĆ

Experimental and Theoretical Investigations of Intermetallic Interactions in Transition Metal Coordination and Organometallic Complexes

Résumé

Ce travail de thèse démontre l'importance d'intégrer des outils théoriques à des observations expérimentales dans le but d'étudier le rôle des interactions non-covalentes et plus précisément de la dispersion dans la chimie des métaux de transition. Plusieurs thèmes ont ainsi été abordés comme les interactions d'empilement entre chélates de métaux de transition à l'état solide; l'influence de la chiralité sur l'oligomérisation en solution de complexes plans carrés de Rh(I) isonitrile; la stabilité et inactivité inhabituelles de complexes de type cis-platine en solution concentrée. Les résultats obtenus par titration calorimétrique isotherme ont permis d'évaluer la capacité de méthodes théoriques à reproduire avec précision les résultats expérimentaux. Les calculs ont démontré qu'un traitement théorique approprié des effets de la dispersion et de la solvatation, donne des valeurs cohérentes avec les résultats expérimentaux. Cependant, des améliorations supplémentaires sont nécessaires.

Mots-clés : Dispersion, Théorie de la fonctionnelle de la densité, Complexes organométalliques, Interactions noncovalent, Calorimétrie, Titration calorimétrique isotherme, Benchmark, Etudes expérimentales et théoriques

Résumé en anglais

This thesis has shown the importance of integration of theoretical calculations and experimental investigations in studying the role of non-covalent interactions and particularly dispersion interactions in transition metal chemistry. Several subjects were addressed, such as stacking interactions of chelates in transition metal complexes in solid state, influence of chirality on the oligomerization of Rh(I) isonitrile complexes in solution and the stability of the cis-platin type complexes in concentrated solutions. Isothermal titration calorimetry proved to be very useful in the studies by providing accurate experimental data on the thermochemistry of addressed processes. This data was used to gauge the ability of the theoretical methods to accurately reproduce the experimental results. Calculations have shown that the proper treatment of dispersion effects and solvation by theoretical models gives values in relatively good agreement with experiments, but further improvements are needed.

Keywords : Dispersion, Density Functional Theory, Organometallic complexes, Non-covalent interactions, Calorimetry, Isothermal Titration Calorimetry, Benchmark, Experimental and theoretical investigations

BIOGRAFSKI PODACI

Predrag Petrović je rođen 19. februara 1983. godine u Brčkom, Bosna i Hercegovina. Završio je gimnaziju u Smederevu. Hemijski fakultet Univerziteta u Beogradu upisao je 2001. godine. Diplomirao je 2008. godine. Poslediplomske studije na Katedri za neorgansku hemiju Hemijskog fakulteta Univerziteta u Beogradu upisao je 2008. godine. Master tezu pod naslovom "*Steking interakcije između fenantrolinskih liganada u kristalnim strukturama kvadratno-planarnih kompleksa metala*" odbranio je 23. septembra 2010. godine i tako stekao zvanje *master hemičar*.

Zaposlen je kao istraživač saradnik u Inovacionom centru Hemijskog fakulteta.

Pedagoški rad

Predrag Petrović je izvodio vežbe na Hemijskom fakultetu Univerziteta u Beogradu iz sledećih predmeta:
- Neorganska hemija 2 (studijska grupa diplomirani hemičar, 2013.)

Studijski boravci i međunarodna saradnja

Kao stipendista DAAD fondacije boravio je na Maks Plank institutu za fizičku hemiju čvrstog stanja u Drezdenu, u periodu od septembra do decembra 2009. godine.

B. OBJAVLJENI NAUČNI RADOVI I SAOPŠTENJA

Rezultate svojih istraživanja objavio je u 6 naučnih radova publikovana u međunarodnim časopisima (4 rada u vrhunskim međunarodnim časopisima – M21 i 1 rad u istaknutom međunarodnom časopisu – M22) i 15 saopštenja na domaćim i međunarodnim naučnim skupovima.

Rad u vrhunskom međunarodnom časopisu (M21)

1. Wissam Iali, Predrag Petrović, Michel Pfeffer, Stefan Grimme and Jean-Pierre Djukic, **The inhibition of iridium-promoted water oxidation catalysis (WOC) by cucurbit[n]urils,** Dalton Trans, 2012, 41, 12233-12243 **(IF=3,806)**
2. Predrag V. Petrović, Goran V. Janjić, Snežana D. Zarić, **Stacking interactions between square-planar metal complexes with 2, 2'-bipyridine ligands. Analysis of the crystal structures and quantum chemical calculations,** Cryst. Growth Des., 2014, 14(8), 3880-3889 **(IF=4,558)**
3. Predrag V. Petrović, Stefan Grimme, Snežana D. Zarić, Michel Pfeffer and Jean-Pierre Djukic, **Experimental and theoretical investigations on the self-association of Oxaliplatin**, Phys. Chem. Chem. Phys., 2014, 16(28), 14688-14698 **(IF= 3,829)**
4. A. Hansen, C. Bannwarth, S. Grimme, P. Petrović, C. Werlé and J.-P. Djukic, **The Thermochemistry of London Dispersion-Driven Transition Metal Reactions: Getting the „Right Answer for the Right Reason"**, ChemistryOpen, 2014, accepted, DOI: 10.1002/open.201402017 **(IF=2,938)**

Rad u istaknutom međunarodnom časopisu(M22)

1. Goran V. Janjić, Predrag Petrović, Dragan Ninković, Snežana D. Zarić, **Geometries of stacking interactions between phenanthroline ligands in crystal structures of square-planar metal complexes**, J. Mol. Model., 2011, 17(8), 2083-92 **(IF=1,797)**

Rad u međunarodnom časopisu (M23)

1. G. V. Janjić, P. Petrović, D. B. Ninković, D. Ž. Veljković, A. Kapor and S. D. Zarić, S**tacking interactions between pyridine fragments in crystal structures of terpyridyl complexes,** Studia UBB *Chemia*, 2010, *LV*, 3. **(IF=0,231)**

Saopštenja sa međunarodnog skupa štampana u celini (M33)

Prezentacija u vidu postera:

1. Snežana Zarić, Goran Janjić, Dragan Ninković, Predrag Petrović, **Stacking interactions between phenantroline ligands in crystal structures of square-planar metal complexes***, 10th International Symposium on Metal Elements in Environment, Medicine and Biology, Timisoara, Romania, November, 2010.

Saopštenja sa međunarodnog skupa štampana u izvodu (M34)

Saopštenja u vidu postera:

1. D. Ninković, **P. Petrović**, G. Janjić, **Stacking interaction between 1, 10-phenanthroline ligands in crystal structures of metal complexes**, Humbolt conference on noncovalent interactions, Vršac, Serbia, 15-18.11.2007.
2. S. D. Zarić, G. Janjić, D. Sredojević, D. Veljković, J. Andrić, D. Ninković, **P. Petrović**, D. Vojislavljević, **Noncovalent interactions of aromatic molecules**, XXII Congress and General Assembly of the International Union of Crystallography, Madrid, Spain, 2011.
3. D. B. Ninković, **P. V. Petrović**, G. V. Janjić, S. D. Zarić, **Crystalographyc analysis of stacking interactions between phenanthroline ligands**, Workshop on crystal engineering, University of Fribourg, Switzerland, 23-25.07.2012
4. Snežana Zarić, Goran Janjić, Dragan Ninković, **Predrag Petrović**, **The structural and photochemical properties of metal complexes with phenantroline ligands**, International Workshop – Sensing Applications of Supramolecular Chemistry, SupraChem@Balkans.eu, Plovdiv, Bulgaria, Mart, 2013
5. Jean-Pierre Djukic, **Predrag Petrović**, Stefan Grimme, Michaele Pfeffer, Wissam Iali, **The inhibition of iridium-promoted water oxidation catalysis (woc) by cucurbitnurils**, International Workshop – Sensing Applications of Supramolecular Chemistry, SupraChem@Balkans.eu, Plovdiv, Bulgaria, Mart, 2013

6. Snežana Zarić, Goran Janjić, **Predrag Petrović**, Dušan Sredojević, **Study of the stacking interactions in squere-planar metal complexes with 2,2'-bipyridine ligands**, International Summer School on Supramolecular Chemistry, SupraChem@Balkans.eu, Belgrade, Serbia, August, 2013

7. Snežana Zarić, Goran Janjić, **Predrag Petrović**, Suzana Đurđević, **Study of Cl…π interactions with parallel orientation of aromatic rings**, International Summer School on Supramolecular Chemistry, SupraChem@Balkans.eu, Belgrade, Serbia, August, 2013

8. S. D. Zarić, G. V. Janjić, D. N. Sredojević, D. Veljković, J. Andrić, D. Ninković, D. Vojislavljević, **P. Petrović**, **Noncovalent interactions of aromatic molecules**, IUPAC, 44th World Chemistry Congres, Istanbul, Turkey, August 11-16, 2013.

9. **Predrag V. Petrović**, Jean-Pierre Djukic, Stefan Grimme, Snežana D. Zarić, **On the self-agregation of oxaliplatin in solution and in the gas phase: experimental and theoretical investigations on the origins of self-association,** 9th European Conference of Computational Chemistry (EuCo-CC9), Sopron, Hungary, September 2013

10. S. D. Zarić, G. V. Janjić, D. Sredojević, D. Ž. Veljković, J. Andrić, D. Ninković, D. Vojislavljavić, **P. Petrović**, **Noncovalent interactions in systems with aromatic molecules and metal ions**, Modeling Interactions in Biomolecules, Marianske Lazne, Czech Republic, September 16-19, 2013.

Saopštenja sa skupa nacionalnog značaja štampana u izvodu (M64)

Usmena prezentacija:

1. **P. Petrović**, S. Grimme, S. Zarić, J. Djukic, **Understanding so-called d^{10}-d^{10} interactions: their actual role in the oligomerization of anti-cancer Pt compounds and the role of the dispersion,** Journée des doctorants en chimie 2012, Strasbourg, France, Nov 2012

2. **P.V. Petrović**, G.V. Janjić, D.N. Sredojević, S.D. Zarić, **Stacking interactions between 2, 2'-bipyridine ligands in crystal structures of square-planar metal complexes,** XX Conference of Serbian Crystallographic Society, Beograd, Serbia, Jun 2013

Prezentacija u vidu postera:

1. D. Ninković, **P. Petrović**, G. Janjić, S. Zarić, **Crystal packing in crystal structures of metal complexes with 1,10-phenanthroline ligands**, 46th Meeting of Serbian Chemical Society, Beograd, Serbia, 21. feb. 2008.

2. D. Ninković, **P. Petrović**, G. Janjić, S. Zarić, **Study of Stacking Interactions in Crystal Structures in Square-planar and Tetrahedral Metal Complexes With Phenantroline Ligands**, XV Konferencija Srpskog Kristalografskog Društva, Donji Milanovac, jul 2008

Прилог 1.

1 Изјава о ауторству

Потписани-а   <u>Предраг Петровић</u>

број индекса   <u>ДХ27/2010</u>

Изјављујем

да је докторска дисертација под насловом

<u>Експериментално и теоријско испитивање интерметалних интеракција у координацији прелазних метала и органометалним комплексима</u>

- резултат сопственог истраживачког рада,

- да предложена дисертација у целини ни у деловима није била предложена за добијање било које дипломе према студијским програмима других високошколских установа,

- да су резултати коректно наведени и

- да нисам кршио/ла ауторска права и користио интелектуалну својину других лица.

Потпис докторанда

У Београду,   <u>07.10.2014.</u>

                               _____

Прилог 2.

2 Изјава о истоветности штампане и електронске верзије докторског рада

Име и презиме аутора   Предраг Петровић

Број индекса   ДХ27/2010

Студијски програм   Доктор хемијских наука

Наслов рада:

Експериментално и теоријско испитивање интерметалних интеракција у координацији прелазних метала и органометалним комплексима

Ментори   др Снежана Зарић и др Jean-Pierre Djukic

Потписани/а   Предраг Петровић

Изјављујем да је штампана верзија мог докторског рада истоветна електронској верзији коју сам предао/ла за објављивање на порталу **Дигиталног репозиторијума Универзитета у Београду.**

Дозвољавам да се објаве моји лични подаци везани за добијање академског звања доктора наука, као што су име и презиме, година и место рођења и датум одбране рада.

Ови лични подаци могу се објавити на мрежним страницама дигиталне библиотеке, у електронском каталогу и у публикацијама Универзитета у Београду.

Потпис докторанда

У Београду,   07.10.2014.

_____

Прилог 3.

3   Изјава о коришћењу

Овлашћујем Универзитетску библиотеку „Светозар Марковић" да у Дигитални репозиторијум Универзитета у Београду унесе моју докторску дисертацију под насловом:

Експериментално и теоријско испитивање интерметалних интеракција у координацији прелазних метала и органометалним комплексима

која је моје ауторско дело.

Дисертацију са свим прилозима предао/ла сам у електронском формату погодном за трајно архивирање.

Моју докторску дисертацију похрањену у Дигитални репозиторијум Универзитета у Београду могу да користе сви који поштују одредбе садржане у одабраном типу лиценце Креативне заједнице (Creative Commons) за коју сам се одлучио/ла.

1. Ауторство

2. Ауторство - некомерцијално

3. Ауторство – некомерцијално – без прераде

4. Ауторство – некомерцијално – делити под истим условима

5. Ауторство – без прераде

6. Ауторство – делити под истим условима

(Молимо да заокружите само једну од шест понуђених лиценци, кратак опис лиценци дат је на полеђини листа).

Потпис докторанда

У Београду,   07.10.2014

_____

1. Ауторство - Дозвољавате умножавање, дистрибуцију и јавно саопштавање дела, и прераде, ако се наведе име аутора на начин одређен од стране аутора или даваоца лиценце, чак и у комерцијалне сврхе. Ово је најслободнија од свих лиценци.

2. Ауторство – некомерцијално. Дозвољавате умножавање, дистрибуцију и јавно саопштавање дела, и прераде, ако се наведе име аутора на начин одређен од стране аутора или даваоца лиценце. Ова лиценца не дозвољава комерцијалну употребу дела.

3. Ауторство - некомерцијално – без прераде. Дозвољавате умножавање, дистрибуцију и јавно саопштавање дела, без промена, преобликовања или употребе дела у свом делу, ако се наведе име аутора на начин одређен од стране аутора или даваоца лиценце. Ова лиценца не дозвољава комерцијалну употребу дела. У односу на све остале лиценце, овом лиценцом се ограничава највећи обим права коришћења дела.

 4. Ауторство - некомерцијално – делити под истим условима. Дозвољавате умножавање, дистрибуцију и јавно саопштавање дела, и прераде, ако се наведе име аутора на начин одређен од стране аутора или даваоца лиценце и ако се прерада дистрибуира под истом или сличном лиценцом. Ова лиценца не дозвољава комерцијалну употребу дела и прерада.

5. Ауторство – без прераде. Дозвољавате умножавање, дистрибуцију и јавно саопштавање дела, без промена, преобликовања или употребе дела у свом делу, ако се наведе име аутора на начин одређен од стране аутора или даваоца лиценце. Ова лиценца дозвољава комерцијалну употребу дела.

6. Ауторство - делити под истим условима. Дозвољавате умножавање, дистрибуцију и јавно саопштавање дела, и прераде, ако се наведе име аутора на начин одређен од стране аутора или даваоца лиценце и ако се прерада дистрибуира под истом или сличном лиценцом. Ова лиценца дозвољава комерцијалну употребу дела и прерада. Слична је софтверским лиценцама, односно лиценцама отвореног кода.